Liquid Rocket Motor Combustion Stability Using Coaxial Injectors and Supercritical Droplet Combustion and Dynamics

Final Report
Submitted to

Air Force Office of Scientific Research
AFOSR/NA
Bolling AFB, D.C. 20332-0001

Prepared
by

Michael M. Micci and Vigor Yang
The Pennsylvania State University
Propulsion Engineering Research Center
University Park, PA 16802

May 1995

DISCLAIMER NOTICE

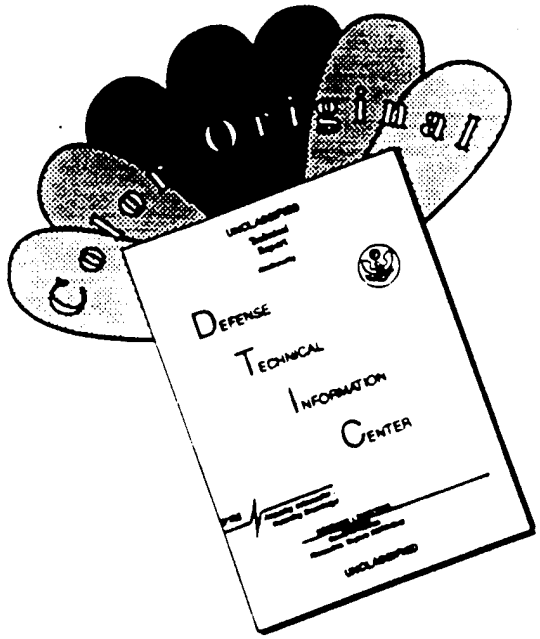

THIS DOCUMENT IS BEST QUALITY AVAILABLE. THE COPY FURNISHED TO DTIC CONTAINED A SIGNIFICANT NUMBER OF COLOR PAGES WHICH DO NOT REPRODUCE LEGIBLY ON BLACK AND WHITE MICROFICHE.

Liquid Rocket Motor Combustion Stability Using Coaxial Injectors and Supercritical Droplet Combustion and Dynamics

Final Report
Submitted to

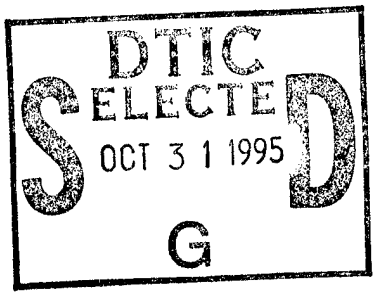

Air Force Office of Scientific Research
AFOSR/NA
Bolling AFB, D.C. 20332-0001

Prepared
by

Michael M. Micci and Vigor Yang
The Pennsylvania State University
Propulsion Engineering Research Center
University Park, PA 16802

May 1995

REPORT DOCUMENTATION PAGE

Form Approved
OMB No 0704-0188

1. AGENCY USE ONLY (Leave blank)	2. REPORT DATE	3. REPORT TYPE AND DATES COVERED
	31 May 95	Final Technical Report

4. TITLE AND SUBTITLE
Liquid Rocket Motor Combustion Stability Using Coaxial Injectors and Supercritical Droplet Combustion and Dynamics

5. FUNDING NUMBERS
PE - 61102F
PR - 2308
SA - AS
G - F49620-93-1-0126

6. AUTHOR(S)
Michael M. Micci and Vigor Yang

7. PERFORMING ORGANIZATION NAME(S) AND ADDRESS(ES)
Pennsylvania State University
111 Research Building East
University Park, PA 16802

8. PERFORMING ORGANIZATION REPORT NUMBER

9. SPONSORING / MONITORING AGENCY NAME(S) AND ADDRESS(ES)
Dr. Mitat A. Birkan
AFOSR/NA
110 Duncan Ave., #B115
Bolling AFB, DC 20332-0001

10. SPONSORING / MONITORING AGENCY REPORT NUMBER

11. SUPPLEMENTARY NOTES

12a. DISTRIBUTION / AVAILABILITY STATEMENT
Approved for public release; distribution is unlimited

12b. DISTRIBUTION CODE

13. ABSTRACT *(Maximum 200 words)*

Cold-flow experiments with a full-size SSME preburner shear coaxial injector element using liquid and gaseous nitrogen at pressures up to 4 MPa showed that the intact liquid core decreased in length with increasing chamber pressure up to the critical pressure, after which it increased in length. Increasing the liquid to gas mass flow rate ratio resulted in an increase in the length of the liquid core. LDV measurements showed flow recirculation downstream of the LOX post. Results from a linearized model of the injector, combustion and vaporization processes compared well to unsteady pressure measurements made during liquid oxygen/gaseous hydrogen hot-fire tests.

Vaporization and combustion of liquid droplets in both subcritical and supercritical environments have been studied systematically. A variety of liquid propellants and propellant simulants, including hydrocarbon and cryogenic fluids, in both steady and oscillatory environments were treated numerically. Because the model allows solutions from first principles, a systematic examination of the droplet behavior over wide ranges of pressure, temperature, and ambient flow velocity is made possible. Results can not only enhance the basic understanding of the problem, but can also serve as a basis for establishing droplet vaporization and combustion correlations for the study of liquid rocket engine combustion, performance, and stability.

14. SUBJECT TERMS	15. NUMBER OF PAGES
atomization; droplet vaporization and combustion; combustion instability.	16. PRICE CODE

17. SECURITY CLASSIFICATION OF REPORT	18. SECURITY CLASSIFICATION OF THIS PAGE	19. SECURITY CLASSIFICATION OF ABSTRACT	20. LIMITATION OF ABSTRACT
Unclassified	Unclassified	Unclassified	UL

LIQUID MOTOR COMBUSTION STABILITY USING COAXIAL INJECTORS

Final Report
for the period
2/1/93 - 5/31/95

Submitted to:

Air Force Office of Scientific Research
Bolling AFB, DC 20332-0001

By:

Michael M. Micci
Department of Aerospace Engineering
The Pennsylvania State University
University Park, PA 16802

STATEMENT OF WORK

1. Use a Phase Doppler Particle Analyzer to measure the spray size and velocity distribution from shear coaxial injectors under steady conditions as a function of the relative gas/liquid velocity. Liquid oxygen will be used for the central liquid flow and either nitrogen or helium for the outer annular gas. The possibility of using gaseous hydrogen for the final series of tests will be examined. Use a laser diode LDV with a transparent injector to examine the recirculation region at the base of the injector. The following parameters will be investigated:

   a) Chamber pressures up to 1500 psia.

   b) Injector design in terms of flow area ratio, LOX post tip land width and liquid flow recess distance.

2. Use the measured spray size and velocity distributions as input to Penn State numerical codes to examine the effects of atomization on predicted motor stability and to establish an experimental database to provide guidance towards the development of an atomization model. Compare results to hydrogen temperature ramping test results where available (NASA Lewis, Rocketdyne).

3. Examine the effect of injector pressure drop on propellant feed system caused combustion instabilities. Experimentally characterize the effects of operating conditions and injector design on injector pressure drop.

4. Measure droplet sizes and velocities under combusting supercritical conditions using a PDPA. Investigate the effects of relative gas/liquid velocities and injector geometry. Attempt to examine the recirculation region at the base of the LOX post by means of a laser diode LDV system. Examine any effects of either the combustion process or the supercritical conditions on the injector pressure drop.

5. Use the measured droplet sizes and velocities under combusting supercritical conditions as input to the chamber stability codes developed at Penn State as well as provide the guidance for the development of injector atomization models.

PROGRESS AND ACCOMPLISHMENTS

Experimental Facility

Cold flow experiments with liquid nitrogen were conducted at the Cryogenic Combustion Facility of The Pennsylvania State University. The facility was designed for hot fire testing of subscale rocket engines using liquid oxygen and gaseous hydrogen as the propellant and can accommodate other propellant combinations under hot fire or cold flow conditions. Facility performance is rated at 0.45 kg/s of liquid oxygen and 0.11 kg/s of gaseous hydrogen for chamber pressures up to approximately 100 bars. The propellant feed system is divided into two gas supply lines for primary and secondary gas flows and a cryogenic liquid supply line which includes a 114 liter vacuum jacketed storage tank, tank pressurization system, and liquid nitrogen cooling jacket. Flow metering was accomplished with critical flow venturies fitted with pressure transducers and thermocouples upstream and downstream of the venturi.

The pressure vessel was designed for cold flow operation at pressures up to 100 bars. The interior dimensions of 4 inches square by 9 inches long permit the investigation of the complete spray field while avoiding window contamination by impinging droplets. There are four gas ports around the injector to provide additional gas for chamber pressurization and window purging. Pressure and temperature are measured in the chamber as well as in the injector plenum region upstream of the fuel annulus and in the cryogenic liquid supply line. To facilitate axial and radial scans of the injector spray, the entire chamber was mounted on a 2-D translation table. Positioning in the radial direction was performed by a stepping motor while axial positioning required manual operation.

Photographic Studies of Shear Coaxial Injectors Using Liquid/Gaseous Nitrogen

Two flow visualization techniques were pursued to examine the overall structure and break-up processes of the LN_2/GN_2 spray under varying conditions. The first approach to visualize the spray involved the imaging of Mie scattered light from a thin laser sheet passing through the axis of the spray. A frequency doubled Nd:YAG laser (532 nm) pulsed at 10 Hz with a pulse duration of 10 ns provided the light source while a lens pair consisting of a spherical and cylindrical lens formed the laser sheet. The scattered light was collected at 90 degrees to the sheet with a 35 mm Nikon camera. To eliminate ambient light, a 1 nm bandpass filter centered at 532 nm was installed in front of the camera lens.

Although the laser sheet photographs provided useful images of the overall structure of the dense liquid core region, minimal information was available on the distribution of LN_2 droplets within the spray field. Since this information is of value in determining optimal regions for PDPA measurements, a modified approach was then undertaken wherein a strobe light replaced the pulsed laser sheet for spray illumination. The strobe light was directed toward the back side of the spray, off center from the camera in the direction of the injector face. With this orientation both the liquid core region and regions of high number density and large droplet concentrations could be detected. The flash duration of the strobe was 3 μs at a frequency of 10 Hz.

The objective of the LN_2/GN_2 tests was to characterize the effects of chamber pressure and liquid to gas mixture ratio on the atomization and vaporization of liquid nitrogen serving as a simulant to liquid oxygen. The baseline dimensions of the shear coaxial injector were derived from the dimensions of the prototype injector element of the fuel preburner to the Space Shuttle's main engine. A second LOX post was fabricated with a 7° taper at the tip to match the shape of the production injector element. Pressure and temperature were measured in the fuel plenum region upstream of the fuel annulus and in the cryogen supply line at the entrance to the LOX post. For the elevated pressures required of LN_2 testing, a pressure chamber was constructed to operate at pressures up to 10.0 MPa and to provide optical access. Flow visualization tests were performed with the nontapered LOX post at chamber pressures between 2.2 and 4.1 MPa and at two liquid to gas mixture ratios of 0.80 and 1.58. To determine if any observable differences in liquid atomization exists between the two LOX post designs, several stroboscope tests were conducted with both LOX posts operating at the same mixture ratio and at chamber pressures from 2.2 to 3.29 MPa.

The first series of tests illustrated the effect of chamber pressure on the overall spray morphology of the coaxial injector using the nontapered LOX post. Details are given in Ref. 1 (Appendix A) and are briefly summarized here. The photographs were imaged with the laser sheet. It is expected that in the case of large, dispersed sprays differences in the gas temperature may influence the behavior of the spray downstream of the dense liquid core region but should not affect significantly the breakup behavior of the liquid jet or the distribution of droplets around the jet, since the conditions in this region are better represented by the gas injection temperature. In general, the photographs depict an overall contraction of the large scale liquid structures (liquid core and detached ligaments) and droplet flow regions with increasing ambient pressure. Regions of droplet flow are most evident

downstream of the liquid structures, while very little droplet production is observed along the liquid column close to the injector exit. With rising chamber pressure the gas density enhances the breakup of the jet, but reduces secondary atomization due to a decrease in the slip velocity between the gas and droplet[2]. The large gas mass flux appears to have rapidly vaporized droplets surrounding the core except for those in the shadow of the LN_2 jet, a region characterized by lower gas temperatures and velocities.

In a second series of tests the gas mass flow rate was decreased to approximately half of the value of the previous tests, while the chamber pressure was varied from 2.34 MPa to 2.79 MPa. The photographic results of these tests were obtained as well with the laser sheet visualization technique. Overall, the reduction in gas mass flow rate resulted in a larger, more dispersed spray indicating a strong effect of mixture ratio on the atomization and vaporization of liquid nitrogen. The behavior of the spray with respect to increasing chamber pressure followed the same trend as before, in that the LN_2 spray contracts in size as the chamber pressure increases.

A third series of tests were performed with the tapered LOX post using the stroboscope to visualize the spray. The stroboscopic image provides more detail on the structure of the liquid core and detached ligaments than the laser sheet images but less information on the droplet flow region. Contradictory to the previously observed contraction of the spray with increasing pressure, the liquid core breakup length significantly increased for a chamber pressure greater than the critical pressure (3.4 MPa). This behavior may be attributed to the drop in relative velocity between the gas and liquid at very high chamber pressures, which may surpass any enhancements to liquid breakup due to increased gas density, and may be related as well to the increase in droplet evaporation times observed in the supercritical region[3]. Stroboscope tests with the nontapered LOX post under similar operating conditions revealed the same behavior for pressures above and below the critical point but indicated little differences in spray morphology between the two LOX post designs.

PDPA Studies of Shear Coaxial Injectors Using Water/Air

The injector was operated at 6.0 g/s of water and 3.7 g/s of air using both the tapered and non-tapered LOX post recessed inside the annulus. Data on droplet mean velocity, mean size, number density and volume flux were obtained as a function of radial position at 5 cm downstream of the injector face. The spray data depicted noticeable differences between the two sprays. The velocities on the injector centerline are approximately equal

for both configurations but depart outward in the spray. A more rapid drop in axial velocity for the tapered post suggests that the droplets are traveling faster in the radial direction than in the axial direction. With the tapered post smaller Sauter mean diameters are found on the centerline and increase radially outward in the spray. Overall, the tapered LOX post produced smaller droplets within the region of the spray probed with the PDPA. In the case of the tapered post the distribution of volume flux is rather uniform throughout the spray as compared to the steep distribution obtained for the nontapered post. The occurrence of this distribution is due to the opposite trends between the mean velocity and the number density and drop size. That is, the steep velocity profile compensates for the hollow cone distribution in drop size and number density to create the uniform volume flux distribution. Based on this distribution the mixing efficiency of the tapered post is higher than that of the nontapered post.

Recirculation Region

The original injector design with the straight LOX post was modified in order to allow LDV access into the recess region by inserting a Pyrex tube concentrically around the LOX post, such that the fuel annulus was defined by a transparent boundary 1.02 mm thick. The inner diameter of the Pyrex fuel annulus was 5.00 mm. All measurements were taken using Aerometrics' Phase Doppler Particle Analyzer (PDPA) with the droplet diameter measurement function disabled. Measurements of mean axial velocity were taken inside the injector recess region as well as downstream of the injector. Water was used as the LOX simulant and either air or gaseous nitrogen for the gaseous fuel simulant. The air flow rate was 1.8 g/s and the water flow rates were either 1.9 or 4.5 g/s. Downstream of the injector face only positive velocities were measured. It was found that the velocity drops to a negative value (reverse flow) approximately 0.5 mm downstream of the LOX post base before becoming positive. Larger negative values of the velocity were observed for lower liquid flow rates. Thus it appears that gas recirculation does exist in the recess region of a shear coaxial injector element and that the strength of the recirculation is a function of the operating conditions.

Injector Coupling

Some previous experimental evidence has indicated that the spontaneous instability condition for a hydrogen/oxygen rocket was determined by the hydrogen pressure drop through the injector[4,5]. Below a critical

minimum value for the pressure drop, chamber oscillations evidently can couple to the propellant feed system, causing a combustion instability in the chamber. However, the value of this critical pressure drop was a function of the injector and chamber design.

A simple model based on the Rayleigh criterion was constructed for the flow dynamics of several processes in the system to determine the effect of various design and operating parameters on combustion stability. The mechanisms included are the fuel flow through the injector, the vaporization of oxidizer in the chamber, and the flow of exhaust gases through the nozzle.

The Rayleigh criterion states that a wave will grow if heat or mass is added in phase with pressure. Conversely, the wave will damp if the addition is out of phase. If several mechanisms are contributing to the heat or mass release, then the wave growth is determined by the net in-phase or out-of-phase heat or mass addition. By assuming that both the heat or mass addition and the pressure oscillations can be represented by a perturbation added to their steady state values, linear models of the dynamic response of the processes may be obtained. A response factor is defined as the real, or in-phase, part of the mass flow perturbation with respect to the chamber pressure perturbation. The response factor can be either positive or negative depending on the phase angle between the pressure and flow perturbations.

A lumped-element model was developed similar to Reference 6 to determine the dynamic response of the fuel flow through the injector. The flow through the dome, the orifice flow into the entrance of the annulus and the flow through the annulus are represented by perturbation forms of the mass and momentum balances. The pressure at the exit of the annulus was assumed to equal the mean chamber pressure. These equations may be combined to give the transfer function and inverting this transfer function gives the amplitude and phase shift.

The injector response factor was calculated as a function of frequency and gaseous fuel temperature for the experimental conditions experienced during the cold-flow LN_2/GN_2 experiments. During these experiments, high frequency pressure oscillations were measured in the chamber and the injector fuel plenum. The recorded high frequency pressure oscillations were spectrally analyzed to determine the frequencies and magnitudes of any acoustic oscillations within either the chamber or the injector fuel plenum. Oscillations at the same frequency in both the chamber and the plenum were found at two frequencies. It was found that at the frequency where the injector was more strongly damping, the experimentally measured ratio of the pressure oscillation amplitude in the chamber to

the amplitude in the plenum was less.

Subscale Hot-Fire Rocket Combustion Chamber

Injector faceplates of several existing and proposed liquid propellant rocket engines were reviewed to ascertain the local grouping of injector elements around a single element. Although combustion chambers are generally cylindrical in design, the immediate boundary of a single injector element is more accurately represented by a hexagon formed by six adjacent injector elements. A hexagon enclosing a 2.82 cm circle was selected for the chamber interior cross-section allowing flat windows for optical access for laser based diagnostic devices. With the six sided polygon flat windows can be mounted onto the chamber at opposite sides or at an inclination of 60° to the principal axes of the windows.

The chamber, as illustrated in Fig. 1, is modular in design allowing for simple variation of the chamber length, location of optical access, injector design and throat diameter. The individual chamber segments include the injector segment, window segment, igniter segment, blank segment and nozzle segment. With all segments in place the interior length of the combustion chamber measures 25.7 cm. The chamber is mounted together with a hydraulic press and sealed between segments with standard polymer O-rings.

The injector segment is separated into two concentric brass sections. The forward section contains a threaded insert which forms the outer diameter of the fuel annulus and may be replaced between tests without complete chamber disassembly. The rear section provides the coupling of the injector to the propellant feed system. In addition, fuel plenum pressure, both the steady and oscillating components, as well as fuel injection temperature are measured in the rear section. The pressure and temperature of the liquid oxygen are measured in the liquid supply line at the entrance to the LOX post. The baseline dimensions of the injector were modeled after the injector element of the SSME preburner. Additional fuel annuli were fabricated for the first series of tests in which the effect of gas-to-liquid velocity ratio, density ratio and mixture ratio on injector performance were to be examined.

Detail of the window segment is provided in Figure 2, illustrating the 60° orientation of the window principal axes. The segment is intended for droplet size and velocity measurements within the liquid oxygen spray using a phase Doppler interferometric device. To reduce or eliminate contaminants from collecting on the windows during engine testing, a purge gas section was incorporated into the design of the window segment. Eight small

holes inject nitrogen gas across the inner surface of the windows within the window recess region. Preliminary tests with the window segment located at the chamber midsection verified adequate window purging with nitrogen flow rates less than 10% of the total propellant flow rate. Measurements of the chamber inner surface temperature and the steady and oscillating components of chamber pressure are made in this segment.

The nozzle segment houses a graphite nozzle throat insert that is sized for a specific propellant mass flow rate and chamber pressure. A stainless steel flange retains the insert within the nozzle segment while serving a second function as a pressure relief mechanism. During instances of excessive chamber pressures, the nozzle flange is designed to break away from its fasteners allowing for nozzle removal and rapid chamber depressurization. Propellant ignition is accomplished with a gaseous oxygen/gaseous hydrogen torch igniter. Both gases are introduced into a small combustion chamber attached to the side of the igniter segment and ignited by a high voltage, electrical discharge. The resulting flame is drawn into the main chamber to light the main propellant.

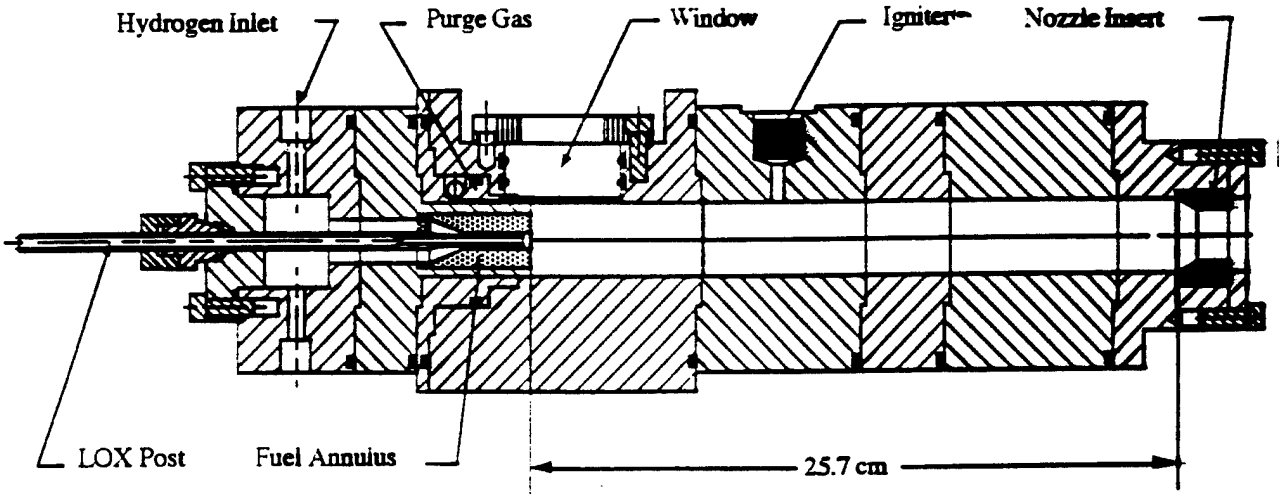

Fig. 1 Single element rocket combustion chamber.

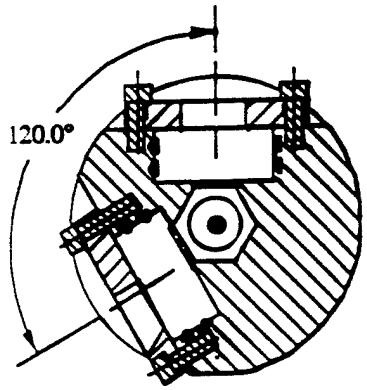

Fig. 2 Detail of window cross-section.

References

1. Glogowski, M., Bar-Gill, M., Puissant, C., Kaltz, T., Milicic, M. and Micci, M., "Shear Coaxial Injector Instability Mechanisms," AIAA 94-2774, 30th AIAA/ASME/SAE/ASEE Joint Propulsion Conference, Indianapolis, IN, June 27-29, 1994.

2. Mayer, W. and Krülle, G., "Rocket Engine Coaxial Injector Liquid/Gas Interface Flow Phenomena," AIAA 92-3389, July 1992.

3. Sankar, S.V., Wang, G., Brena de la Rosa, A., Rudoff, R.C., Isakovic, A., and Bachalo, W.D., "Characterization of Coaxial Rocket Injector Sprays Under High Pressure Environments," AIAA 92-0228, 30th Aerospace Sciences Meeting & Exhibit, Reno, Nevada, January 1992.

4. Conrad, E. W., Bloomer, H. E., Wanhainen, J. P. and Vincent, D. W., Interim Summary of Liquid Rocket Acoustic-Mode-Instability Studies at a Nominal Thrust of 20,000 Pounds, NASA TN D-4968, Dec. 1968.

5. Hannum, N. P., Russell, L. M., Vincent, D. W. and Conrad, E. W., Some Injector Element Detail Effects on Screech in Hydrogen-Oxygen Rockets, NASA TM X-2982, Feb. 1974.

6. Feiler, C. E., and Heidmann, M. F., Dynamic Response of Gaseous Hydrogen Flow System and Its Application to High-Frequency Combustion Instability, NASA TN D-4040, June 1967.

CUMULATIVE CHRONOLOGICAL LIST OF WRITTEN PUBLICATIONS

"Shear Coaxial Injector Spray Characterization," Kaltz, T., Milicic, M., Glogowski, M., and Micci, M., AIAA Paper 93-2190. Presented at the 29th AIAA/ASME/SAE/ASEE Joint Propulsion Conference, June 28-30, 1993, Monterey, CA.

"Shear Coaxial Injector Instability Mechanisms," M. Glogowski, M. Bar-Gill, C. Puissant, T. Kaltz, M. Milicic and M. Micci, AIAA Paper 94-2774, Proceedings of the 30th AIAA/ASME/SAE/ASEE Joint Propulsion Conference, June 27-29, 1994, Indianapolis, IN.

"Experimental Characterization of Shear Coaxial Injectors Using Liquid/Gaseous Nitrogen," C. Puissant, M.J. Glogowski, and M.M. Micci, Proceedings of the Sixth International Conference on Liquid Atomization and Spray Systems, July 18-22, 1994, Palais des Congres, Rouen, France, July 18-22, 1994, pp. 672-679.

LIST OF PROFESSIONAL PERSONNEL ASSOCIATED WITH THE RESEARCH EFFORT

Professional Staff

Michael M. Micci, Associate Professor, Aerospace Engineering
Moshe Bar-Gill, Adjunct Senior Research Assistant, Visiting from RAFAEL, Israel, 8/93 - 8/94.
Christopher Puissant, Adjunct Research Assistant, Visiting from SEP, Vernon, France, 11/93 - 1/95.
Jean-Louis Thomas, Adjunct Research Assistant, Visiting from SEP, Vernon, France, 3/95 - 5/96.
Xing Yaoquo, Adjunct Senior Research Assistant, Visiting from Northwestern Polytechnical University, Xi'an, China, 3/95 - 9/95.

Graduate Students

Michael Glogowski, August 1991 - present
M.S. Thesis Title: An Experimental Investigation of the Noncombusting Spray Characteristics of a Single Shear Coaxial Injector Operating with LOX/GH_2 Simulants.
Marty Milicic, August 1991 - August 1993
M.S. Thesis Title: Recirculation Measurements in a Shear Coaxial Injector Element.
Teresa Kaltz, August 1992 - May 1994
M.S. Thesis Title: Investigation of High-Frequency Pressure Oscillations For Single Element Coaxial Injector Cold Flow Studies.
Alfred Maskrey, Jan. 1994 - present

INTERACTIONS

Papers Presented

"Mesures de PDPA du Jet Produit par un Injecteur Coaxiau (PDPA Measurements of the Spray Produced by a Coaxial Injector)," Micci, M. Presented at SEP, May 17, 1993, Vernon, France.

"Liquid Rocket Motor Combustion Stability Using Coaxial Injectors," Kaltz, T., Milicic, M., Glogowski, M. and Micci, M. M. Presented at the AFOSR Contractor's Meeting on Propulsion, June 14-18, 1993, Atlantic City, NJ.

"Shear Coaxial Injector Instability Mechanisms," Bar-Gill, M., Kaltz, T., Glogowski, M. and Micci, M. M. Presented at the Fifth Annual Symposium of the NASA/Penn State Propulsion Engineering Research Center, Sept. 8-9, 1993, University Park, PA.

"Liquid Rocket Motor Combustion Stability Using Coaxial Injectors," Presented at the AFOSR Contractors Meeting on Propulsion Research, June 5-10, 1994, Lake Tahoe, NV.

"Shear Coaxial Injector Instability Mechanisms," M. Glogowski, M. Bar-Gill, C. Puissant, T. Kaltz, M. Milicic and M. Micci, AIAA Paper 94-2774, Presented at the 30th AIAA/ASME/SAE/ASEE Joint Propulsion Conference, June 27-29, 1994, Indianapolis, IN.

"Experimental Characterization of Shear Coaxial Injectors Using Liquid/Gaseous Nitrogen," C. Puissant, M.J. Glogowski, and M.M. Micci, Proceedings of the Sixth International Conference on Liquid Atomization and Spray Systems, Palais des Congres, Rouen, France, July 18-22, 1994, pp. 672-679.

"Caracterisation Experimentale Des Injecteurs Coaxiaux Azote Liquide/Azote Gazeux," Presented at ONERA, Chatillon and Palaiseau, France, August 2-3, 1994.

"Caracterisation Experimentale Des Injecteurs Coaxiaux Azote Liquide/Azote Gazeux," Presented at SEP, Vernon, France, August 5, 1994.

"Shear Coaxial Injector Instability Mechanisms," Puisant, C., Kaltz, T., Glogowski, M., and Micci, M.M. Presented at the Propulsion Engineering Research Center, Sixth Annual Symposium, NASA Lewis Research center, September 13-14, 1994, Cleveland, Ohio.

Visits

One day visit to the University of Orleans, France, to discuss coaxial atomization with Prof. Iskender Gakalp.

Appendix A

AIAA 94-2774
Shear Coaxial Injector Instability Mechanisms

M. Glogowski, M. Bar-Gill, C. Puissant, T. Kaltz,
M. Milicic and M. Micci
The Pennsylvania State University
University Park, PA

30th AIAA/ASME/SAE/ASEE Joint Propulsion Conference
June 27-29, 1994 / Indianapolis, IN

SHEAR COAXIAL INJECTOR INSTABILITY MECHANISMS

M. Glogowski+ , M. Bar-Gill* , C. Puissant* , T. Kaltz+, M. Milicic# and M. Micci†
Department of Aerospace Engineering & Propulsion Engineering Research Center
The Pennsylvania State University
University Park, PA 16802 USA

ABSTRACT

There is no definitive knowledge of which of several concurrent processes ultimately results in unstable combustion within liquid propellant rocket motors employing shear coaxial injectors. Possible explanations are a detrimental change in the atomization characteristics due to a decrease in the velocity ratio, the disappearance of a stabilizing recirculation region at the base of the LOX post or a change in the gas side injector pressure drop allowing acoustic coupling to the propellant feed system. The spray characteristics of a shear coaxial injector were examined under noncombusting conditions with water and air at atmospheric pressure and with liquid and gaseous nitrogen at elevated pressures. Two injectors were evaluated with different LOX post designs, nontapered and tapered. Initial spray visualization tests with water and air revealed two modes of atomization, namely a resonant and nonresonant mode, and an inherent periodicity in the clustering of droplets within the spray. Subsequent measurements with a phase Doppler interferometric device quantified the differences in spray characteristics between the two modes. Tests at elevated pressure using $LN2/GN_2$ did not provide any indication of the resonant mode. Visualization tests did reveal a contraction of the spray with increasing chamber pressures below the critical pressure. At pressures above the critical point, stroboscope images revealed an elongation of the liquid breakup length. Droplet size and velocity measurements were made for three oxidizer to fuel mixture ratios and a range of chamber pressures. The results indicated improved atomization at lower mixture ratios, but increased droplet sampling difficulty. Velocity measurements in the recess region at the base of the LOX post were obtained with water and air at atmospheric pressure and revealed reverse flow indicative of a recirculation region. Finally, the results for the injector response from a linearized lumped-element model are presented as a function of temperature and frequency and compared to experimental results.

NOMENCLATURE

A	area of annulus
d_f	fuel annulus inner diameter
d_i	post inner diameter
d_o	post outer diameter
C	capacitance term (Eqtn. 8)
g	gravitational constant
I	inertia term (Eqtn. 9)
L	annulus length
$\dot{m}$	mass flow rate
N	response factor
P_c	chamber pressure
P_d	plenum pressure
P_1	annulus entrance pressure
s	Laplace operator
T	temperature
U	velocity
V	plenum volume
W	mass flow rate through injector, model notation
W_j	mass flow rate:jth mechanism, model notation
W_T	total mass flow rate, model notation
ρ	density
σ	liquid surface tension
γ	specific heat ratio
θ	phase angle between P_c' and W'
ω	frequency
μ	viscosity
ΔP	$P_d - P_1$
ΔP_g	$P_d - P_c$, fuel pressure drop

Subscripts

g	gas or fuel
H_2	hydrogen
l	liquid or oxidizer
lox	liquid oxygen
max	peak amplitude of sine wave

Superscripts

-	average value
'	perturbation quantity, $(x-\bar{x})/\bar{x}$

+ Graduate Assistant, Student Member AIAA

* Adjunct Research Associate

Graduate Student, currently at TRW

† Associate Professor, Aerospace Engineering, Member AIAA

INTRODUCTION

Shear coaxial injectors are currently found in liquid propellant rocket engines which use liquid oxygen and hydrogen as the propellant, such as the Space Shuttle Main Engine (SSME) and the first stage Ariane 5 Vulcain engine. Their use in such bipropellant systems enables an effective means of liquid oxidizer atomization by the gaseous fuel and subsequent mixing of the propellant. Liquid oxygen is injected into the combustion chamber through a central tube while hydrogen in a gaseous form is fed through an outside annular passage at a high velocity relative to the liquid jet. Impelled by liquid turbulence and gas to liquid interfacial interactions, liquid is stripped from the jet and entrained into the surrounding shear flow where the liquid ligaments and droplets experience further breakup and atomization. The resulting spray then vaporizes and mixes with the gaseous fuel to produce a volatile mixture for combustion. Since the spatial distribution of the droplets downstream of the injector faceplate establishes the conditions for the release of mass and energy within the chamber, the emergence of unstable pressure oscillations within the chamber is strongly coupled to the atomization, vaporization and burning characteristics of the injector spray. Such combustion instabilities are an inherent phenomenon of liquid propellant rocket engines, in which strong exothermic reactions occur within a small volume, high pressure environment. Small fluctuations at the onset of or during steady state operation may initiate resonant pressure oscillations that grow rapidly in amplitude and eventually lead to the failure of the engine.

Extensive engine testing during the 1960's discovered a strong dependency of engine stability on the fuel temperature at injection. This observation lead to a stability rating technique, in which the fuel temperature was ramped to decreasing values during steady state engine operation. The temperature at which the engine transitioned into an unstable mode of operation became a measure of the stability of the engine, lowest temperatures meaning highest engine stability. The parametric tests on a full scale, 20,000 lb. engine at NASA Lewis isolated the effects of several injector design and operating parameters on the hydrogen temperature stability limit. The most significant appeared to be the relative velocity between the fuel and oxidizer, a presumption supported by the argument that a large momentum exchange between the two fluids is necessary for the disruption of the liquid jet. Wanhainen et al.[1] showed that unstable combustion arose for a variety of injector mass flow rates and exit areas when the ratio of fuel to oxidizer velocities dropped below 6.5. In terms of engine design parameters, the LOX post recess depth and fuel injection angle relative to the LOX post both enhanced the stability of the engine by lowering the fuel temperature stability limit. Ultimately, these parameters were incorporated into a single correlation, which accounted for all variations in injector design and operation investigated in this work[2]. Based on the hydrogen threshold temperature, the correlation is stated as

$$T_{H_2} \approx \left(\frac{P_c}{\Delta P_{H_2}}\right)^{1/2} \frac{1}{\rho_{lox} d_{lox}^{1.25}} \left(\frac{\dot{m}_{lox}}{\dot{m}_{H_2}}\right)^{1/2} \qquad (1)$$

which illustrates that for a given engine chamber pressure , P_c, and mixture ratio, $\dot{m}_{lox}/\dot{m}_{H_2}$, the fuel side pressure drop, ΔP_{H_2}, governs the stability characteristics of the engine. This result would suggest that instability is driven by an acoustic coupling between the injector hydrodynamics and spray formation and combustion processes within the chamber since higher pressure drops can be effected by modifications to the fuel annulus inlet configuration in addition to higher gas exit velocities. The contribution of liquid jet diameter to the hydrogen threshold temperature is less apparent due to the uncertainty of the effect of larger jet diameter on liquid jet atomization. By increasing the jet diameter for a fixed liquid mass flow rate, the liquid will exit the injector at a lower velocity and likewise produce a larger relative velocity that may improve atomization. On the other hand, the resultant increase in the interfacial surface area may reduce the momentum exchange per unit area and consequently worsen the atomization of the jet.

Another proposed explanation for the emergence of unstable operation in liquid propellant rocket engines is that a recirculation region acting as a flameholder exists downstream of the LOX post tip. Below a minimum relative velocity between the liquid oxygen and gaseous hydrogen, the recirculation region becomes too weak to act as a flameholder and the combustion zone moves away from the injector face to a location where it can interact more strongly with the chamber acoustics modes. Liang and Schumann have examined this idea with an experimental and computational investigation of gaseous oxygen and hydrogen coaxial injectors[3]. They examined several injectors designed to produce recirculation regions of different sizes but found that all injectors tested showed the combustion region anchored to the base of the injector. Cox made LDV measurements of the gas velocity in the fuel annulus in an SSME injector element and found flow separation at the start of the LOX post taper[4].

In general, the underlying physical processes influencing combustion instability are not completely understood due to a deficiency in experimental data on the characteristics of the injector spray and in computer codes capable of analyzing the complex, unsteady, three dimensional processes within the engine. With the

present developmental status of high performance computer architectures and advanced numerical algorithms, sophisticated computer models are being generated to provide performance and stability predictions in the design of future liquid propellant rocket engines[5]. In order to validate these models, accurate experimental data is required on the characteristics of the injector flowfield[6]. This information includes the spatial and time varying distribution of droplet size and velocity, turbulence scale and intensity, structure of the chemical reaction zones, and the distribution of temperature and concentration of the reactants and products throughout the flow field.

Advanced laser based diagnostic techniques have been devised concurrent to the improved development of computer codes and are capable of obtaining the required information on the spray. As a consequence, the impetus in academia and industry is to exploit the wide variety of available laser based diagnostic techniques for the characterization of the complete injector atomization, vaporization and combustion processes under conditions similar to actual engine operation. As a precursor to combusting conditions, many cold flow experiments have been performed with a single shear coaxial injector using water as the liquid oxygen simulant in order to investigate the mechanisms of liquid jet atomization without the influence of combustion[7-10]. Common fuel simulants have been air, nitrogen and helium. Since liquid nitrogen offers better similitude with liquid oxygen in terms of its low boiling temperature and the important physical properties which influence atomization, namely density, viscosity and surface tension, injectors have also been tested with LN_2 and either gaseous nitrogen or gaseous helium as the fuel simulant[11,12].

At the Propulsion Engineering Research Center of The Pennsylvania State University, multiple laser based diagnostic techniques are being used in the characterization of a unielement shear coaxial injector under combusting and noncombusting conditions and elevated pressures[13,14]. The focus of the present research effort was to characterize the evolutionary behavior of an atomizing and evaporating spray produced by a single shear coaxial injector operating under noncombusting conditions. To this end a laboratory injector was designed and fabricated for operation at atmospheric and elevated pressures. Water and liquid nitrogen were selected to serve as simulants to liquid oxygen while air and gaseous nitrogen supplanted gaseous hydrogen as the fuel. Preliminary investigations began with the combination of water and air to examine injector atomization characteristics without the influence of liquid vaporization. Through these tests general trends in atomization, both qualitative and quantitative, were to be observed for comparison to the subsequent high pressure investigations with liquid and gaseous nitrogen. Furthermore, investigations of the recirculation region with water and air provide an evaluation of the feasibility of this technique for future investigations under reacting conditions. Nonintrusive diagnostic techniques were implemented to obtain information on the global behavior of the spray and to quantify the important spray parameters, namely droplet mean size and mean axial velocity, at several locations within the spray. The techniques included planar laser imaging and stroboscopic photography to visualize the morphology of the spray and phase Doppler interferometry to measure the droplet parameters. In order to detect potential coupling between the chamber and injector acoustics, a simplified stability model was constructed for the flow dynamics of several processes in a cold flow pressure chamber. In support of this effort, the chamber and injector pressure oscillations were measured to evaluate the analytical results of the model.

RESEARCH APPROACH

On the Simulation of LOX/GH_2

To observe the injector spray characteristics without the influence of combustion, cold flow tests are often performed with alternative liquids and gases that offer a high degree of similitude with the actual propellants (LOX/GH_2) with respect to the important physical properties which influence the spray formation processes, namely liquid viscosity and surface tension and gas density. In the present research effort water and liquid nitrogen were used as simulants to liquid oxygen while air and gaseous nitrogen served as the simulants to hydrogen. The relevant physical properties of these simulants are compared to those of LOX/GH_2 in Table 1. Pressure and temperature, at which the properties were evaluated, are included in the table and correspond to the operating conditions of the SSME preburner in the case of LOX/GH_2 and to the expected baseline run conditions in the case of the simulants. These conditions are listed in Table 2.

Based on the large differences in liquid viscosity and surface tension between liquid oxygen and water, water is not expected to yield spray characteristics similar to liquid oxygen. Furthermore, water is not subject to evaporation processes at the injection temperature of the air. Nevertheless, its availability and ease of use make water a preferred liquid for the study of the fundamental processes of liquid jet breakup and atomization. For this reason water has been selected for use with air in the initial spray characterization tests. At the baseline pressure and temperature specified in Table 1 liquid nitrogen offers physical properties closer to those of liquid oxygen, especially in the case of liquid viscosity and surface tension. Since the boiling temperature of LN_2 at 2.5 MPa is significantly less than the coflowing, nitrogen gas temperature, liquid nitrogen

will undergo evaporation, thereby providing more insight into evaporation effects on spray evolution. The lower density of LN_2 may not introduce spray behavioral differences when considering the ratio of liquid to gas density to be a more influential parameter in liquid atomization than liquid density alone. For LN_2/GN_2 the density ratio is 20.1 while that for LOX/GH_2 is 26.5.

In Table 2 the conditions for LN_2/GN_2 were selected to approximate the injection velocities of LOX and H_2. Although the sound speed for gaseous nitrogen limited the maximum exit velocity to approximately 300 m/s, the resulting mass flow rate of gaseous nitrogen provided a mixture ratio almost equal to that of the preburner. The conditions for water/air were chosen to produce a similar mixture ratio and relative velocity while insuring proper atomization of the water jet. Overall, a large degree of similitude is achieved between LOX/GH_2 and LN_2/GN_2. Most nondimensional parameters, including mixture ratio and velocity ratio, are of the same order of magnitude between these two fluid combinations with the only exception being the gas Reynolds number. According to Farago and Chigier[15], the breakup of the liquid jet can be correlated by the liquid Reynolds number and aerodynamic Weber number. The magnitude of these parameters are very close for LN_2/GN_2 and LOX/GH_2 suggesting that both combinations would possess similar breakup characteristics. The water/air combination differs significantly from LOX/GH_2 in terms of the nondimensional parameters and consequently is expected to yield different characteristics in atomization.

Experimental Set-Up.

The baseline dimensions of the shear coaxial injector are shown in Fig. 1 and were derived from the dimensions of the prototype injector element of the fuel preburner to the Space Shuttle's main engine. A second LOX post was fabricated with a 7° taper at the tip to match the shape of the production injector element. Pressure, both the mean and oscillating components, and temperature were measured in the fuel plenum region upstream of the fuel annulus. The mean pressure and static temperature of the liquid simulant were measured in the liquid supply line at the entrance to the LOX post.

For the elevated pressures required of LN_2 testing, a pressure chamber was constructed to operate at pressures up to 10.0 MPa and to provide optical access for laser based diagnostic techniques. The chamber, which is depicted in Fig. 2, is 22.9 cm in length and has a square cross-section with sides measuring 10.2 cm. Optical access is through 2.54 cm thick plexiglass plates mounted to both sides of the chamber and reinforced with high strength, carbon steel flanges, 1.27 cm thick. Slits measuring 3.2 cm wide by 15.2 cm long were cut into the flanges to maintain optical accessibility to the chamber. The position of these slits depended on the diagnostic technique in use, as is illustrated in Fig. 2 for the case of phase Doppler interferometry. Four ports drilled into the injector end of the chamber serve to provide additional gas for chamber pressurization and to suppress recirculating flow. By the replacement of the nozzle plate a range of chamber pressures can be investigated for specific propellant mass flow rates. Mean chamber pressure and internal gas temperature were measured at the center of the chamber as illustrated in Fig. 2. High frequency pressure oscillations were measured at the exit plane of the injector. To facilitate particle sizing and velocity measurement at several axial and radial locations of the spray, the entire chamber was mounted on a 2-D translation platform and connected by flexible lines to the propellant feed system.

Test Facility

The initial spray characterization tests were performed at atmospheric pressure using water and air. Water was tapped from the local area network and metered into a graduated cylinder to determine the liquid mass flow rate. Air was supplied by compressors within the Center and regulated by means of a standard pressure gauge rated at 100 psig. Knowing the supply pressure and temperature of air within the plenum region of the injector, the air mass flow rate was calculated from the isentropic relations for a truncated nozzle, corrected for two-dimensional and turbulence effects.

The cold flow experiments with liquid nitrogen were performed at the Cryogenic Combustion Laboratory of The Pennsylvania State University. The laboratory was designed for the experimentation of subscale rocket engines and can accommodate liquid oxygen and gaseous hydrogen and other propellant combinations under reacting or cold flow conditions. Facility performance is rated at 0.45 kg/s of liquid oxygen and 0.11 kg/s of gaseous hydrogen for chamber pressures up to approximately 8.0 MPa. The supply of gaseous nitrogen to the injector and the four purge ports was from the primary and secondary supply lines of the gaseous hydrogen feed subsystem of the laboratory. Two subsystems comprise the overall gas feed system and are supplied by clusters of pressurized gas cylinders. Liquid nitrogen was supplied to the test section from a 114 liter vacuum jacketed storage tank by a gaseous nitrogen dome loading system. To reduce the time required for cooling down the cryogen supply lines, a liquid nitrogen cooling jacket was installed onto the lines between the storage tank and the test section. Flow metering for both gaseous and liquid propellants was accomplished with critical flow venturies fitted with pressure transducers and thermocouples upstream and downstream of the venturi. Since cavitation is a significant concern in LN_2 atomization experiments at

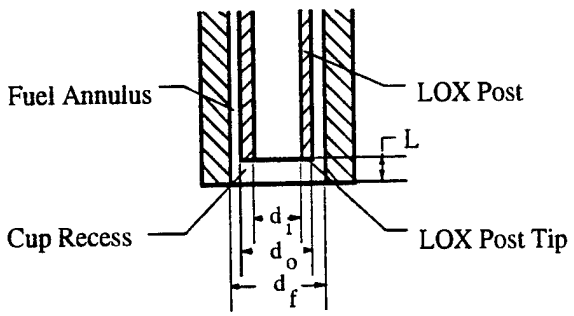

Baseline Dimensions

Fuel Annulus Diameter, d_f	5.03 mm
LOX Post Outer Diameter, d_o	3.76 mm
LOX Post Inner Diameter, d_i	2.26 mm
Post Tip Land Width	0.76 mm
Recess Length, L	2.54 mm

Figure 1. Shear coaxial injector schematic with baseline dimensions.

Table 1 Comparison of propellant/simulant physical properties.

PROPERTIES (units)	OXIDIZER			FUEL		
	LOX	LN_2	H_2O	H_2	N_2	Air
P (MPa)	34.1	2.5	0.1	34.1	2.5	0.1
T (K)	114	115	290	153	290	290
ρ (kg/m3)	1125	588	1000	42.5	29.2	1.25
μ (μPa·s)	115.5	46.6	1377	5.76	17.9	17.6
σ (mN/m)	7.41	1.39	74.22	-	-	-

Table 2 Comparison of injector operating conditions.

Operating Conditions (units)	Symbol/ Formula	SSME Preburner	LN_2/N_2 Simulants	H_2O/Air Simulants
Chamber Pressure (MPa)	P_c	34.1	2.5	0.1
Fuel Pressure Drop (MPa)	ΔP_g	2.95	1.56	0.062
Fuel mass flow (kg/s)	$\dot{m}_g$	0.138	0.077	0.0033
Ox. mass flow (kg/s)	$\dot{m}_l$	0.135	0.071	0.0031
Fuel exit velocity (m/s)	U_g	360	300	260
Ox. exit velocity (m/s)	U_l	30	30	0.8
Relative velocity (m/s)	$U_g - U_l$	330	270	259
Velocity ratio	U_g/U_l	12	10	325
Density ratio	ρ_l/ρ_g	26.5	20.2	726
Mixture ratio	$\dot{m}_l/\dot{m}_g$	0.98	0.92	0.94
Momentum ratio	$\dot{m}_g U_g/\dot{m}_l U_l$	12.2	10.8	347
Gas Re No (x10^6)	$\rho_g U_g(d_f - d_o)/\mu_g$	3.37	0.62	0.028
Liquid Re No (x10^5)	$\rho_l U_l d_i/\mu_l$	6.60	8.56	0.013
Weber No. (x10^5)	$\rho_g(U_g - U_l)d_i/\sigma_l$	14.12	34.61	0.026
Ohnesorge No. (x10^{-4})	$\mu_l/\sqrt{\rho_l \sigma_l d_i}$	8.42	10.84	33.62

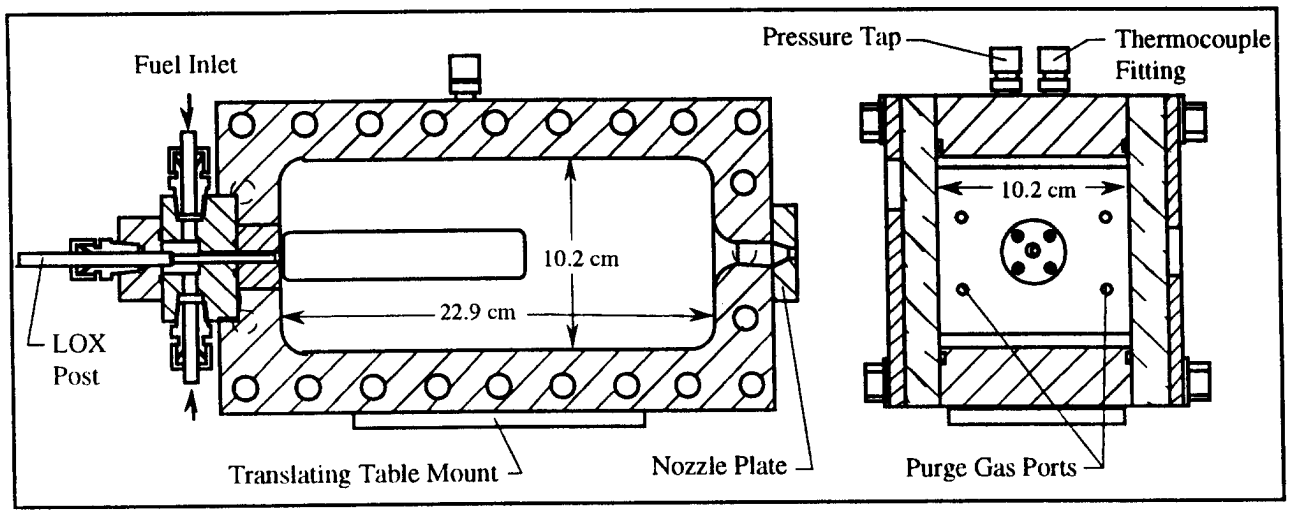

Figure 2. Pressure vessel for LN2/GN2 atomization studies.

subcritical conditions, a criterion was established based on the work by Nurick[16] to determine whether a test was influenced by LN_2 cavitation. The criterion required that the difference between the LOX post upstream pressure and vapor pressure must exceed the pressure drop through the LOX post by a factor determined from the entrance geometry and discharge coefficient of the LOX post. Although actual LOX/GH_2 rocket engines operate in the supercritical regime, the dynamics of cavitation at subcritical pressures could yield spray structures, drop size distributions, and overall propellant mixing quality not concurrent with ideal injector operation.

Spray Visualization Technique.

The global characteristics of the shear coaxial injector spray were examined by imaging the scattered light from a laser sheet passing through the axis of the spray and, in a separate test series, from a stroboscope illuminating the backside of the spray. With this approach the momentary structure of the spray, including the liquid core and large, detached ligaments, could be visualized for evaluation of the effects of injector design, propellant flow rates and ambient conditions. Furthermore, dilute droplet flow regions could be identified within the spray for subsequent droplet sizing and velocity measurement by means of phase Doppler interferometry. For the laser sheet imaging tests a frequency doubled Nd:YAG laser (532 nm), pulsed at 10 Hz with a pulse duration of 10 ns, was used with a spherical and cylindrical lens combination to form a laser sheet with a thickness of approximately 0.15 mm and negligible divergence at the injector centerline. The scattered light from the spray was visualized perpendicular to the sheet with a 35 mm Nikon camera. A 1 nm bandpass filter centered at 532 nm was installed in front of the camera lens to eliminate ambient light. This technique as well as the stroboscope technique were employed during the liquid nitrogen tests at elevated pressures. For the water/air tests only the stroboscope was used to illuminate the spray. The orientation of the stroboscope for both tests was toward the backside of the spray with respect to the camera and in the direction of the injector face. Preliminary flow visualization experiments with water and air at atmospheric pressure revealed that both the dispersed droplet region and the structure of the liquid core may be imaged at this orientation with the 35 mm camera. The flash rate of the strobe was set at 10 Hz with a flash duration of 3 μs.

Phase Doppler Interferometry.

Quantitative information on the spray and recirculation region was pursued with a phase Doppler interferometric (PDI) device, developed by Aerometrics, which enabled simultaneous measurement of the temporally averaged droplet size and velocity distribution at a point within the spray[17]. The optical configuration for these tests included a CW argon ion laser emitting at 514.5 nm, a Bragg cell based transmitter, and a receiver oriented at 30° from the forward direction of the transmitter optical axis. The transmitter was fitted with a 500 mm f.l. lens to form a focused beam waist of 234 μm. Using a 100 μm x 1 mm spatial filter and a lens pair consisting of a 495 mm f.l. collection lens and a 250 mm f.l. focusing lens within the receiver, the effective probe area became approximately 212 μm x 234 μm. Doppler signal filtering, acquisition and analysis were performed by dedicated processing electronics and software developed by Aerometrics. During the LN_2/GN_2 tests data sampling was over a 2.5 second interval triggered by a

programmable laboratory controller at 2.5 seconds into each test, at which point the pressure within the chamber had reached a steady value.

Analytical Modeling of Injector Response

A simple model based on the Rayleigh criterion was constructed for the flow dynamics of two processes in the cold flow liquid rocket chamber to determine the effect of various design and operating parameters on combustion stability. The mechanisms included are the fuel flow through the injector, and the flow of exhaust gases through the nozzle.

The Rayleigh criterion states that a wave will grow if heat or mass is added in phase with pressure. Conversely, the wave will damp if the addition is out of phase. If several mechanisms are contributing to the heat or mass release, then the wave growth is determined by the net in-phase or out-of-phase heat or mass addition. By assuming that both the heat or mass addition and the pressure oscillations can be represented by a perturbation added to their steady state values, linear models of the dynamic response of the processes may be obtained.

A response factor is defined as the real, or in-phase, part of the mass flow perturbation with response to the chamber pressure perturbation. The response factor for a transverse mode was derived in Reference 18:

$$N = \frac{W'_{max}}{P'_{c,max}} \cos\theta \qquad (2)$$

The response factor can be either positive or negative depending on the phase angle between the pressure and flow perturbations. The analytical derivation of the response factor for the various flow processes is detailed in the Appendix.

The stability limit for a transverse mode of oscillation within the chamber was derived in Reference 19 from a mass balance of an axial column of gas:

$$\left[\Sigma_j \frac{W_j}{W_T} N_j\right]_{in} = \left[\Sigma^j \frac{W_j}{W_T} N_j\right]_{out} \qquad (3)$$

This relation thus represents the total response as a linear combination of each response factor weighted by the fraction of mass flow contributed by that process. A positive response corresponds to an unstable system, while a negative response indicates stability.

WATER/AIR RESULTS

Spray Visualization

The majority of the spray visualization tests were performed with the shear coaxial injector using the nontapered LOX post recessed to 2.54 mm inside the fuel annulus. The water flow rate was varied between 3.0 g/s and 54.0 g/s with air supply pressures up to 184 kPa. Higher supply pressures were not possible due to flow choking considerations within the fuel annulus. To examine the effect of injector design on spray morphology, additional tests were conducted without the post recessed and with the tapered LOX post recessed to 2.54 mm.

Aside from the expected improvement in atomization with decreasing water flow rate or increasing air flow rate, several interesting phenomena were observed during these tests. At all water mass flow rates the spray produced regions of high and low droplet number density occurring at wave-like frequency. These droplet clusters appeared most distinctly at the edge of the spray and at the highest mass flow rate of air. The wavelength, or distance between adjacent clusters, was shortest at this flow rate and increased with decreasing air mass flow rate. Furthermore, it appeared that the bandwidth of these waves widened at lowering air mass flow rates. This behavior is depicted in Fig. 3 for 6.0 g/s of water and 3.7 g/s of air using the nontapered LOX post without a recess. The figure illustrates the inherent periodicity of liquid jet disruption and droplet flow within the spray. Faragó and Chigier have identified this behavior as a normal mode of jet disintegration from their experiments with a twin fluid atomizer[15]. The occurrence of periodic, coherent structures within a shear coaxial injector spray supports their findings while revealing an unsteadiness of the spray that can affect the evaporation and combustion characteristics of the spray and likewise the overall stability characteristics of the engine.

During these tests an unusual whistling noise, characteristic of a resonating pipe, emanated from the injector when the post was recessed inside the fuel annulus. This behavior arose with both post shapes but was less pronounced with the nontapered post. No noticeable change in the structure of the spray was observed with the nontapered post upon the emergence of the whistling phenomenon. Furthermore, the amplitude of the noise was relatively low, which in conjunction with the steady spray behavior would suggest that the nontapered post operated close to a point of resonance. Tests performed without a recessed post produced no whistling noise over the entire range of air supply pressures and water mass flow rates.

Operation with the tapered LOX post at the nominal recess depth of 2.54 mm revealed the most noticeable change in the behavior of the spray. With increasing air supply pressure, the injector transitioned from a nonresonant mode of operation to a resonant mode at a specific air pressure. At the point of resonance the injector spray shifted from a solid cone to

a hollow cone with a significant increase in the spray's angle of divergence. The liquid jet experienced enhanced atomization as the breakup length approached the injector exit. Furthermore, the amplitude of the whistling noise became more audible with this post shape and increased with increasing air mass flow rate. Fig. 3b depicts the tapered post operating at resonance with 6.0 g/s of water and 3.7 g/s of air. Resonance was detected at 126 kPa of air for this water flow rate. As seen from Figs. 3a and 3b, the onset of resonant atomization has resulted in a marked change in the overall behavior of the spray. The consequences of this behavior are profound and encompass a possible means of improved injector performance or a mechanism for injector destabilization.

Droplet Size and Velocity Measurements

Since a complete characterization of the injector spray field has been conducted by Zaller and Klem[9] at several water and air mass flow rates, the emphasis of this effort was to obtain a database of spray characteristics for comparison to the subsequent elevated pressure tests with liquid nitrogen and to quantify the observed differences between the two modes of atomization. The injector was operated at 6.0 g/s of water and 3.7 g/s of air using both the tapered and non-tapered LOX post recessed inside the annulus. Based on the visualization tests, the nontapered post is not expected to transition into a resonating mode of atomization as the tapered LOX post under similar conditions. Data on droplet mean velocity and mean size were obtained as a function of radial position at 5 cm downstream of the injector face. The spray data are plotted in the following four figures and depict noticeable differences between the two sprays. In Fig. 4 the data on droplet mean axial velocity illustrate a steepening of the velocity profile when transitioning into the resonating condition with the tapered post from the non resonating condition with the nontapered post. Interestingly, the velocities on the injector centerline are approximately equal for both configurations but depart outward in the spray. The more rapid drop in axial velocity for the tapered post would suggest that the droplets are traveling faster in the radial direction than in the axial direction.

Examination of the resultant mean drop size distribution in Fig. 5 reveals a more pronounced departure from the normal behavior of the spray. According to the results of Ref. 9, the Sauter mean diameter is expected to decrease at increasing radial distances from the injector centerline, a trend which is observed in Fig. 5 for the nontapered post. With the tapered post smaller Sauter mean diameters are found on the centerline and increase radially outward in the spray. Overall, the tapered LOX post produced smaller droplets within the region of the spray probed with the PDPA. At the centerline the difference in sizes is most substantial and decreases when moving out in the spray.

(a) Nontapered post w/o recess

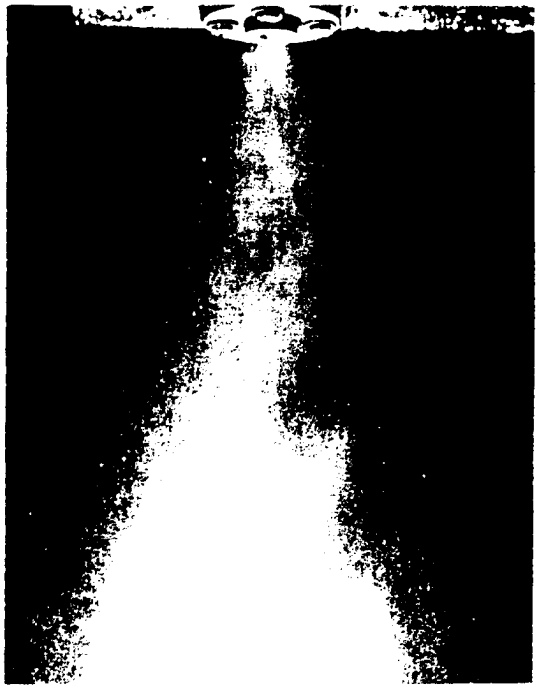

(b) Tapered post w/recess

Fig. 3 Photographic results of atmospheric water/air spray at 6.0 g/s of water and 3.7 g/s of air.

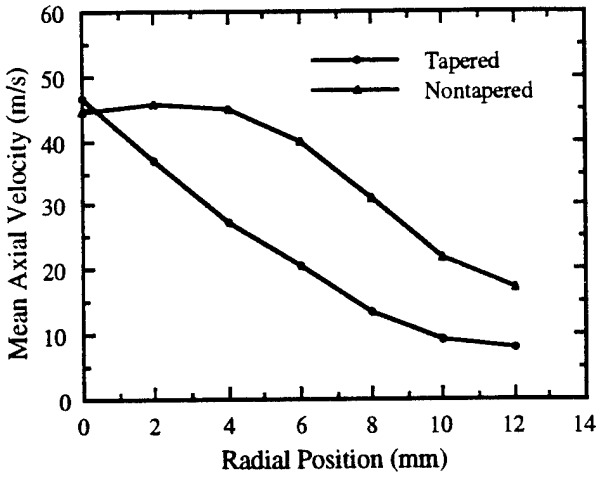

Fig. 4 Radial variation in droplet mean axial velocity for two LOX post shapes.

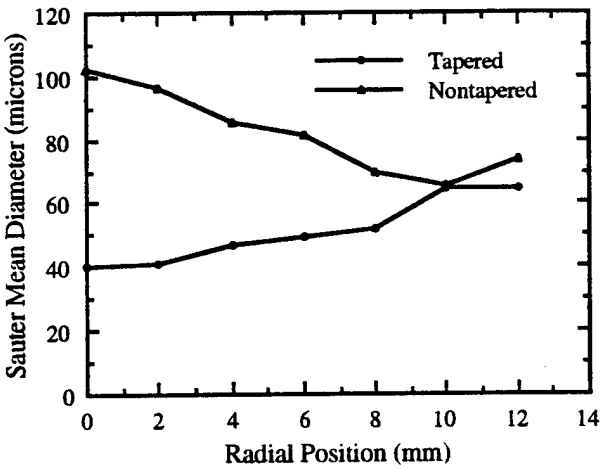

Fig. 5 Radial variation in droplet Sauter mean diameter for two LOX post shapes.

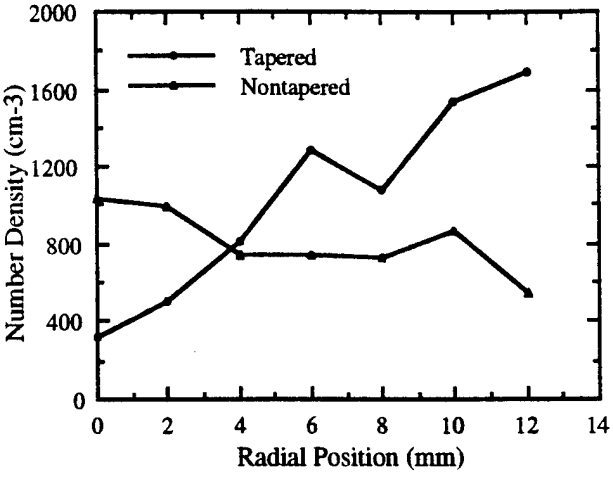

Fig. 6 Radial variation in droplet number density for two LOX post shapes.

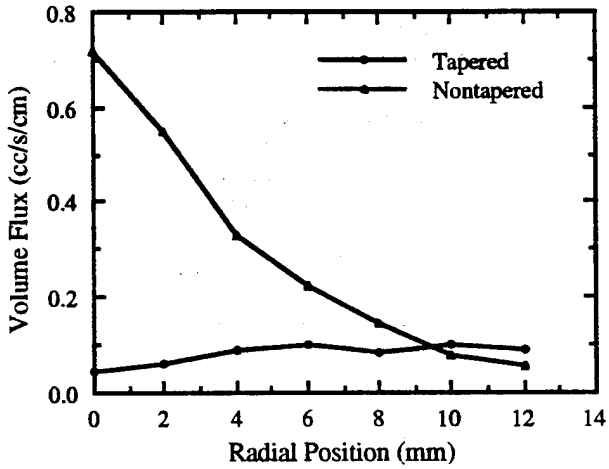

Fig. 7 Radial variation in droplet volume flux for two LOX post shapes.

The distribution of droplet number density is presented in Fig. 6 for both injector configurations. The distribution for the tapered post corroborates the hollow cone behavior observed in the spray visualization tests. That is, the majority of drops reside at the edge of the spray with a decreasing number toward the center. The volume flux of droplets at each point of measurement is plotted in Fig. 7 for both injector configurations. In the case of the tapered post the distribution of volume flux is rather uniform throughout the spray as compared to the steep distribution for the nontapered post. The occurrence of this distribution is due to the opposite trends between the mean velocity and the number density and drop size. That is, the steep velocity profile compensates for the hollow cone distribution in drop size and number density to create the uniform volume flux distribution. Based on this distribution the burning efficiency of the tapered post under resonating conditions may be expected to be higher than that of the nontapered post. But if the range over which the resonance condition occurs is narrow, this condition may result in a mechanism of combustion instability when the injector transitions intermittently between the two modes as a result of pressure fluctuations within the injector and combustion chamber.

Recirculation Region

The original injector design with the straight LOX post was modified in order to allow LDV access into the recess region. This was accomplished by inserting a Pyrex tube concentrically around the LOX post, such that the fuel annulus was defined by a transparent boundary 1.02 mm thick. The inner diameter of the Pyrex fuel annulus was 5.00 mm. All measurements

were taken using Aerometrics' Phase Doppler Particle Analyzer (PDPA) with the droplet diameter measurement function disabled. The system incorporates a 40 MHz frequency shift of one beam through the use for a Bragg Cell so that the direction of the particle may be obtained along with the velocity measurement. Both the transmitting and receiving optics were aligned at angles of 15 degrees from the horizontal.

With the optics in this configuration and the presence of the curved Pyrex surface, the refraction of the beams as well as any probe volume effects must be considered. In this case, the cylinder is larger than the diameter of the laser beam. Therefore, the probe volume will not undergo any appreciable distortion. Refraction of the beam, however, does occur and is a function of the radius of curvature, the refractive indices of the media and the height above the plane which crosses the centerline of the injector at an angle of 15 degrees (defined by the angle of the incoming beams). Translation of the probe volume within the fuel annulus addressed this refractive effect to determine accurately the location of data sampling within the recess region.

Measurements of mean axial velocity were taken inside the injector recess region as well as downstream of the injector. Downstream of the injector face only positive velocities were measured. Water was used as the LOX simulant and either air or gaseous nitrogen for the gaseous fuel simulant.

Fig. 8 shows the line along which the mean axial velocity measurements were taken. These measurements are depicted in Fig. 9 as a function of the axial distance from the LOX post base. The air flow rate was 1.8 g/s and the water flow rates were either 1.9 or 4.5 g/s. It can be seen that the velocity drops to a negative value approximately 0.5 mm downstream of the LOX post base before becoming positive. Larger negative values

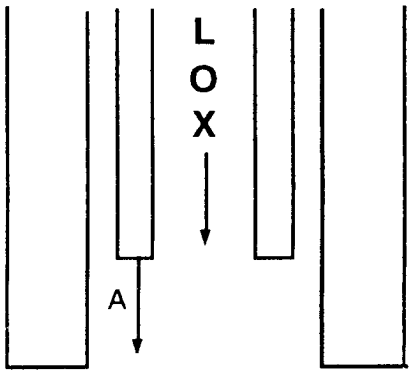

Fig. 8 Injector element orifice showing location of velocity measurement scans.

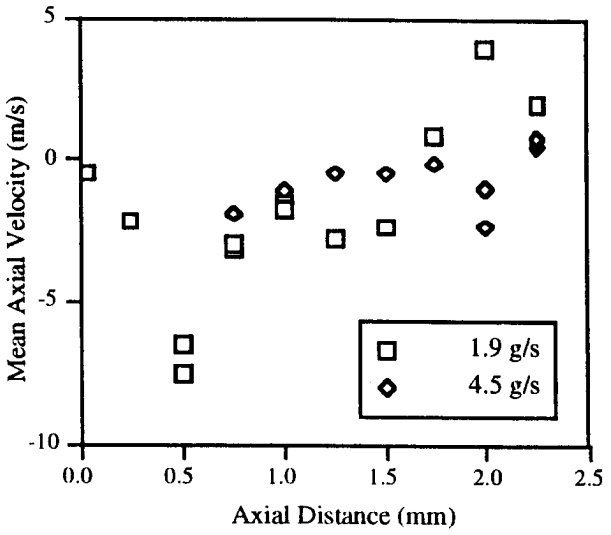

Fig. 9 Droplet mean axial velocity as a function of axial distance within the injector recess region.

of the velocity were observed for lower liquid flow rates. Thus it appears that gas recirculation does exist in the recess region of a shear coaxial injector element and that the strength of the recirculation is a function of the operating conditions.

LN_2/GN_2 RESULTS

Spray Visualization.

Visualization tests using both techniques were performed with the nontapered LOX post at chamber pressures between 2.2 and 4.1 MPa and at two liquid to gas mixture ratios of 0.80 and 1.58. To determine if any observable differences in liquid atomization existed between the two LOX post designs, specifically with respect to the emergence of a resonating mode of operation, several stroboscope tests were conducted with both LOX posts operating at the same mixture ratio and at a range of chamber pressures.

The first series of photographs in Fig. 10 correspond to the run conditions of tests A1 to A3 of Table 1 and illustrate the effect of chamber pressure on the overall spray morphology of the coaxial injector using the nontapered LOX post recessed within the annulus. The photographs were imaged with the laser sheet and have been digitally reproduced from color photographs to improve image quality for photoduplication and to accentuate noticeable structures within the spray. The pressure drop from 2.93 to 2.32 MPa was a result of lowering average gas temperatures within the chamber from test to test. It is expected that in the case of large, dispersed sprays differences in the gas temperature may influence the behavior of the spray downstream of the dense liquid core region but should not affect significantly the breakup behavior of the liquid

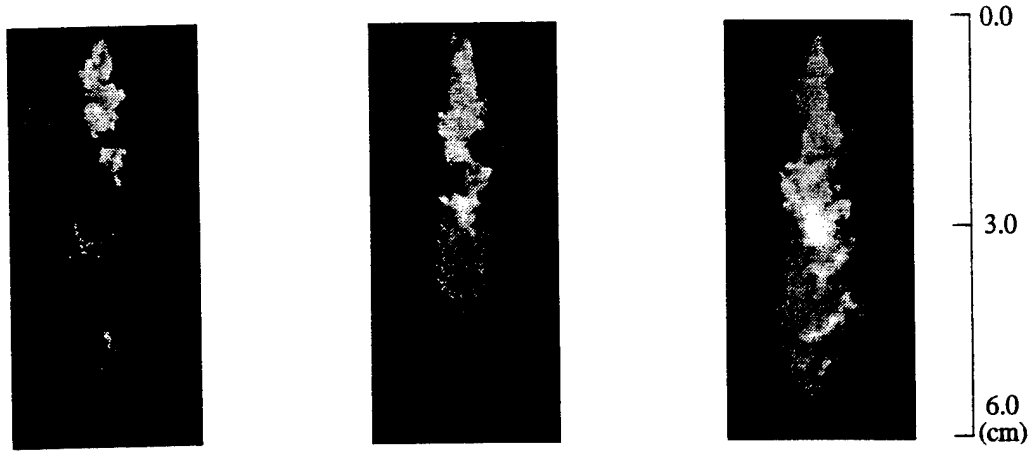

(a) 2.93 MPa (test A1) (b) 2.60 MPa (test A2) (c) 2.32 MPa (test A3)

Fig. 10 Effect of chamber pressure on LN_2/GN_2 spray (mean mixture ratio : 0.78).

jet or the distribution of droplets around the jet, since the conditions in this region are better represented by the gas injection temperature.

In general, Fig. 10 depicts an overall contraction of a dense liquid core region with increasing chamber pressure. Regions of droplet flow are most evident downstream of this region and decrease in number density and size with increasing pressure. Based on the comparatively small size of the spray depicted in Fig. 10, evaporation is considered an important mechanism in the evolutionary behavior of the spray. In the classical description of shear coaxial injector atomization, liquid ligaments and droplets are produced from the effluent jet as a result of unstable surface wave growths induced by liquid turbulence and a shearing force between the surrounding gas and liquid. These ligaments and droplets in turn undergo secondary atomization through surface deformation and breakup by aerodynamic forces resulting in a spray of polydisperse

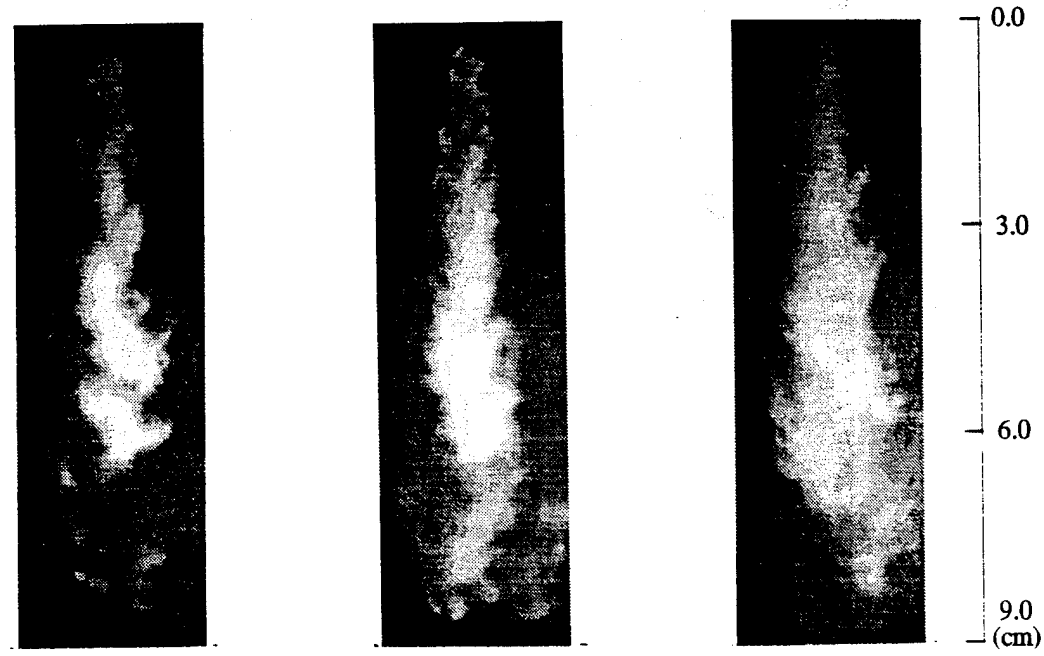

(a) 2.79 MPa (test A4) (b) 2.63 MPa (test A5) (c) 2.34 MPa (test A6)

Fig. 11 Effect of chamber pressure on LN_2/GN_2 spray (mean mixture ratio : 1.57).

Table 3. Operating conditions for LN_2/GN_2 spray visualization tests.

Test No.	P_c (MPa)	$\dot{m}_l$ (kg/s)	$\dot{m}_g$ (kg/s)	$\dot{m}_l/\dot{m}_g$	U_g/U_l	$U_g - U_l$(m/s)	ρ_g/ρ_l
A1	2.93	0.050	0.062	0.81	8.99	164.8	0.061
A2	2.60	0.049	0.062	0.79	10.06	184.3	0.056
A3	2.32	0.046	0.063	0.74	11.58	203.9	0.052
A4	2.79	0.052	0.033	1.58	4.82	82.3	0.060
A5	2.63	0.052	0.033	1.58	5.06	87.7	0.057
A6	2.34	0.050	0.033	1.54	5.87	103.9	0.051
A7	2.94	0.076	0.094	0.82	8.68	244.0	0.065
A8	3.97	0.076	0.094	0.81	6.99	183.6	0.081

droplets around the liquid jet. With rising chamber pressure the gas density enhances the breakup of the jet[20], which is observed in Fig. 10, but reduces secondary atomization due to a decrease in the slip velocity between the gas and droplet. As a consequence, larger droplets pervade the spray of a nonevaporating liquid at higher chamber pressures[10] although shorter liquid breakup lengths may exist. As seen in Fig 10, the large gas mass flux appears to have rapidly vaporized the droplets surrounding the core except for those in the shadow of the LN_2 jet, a region characterized by lower gas temperatures and velocities. The rate of liquid vaporization is further enhanced by the increasing chamber pressure through a combined reduction in the latent heat of vaporization and in the liquid surface tension resulting in the observed contraction of the droplet flow region.

In tests A4 to A6 of Table 1 the gas mass flow rate was decreased to approximately half of the value of tests A1 to A3, while the chamber pressure was varied from 2.34 MPa to 2.79 MPa. The photographic results of these tests have been digitally reproduced in Fig. 11 and were obtained as well with the laser sheet visualization technique. Overall, the reduction in gas mass flow rate has resulted in a larger, more dispersed

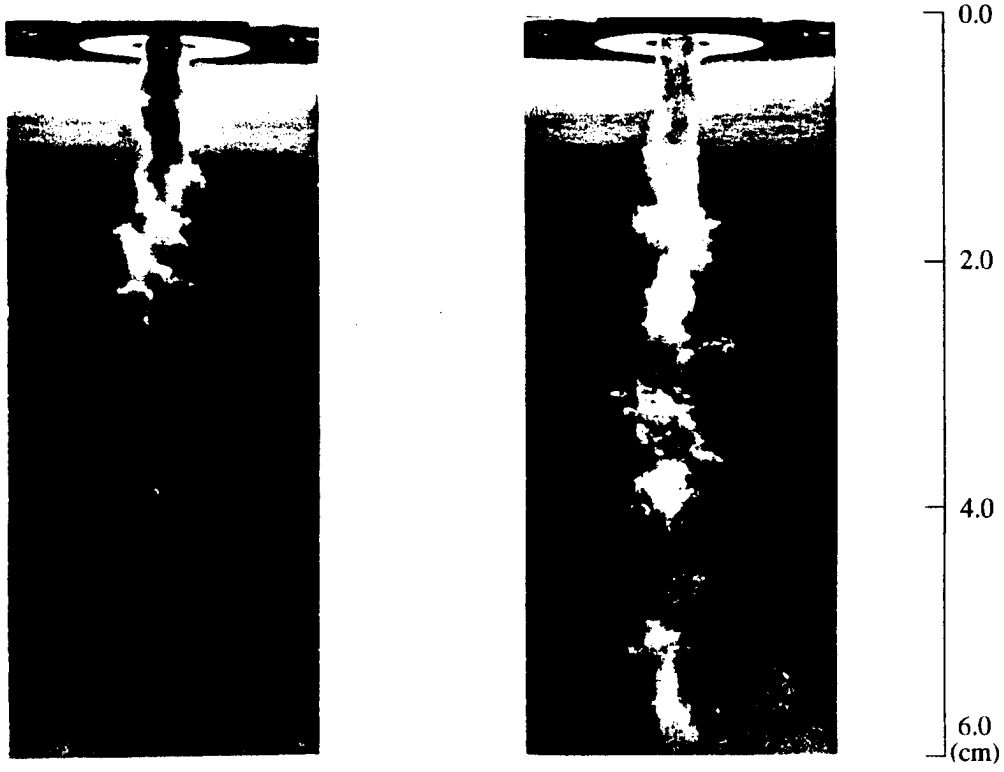

(a) 2.94 MPa (test A7) (b) 3.97 MPa (test A8)

Fig. 11 Stroboscope results for tapered LOX post at sub- and supercritical pressures (mixture ratio : 0.81).

Table 4. Operating Conditions and Droplet Size and Velocity Data for LN_2/GN_2 PDI Tests.

Test No.	P_c (MPa)	$\dot{m}_l$ (kg/s)	$\dot{m}_g$ (kg/s)	$\dot{m}_l/\dot{m}_g$	U_g/U_l	$U_g - U_l$ (m/s)	ρ_g/ρ_l
B1	2.63	0.073	0.033	2.24	3.87	86.0	0.053
B2	2.40	0.072	0.033	2.19	4.20	95.5	0.050
B3	2.37	0.070	0.033	2.15	4.30	96.5	0.049
B4	2.41	0.071	0.032	2.20	4.23	95.3	0.050
B5	2.45	0.075	0.047	1.60	5.74	141.6	0.050
B6	2.37	0.071	0.063	1.14	7.53	193.5	0.053

Test	Pos. (cm)		Axial Velocity (m/s)		Droplet Size (μm)		No. of	Percent
No.	Z	R	Mean	Deviation	Arithmetic	Sauter	Droplets	Validation
B1	12	0	15.9	3.5	10.1	96.7	512	28
B2	12	0	14.4	3.6	11.2	97.3	2514	25
B3	12	0.5	9.3	4.5	12.9	91.6	375	4
B4	10	0	14.8	4.3	14.1	105.5	562	4
B5	10	0	20.8	7.1	7.5	110.3	151	19
B6	6	0	37.1	11.1	8.4	118.3	121	8

spray indicating a strong effect of mixture ratio on the atomization and vaporization of liquid nitrogen. The behavior of the spray with respect to increasing chamber pressure follows the same trend as tests A1 to A3, in that the LN_2 spray contracts in size as the chamber pressure increases. In terms of droplet sampling with the phase Doppler interferometric device, these reduced gas flow conditions are advantageous in that the observable dilute spray region is spread over a larger volume. The droplet flow regions of tests A1 to A3 appear confined close to the liquid core amounting to potential difficulties in droplet sampling.

Tests A7 and A8 were performed with the tapered LOX post using the stroboscope to visualize the spray. Test A7 depicted in Fig. 12a matches closely the chamber pressure and mixture ratio of test A1, but was conducted with substantially higher liquid and gas mass flow rates. Regardless of this difference, the lengths of the intact liquid core appear very similar between the two tests. It is evident though that the stroboscopic image provides more detail on the structure of the liquid core and detached ligaments than the laser sheet images but less information on the droplet flow region. Fig. 12b shows the structure of the jet issuing from the injector at a supercritical pressure of 3.97 MPa. Contradictory to the observed contraction of the spray with increasing pressure, the liquid core breakup length has significantly increased for a chamber pressure greater than the critical pressure (3.4 MPa). This behavior may be attributed to the drop in relative velocity between the gas and liquid at increasing chamber pressures, which may surpass any enhancements to liquid breakup due to increased gas density, and may be related as well to the increase in droplet evaporation times observed in the supercritical region[21]. Stroboscope tests with the nontapered LOX post under similar operating conditions revealed the same behavior for pressures above and below the critical point but indicated little differences in spray morphology between the two LOX post designs.

Droplet Size and Velocity Measurements.

For droplet sizing and velocity measurement only the nontapered LOX post injector design was examined at liquid to gas mixture ratios of approximately 2.2, 1.6 and 1.1 for a nominal liquid nitrogen flow rate of 0.072 kg/s. Chamber pressures ranged from 2.20 to 3.29 MPa. Based on past difficulty in obtaining a large statistical sampling of droplets with the injector operating with a mixture ratio close to unity, the present effort began with the gas mass flow rate at almost half of the liquid mass flow rate. According to the photographic results of the flow visualization tests (Fig. 11), these conditions result in a dilute droplet flow region dispersed over a larger volume, which effectively reduces both the droplet number density and signal attenuation due to multiple particle scattering. The average gas and liquid mass flow rates were 0.032 and 0.072 kg/s, respectively, yielding a liquid to gas mixture ratio of approximately 2.20. Fig. 13 illustrates the effect of chamber pressure on the number of droplets collected over a 2.5 second sampling interval at 12 cm downstream of the injector on the injector centerline. With an increase in chamber pressure the number of droplets sampled over this interval decreased dramatically. This trend would suggest that the droplet number density has declined due to the contraction of the spray at higher pressures as observed in Fig. 11 and/or that the optical alignment has been affected by the increased gas density (i.e. changing refractive index).

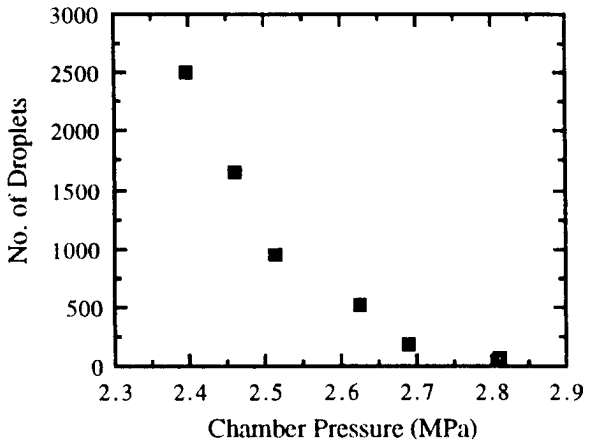

Fig. 13.Effect of chamber pressure on number of droplets sampled over 2.5 sec interval.

The effect of chamber pressure on droplet size and mean axial velocity was found to be negligible as is seen in the results of tests B1 and B2 of Table 2.

Additional tests were performed to examine the effect of position and gas mass flow rate on the droplet sampling rate and characteristic parameters. Tests B2, B3, and B4 provide a comparison of the spray measurements taken at three different locations in the spray for approximately equal operating conditions. Best data was obtained at 12 cm downstream from the injector on the centerline as seen by the large number of droplets and good ratio of valid droplet samples to attempted samples (percent validation) of test B2. For the same axial distance away from the injector but 5 mm off axis, the number of droplets acquired over the sampling interval decreased. The droplet data show that the droplet mean axial velocity decreased in the radial direction while the droplet size represented by the arithmetic mean diameter changed negligibly. The results of test B4 for an axial position of 10 cm exhibit the expected increase in droplet mean velocity and droplet size when probing closer to the injector face.

The effect of gas mass flow rate is seen from the results of tests B4, B5 and B6. Test B5 was conducted at a higher gas flow rate of 0.047 kg/s at the same location as test B4. The flow rate was further increased to 0.063 kg/s in test B6. But, due to the marked contraction of the spray at this gas flow rate, measurements were made at 6 cm downstream from the injector for this test. The results of test B5 and B6 reveal the expected increase in droplet mean velocity with increasing gas mass flow rate due to the higher gas injection velocities. Although the low number of droplets collected in the last two tests does not permit an accurate evaluation of the mean droplet size for all three tests, the droplet size distributions have been superimposed in Fig 14 to illustrate the general behavior of the spray with varying liquid to gas mixture ratios At the lower mixture ratio of test B6, the majority of droplets fall in the smallest size range of Fig. 14. As the gas mass flow rate decreases to approximately 3/4 and 1/2 of that in test B6, the droplet distribution shifts to larger droplet sizes. In the case of tests B4 and B5, which were both conducted at the same position in the spray, this trend confirms the reduction in droplet size and number due to enhanced vaporization and atomization with increasing gas mass flow rate. The large difference between the arithmetic mean diameter and Sauter mean diameter in the tests arose from the bimodal distribution in the sampled droplets as seen in Fig. 14. The small number of large droplets at the upper end of the size range, observed during all of the tests, may be due to remnants of the liquid core and/or coalesced small droplets. As seen in Table 4, their effect on the Sauter mean diameter is most pronounced with decreasing mixture ratio, although their number is lowest at these mixture ratios.

Injector Response Results

The injector response factor was calculated as a function of frequency and gaseous fuel temperature for the experimental conditions experienced during the cold flow LN_2/GN_2 experiments. During these experiments, high frequency pressure oscillations were measured in

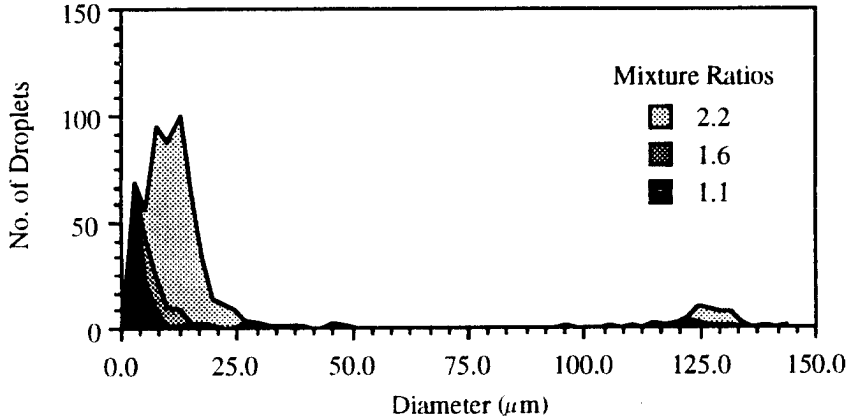

Fig. 14. Droplet size distribution for three oxidizer to fuel mixture ratios (P_C = 2.4 MPa).

the chamber and the injector fuel plenum. Figure 15 shows the injector response (real part) as a function of fuel temperature for several frequencies. It can be seen that at high frequencies the response is near zero, at intermediate frequencies the response is negative and almost constant and at low frequencies the response becomes strongly positive as the fuel temperature decreases. Fig. 16 shows the injector response as a function of frequency for the gas temperature used during the experiments. The response is positive for low frequencies but then switches to negative before decaying to zero as the frequency increases.

The recorded high frequency pressure oscillations were spectrally analyzed to determine the frequencies and magnitudes of any acoustic oscillations within either the chamber or the injector fuel plenum. Oscillations at the same frequency in both the chamber and the plenum were found at two frequencies. Table 5 compares the calculated injector response at those two frequencies to the measured ratios of the pressure oscillation amplitude in the chamber to the amplitude in the plenum. It can be seen that at the frequency where the injector was more strongly damping, the measured ratio of amplitudes was less. Future work for both the analysis and the experiments will include the effects of combustion.

Table 5 Comparison of calculated injector response to the ratio of measured pressure oscillation in the chamber to the amplitude in the plenum.

Frequency (Hz)	Injector Response	Measured P'_{cham}/P'_{plenum}
2000	-0.25	0.26
5800	-0.04	0.62

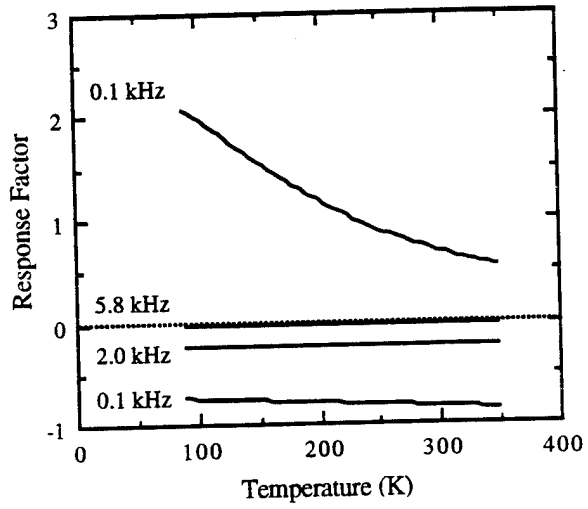

Fig. 15 Injector response as a function of gaseous fuel temperature for several frequencies.

CONCLUSIONS

An experimental investigation of the spray produced by a single shear coaxial injector has been performed under noncombusting conditions. Two fluid combinations were selected for spray characterization using stroboscopic photography and planar laser imaging to visualize the global spray characteristics and phase Doppler interferometry to measure droplet size and velocity. Initial tests were performed with water and air at atmospheric pressure. Using the tapered LOX post recessed into the fuel annulus, the injector transitioned into a condition of resonance characterized by a whistling noise and a significant modification to the overall structure of the spray. Injector operation with the nontapered post produced a near resonance condition that exhibited a lower amplitude whistling noise but did not effect a change in the spray morphology. No evidence of injector resonance was encountered upon elimination of the LOX post recess. Stroboscopic images emphasized the magnitude of this phenomenon on the atomization characteristics of the liquid jet with two post/annulus configurations. Measurements of droplet size and velocity at a single cross-section of the spray illustrated a significant quantitative difference between nonresonant atomization and resonant atomization.

Spray visualization tests with LN_2/GN_2 at elevated pressures illustrated the strong influence of liquid to gas mixture ratio and chamber pressure on the overall morphology of the spray. Higher mixture ratios yielded large, poorly atomized and vaporized sprays while increasing chamber pressures below the critical point resulted in a contraction of the spray. For a mixture ratio near unity and pressures above the critical point the spray ceased to contract and extended deeper

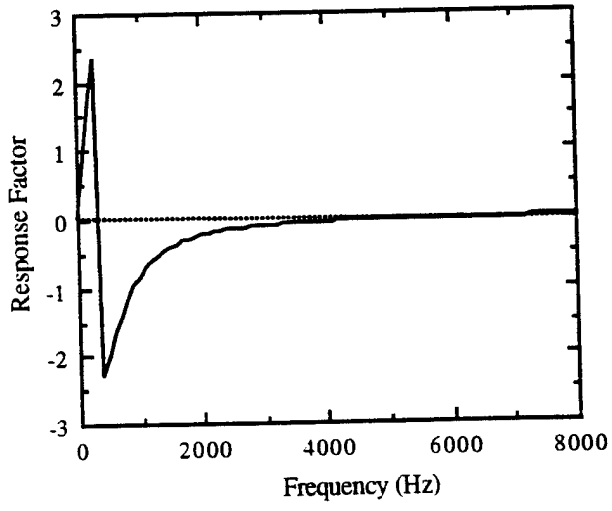

Fig. 16 Injector response as a function of frequency for the gas temperature during the experiments.

into the chamber. Measurements of droplet size and mean velocity as a function of mixture ratio and chamber pressure have been performed. The results confirm the improved atomization of the spray with decreasing mixture ratio, but reveal potential concerns of droplet sampling in dense cryogenic sprays at elevated pressures and reduced temperatures.

Results from a linearized lumped-element model of the response for a cryogenic shear coaxial injector show that the injector response may shift from stabilizing to destabilizing as the gaseous fuel temperature decreases for certain frequencies. The analytical results compared well to chamber high frequency pressure measurements.

The first velocity measurements ever taken in the recess region of a recirculation region of an injector element showed reverse flow indicative of a recirculation region. Measurements will be expanded to quantify the size and strength of the recirculation region as a function of operating conditions and injector design.

ACKNOWLEDGMENTS

This work was supported by AFOSR Grant F49620-93-1-0126 and NASA Grant NAGW-1356, Supplement 6. C. Puissant wishes to acknowledge the financial support of the Societe Europeenne de Propulsion.

APPENDIX

Response Factors

A lumped-element model was developed similar to Reference 22 to determine the dynamic response of the fuel flow through the injector. The dynamics of the flow through the dome is represented by a mass balance. In perturbation form, this relation is:

$$\frac{\overline{\rho}V}{\gamma\overline{W}}sP'_d = -W' \tag{4}$$

The orifice flow relation represents the flow from the dome into the entrance of the annulus:

$$W' = \frac{1}{2}\left[\frac{\overline{P_d}}{\Delta P}P'_d + \left(\frac{1}{\gamma} - \frac{\overline{P_1}}{\Delta P}\right)P'_1\right] \tag{5}$$

The flow through the annulus is represented by a momentum balance assuming plug flow:

$$P'_1 - P'_c = \frac{\overline{W}L}{g\overline{P}_c A}sW' \tag{6}$$

The pressure at the exit of the annulus was assumed to equal the mean chamber pressure.

These equations may be combined to give the transfer function:

$$\frac{W'}{P'_c} = -\frac{\left(\frac{\overline{P_1}}{\Delta P} - \frac{1}{\gamma}\right)\left(\frac{\Delta P}{P_d}\right)Cs}{1 + 2\frac{\Delta P}{P_d}Cs + \frac{\Delta P}{P_d}\left(\frac{\overline{P_1}}{\Delta P} - \frac{1}{\gamma}\right)CIs^2} \tag{7}$$

where:

$$C = \frac{\overline{\rho}V}{\gamma\overline{W}} \tag{8}$$

and

$$I = \frac{\overline{W}L}{gA\overline{P}_c} \tag{9}$$

Inverting this transfer function gives the following amplitude and phase shift:

$$\frac{W'_{max}}{P'_{c,max}} = \left(\frac{\overline{P_1}}{\Delta P} - \frac{1}{\gamma}\right)\left(\frac{\Delta P}{\overline{P_d}}\right)C\omega \Big/ \left\{\left[1 - \frac{\Delta P}{\overline{P_d}}\left(\frac{\overline{P_1}}{\Delta P} - \frac{1}{\gamma}\right)IC\omega^2\right]^2 + \left[2\frac{\Delta P}{\overline{P_d}}C\omega\right]^2\right\}^{\frac{1}{2}} \tag{10}$$

$$\theta = \frac{\Pi}{2} - \tan^{-1}\frac{2\frac{\Delta P}{\overline{P_d}}C\omega}{1 - \frac{\Delta P}{\overline{P_d}}\left(\frac{\overline{P_1}}{\Delta P} - \frac{1}{\gamma}\right)IC\omega^2} \tag{11}$$

Assuming adiabatic flow, the response factor for the nozzle can be expressed as:

$$\frac{W'_{max}}{P'_{c,max}} = -\frac{1}{\gamma} \tag{12}$$

REFERENCES

1. J.P. Wanhainen, H.C. Parish and E.W. Conrad, "Effect of Propellant Injection Velocity on Screech in 20,000-Pound Hydrogen-Oxygen Rocket Engine," NASA TN D-3373, 1966.
2. E.W. Conrad, H.E. Bloomer, J.P. Wanhainen and D.W. Vincent, "Interim Summary of Liquid Rocket Acoustic Mode Instability Studies at a Nominal Thrust of 20,000 Pounds," NASA TN D-4968, 1968.
3. P.-Y. Liang and M.D. Schumann, "A Numerical Investigation of the Flame-Holding Mechanism Downstream of a Coaxial Injector Element," *Proceedings of the 24th JANNAF Combustion Meeting*, CPIA Publication 476, Vol. 3, Oct. 1987.

4. G.B. Cox, "Rocket Engine Injection Element Characterization," AIAA 88-3135, 24th Joint Propulsion Conference, Boston, MA, July 11-13, 1988.
5. J.A. Muss, T.V. Nguyen and C.W. Johnson, "User's Manual for Rocket Combustor Interactive Design (ROCCID) and Analysis Computer Program," Vol 1-User's Manual, NASA CR-1087109, May, 1991.
6. R.J. Jensen, "A Summary of the JANNAF Workshop on Liquid Rocket Engine Combustion Driven Instability Mechanisms," 26th JANNAF Combustion Meeting, Vol. 2, D.L. Becker, ed., CPIA-PUBL-529-VOL-2, Chemical Propulsion Information Agency, Laurel, Maryland, 1989.
7. H. Gomi, Pneumatic Atomisation with Coaxial Injectors: Measurements of Drop Sizes by the Diffraction Method and Liquid Phase Fraction by the Attenuation of Light, NAL-TR-888T, 1986.
8. L. Vingert, Coaxial Injector Spray Characterization for the Ariane 5 Vulcain Engine, 6th Annual Conference, Liquid Atomization and Spray Systems-Europe, Pise, July 1990.
9. M.M. Zaller and M.D. Klem, Coaxial Injector Spray Characterization Using Water/Air as Simulants, NASA-TM-105322, 1992.
10. S.V. Sankar, G. Wang, A. Brena de la Rosa, R.C. Rudoff, A. Isakovic, and W.D. Bachalo, Characterization of Coaxial rocket Injector Sprays Under High Pressure Environments, AIAA 92-0228, 30th Aerospace Sciences Meeting & Exhibit, Reno, Nevada, Jan. 1992.
11. T. Kaltz, M. Milicic, M. Glogowski, and M. M. Micci, Shear Coaxial Injector Spray Characterization, AIAA 93-2190, 29th Joint Propulsion Conference, Monterey, California, June 1993.
12. P. Gicquel, L. Vingert, and P. Millan, Faisabilite de Mesures Granulometriques dan des Sprays Cryogeniques d'Injectors Coaxiaux, 3ème Congrès Francophone de Vélocimétrie Laser, Toulouse, Sept. 1992.
13. M.D. Moser, J.J. Merenich, S. Pal and R.J. Santoro, "OH-Radical Imaging and Velocity Field Measurements in a Gaseous Hydrogen/Oxygen Rocket," AIAA 93-2036, 29th Joint Propulsion Conference, Monterey, California, June 1993.
14. S. Pal, M.D. Moser, H.M. Ryan, M.J. Foust and R.J. Santoro, "Flowfield Characteristics in a Liquid Propellant Rocket," AIAA 93-1882, 29th Joint Propulsion Conference, Monterey, California. June 1993.
15. Z. Faragó and N. Chigier, "Classification of Round Liquid Jet Disintegration in Coaxial Air Streams," *Proceedings of the International Conference on Liquid Atomization and Spray Systems*, Gaithersburg, MD, July 1991, pp. 661-668.
16. W.H. Nurick, Orifice Cavitation and Its Effect on Spray Mixing, *J. of Fluids Engineering*, Dec. 1976.
17. W.D. Bachalo and M.J. Houser, Phase/Doppler Spray Analyzer for Simultaneous Measurements of Drop Size and Velocity Distributions, *Optical Engineering*, Vol. 23, No. 5, 1984.
18. M.F. Heidmann and P.R. Wieber, *Analysis of Frequency Response Characteristics of Propellant Vaporization*, NASA TN D-3749, June 1966.
19. D.T. Harrje and F.H. Reardon, *Liquid Propellant Rocket Combustion Instability*, NASA SP-194, 1972.
20. W. Mayer and G. Krülle, Rocket Engine Coaxial Injector Liquid/Gas Interface Flow Phenomena, AIAA 92-3389, 28th Joint Propulsion Conference, Nashville , Tennessee, July 1992.
21. G.M. Faeth, D.P. Dominicis, J.F. Tulpinsky, and D.R., Olson, Supercritical Bipropellant Droplet Combustion, *Twelfth Symposium (International) on Combustion*, The Combustion Institute, 1969.
22. C.E. Feiler and M.F. Heidmann, *Dynamic Response of Gaseous Hydrogen Flow System and Its Application to High-Frequency Combustion Instability*, NASA TN D-4040, June 1967.

Supercritical Droplet Combustion and Dynamics

Final Report
for the period
2/1/93 - 5/31/95

Submitted to:

Air Force Office of Scientific Research
Bolling AFB, DC 20332-0001

By:

Vigor Yang
Department of Mechanical Engineering
The Pennsylvania State University
University Park, PA 16802

ABSTRACT

Vaporization and combustion of liquid droplets in both subcritical and supercritical environments have been studied systematically. A variety of liquid propellants and propellant simulants, including hydrocarbon and cryogenic fluids, in both steady and oscillatory environments are treated. The formulation is based on the full conservation equations for both gas and liquid phases, and accommodates variable properties and finite-rate chemical kinetics. Full account is taken of thermodynamic non-idealities and transport anomalies at high pressures, as well as liquid/vapor phase equilibrium for multi-component mixtures. Because the model allows solutions from first principles, a systematic examination of the droplet behavior over wide ranges of pressure, temperature, and ambient flow velocity is made possible. Results can not only enhance the basic understanding of the problem, but also serve as a basis for establishing droplet vaporization and combustion correlations for the study of liquid rocket engine combustion, performance, and stability.

A series of calculations have been performed to understand the effects of ambient flow conditions on droplet gasification behavior. Results indicate that the velocity and thermodynamic state of the ambient flow have strong influence on the mass, momentum, and energy transport in the droplet gasification and burning processes. The droplet gasification rate increases progressively with pressure and ambient Reynolds number. In addition, the amplitude of pressure-coupled droplet vaporization response increases with increasing pressure owing to the susceptibility of enthalpy of vaporization to ambient flow oscillations at high pressures. However,

the effect of mean pressure on the phase angle of the droplet vaporization response appears quite limited.

Detailed flow structures and thermodynamic property variations are examined to reveal underlying mechanisms for droplet gasification and burning, as well as deformation and breakup dynamics at supercritical pressures. Correlations of droplet lifetime and aerodynamic drag coefficient are developed as functions of fluid thermodynamic state, Reynolds number, and vaporization transfer number.

TABLE OF CONTENTS

LIST OF TABLES

LIST OF FIGURES

NOMENCLATURE

a	Helmholtz free energy
A	Surface area
$\mathbf{A}, \mathbf{B}$	Convective-flux Jacobians
b	Volumetric parameter for SRK equation of state
$\mathcal{B}$	Spalding transfer number
C_D	Drag coefficient
C_p	Constant-pressure specific heat
$\mathbf{D}$	Source-term Jacobian
$\mathcal{D}_{ij}$	Binary mass diffusivity
$\mathcal{D}_{im}$	Mass diffusivity of component i in mixture
e	Specific internal energy
e_t	Specific total internal energy
E, F	Convective flux vectors in axial and radial directions, respectively
E_v, F_v	Diffusion flux vectors in axial and radial directions, respectively
f	Fugacity
f, $\hbar$	Scaling factors for corresponding-state principle
$\mathcal{F}_\mu$	Scaling factor for viscosity
$\mathcal{F}_\lambda$	Scaling factor for thermal conductivity
g	Gibbs free energy
h	Specific enthalpy
J	Coordinate transformation Jacobian
k_{ij}	Binary interaction constant of energy
ℓ_{ij}	Binary interaction constant of volume
m	Total mass of droplet
$\dot{m}''_v$	Gasification flux of droplet
M	Molecular weight
$\mathcal{M}_a$	Mach number
n_i	Number of mole

p	Pressure
p_0	Mean pressure
p_g	Gauge pressure
p^s	Saturation pressure
P	Arbitrary fluid property
q_e	Energy diffusion flux
$q_{m,i}$	Mass diffusion flux of species i
Q	Dependent variable vector
$Q_{s\rightarrow\ell}$	Energy flux conducted into droplet
$Q_{s\rightarrow g}$	Energy flux carried away by gasified fuel
$Q_{g\rightarrow s}$	Energy flux conducted from ambient gases to droplet surface
r_s	Instantaneous droplet radius
$\dot{r}_s$	Droplet surface regression rate
$\mathcal{R}$	Gas constant
$\mathcal{R}_u$	Universal gas constant
R_p	Vaporization response function
s	Specific entropy
S	Source term vector
t	Time
T	Temperature
u, v	Velocity components in axial and radial directions, respectively
u_g	Grid moving velocity
u_r	Velocity in radial direction in spherical coordinates
U, V	Contravariant velocities
v	Molar volume
w	Vaporization rate
w	Angular frequency
$\dot{w}_i$	Rate of production of species i
X_i	Mole fraction of species i
$\mathcal{X}$	Correction factor of non-correspondence for ECS method
Y_i	Mass fraction of species i

Z	Compressibility
$\hat{Z}$	Pseudo-time vector for primitive variables

Greek Symbols

α	Intermolecular force parameter for SRK equation of state
$\alpha_a,\ \alpha_b$	Droplet acceleration parameters
α_s	Thermal diffusivity on droplet surface
β	Scaling factor of pressure
$\boldsymbol{\Gamma}$	Preconditioning matrix
ΔV	Volume of control volume cell
$\Delta\lambda_{crit}$	Critical enhancement for thermal conductivity
$\Delta\lambda_{exc}$	Dense fluid correction for thermal conductivity
Δh_v	Latent heat of vaporization
ϵ	Lennard-Jones energy parameter
ϵ_{AD}	Artificial dissipation rate
$\eta,\ \xi$	Curvilinear coordinates
Ω_D	Lennard-Jones intermolecular potential function
Θ	Non-dimensional temperature
Θ_p	Phase angle of droplet vaporization response function
θ	Shape factor of energy
λ	Thermal conductivity
μ	Viscosity
$\boldsymbol{\mu}$	Chemical potential
ρ	Density
σ	Lennard-Jones length parameter
τ	Pseudo time
$\boldsymbol{\tau_{ii}}$	Normal stress in i direction
$\boldsymbol{\tau_{ij}}$	Shear stress in i direction on j surface
τ_v	Droplet lifetime
ϕ	Shape factor of molecular size
ω	Pitzer's acentric factor

Subscripts

c	Critical property
s	Droplet surface
F	Fuel species
g	Grid system
i	Quantity of species i
R_+	Droplet surface on gas side
R_-	Droplet surface on liquid side
∞	Ambient flow
0	Reference fluid
m	Mixture
x	Vector in axial direction
r	Vector in radial direction
η	Vector in η direction
ξ	Vector in ξ direction

Superscripts

$'$	Fluctuation term
$\bar{}$	Mean quantity
$*$	Reduced by value at critical point
0	Ideal gas property
v	Vapor phase
ℓ	Liquid phase

CHAPTER 1

INTRODUCTION

Many practical liquid-propellant rocket propulsion systems involve droplet vaporization and spray combustion in high-pressure environments[1–3]. Liquid propellants are usually delivered to liquid-rocket combustion chambers as a spray of droplets, which then undergo a sequence of vaporization, ignition, and combustion processes at pressure levels well above the thermodynamic critical points of the liquids. Under these conditions, droplets initially injected at subcritical temperatures may heat up and experience a thermodynamic state transition into the supercritical regime during their lifetimes, as shown in Fig. 1.1. Consequently, the sharp distinction between gas and liquid disappears, and the entire system exhibits many distinct characteristics which conventional droplet theories developed for low-pressure cases can not deal with.

To clarify this problem, it is useful to examine the behavior of an isolated liquid droplet when suddenly confronted with a stream having a thermodynamic state in the supercritical regime of the liquid (see Figure 1.2). As the droplet is heated by the ambient gas, its temperature increases and finally exceeds the critical point. Several important aspects must be noted during this process. First, when the droplet surface approaches its thermodynamic critical state, the difference in densities of gas and liquid phases become smaller. The characteristic times of the transport processes near the droplet surface in both phases have the same order of magnitude. Therefore, the transient effects in the gas phase are as important as

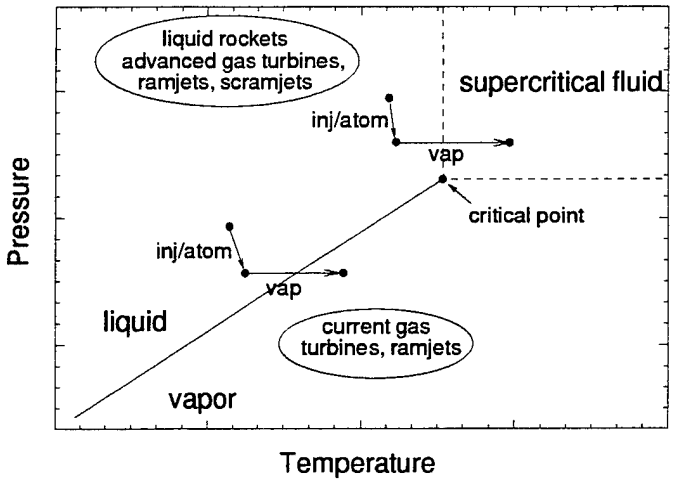

Figure 1.1. Operating Conditions of Advanced Air-breathing and Rocket Engines.

those in the liquid phase; the quasi-steady condition may never be reached during the lifetime of the droplet[4]. Second, the latent heat of vaporization decreases to zero at the critical point. Conventional low-pressure models may erroneously predict the vaporization rate if the variation of latent heat with pressure is not properly taken into account. In addition, if the droplet is moving, the behavior of liquid deformation and breakup may be altered considerably due to the diminished value of surface tension. Third, at high pressure, effects of thermodynamic non-idealities and property variations play decisive roles in determining transport properties and interface thermodynamic relationships. The solubility of the ambient gas in the liquid phase increases with pressure; the classical Raoult's law for ideal mixtures is not applicable in the phase-equilibrium analysis. One must develop a more comprehensive model for vapor-liquid interface conditions in terms

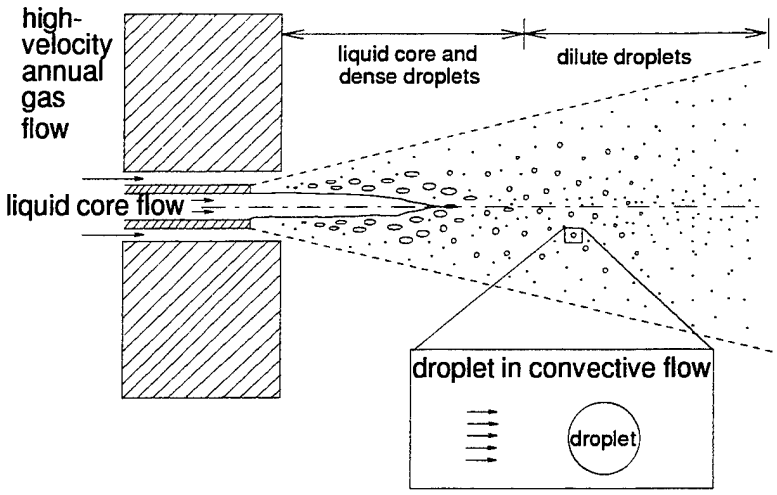

Figure 1.2. Liquid Spray from an Co-axial Injector.

of fugacity. Finally, when the droplet exceeds its critical state, it essentially becomes a puff of dense fluid. The entire field becomes a continuous medium, and no distinct liquid/vapor interface can be identified.

1.1 Literature Survey

Attempts to study droplet vaporization and combustion in the supercritical regime have been made for three decades. The earliest development of a predictive model was initiated by Spalding[5]. He considered the problem of supercritical combustion of an isolated fuel droplet in an stagnant environment by approximating the droplet as an instantaneous point source of dense gas. The formulation was based on a simplified one-dimensional model with constant physical properties; real-gas effects and density variations were ignored. The analysis was then refined

by Rosner[6] to include finite distributed sources. Results of both studies, substantially in agreement, demonstrated the transient characteristics of droplet burning under supercritical conditions. The same problem was examined by a number of researchers (notably Brzustowski[7], Chervinsky[8], and Polymeropoulos and Peskin[9]) in order to investigate the influences of convection, density variation, and finite-rate chemical kinetics. Recently, Lee *et al.*[10] investigated the stagnant-point evaporation of a liquid fuel at near and super-critical conditions. Because of the complexity of this problem, many important high-pressure phenomena (including solubility of ambient gases in the liquid phase, thermodynamic non-idealities, and property variations) were ignored.

In 1963, Wieber[11] proposed, in accordance with a low-pressure quasi-steady model, that a droplet may undergo a certain amount of evaporation prior to reaching the critical condition. This observation was later confirmed experimentally by Faeth *et al.*[12] in a study of supercritical bipropellant droplet combustion. Systematic treatment of droplet vaporization at near critical conditions was initiated by Manrique and Borman[13] and Savery and Borman[14], based on a quasi-steady model. They concluded that the effects of thermodynamic non-idealities, property variations, and high-pressure corrections for phase equilibrium modify the vaporization mechanism significantly. In particular, an appreciable amount of ambient gas may dissolve in the liquid phase, causing an intrinsic change in the entire process. In light of these findings, Lazar and Faeth[15] and Canada and Faeth[16] conducted a series of experimental and theoretical studies on droplet combustion in both stagnant and forced-convective environments, with special attention focused on the high-pressure phenomena of phase equilibrium. The effects of forced convection in the gas phase were treated by conventional multiplicative corrections.

The assumptions of quasi-steadiness and uniform property distributions adopted in the analyses of Borman and Faeth were later relaxed to include several important aspects of droplet vaporization and combustion. In works by Matlosz *et al.*[17], Rosner and Chang[18], Kadata and Hiroyasu[19], and Curtis and Farrel[20], the effects of transient processes, natural convection, and the conditions under which a droplet may be driven to its critical point were examined.

Many practical liquid propellants consist of multicomponent mixtures. Even for pure cryogenic propellants such as liquid oxygen, the solubility of ambient gases in the liquid phase causes the droplet to become a multicomponent system. As a result of different volatilities and diffusivities of the liquid constituents, the vaporization and combustion processes present several features distinct from those of a simple component system. The major problem in treating multicomponent systems is to specify the state of mixedness of the liquid phase. Mass diffusion in the liquid phase is usually slower than heat diffusion; therefore, convection and transient effects are potentially more important for mass transfer than for heat transfer. At high pressures, the problem becomes even more difficult, due to the dissolution of ambient gases in the liquid phase and rapid variations of physical properties near the critical point. Jin and Borman[21] carried out a simplified analysis of multicomponent fuel droplet vaporization at elevated pressures and temperatures, noting the significance of liquid-phase transport. Several calculated results were given for pentane/octane mixtures. The potential for this particular fuel to undergo microexplosions was also discussed briefly.

Hsieh et al.[4] recently developed a comprehensive analysis to investigate hydrocarbon fuel-droplet vaporization at near-critical conditions. The model is based on full time-dependent conservation equations, with thorough treatment of

property variations and high-pressure vapor-liquid phase equilibrium. Because of its completeness, the model enables systematic examination of droplet vaporization in a high-pressure environment. Results of Hsieh's work indicate that ambient pressure strongly influences the vaporization process and that the droplet evaporation rate increases progressively with pressure. In the extreme case, droplets may reach their critical states before the end of their lifetimes, thereby causing a significant change in the vaporization process.

Although the preceding studies have provided significant information to understanding the physics and chemistry of droplet vaporization and combustion at high pressures, a number of fundamental problems remain unresolved. First, much of the previous work employed certain assumptions and empirical correlations which were extrapolated from low-pressure cases and involved a considerable number of uncertainties. Second, no unified treatment of the entire droplet history, in particular the transition from subcritical to supercritical state, was made. Almost all of the models for supercritical droplet vaporization and combustion assumed that the droplet reaches its critical state instantaneously upon introduction into a supercritical environment. Neither initial heat-up transients nor non-uniformities of property distributions in the droplet were taken into account in these analyses. Third, very little is known about multicomponent systems, ignition transients, and effects of forced convection. It is difficult, therefore, to apply the results for a single droplet to a spray environment without introducing errors. Fourth, almost no attempt was made to investigate the dynamic responses of droplet transport to ambient flow oscillations. In the study of combustion instabilities, these responses are particularly important since the interactions between droplet vaporization/combustion and acoustic wave oscillations represent one of

the major (if not the most significant) mechanisms for driving unsteady motions in a rocket motor.

In order to correct the deficiencies of existing models for high-pressure droplet vaporization and combustion, the following research topics are required:

1. comprehensive analysis of multicomponent droplet vaporization and combustion in both quiescent and forced-convective environments, including calculations of detailed physical and chemical processes;
2. examination of the effects of droplet interactions on interface mass, momentum, and energy transfer at high pressure;
3. establishment of correlations for droplet vaporization and combustion in terms of ambient flow conditions and droplet states;
4. investigation of droplet ignition transients; and
5. study of the dynamic responses of droplet transport rates to ambient flow oscillations.

1.2 Research Objectives

The physical and chemical mechanisms associated with droplet vaporization and combustion at high pressure are extremely complicated. Many intricate flow, transport, and combustion processes occur in various parts of the liquid- and gas-phase regions. In view of the inadequacy of existing theories and experimental techniques, a theoretical investigation of the problem using direct numerical simulation methods is conducted here.

The overall objective of this work is to answer some of the fundamental questions regarding liquid-propellant droplet vaporization and combustion in a high-pressure environment. Specific program objectives are:

1. to acquire basic understanding of physical and chemical mechanisms involved in the vaporization and combustion of isolated multicomponent liquid-propellant droplets in both stagnant and forced-convective environments;
2. to establish droplet vaporization and combustion correlations for the study of liquid-propellant spray combustion and two-phase flow fields in rocket engines;
3. to investigate dynamic responses of droplet vaporization to ambient flow oscillations; and
4. to incorporate the droplet vaporization response functions developed in this project into existing stability analyses for examining the unsteady behavior of a rocket engine.

The present theoretical research represents a series of investigations into the behavior of liquid-propellant droplets at elevated pressures and temperatures. In addition to contributions to the knowledge base of the fundamental mechanisms of droplet vaporization and combustion, results can be applied effectively to existing spray models for engine performance and stability predictions. In the following chapters, droplet behavior for both hydrocarbon and cryogenic propellants are investigated. The theoretical models, including conservation laws of physics and a unified evaluation scheme for thermophysical properties, are first described

in Chapter 2. Since all the governing equations are strongly coupled together, a robust numerical scheme capable of treating transient, low Mach-number compressible flows is adopted. Chapter 3 explains this numerical method and associated discretization procedure. Chapter 4 focuses on droplet vaporization and combustion in quiescent environments where the pressure and temperature are either above or below the critical points of the propellants. Effects of ambient pressure on droplet behavior are studied systematically. Many intricate flow, transport, and combustion processes occurring in various parts of the liquid and gas-phase regions are discussed in detail. Dynamic responses of liquid-fuel droplet vaporization to ambient pressure oscillations are examined in Chapter 5. The analysis extends the model of droplet combustion described in Chapter 4, and includes a periodic pressure oscillation in the ambient flow. The purpose is to provide a detailed understanding of pressure-coupled droplet vaporization response, including the amplification gain and time delay due to the transient processes involved in the vaporization process. Chapter 6 investigates the effects of flow convection on supercritical droplet gasification mechanisms. The work treats multi-dimensional flowfields in both the droplet interior and surrounding gases. Because the model is based on the complete conservation laws of mass, momentum, energy, and species, several important transient phenomena, including droplet dynamics and interphase transport, can be thoroughly studied. Finally, conclusions of the present work are summarized in Chapter 7.

CHAPTER 2

THEORETICAL FORMULATION

2.1 Droplet Behavior in Quiescent Environments

Vaporization and combustion of an isolated liquid droplet in a quiescent environment are first considered. This configuration allows researchers to focus on the effects of pressure on the thermodynamic and transport processes involved. The initial temperature of the droplet is subcritical, but the ambient temperature and pressure are in the supercritical regime of the liquid species, as shown in Fig. 2.1(a). As a result of heat transfer from the surrounding gases, the surface temperature increases, and may reach its critical mixing point during the droplet lifetime. Prior to occurrence of the critical mixing condition, the droplet surface provides a well-defined interfacial boundary which separates the liquid phase from the ambient gases. To facilitate formulation, these two regions are treated separately, then linked together at the droplet surface by requiring liquid-vapor phase equilibrium and continuities of mass and energy. The procedure eventually determines the droplet vaporization rate and interface conditions, e.g., surface temperature, species concentrations, and enthalpy of vaporization. When the surface becomes critical, the sharp distinction between gas and liquid vanishes. The latent heat of vaporization reduces to zero, with no abrupt phase change involved in the vaporization process. The density and temperature of the entire field (including both liquid droplet and ambient gases) as well as their gradients vary continuously across the droplet surface. The droplet interior, however, remains at the

liquid state with a subcritical temperature distribution. Under this situation, the droplet regression is best characterized by the motion of the surface which attains the critical mixing temperature of the system.

2.1.1 Governing Equations

The analysis is based on the time-dependent conservation laws of physics for a multicomponent system. For problems involving moving boundaries and complicated two-phase flows, the finite-volume formulation offers definite advantages over the differential formulation due to the physical clarity of the method. If body forces, viscous dissipation and radiation are ignored, the dynamic behavior of the flowfield can be described by the following formulation.

Mass:

$$\frac{\partial}{\partial t}\int_{\Delta V}\rho dV + \int_A \rho(u_r - u_g)dA = 0 \tag{2.1}$$

Momentum:

$$\frac{\partial}{\partial t}\int_{\Delta V}\rho u_r dV + \int_A \rho u_r(u_r - u_g)dA + \int_A p dA = \int_A \tau_{rr} dA \tag{2.2}$$

Energy:

$$\frac{\partial}{\partial t}\int_{\Delta V}\rho e_t dV + \int_A \rho e_t(u_r - u_g)dA + \int_A p u_r dA = \int_A q_e dA \tag{2.3}$$

Species Concentration:

$$\frac{\partial}{\partial t}\int_{\Delta V}\rho Y_i dV + \int_A \rho Y_i(u_r - u_g)dA = \int_A q_{m,i} dA + \int_{\Delta V}\dot{w}_i dV \tag{2.4}$$

where the surface and volume integrations are carried out over a finite spherical control volume concentric with the droplet (see Fig. 2.2). The physical variables

(a)

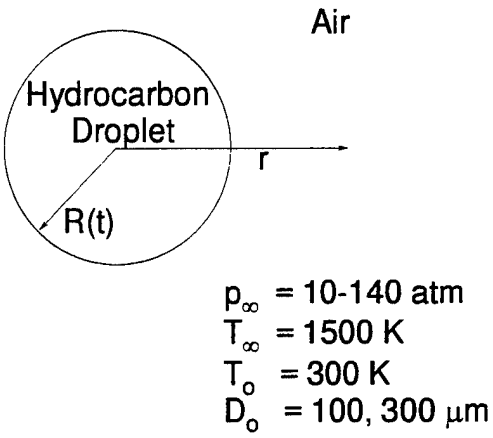

(b)

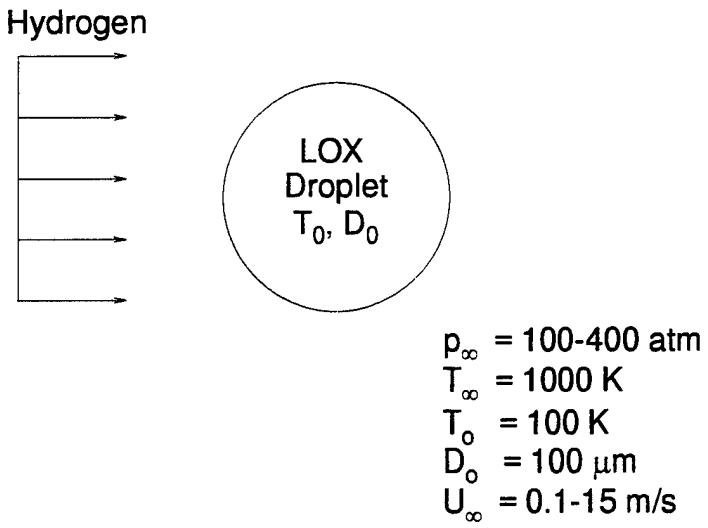

Figure 2.1. Schematic Diagrams of Droplet Vaporization and Combustion: (a) in Quiescent Environments. (b) in Forced Convective Environments.

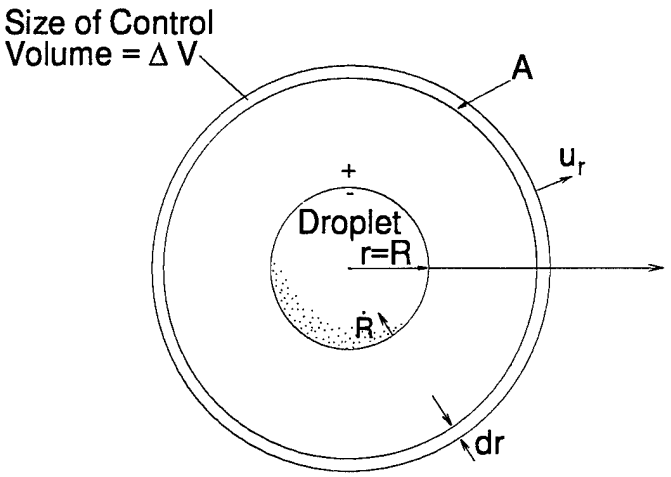

Figure 2.2. Schematic of a Spherical Droplet.

ρ, u_r, p, Y_i, and $\dot{w}_i$ are density, radial velocity, pressure, species concentration and rate of production of species i, respectively, and u_g the grid moving velocity. The specific total internal energy is written as

$$e_t = h - \frac{p}{\rho} + \frac{1}{2}u_r^2 \tag{2.5}$$

with h the specific enthalpy. In a spherically symmetric coordinate, the normal stress τ_{rr} takes the form

$$\tau_{rr} = \frac{1}{r^2}\frac{\partial}{\partial r}\left(r^2\mu\frac{\partial u_r}{\partial r}\right) - \frac{2\mu u_r}{r^2} \tag{2.6}$$

where μ is the viscosity and r the radial coordinate relative to the droplet center. Thermal and species diffusions are evaluated using Fourier's and Fick's laws, respectively.

$$q_e = -\lambda \frac{\partial T}{\partial r} - \rho \sum_{i=1}^{N} h_i \mathcal{D}_{im} \frac{\partial Y_i}{\partial r} \tag{2.7}$$

$$q_{m,i} = -\rho \mathcal{D}_{im} \frac{\partial Y_i}{\partial r} \tag{2.8}$$

where the index N is the number of species considered, and T, λ, h_i, and $\mathcal{D}_{im}$ the temperature, thermal conductivity, specific enthalpy and effective mass diffusion coefficient for species i, respectively.

A moving grid system is employed to simplify the problem associated with droplet surface motion. In the gas phase, all the finite-volume cells move uniformly toward the center at a speed of u_g, taken to be the droplet surface regression rate, $u_g = dR/dt$. In the liquid phase, owing to the finite radius of the droplet, a time-varying grid system is used, with the grid moving velocity equal to the instantaneous local flow velocity.

For convenience, the conservation equations are collected into a vector form

$$\frac{\partial}{\partial t} \int_{\Delta V} Q dV + \int_A (E - E_v) dA - u_g \int_A Q dA = \int_{\Delta V} S dV \tag{2.9}$$

where

$$Q = \begin{pmatrix} \rho \\ \rho u_r \\ \rho e_t \\ \rho Y_i \end{pmatrix}$$

$$E = \begin{pmatrix} \rho u_r \\ \rho u_r^2 + p \\ (\rho e_t + p) u_r \\ \rho u_r Y_i \end{pmatrix} \qquad E_v = \begin{pmatrix} 0 \\ \tau_{rr} \\ q_e \\ q_{m,i} \end{pmatrix}$$

$$S = \begin{pmatrix} 0 \\ 0 \\ 0 \\ \dot{w}_i \end{pmatrix}$$

All the variables of Q in the vector equation are treated simultaneously in a fully coupled manner.

2.1.2 Boundary Conditions

Liquid Phase

A symmetric boundary condition is implemented at the droplet center($r = 0$). That is, the radial velocity and gradients of pressure, temperature and species concentration must be zero at the droplet center.

$$u_r\Big|_{r=0} = 0 \tag{2.10}$$

$$\frac{\partial p}{\partial r}\Big|_{r=0} = \frac{\partial T}{\partial r}\Big|_{r=0} = \frac{\partial Y_i}{\partial r}\Big|_{r=0} = 0 \tag{2.11}$$

Gas Phase

Since the convective velocity is negligible small in the far field, the pressure is set to be the ambient pressure. In addition, the gradients of temperature, velocity,

and species concentration are zero. In mathematical form, they can be expressed as follows.

$$p\Big|_{r\to\infty} = p_\infty \tag{2.12}$$

$$\left.\frac{\partial u_r}{\partial r}\right|_{r\to\infty} = \left.\frac{\partial T}{\partial r}\right|_{r\to\infty} = \left.\frac{\partial Y_i}{\partial r}\right|_{r\to\infty} = 0 \tag{2.13}$$

2.1.3 Matching Conditions at Liquid/Vapor Interface

The physical processes in each phase must be linked at the droplet surface to provide the interfacial boundary conditions (including temperature, density, and species concentration) and the vaporization rate at subcritical conditions. Matching is accomplished by requiring the prevalence of thermodynamic phase equilibrium and continuities of mass and energy fluxes, as shown in Figs. 2.3(a)-(d).

Mass Balance for the Mixture

$$\dot{m}_v'' = \rho(u_r - u_{g,s})\Big|_{r=R_+} \tag{2.14}$$

Mass Balance for Species i

$$\left[\dot{m}_v'' Y_i - \rho\mathcal{D}_{im}\frac{\partial Y_i}{\partial r}\right]_{r=R_-} = \left[\dot{m}_v'' Y_i - \rho\mathcal{D}_{im}\frac{\partial Y_i}{\partial r}\right]_{r=R_+} \tag{2.15}$$

Force Balance

$$p^\ell - p^v = 0 \tag{2.16}$$

Energy Balance

$$-\lambda\left.\frac{\partial T}{\partial r}\right|_{r=R_-} = -\lambda\left.\frac{\partial T}{\partial r}\right|_{r=R_+} + \sum_{i=1}^{N}\left[\dot{m}_v'' Y_i - \rho\mathcal{D}_{im}\frac{\partial Y_i}{\partial r}\right]_{r=R_+}\Delta h_{v,i} \tag{2.17}$$

where $\dot{m}_v''$ is the droplet mass gasification rate per unit surface area, and $\Delta h_{v,i}$ the specific enthalpy of vaporization of species i. The subscripts R_+ and R_- represent conditions at the droplet surface on the gas and liquid sides, respectively.

When the droplet surface reaches the critical mixing point, the sharp distinction between gas and liquid phases disappears. The entire flowfield (including both liquid droplet and ambient gases) essentially becomes a continuous medium, with no abrupt phase transition. Under this situation, interfacial matching conditions are no longer needed, and the entire flow field can be treated as a single-phase fluid.

2.2 Droplet Behavior in Forced-Convective Environments

The second case deals with cryogenic fluid droplets in supercritical streams. A liquid oxygen (LOX) droplet initially with a uniform distribution of subcritical temperature is introduced into hydrogen flows, where the pressure and temperature are both in the supercritical regime of oxygen, as shown in Fig. 2.1(b). As a result of heat transfer from the ambient stream, the droplet surface reaches the thermodynamic critical mixing state almost instantaneously upon introduction to the hydrogen gas due to the cryogenic fluid property of oxygen. Once this occurs, the enthalpy of vaporization and surface tension vanish. The entire flowfield (including both droplet and surrounding gases) becomes essentially a continuous medium, and no well-defined liquid/vapor interfacial boundary exists as for a subcritical droplet. The temperature and density, as well as their spatial gradients, vary smoothly throughout the domain from the liquid core to the far field. In the following, a single-phase multidimensional fluid model is adopted to facilitate the analysis.

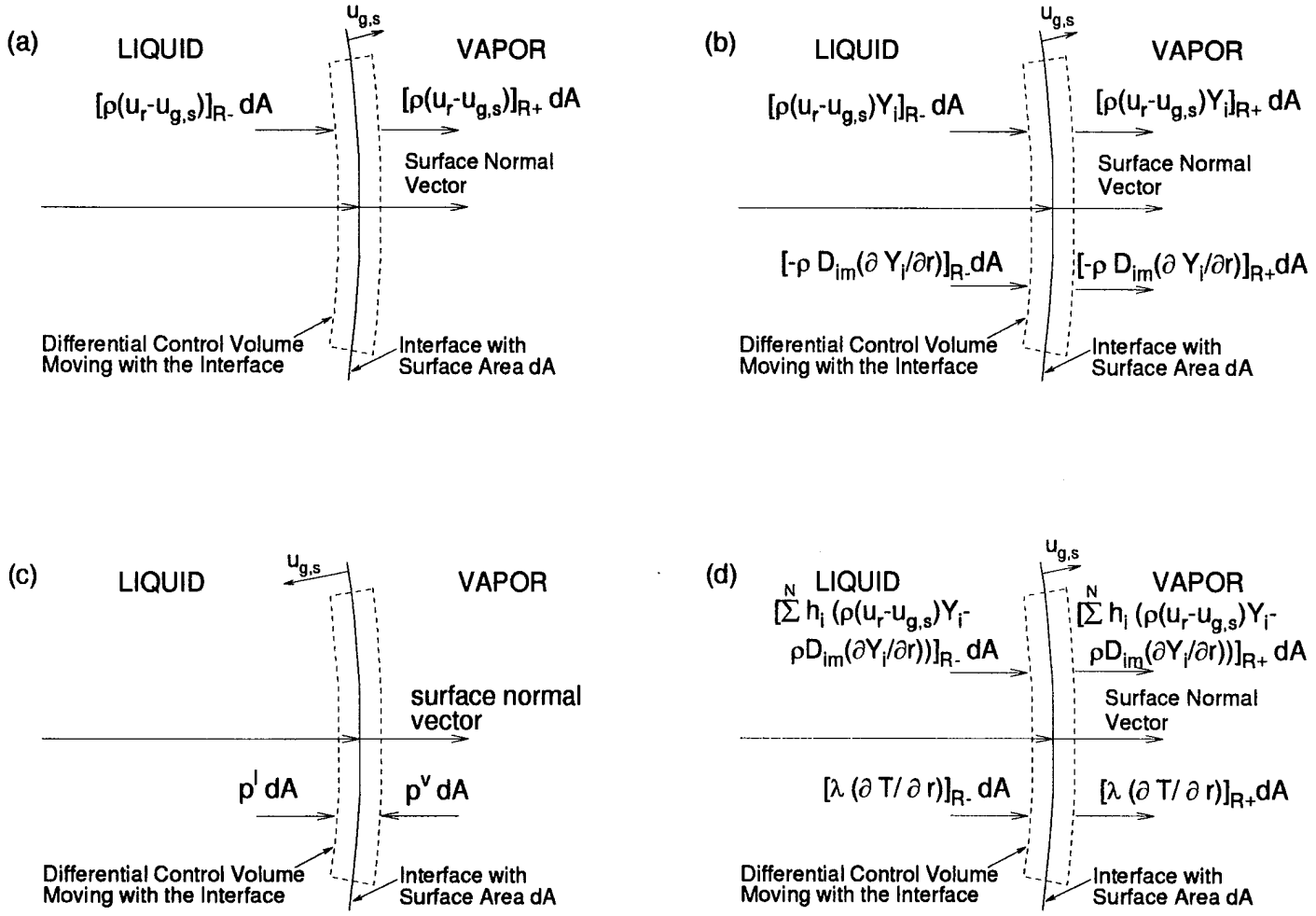

Figure 2.3. Matching Conditions at Liquid/Vapor Interface: (a) Mass Fluxes across Droplet Surface. (b) Mass Fluxes of Species i at Liquid/Vapor Interface. (c) Force Balance at Droplet Surface. (d) Energy Transport across a Liquid/Vapor Interface.

2.2.1 Governing Equations

The flow field is assumed to be laminar and axisymmetric. If body forces and radiation are ignored, the governing equations can be written in the following conservative form.

Mass:

$$\frac{\partial \rho}{\partial t} + \frac{\partial \rho u}{\partial x} + \frac{\partial \rho v}{\partial r} = 0 \tag{2.18}$$

Axial-momentum:

$$\frac{\partial \rho u}{\partial t} + \frac{\partial}{\partial x}(\rho u^2 + p) + \frac{\partial \rho uv}{\partial r} = \frac{\partial \tau_{xx}}{\partial x} + \frac{\partial \tau_{rx}}{\partial r} - \frac{2}{3}\frac{\partial}{\partial x}(\mu v) \tag{2.19}$$

Radial-momentum:

$$\begin{aligned} \frac{\partial \rho u}{\partial t} + \frac{\partial \rho uv}{\partial x} \quad &+ \quad \frac{\partial}{\partial r}(\rho v^2 + p) = \frac{\partial \tau_{xr}}{\partial x} + \frac{\partial \tau_{rr}}{\partial r} \\ &+ \quad \left[p - \frac{4}{3}\mu\frac{v}{r} + \frac{2}{3}\mu\frac{\partial u}{\partial x} + \frac{2}{3}\mu\frac{\partial v}{\partial r} - \frac{2}{3}\frac{\partial}{\partial r}(\mu v)\right] \end{aligned} \tag{2.20}$$

Energy:

$$\begin{aligned} \frac{\partial \rho e_t}{\partial t} + \frac{\partial}{\partial x}[(\rho e_t + p)u] \quad &+ \quad \frac{\partial}{\partial r}[(\rho e_t + p)v] = \frac{\partial}{\partial x}(u\tau_{xx}) + \frac{\partial}{\partial r}(u\tau_{rx}) \\ &+ \quad \frac{\partial}{\partial x}(v\tau_{xr}) + \frac{\partial}{\partial r}(v\tau_{rr}) + \frac{\partial (q_e)_x}{\partial x} + \frac{\partial (q_e)_r}{\partial r} \\ &- \quad \frac{2}{3}\frac{\partial}{\partial x}(\mu uv) - \frac{2}{3}\frac{\partial}{\partial r}(\mu v^2) \end{aligned} \tag{2.21}$$

Species Concentration:

$$\frac{\partial \rho Y_i}{\partial t} + \frac{\partial \rho u Y_i}{\partial x} + \frac{\partial \rho v Y_i}{\partial r} = \frac{\partial (q_{m,i})_x}{\partial x} + \frac{\partial (q_{m,i})_r}{\partial r} \tag{2.22}$$

The physical variables t, u, v, and Y_i are the time, velocity components in the axial and radial (x- and r-) directions, respectively, and the mass fraction of component i. The specific total internal energy is written as

$$e_t = h - \frac{p}{\rho} + \frac{1}{2}(u^2 + v^2) \tag{2.23}$$

The normal stresses, τ_{xx} and τ_{rr}, and shear stresses, τ_{xr} and τ_{rx} are

$$\tau_{xx} = \mu\left(\frac{4}{3}\frac{\partial u}{\partial x} - \frac{2}{3}\frac{\partial v}{\partial r}\right) \tag{2.24}$$

$$\tau_{xr} = \tau_{rx} = \mu\left(\frac{\partial u}{\partial r} + \frac{\partial v}{\partial x}\right) \tag{2.25}$$

$$\tau_{rr} = \mu\left(\frac{4}{3}\frac{\partial v}{\partial r} - \frac{2}{3}\frac{\partial u}{\partial x}\right) \tag{2.26}$$

where μ is the viscosity.

Fourier's and Fick's laws are applied to evaluate the thermal and species diffusion fluxes.

$$(q_e)_x = -\lambda\frac{\partial T}{\partial x} - \rho\sum_{i=1}^{N} h_i \mathcal{D}_{im}\frac{\partial Y_i}{\partial x} \tag{2.27}$$

$$(q_e)_r = -\lambda\frac{\partial T}{\partial r} - \rho\sum_{i=1}^{N} h_i \mathcal{D}_{im}\frac{\partial Y_i}{\partial r} \tag{2.28}$$

$$(q_{m,i})_x = -\rho\mathcal{D}_{im}\frac{\partial Y_i}{\partial x} \tag{2.29}$$

$$(q_{m,i})_r = -\rho\mathcal{D}_{im}\frac{\partial Y_i}{\partial r} \tag{2.30}$$

where T, λ, and $\mathcal{D}_{im}$ are the temperature, thermal conductivity, and mass diffusivity for species i in mixture, respectively.

2.2.2 Boundary Conditions

Centerline Boundary Condition

The centerline boundary conditions are specified based on flow symmetry, which are given by setting the normal velocity and gradients of the pressure, tangential velocity, temperature, and species concentration to zero.

$$v\Big|_{r=0} = 0 \tag{2.31}$$

$$\frac{\partial p}{\partial r}\Big|_{r=0} = \frac{\partial u}{\partial r}\Big|_{r=0} = \frac{\partial T}{\partial r}\Big|_{r=0} = \frac{\partial Y_i}{\partial r}\Big|_{r=0} = 0 \tag{2.32}$$

Inflow Boundary Condition

For a subsonic inflow, the temperature, species concentration, and axial and tangential velocities are specified. The pressure is extrapolated from the interior cells.

Outflow Boundary Condition

Since the outflow is subsonic, a back pressure is specified, with other flow variables extrapolated from the interior.

2.3 Thermophysical Properties

One major challenge in the present analysis is the establishment of a unified property evaluation scheme capable of treating thermophysical properties over the entire mixture thermodynamic state from compressed liquid to dilute gas. These properties can be generally divided into two classes: thermodynamic (i.e., density, internal energy, and specific heat) and transport (i.e., viscosity, thermal conductivity, and mass diffusivity) properties. At high pressure, models normally used

to represent ideal-gas behavior may encounter significant errors. From the microscopic point of view, the intermolecular mean free paths tend to decrease with increasing pressure; the molecular volume and intermolecular forces are no longer negligible as for the ideal fluids. For convenience, each property is expressed as the sum of an ideal-gas property at the same temperature and a thermodynamic departure function which takes into account the dense-fluid correction. This departure function quantifies thermodynamic nonideality and can be derived directly from a given equation of state.

For a multicomponent system, accounting for changes in properties due to mixing is much more complicated. A pseudo pure substance model is adopted to evaluate the properties of a mixture, treating the mixture as a single-phase fluid with its own set of properties evaluated via the extended corresponding-state (ECS) principle. This method improves the prediction accuracy and only limited data (i.e., critical properties and Pitzer's acentric factors) for each constituent component are needed. Successful application of the corresponding-state argument for the evaluation of fluid p-V-T properties also encourages similar improvement in the prediction of thermophysical data. Density serves as an important parameter in the evaluation process, mainly due to the fact that the temperature dependence of properties at constant density is much smaller when compared with that at constant pressure. In the following, the corresponding-state method in conjunction with the mixture combining rule is first discussed, followed by a brief summary of the equations of state used in the present study. Finally, the evaluation schemes for both thermodynamic and transport properties are addressed thoroughly.

2.3.1 Extended Corresponding-State Principle

Two scaling factors are used to characterize the conformal mappings of temperature and density between the mixture of interest and the reference fluid[21,22].

$$f_m = \frac{T}{T_0} \;\; ; \qquad \hbar_m = \frac{\rho_0}{\rho} \tag{2.33}$$

The former represents the conformation of temperature, while the latter characterizes the effect of mixture molecular size. The subscripts m and 0 refer respectively to the fluid of interest and the reference fluid. Assuming all components in a mixture obey the extended corresponding-state principle, the following mixing rules for a multicomponent system are applied to the scaling factors

$$\begin{aligned} f_m &= \hbar_m^{-1} \sum_{i=1}^{N} \sum_{j=1}^{N} X_i \, X_j \, f_{ij} \, \hbar_{ij} \\ \hbar_m &= \sum_{i=1}^{N} \sum_{j=1}^{N} X_i \, X_j \, \hbar_{ij} \end{aligned} \tag{2.34}$$

where N and X_i are the number of species and the mole fraction of species i. The two binary scaling factors f_{ij} and $\hbar_{ij}$ are defined as

$$\begin{aligned} f_{ij} &= (f_i f_j)^{1/2}(1 - k_{ij}) \\ \hbar_{ij} &= \frac{1}{8}(\hbar_i^{1/3} + \hbar_j^{1/3})^3(1 - \ell_{ij}) \end{aligned} \tag{2.35}$$

where k_{ij} and ℓ_{ij} are binary interaction parameters accounting for the effects of energy and molecular size, respectively. In order to model the quantum behavior of hydrogen, interaction parameters for a hydrogen-containing mixture are specially treated by a generalized correlation proposed by Valderrama and Reyes[23].

$$k_{ij} = A - B/T_j^*$$

$$\ell_{ij} = 1 + 0.07 \ln[(D_{big}/D_{small})] \tag{2.36}$$

where

$$\begin{aligned} [D_{big}/D_{small}] &= [\mathrm{v}_{c,big}/\mathrm{v}_{c,small}]^{1/3} \\ A &= 0.1805 + 3.21\omega_j + 2.437\omega_j^2 \\ B &= 0.1323 + 0.5507\omega_j + 3.5994\omega_j^2 \end{aligned} \tag{2.37}$$

where $[D_{big}/D_{small}]$ is always greater than 1 and v_c is the critical molar volume. The variable T^* is the reduced temperature and ω Pitzer's acentric factor. The subscripts i and j denote the hydrogen and non-hydrogen components, respectively.

The scaling factors (f_i and $\hbar_i$) for each individual component can be obtained by a two-parameter corresponding state principle[21,22].

$$\begin{aligned} f_i &= (T_{c,i}/T_{c,0})\ \theta_i(T_i^*, \mathrm{v}_i^*, \omega_i) \\ \hbar_i &= (\mathrm{v}_{c,i}/\mathrm{v}_{c,0})\ \phi_i(T_i^*, \mathrm{v}_i^*, \omega_i) \end{aligned} \tag{2.38}$$

where T_c is the critical temperature and θ_i and ϕ_i are the so-called shape factors which are functions of Pitzer's acentric factor (ω_i) and reduced temperature and molar volume (T_i^* and v_i^*). The analytical expressions for θ_i and ϕ_i proposed by Leach and Leland[24] take the forms

$$\begin{aligned} \theta_i(T_i^*, \mathrm{v}_i^*, \omega_i) &= 1 + (\omega_i - \omega_0)\ F(T_i^*, \mathrm{v}_i^*) \\ \phi_i(T_i^*, \mathrm{v}_i^*, \omega_i) &= [1 + (\omega_i - \omega_0)\ G(T_i^*, \mathrm{v}_i^*)]Z_{c,0}/Z_{c,i} \end{aligned} \tag{2.39}$$

and

$$F(T_i^*, \mathrm{v}_i^*) = a_1 + b_1 \ln T_i^+ (c_1 + d_1/T_i^+)(\mathrm{v}_i^+ - 0.5)$$

$$G(T_i^*, \mathrm{v}_i^*) = a_2(\mathrm{v}_i^+ + b_2) + c_2(\mathrm{v}_i^+ + d_2)\ln T_i^+ \tag{2.40}$$

$$\begin{aligned} T_i^+ &= min\{2, max\{T_i^*, 0.5\}\} \\ \mathrm{v}_i^+ &= min\{2, max\{\mathrm{v}_i^*, 0.5\}\} \end{aligned} \tag{2.41}$$

where Z is the compressibility factor, and the asterisk $*$ represents reduced properties defined as the values which are divided by the corresponding quantity at the critical point. Constants a_i, b_i, c_i, and d_i are coefficients for shape-factor correlations and can be found in Ref. [24].

2.3.2 Equations of State

An adequate equation of state is required to complete the formulation for the property evaluation. In the following, two commonly used equations of state are described: the Soave-Redlich-Kwong (SRK) and Benedict-Webb-Rubin (BWR) equations of state.

2.3.2.1 Soave-Redlich-Kwong Equation of State

The Soave-Redlich-Kwong equation of state is an extension of the original Redlich-Kwong equation of state by introducing an acentric factor and a temperature dependence into the cohesive energy term to account for the effect of non-sphericity on fluid p-V-T properties. It takes the form

$$p = \frac{\mathcal{R}_u T}{\mathrm{v} - b} - \frac{\alpha a}{\mathrm{v}(\mathrm{v} + b)} \tag{2.42}$$

where $\mathcal{R}_u$ and v are the universal gas constant and molar volume, respectively. The mass-averaged parameters αa and b for a mixture are determined using the van der Waals one-fluid combining rule[25].

$$\alpha a = \sum_{i=1}^{N}\sum_{j=1}^{N} X_i X_j \alpha_{ij} a_{ij}, \qquad b = \sum_{i=1}^{N} X_i b_i \tag{2.43}$$

where X_i is the mole fraction of species i, and the cross mixture parameter $\alpha_{ij}a_{ij}$ for the ij pair is

$$\alpha_{ij}a_{ij} = (1 - k_{ij})\sqrt{\alpha_i \alpha_j a_i a_j} \tag{2.44}$$

where k_{ij} is the interaction coefficient which accounts for the deviation from the geometric-mean combining rule for αa, and α_i is an empirical function of reduced temperature and Pitzer's acentric factor. For most of hydrocarbon fuels and certain non-hydrocarbons, α_i can be expressed as

$$\alpha_i = [1 + S_i(1 - \sqrt{T^*})]^2 \tag{2.45}$$

with T^* the reduced temperature. The expression for S_i suggested by Graboski and Daubert[26] is given below.

$$S_i = 0.48508 + 1.55171\omega_i - 0.15613\omega_i^2 \tag{2.46}$$

where ω_i is Pitzer's acentric factor of component i. In Eqs. (2.43) and (2.44), the energy and volume constants a_i and b_i depend on the critical properties of each species and take the form

$$\begin{aligned} a_i &= 0.42747\frac{\mathcal{R}_u^2 T_{c,i}^2}{p_{c,i}} \\ b_i &= 0.08664\frac{\mathcal{R}_u T_{c,i}}{p_{c,i}} \end{aligned} \tag{2.47}$$

with $T_{c,i}$ and $p_{c,i}$ the critical temperature and pressure of component i, respectively.

If the compressibility factor is introduced to characterize the thermodynamic non-ideality, the equation of state is rewritten as

$$pv = Z\mathcal{R}_u T \tag{2.48}$$

Substitution of (2.48) into (2.42) and rearrangement of the result lead to a cubic polynomial equation for the compressibility factor Z.

$$Z^3 - Z^2 + (A - B - B^2)Z - AB = 0 \tag{2.49}$$

where

$$A = \frac{\alpha a p}{\mathcal{R}_u^2 T^2}, \qquad B = \frac{bp}{\mathcal{R}_u T} \tag{2.50}$$

Equation (2.49) can be solved to obtain three roots which take the form

$$Z = \frac{1}{3} + A' + B', \quad \frac{1}{3} - \frac{A'+B'}{2} + \frac{A'-B'}{2}\sqrt{3}i, \quad \frac{1}{3} - \frac{A'+B'}{2} - \frac{A'-B'}{2}\sqrt{3}i \tag{2.51}$$

where

$$\begin{aligned} A' &= \sqrt[3]{-\frac{d}{2} + \sqrt{\frac{d^2}{4} + \frac{c^3}{27}}} \\ B' &= \sqrt[3]{-\frac{d}{2} - \sqrt{\frac{d^2}{4} + \frac{c^3}{27}}} \end{aligned} \tag{2.52}$$

and

$$\begin{aligned} c &= A - B - B^2 - \frac{1}{3} \\ d &= \frac{1}{27}\left[\rho(A - B - B^2) - 27AB - 2\right] \end{aligned} \tag{2.53}$$

For a system involving two phases, at a given temperature and pressure, the smallest real root is designated to the liquid phase, while the largest to the gas phase.

2.3.2.2 Benedict-Webb-Rubin Equation of State

Although the Benedict-Webb-Rubin (BWR) equation of state is more complicated than classical cubic equations of state (e.g., the SRK equation of state), it has demonstrated superior performance over wide ranges of temperature and pressure. However, the constants for the BWR equation of state are valid only for a limited number of pure compounds[27–29]. To overcome this constraint, an extended corresponding-state (ECS) principle is used. The basic idea is to assume the properties of a single phase fluid can be evaluated via conformal mappings of temperature and density to those of a given reference fluid. As a result, only the BWR constants for the reference substance are needed.

Under the assumption of the ECS principle, the density of a mixture can be evaluated by

$$\rho(T, p, X_i) = \frac{\rho_0(T_0, p_0)}{\hbar_m(T, p, X_i)} \tag{2.54}$$

where $\hbar_m$ is the scaling factor and ρ_0, T_0, and p_0 are the density, temperature and pressure, respectively, of the reference fluid at the corresponding state defined by Eq. (2.33). The related temperature at the conformal state takes the form

$$T_0 = \frac{T}{f_m(T, p, X_i)} \tag{2.55}$$

Based on the general compressibility theory[30], the corresponding pressure for reference fluid is evaluated by

$$p_0 = p\left[\frac{\hbar_m(T, p, X_i)}{f_m(T, p, X_i)}\right] \tag{2.56}$$

To ensure the accuracy of density prediction, a generalized BWR equation of state developed by Jacobsen and Stewart[31] is adopted for the reference fluid.

TABLE 2.1
BWR Parameters as Functions of Temperature.

$a_1(T)$	=	$\mathcal{R}T$
$a_2(T)$	=	$N_1T + N_2T^{1/2} + N_3 + N_4/T + N_5/T^2$
$a_3(T)$	=	$N_6T + N_7 + N_8/T + N_9/T^2$
$a_4(T)$	=	$N_{10}T + N_{11} + N_{12}/T$
$a_5(T)$	=	N_{13}
$a_6(T)$	=	$N_{14}/T + N_{15}/T^2$
$a_7(T)$	=	N_{16}/T
$a_8(T)$	=	$N_{17}/T + N_{18}/T^2$
$a_9(T)$	=	N_{19}/T^2
$a_{10}(T)$	=	$N_{20}/T^2 + N_{21}/T^3$
$a_{11}(T)$	=	$N_{22}/T^2 + N_{23}/T^4$
$a_{12}(T)$	=	$N_{24}/T^2 + N_{25}/T^3$
$a_{13}(T)$	=	$N_{26}/T^2 + N_{27}/T^4$
$a_{14}(T)$	=	$N_{28}/T^2 + N_{29}/T^3$
$a_{15}(T)$	=	$N_{30}/T^2 + N_{31}/T^3 + N_{32}/T^4$

$$p_0(T_0,\rho_0) = \sum_{n=1}^{9} a_n(T_0)\rho_0^n + \sum_{n=10}^{15} a_n(T_0)\rho_0^{2n-17}e^{-\gamma\rho_0^2} \tag{2.57}$$

where γ is 0.04 and the units for pressure, density, and temperature are

pressure (p):	bar
density (ρ):	liter/mole
temperature (T):	Kelvin

The functional forms of $a_i(T)$ are given in Table 2.1, where the coefficients N_i ($i = 1...32$) are dependent on the reference fluid. In the current study, methane is chosen as the reference fluid because of the availability of experimental data for both volumetric and transport properties over a broad range of fluid state. Table 2.2 provides the temperature constants of methane for the BWR equation of state.

TABLE 2.2
Temperature Constants of Methane for the BWR Equation of State.

$N_1 =$	$-1.184347314485\text{x}10^{-2}$	$N_{17} =$	$1.071143181503\text{x}10^{-5}$
$N_2 =$	$7.540377272657\text{x}10^{-1}$	$N_{18} =$	$-9.290851745353\text{x}10^{-3}$
$N_3 =$	$-1.225769717554\text{x}10^{+1}$	$N_{19} =$	$1.610140169312\text{x}10^{-4}$
$N_4 =$	$6.260681393432\text{x}10^{+2}$	$N_{20} =$	$3.469830970789\text{x}10^{+4}$
$N_5 =$	$-3.490654409121\text{x}10^{+4}$	$N_{21} =$	$-1.370878559048\text{x}10^{+6}$
$N_6 =$	$5.301046385532\text{x}10^{-4}$	$N_{22} =$	$1.790105676252\text{x}10^{+2}$
$N_7 =$	$-2.875764479978\text{x}10^{-1}$	$N_{23} =$	$1.615880743238\text{x}10^{+6}$
$N_8 =$	$5.011947936427\text{x}10^{+1}$	$N_{24} =$	$6.265306650288\text{x}10^{-1}$
$N_9 =$	$-2.821562800903\text{x}10^{+4}$	$N_{25} =$	$1.820173769533\text{x}10^{+1}$
$N_{10} =$	$-2.064957753744\text{x}10^{+5}$	$N_{26} =$	$1.449888505811\text{x}10^{-3}$
$N_{11} =$	$1.285951844828\text{x}10^{-2}$	$N_{27} =$	$-3.159999123798\text{x}10^{+1}$
$N_{12} =$	$-1.106266656726\text{x}10^{+0}$	$N_{28} =$	$-5.290335668451\text{x}10^{-6}$
$N_{13} =$	$3.060813353408\text{x}10^{-4}$	$N_{29} =$	$1.694350244152\text{x}10^{-3}$
$N_{14} =$	$-3.174982181302\text{x}10^{-3}$	$N_{30} =$	$8.612049038886\text{x}10^{-9}$
$N_{15} =$	$5.191608004779\text{x}10^{+0}$	$N_{31} =$	$-2.598235689063\text{x}10^{-6}$
$N_{16} =$	$-3.074944210271\text{x}10^{-4}$	$N_{32} =$	$3.153374374912\text{x}10^{-5}$

Although this equation of state must be solved iteratively for density at a given pressure and temperature, the prediction covers a wide range of thermodynamic state, and as such promotes the establishment of a unified evaluation scheme of thermophysical properties. Figure 2.4 shows the error of density prediction for oxygen at supercritical pressures of interest (100 and 400 atm) by three commonly used equations of state, i.e., the Benedict-Webb-Rubin (BWR) equation of state with extended corresponding-state principle (ECS), Peng-Robinson (PR), and Soave-Redlich-Kwong (SRK) equations of state. The BWR equation of state together with the ECS principle shows the deviation as low as 1.5% for both cases (100 and 400 atm). However, the SRK and PR equations of state may miscalculate the density by 13% and 17%, respectively. Figure 2.5 shows the comparison of oxygen density between experimental data and the prediction by the BWR equation

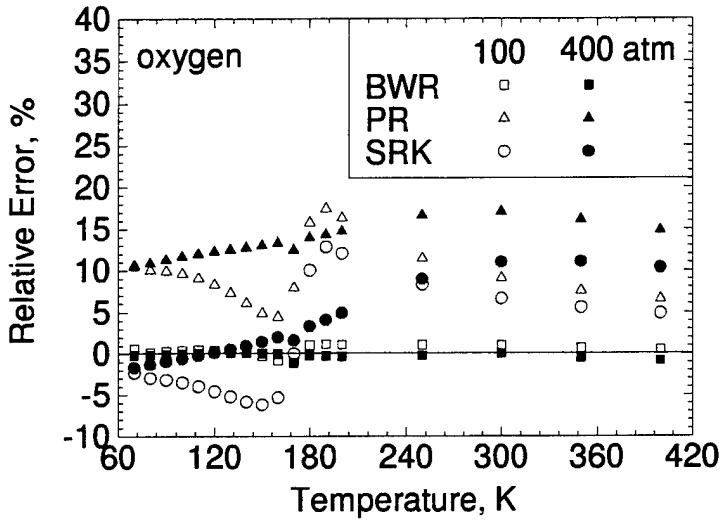

Figure 2.4. Relative Errors of Density Predictions by Three Different Equations of State.

of state in conjunction with the ECS principle. Excellent agreement is obtained over a wide range of fluid states, from compressed liquid to dilute gas.

2.3.3 Thermodynamic Properties

Thermodynamic properties are very important quantities in the analyses of supercritical droplet behavior. Variations in these properties can often be related to local fluid properties (i.e., pressure, temperature, and species concentration). Properties like enthalpy, internal energy, and specific heat of a mixture are expressible as the sum of the ideal-gas property and a correction term accounting for the thermodynamic non-idealities. A detailed derivation can be found in Appendix A.

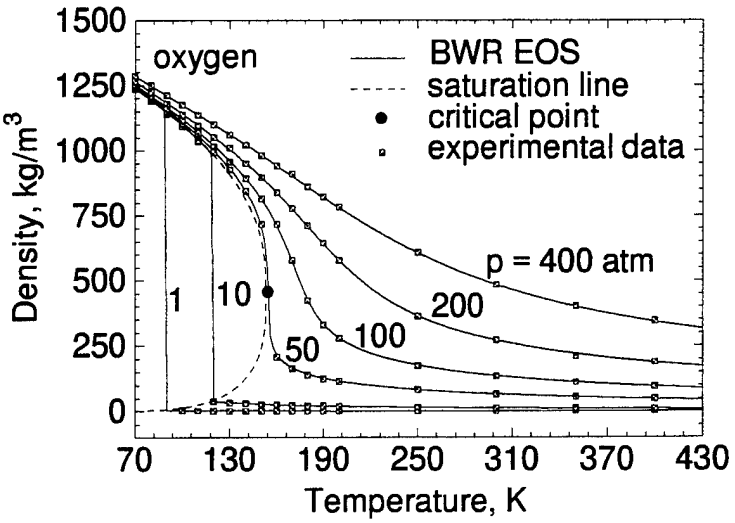

Figure 2.5. Comparison of Density Data Predicted by the BWR Equation of State and Experimental Measurement.

$$h = h^0 + \left\{ \int_{\rho^0}^{\rho} \frac{1}{\rho^2} \left[p - T\left(\frac{\partial p}{\partial T}\right)_\rho \right] d\rho + \mathcal{R}T(Z-1) \right\} \tag{2.58}$$

$$e = e^0 + \left\{ \int_{\rho^0}^{\rho} \frac{1}{\rho^2} \left[p - T\left(\frac{\partial p}{\partial T}\right)_\rho \right] d\rho \right\} \tag{2.59}$$

$$C_p = C_p^0 - \left\{ \int_{\rho^0}^{\rho} \frac{T}{\rho^2} \left(\frac{\partial^2 p}{\partial T^2}\right)_\rho d\rho + \frac{T}{\rho^2} \left(\frac{\partial p}{\partial T}\right)_\rho^2 \Big/ \left(\frac{\partial p}{\partial \rho}\right)_T + \mathcal{R} \right\} \tag{2.60}$$

The second terms represent the departure functions which can be further developed by combining Eqs. (2.33)-(2.41) and (2.57). If the constant-pressure specific heat for all the components in the ideal gas limit are given, the first terms on the right sides of Eqs. (2.58)-(2.60) can be expressed as

$$h^0 = \sum_{i=1}^{N} Y_i \left[h^0_{ref,i} + \int_{T_{ref}}^{T} C^0_{p,i} dT \right] \tag{2.61}$$

$$e^0 = \sum_{i=1}^{N} Y_i \left[e^0_{ref,i} + \int_{T_{ref}}^{T} (C^0_{p,i} - \mathcal{R}) dT \right] \tag{2.62}$$

$$C^0_p = \sum_{i=1}^{N} Y_i C^0_{p,i} \tag{2.63}$$

where Y_i is the mass fraction of component i, and $h^0_{ref,i}$, $e^0_{ref,i}$, and $C^0_{p,i}$ are the ideal-gas enthalpy, internal energy, and specific heat at a reference temperature of T_{ref}, respectively.

2.3.4 Transport Properties

Ely and Hanley proposed a corresponding-state model which is capable of predicting the transport properties of fluid mixtures over the entire p-V-T states[21,32]. This method requires only the common characterization parameters (i.e., critical properties and Pitzer's acentric factor) of each component as input parameters.

Viscosity

The mixture viscosity μ can be evaluated via the corresponding-state argument as

$$\mu(\rho, T, X_i, M_i) = \mu_0(\rho_0, T_0) \mathcal{F}_\mu(\rho, T, X_i, M_i) \tag{2.64}$$

where μ_0 is the value of the reference fluid at the corresponding thermodynamic state. The scaling factor $\mathcal{F}_\mu$ is defined herein as

$$\mathcal{F}_\mu = \left(\frac{M}{M_0}\right)^{1/2} f_m^{1/2}\ \hbar_m^{-2/3} \tag{2.65}$$

where M_0 is the molecular weight of the reference fluid, and the value of the mixture denoted by M can be evaluated by

$$M = \hbar_m^{-8/3} f_m^{-1} \left[\sum_{i=1}^{N}\sum_{j=1}^{N} X_i X_j \hbar_{ij}^{4/3} f_{ij}^{1/2} M_{ij}^{1/2}\right]^2 \tag{2.66}$$

The scaling factors f_m, $\hbar_m$, f_{ij}, and $\hbar_{ij}$ follow the same definitions in Eqs. (2.33) and (2.35). A binary mixing rule is used for the molecular weight.

$$M_{ij} = 2M_iM_j/(M_i + M_j) \tag{2.67}$$

where M_i is the molecular weight of component i. The viscosity for the reference fluid can be written as[21]

$$\mu_0(\rho_0, T_0) = \mu_0^{(1)}(T_0) + \mu_0^{(2)}(T_0)\rho_0 + \Delta\mu_0(\rho_0, T_0)\mathcal{X}_\mu \tag{2.68}$$

where $\mu_0^{(1)}$ and $\mu_0^{(2)}$ represent the viscosity at the dilute-gas limit and the first density correction, respectively. The third term is the high density correction, with $\Delta\mu_0$ being a dense-fluid remainder. These three terms can be evaluated based on the formulas listed in Table 2.3. A small correction factor, $\mathcal{X}_\mu$, is needed to account for possible errors induced by the corresponding state model. The following expression based on the modified Enskog theory is proposed by Hanley[33].

$$\mathcal{X}_\mu = \left\{\left[1 - 1.5\frac{T}{f_m}\left(\frac{\partial f_m}{\partial T}\right)_v\right]\frac{\sum_{i=1}^{N} X_i Z_{c,i}}{Z_{c,0}}\right\}^{1/2}\psi \tag{2.69}$$

where the subscript c refers to the critical values. The correction factor ψ, which empirically accounts for the size effect, is selected to be 1.5.

TABLE 2.3
Correlation of Viscosity for Methane; Units are gram-cm-sec-Kelvin.

$$\mu_0(\rho_0, T_0) = \mu_0^{(1)}(T_0) + \mu_0^{(2)}(T_0)\rho_0 + \Delta\mu_0(\rho_0, T_0)\mathcal{X}_\mu$$

where

$$\begin{aligned}
\mu_0^{(1)}(T) &= \sum_{n=1}^{9} c_n T^{(n-4)/3} \\
\mu_0^{(2)}(T) &= b_1 + b_2[b_3 - \ln(T/b_4)] \\
\Delta\mu_0(\rho, T) &= exp[a_1 + a_2/T]\{exp[(a_3 + a_4/T^{3/2})\rho^{0.1} \\
&+ (\rho/\rho_c - 1)\rho^{0.5}(a_5 + a_6/T + a_7/T^2)] - 1.0\}
\end{aligned}$$

i	a_i	b_i	c_i
1	$-1.0239160427\text{x}10^{+1}$	$1.6969859271\text{x}10^{+0}$	$2.907741307\text{x}10^{+6}$
2	$1.7422822961\text{x}10^{+2}$	$-1.3337234608\text{x}10^{-1}$	$-3.312874033\text{x}10^{+6}$
3	$1.7460545674\text{x}10^{+1}$	1.4	$1.608101838\text{x}10^{+6}$
4	$-2.8476328289\text{x}10^{+3}$	$1.68\text{x}10^{+2}$	$-4.331904871\text{x}10^{+5}$
5	$1.3368502192\text{x}10^{-1}$		$7.062481330\text{x}10^{+4}$
6	$1.4207239767\text{x}10^{+2}$		$-7.116620750\text{x}10^{+3}$
7	$5.0020669720\text{x}10^{+3}$		$4.325174400\text{x}10^{+2}$
8			$-1.445911210\text{x}10^{+1}$
9			$2.037119479\text{x}10^{-1}$

Thermal Conductivity

Evaluation of thermal conductivity must be carried out carefully for two reasons: (1) the one-fluid model must ignore the contribution of diffusion to conductivity, and (2) the effect of internal degrees of freedom on thermal conductivity cannot be correctly taken into account by the corresponding-state argument. As a result, thermal conductivity of a pure substance or mixture is generally divided into two contributions[22],

$$\lambda(\rho, T, X_i, M_i) = \lambda'_m(T, X_i, M_i) + \lambda''_m(\rho, T, X_i, M_i) \tag{2.70}$$

The former arises from the energy transfer via the internal degree of freedom, while the latter is due to the effects of molecular collision or translation. For a mixture, λ'_m can be evaluated via a semi-empirical mixing rule.

$$\lambda'_m = \sum_{i=1}^{N}\sum_{j=1}^{N} X_i X_j \lambda'_{ij} \tag{2.71}$$

where λ'_{ij} is binary thermal conductivity and is defined as

$$\left(\lambda'_{ij}\right)^{-1} = 2\left[(\lambda'_i)^{-1} + (\lambda'_j)^{-1}\right] \tag{2.72}$$

The internal contribution λ'_i is calculated using the modified Eucken correlation[34] for polyatomic gases as

$$\lambda'_i = 1.32\frac{\mu_i^0}{M_i}(C_{p,i}^0 - \frac{5}{2}\mathcal{R}) \tag{2.73}$$

where the properties μ_i^0, M_i, and $C_{p,i}^0$ are the d ıte gas viscosity, molecular weight, and ideal-gas heat capacity of component i, respectively.

In Eq. (2.70), the collisional and translational contribution $\lambda''_m(T, \rho)$ can be evaluated via the extended corresponding-state method.

$$\lambda_m''(T,\rho) = \lambda_0''(\rho_0, T_0)\mathcal{F}_\lambda \mathcal{X}_\lambda \tag{2.74}$$

Following the corresponding-state principle, the scaling factor $\mathcal{F}_\lambda$ is defined herein as

$$\mathcal{F}_\lambda = \left(\frac{M_0}{M_m}\right)^{1/2} f_m^{1/2}\ \hbar_m^{-2/3} \tag{2.75}$$

where the pseudo molecular weight is

$$M_m = f_m^{-1}\ \hbar_m^{8/3}\left[\sum_{i=1}^{N}\sum_{j=1}^{N} X_i X_j M_{ij}^{-1/2}\ f_{ij}^{1/2}\ \hbar_{ij}^{-4/3}\right]^{-2} \tag{2.76}$$

The correction for non-correspondence is applied over the entire collisional or translational contribution to the thermal conductivity and is defined as

$$\mathcal{X}_\lambda = \left\{\left[1 - \frac{T}{f_m}\left(\frac{\partial f_m}{\partial T}\right)_{\mathrm{v}}\right]\frac{Z_{c,0}}{\sum_{i=1}^{N} X_i Z_{c,i}}\right\}^{3/2} \tag{2.77}$$

This expression is derived from the Enskog theory so that the density dependence of the thermal conductivity is simply depended on the derivative term of $(\partial f_m/\partial T)_{\mathrm{v}}$. The value $\lambda_0''(\rho_0, T_0)$ is the equivalent contribution for the reference fluid at the corresponding state. Based on Hanley's model[22], this reference value can be divided into three contributors.

$$\lambda_0''(\rho_0, T_0) = \lambda_0^{(1)}(T_0) + \lambda_0^{(2)}(T_0)\rho_0 + \Delta\lambda_0(\rho_0, T_0) \tag{2.78}$$

where $\lambda_0^{(1)}$ is the value at the dilute-gas limit and can be evaluated by

$$\lambda_0^{(1)} = \frac{15\mathcal{R}_u}{4M_0}\mu_0^0 \tag{2.79}$$

where μ_0^0 is the ideal gas viscosity. The quantities, $\Delta\lambda_0^{(2)}$ and $\Delta\lambda_0$ are the first density and high dense corrections. The mathematical formulas of these correlations for methane can be found in Table 2.4.

Modern theory of transport phenomena predicts an infinite thermal conductivity at the pure-fluid critical point and a large thermal conductivity in the vicinity of the critical point[35,36]. Although this near-critical enhancement has been observed experimentally for several fluids, the theory of non-classical critical behavior predicts that the difference among critical criteria for different components may diminish the significant of the critical anomaly[35,37,38]. Because the effect of the critical point contribution for a mixture is not well defined and is likely to be small, it is not included in the current analysis of droplet vaporization.

Mass Diffusivity of Gas Phase

Estimation of the binary mass diffusivity for a gaseous mixture at high density represents a more challenging task than evaluating the other transport properties[39], due to the lack of a formal theory or even a theoretically based correlation. For a multicomponent mixture, the effective diffusion coefficient $\mathcal{D}_{im}$ for each species i can be related to the binary diffusion coefficients through the following formula:

TABLE 2.4
Correlation of Thermal Conductivity for Methane; Units are gram-cm-sec-Kelvin.

$$\lambda_0''(\rho_0, T_0) = \lambda_0^{(1)}(T_0) + \Delta\lambda_{exc}(\rho_0, T_0) + \Delta\lambda_{crit}(\rho_0, T_0)$$

where

$$\begin{aligned}
\lambda_0^{(1)}(T) &= \frac{15\mathcal{R}_u}{4M_0}\mu_0^0 \\
\lambda_0^{(2)}(T) &= \sum_{n=1}^{9} c_n T^{(n-4)/3} \\
\Delta\lambda_0(\rho, T) &= exp[a_1 + a_2/T]\{exp[(a_3 + a_4/T^{3/2})\rho^{0.1} \\
&+ (\rho/\rho_c - 1)\rho^{0.5}(a_5 + a_6/T + a_7/T^2)] - 1.0\}
\end{aligned}$$

i	a_i	b_i	c_i
1	$-7.1977082270\text{x}10^{+0}$	$-0.252762920\text{x}10^{+0}$	$2.907741307\text{x}10^{+6}$
2	$8.5678222640\text{x}10^{+1}$	$0.334328590\text{x}10^{+0}$	$-3.312874033\text{x}10^{+6}$
3	$1.2471834689\text{x}10^{+1}$	1.12	$1.608101838\text{x}10^{+6}$
4	$-9.8462522975\text{x}10^{+2}$	$0.1680\text{x}10^{+3}$	$-4.331904871\text{x}10^{+5}$
5	$3.5946850007\text{x}10^{-1}$		$7.062481330\text{x}10^{+4}$
6	$6.9798412538\text{x}10^{+1}$		$-7.116620750\text{x}10^{+3}$
7	$-8.7288332851\text{x}10^{+2}$		$4.325174400\text{x}10^{+2}$
8			$-1.445911210\text{x}10^{+1}$
9			$2.037119479\text{x}10^{-1}$

$$\mathcal{D}_{im} = \frac{(1 - X_i)}{\sum_{j \neq i}^{N} (X_j / \mathcal{D}_{ij})} \qquad \text{i} = 1, ..., \text{N} \tag{2.80}$$

where X_i is the mole fraction of species i. The binary mass diffusivity $\mathcal{D}_{ij}$ for the gas phase is obtained using the corresponding-state model proposed by Takahashi[40]. The approach proceeds in two steps. First, the binary mass diffusivity of a dilute mixture is obtained using the Chapman-Enskog theory in conjunction with the Lennard-Jones intermolecular potential-energy function[41].

$$\mathcal{D}_{ij} = 0.0018583 \frac{T^{1.5} (1/M_i + 1/M_j)^{0.5}}{p \sigma_{ij}^2 \Omega_D} \tag{2.81}$$

and

$$\Omega_D = \frac{1.06036}{(T^*)^{0.1561}} + \frac{0.193}{exp(0.47635\ T^*)} + \frac{1.03587}{exp(1.52996\ T^*)} + \frac{1.76474}{exp(3.89411\ T^*)} \tag{2.82}$$

$$\begin{aligned} T^* &= \frac{kT}{\epsilon_{ij}} \\ \epsilon_{ij} &= (\epsilon_i \epsilon_j)^{1/2} \\ \sigma_{ij} &= \frac{1}{2}(\sigma_i + \sigma_j) \end{aligned} \tag{2.83}$$

where k is the Boltzmann constant, and ϵ and σ are the Lennard-Jones parameters which quantify respectively the energy and length scale of gas molecules. These values can be found in Appendix B of Ref. [34] for a variety of species. The calculated data for a dilute mixture is then corrected with a pressure correction which is expressed in a generalized chart in terms of reduced temperature and pressure, as shown in Fig. 2.6. This scheme appears to be the most complete to date, and has demonstrated moderate success in the limited number of tests conducted.

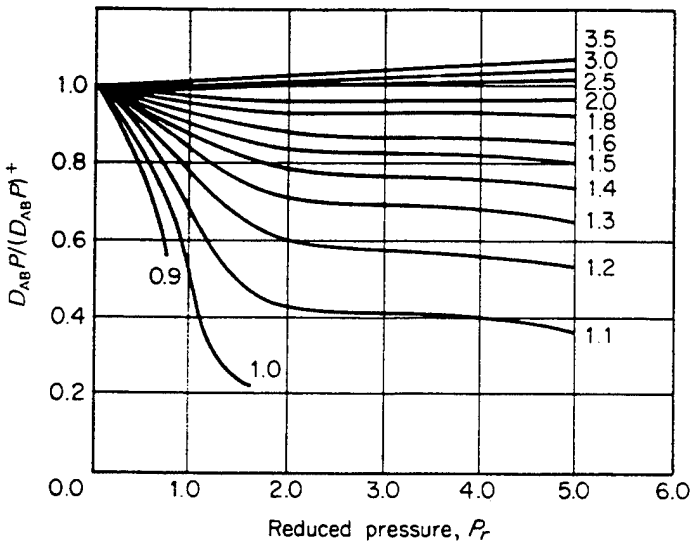

Figure 2.6. High Pressure Correction Factor for Mass Diffusivity Proposed by Takashashi in 1974.

Mass Diffusivity of Liquid Phase

For the liquid phase, the mass diffusivity is evaluated using a model proposed by Perkins and Geankoplis[42].

$$\mathcal{D}_{im} = \mu_m^{-0.8} \sum_{j=1;j\neq i}^{N} X_j \mathcal{D}_{ij} \mu_j^{0.8} \tag{2.84}$$

where μ_m and μ_j are the viscosities for the mixture and component j, respectively. The binary diffusivity $\mathcal{D}_{ij}$ is evaluated using the Hayduk and Minhas model[43].

$$\mathcal{D}_{ij} = 13.3 * 10^{-8} \frac{T^{1.47} \mu_j^{\bar{\epsilon}}}{\mathrm{v}_i^{0.71}} \tag{2.85}$$

where

$$\bar{\epsilon} = (10.2/\mathrm{v}_i) - 0.791$$

μ_j = viscosity of solvent j, cp.

v_i = molar volume of solute i at its normal boiling temperature, $cm^3/mole$.

T = temperature, K.

2.4 Liquid/Vapor Phase Equilibrium

Prior to occurrence of the critical mixing state, thermodynamic vapor-liquid phase equilibrium is assumed to prevail at the droplet surface. This condition first requires that thermal equilibrium be achieved, with the temperatures of both phases being identical.

$$T^v = T^\ell \tag{2.86}$$

where the superscripts v and ℓ represent the values in the vapor and liquid phases, respectively. It is also evident that no unbalanced mechanical forces exist between the two systems, and as such the second condition for phase equilibrium is that the pressures of both phases remain equal.

$$p^v = p^\ell \tag{2.87}$$

For a multicomponent system, the condition of thermodynamic equilibrium is enforced by requiring that the chemical potential of each component be the same in both phases at a given pressure and temperature.

$$\boldsymbol{\mu}^v = \boldsymbol{\mu}^\ell \tag{2.88}$$

If this condition does not hold, there would be a tendency for mass to pass from one phase to the other[30]. Since the partial molar Gibbs function is equivalent to the chemical potential, Eq. (2.88) can be rewritten as

$$g_i^v = g_i^\ell \qquad i = 1, 2, \ldots, N \tag{2.89}$$

Following the definition of fugacity of a component in a mixture

$$\mathcal{R}T d(\ln \boldsymbol{f}_i)_T = dg_i \tag{2.90}$$

$$\lim_{p \to 0} \Big(\boldsymbol{f}_i / X_i p \Big) = 1 \tag{2.91}$$

Equation (2.89) can be expressed in terms of fugacity as

$$\ln \boldsymbol{f}_i^v = \ln \boldsymbol{f}_i^\ell \qquad i = 1, 2, \ldots, N \tag{2.92}$$

The fugacity $\boldsymbol{f}_i$ is related to the volumetric properties of the mixture through the following equation.

$$\ln\Big(\frac{\boldsymbol{f}_i}{pX_i}\Big) = \frac{1}{\mathcal{R}T}\frac{\partial}{\partial n_i}\left\{\int_{\rho^0}^{\rho} \frac{p}{\rho^2} d\rho\right\}_{\rho, T, n_{j \neq i}} \tag{2.93}$$

where ρ is the density of the system, and n_i the number of mole of component i. Note that $\boldsymbol{f}_i$ depends explicitly on pressure, temperature, and mixture composition. As a result, an adequate equation of state is required to complete the formulation for the phase-equilibrium analysis.

Using Soave-Redlich-Kwong equation of state, Eq. (2.93) can be integrated to yield an explicit expression for the fugacity of each species i.

$$\ln(\boldsymbol{f}_i / pX_i) = \frac{b_i}{b}\Big(Z - 1\Big) - \ln\Big(Z - B\Big) - \frac{A}{B}\left[\frac{2\sum_{j=1}^{N} x_j \alpha_{ij} a_{ij}}{\alpha a} - \frac{b_i}{b}\right] \ln\Big(1 + \frac{B}{Z}\Big) \tag{2.94}$$

where A and B are defined in Eq. (2.50). Equation (2.92) can be rewritten as

$$\ln \boldsymbol{f}_i^v = \ln \boldsymbol{f}_i^\ell \qquad i = 1, 2, \ldots, N \tag{2.95}$$

where

$$\ln f_i^v = \ln X_i^v + \ln p + \frac{b_i}{b}\left(Z^v - 1\right) - \ln\left(Z^v - B\right) - \frac{A}{B}\left[\frac{2\sum_{j=1}^{N} X_j^v \alpha_{ij} a_{ij}}{\alpha a} - \frac{b_i}{b}\right] \ln\left(1 + \frac{B}{Z^v}\right) \quad (2.96)$$

$$\ln f_i^\ell = \ln X_i^\ell + \ln p + \frac{b_i}{b}\left(Z^\ell - 1\right) - \ln\left(Z^\ell - B\right) - \frac{A}{B}\left[\frac{2\sum_{j=1}^{N} X_j^\ell \alpha_{ij} a_{ij}}{\alpha a} - \frac{b_i}{b}\right] \ln\left(1 + \frac{B}{Z^\ell}\right) \quad (2.97)$$

In order to close the problem, two more equations are given

$$\begin{aligned} \sum_{j=1}^{N} X_j^v &= 1 \\ \sum_{j=1}^{N} X_j^\ell &= 1 \end{aligned} \quad (2.98)$$

For a binary system ($N = 2$) at a given pressure and temperature, there are four unknowns involved in solving the phase equilibrium conditions. These unknowns include the mole fraction of each component in the gas phase (X_1^v and X_2^v) and those of liquid phase (X_1^ℓ and X_2^ℓ). Therefore, four independent equations are required to solve the unknowns.

To solve these mutually coupled equations, an efficient numerical algorithm using the Newton-Raphson iteration technique is adopted. Each unknown is updated by its respective correction during the iteration. At $(n+1)^{th}$ level, those unknowns are expressed as

$$X_1^{v,(n+1)} = X_1^{v,(n)} + \delta X_1^v \quad (2.99)$$

$$X_2^{v,(n+1)} = X_2^{v,(n)} + \delta X_2^v \tag{2.100}$$

$$X_1^{\ell,(n+1)} = X_1^{\ell,(n)} + \delta X_1^\ell \tag{2.101}$$

$$X_2^{\ell,(n+1)} = X_2^{\ell,(n)} + \delta X_2^\ell \tag{2.102}$$

Substitute Eqs. (2.99)-(2.102) into (2.98) and (2.95)-(2.97), and the corrections for the $(n+1)^{th}$ iteration level can be solved using the following vector form

$$\begin{pmatrix} 1 & 1 & 0 & 0 \\ 0 & 0 & 1 & 1 \\ L_{11}^\ell & L_{12}^\ell & -L_{11}^v & -L_{12}^v \\ L_{21}^\ell & L_{22}^\ell & -L_{21}^v & -L_{22}^v \end{pmatrix} \cdot \begin{pmatrix} \delta X_1^\ell \\ \delta X_2^\ell \\ \delta X_1^v \\ \delta X_2^v \end{pmatrix} = \begin{pmatrix} 0 \\ 0 \\ \boldsymbol{f}_1^{v,(n)} - \boldsymbol{f}_1^{\ell,(n)} \\ \boldsymbol{f}_2^{v,(n)} - \boldsymbol{f}_2^{\ell,(n)} \end{pmatrix}$$

where

$$L_{ik} = \frac{1}{X_i}\frac{\partial X_i}{\partial X_k} - \frac{b_i}{b^2}\frac{\partial b}{\partial X_k}(Z^p - 1) + \frac{b_i}{b}\frac{\partial Z}{\partial X_k} - \frac{\dfrac{\partial Z}{\partial X_k} - \dfrac{\partial B}{\partial X_k}}{Z - B}$$
$$- \frac{\partial}{\partial X_k}\left\{\frac{A}{B}\left[\frac{2\sum_{j=1}^{N} X_j \alpha_{ij} a_{ij}}{\alpha a} - \frac{b_i}{b}\right]\ln\left(\frac{B}{Z}\right)\right\}$$

$$\frac{\partial b}{\partial X_k} = \sum_{i=1}^{N}\frac{\partial X_i}{\partial X_k} b_i = \sum_{i=1}^{N}\delta_{ik} b_i$$

$$\frac{\partial \alpha a}{\partial X_k} = \sum_{i=1}^{N}\sum_{j=1}^{N}\frac{\partial X_i}{\partial X_k} X_j (1 - k_{ij})\sqrt{\alpha_i a_i \alpha_j a_j}$$

$$+ \sum_{i=1}^{N}\sum_{j=1}^{N} X_i \frac{\partial X_j}{\partial X_k}(1-k_{ij})\sqrt{\alpha_i a_i \alpha_j a_j}$$
$$= 2\sum_{i=1}^{N}\sum_{j=1}^{N} \delta_{ik} X_j (1-k_{ij})\sqrt{\alpha_i a_i \alpha_j a_j},$$

$$\frac{\partial A}{\partial X_k} = \frac{p}{\mathcal{R}_u^2 T^2}\frac{\partial \alpha a}{\partial X_k}$$

$$\frac{\partial B}{\partial X_k} = \frac{p}{\mathcal{R}_u T}\frac{\partial b}{\partial X_k}$$

$$\frac{\partial Z}{\partial X_k} = \frac{\frac{\partial A}{\partial X_k}(-Z+B)+\frac{\partial B}{\partial X_k}(Z+2BZ+A)}{3Z^2-2Z+A-B-B^2} \tag{2.103}$$

To facilitate the numerical analysis, initial values of X_1^ℓ, X_2^ℓ, X_1^v and X_2^v are required. At a given X_1^v, the mole fraction of the other component is determined.

$$X_2^v = 1 - X_1^v \tag{2.104}$$

Application of the Raoult's law leads to

$$X_1^\ell = X_1^v \frac{p}{p_1^s}$$

$$X_2^\ell = X_2^v \frac{p}{p_2^s} \tag{2.105}$$

where p_i^s is the saturation pressure of component i.

2.4.1 Enthalpy of Vaporization

Enthalpy of vaporization is defined as the heat absorbed by a component to transform from its liquid phase to vapor at equilibrium temperature and corresponding vapor pressure. It can be evaluated by

$$\Delta h_{v,i} = h_i^v - h_i^\ell \tag{2.106}$$

and

$$h_i = h_i^0 - \mathcal{R}T^2 \frac{\partial}{\partial T}[\ln(\boldsymbol{f}_i/pX_i)] \tag{2.107}$$

where superscript 0 denotes quantity in the ideal state. The enthalpy of vaporization for component i is

$$\Delta h_{v,i} = \mathcal{R}T^2 \Big[\frac{\partial[\ln(\boldsymbol{f}_i^v/p^v X_i^v)]}{\partial T} - \frac{\partial[\ln(\boldsymbol{f}_i^\ell/p^\ell X_i^\ell)]}{\partial T} \Big] \tag{2.108}$$

The explicit form of Eq. (2.108) based on SRK equation of state is given in Appendix B.

2.4.2 Results and Discussion

In 1875, Gibbs proposed a phase rule[30] which takes the form

$$\mathcal{V} = -\mathcal{P} + \mathcal{C} + 2 \tag{2.109}$$

where $\mathcal{P}$ and $\mathcal{C}$ are the numbers of phases and components in the system of interest, respectively, and the quantity $\mathcal{V}$ is the variance which designates the number of intensive properties that must be specified to fix the state of the system. For example, a two-phase mixture of n-pentane (C_5H_{12}) and nitrogen (N_2), the number of phases $\mathcal{P}$ equals 2, the number of component $\mathcal{C}$ is 2, and therefore the value for the variance $\mathcal{V}$ becomes 2. This means that once any two of the intensive properties are given(i.e., pressure, temperature, and mole fraction of a given component in any phase, etc.), the state of the system is fixed, and all other properties can be determined using thermodynamic relationships.

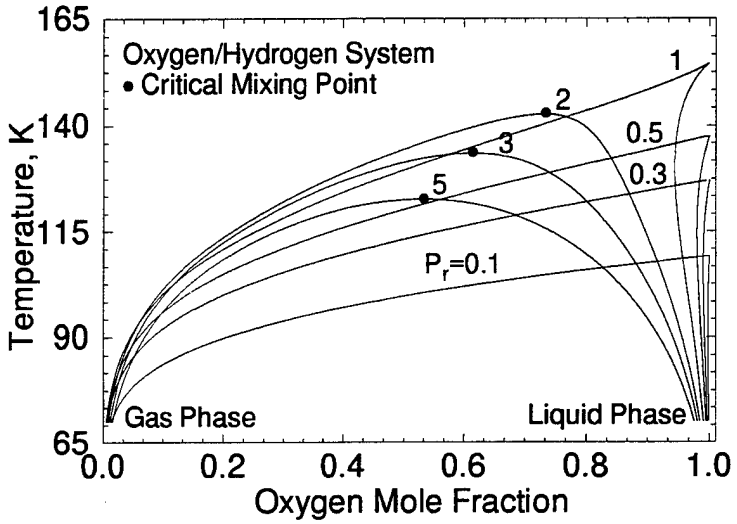

Figure 2.7. Phase Equilibrium Compositions for O_2/H_2 System at Various Pressures.

Figure 2.7 shows the equilibrium compositions for H_2/O_2 system in the pressure range of 5-250 atm, where p_r stands for the reduced pressure of oxygen. In the subcritical regime ($p_r < 1$), the liquid phase consists almost entirely of oxygen. The amount of hydrogen dissolved in the liquid oxygen is quite limited, decreasing progressively with increasing temperature and dropping to zero at the boiling point. However, at supercritical pressures ($p_r > 1$), the hydrogen gas solubility becomes substantial and increases with temperature. For example, the liquid phase contains 8.2-45 % hydrogen (by mole fraction) for $p_r = 5$, depending on temperature. In spite of its high molar concentration, the mass fraction of dissolved hydrogen is much smaller because of the disparity in molecular weight between hydrogen and oxygen. The mass fraction of hydrogen in the liquid phase is only 5 % at the critical mixing point for $p_r = 5$, as opposed to the mole fraction of 45 %.

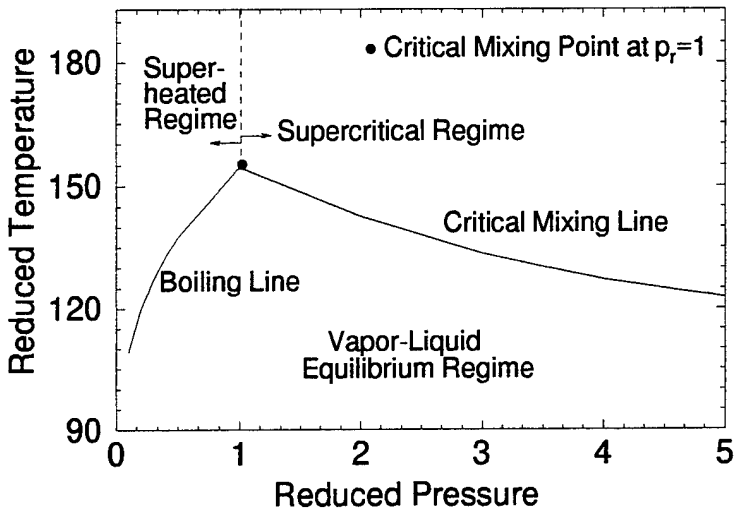

Figure 2.8. Pressure-Temperature Diagram for Phase Behavior of O_2/H_2 System in Equilibrium.

The phase equilibrium results also indicate that the critical mixing temperature decreases with pressure. Consequently, a droplet can reach its critical condition more easily at a higher pressure.

The overall phase-behavior in equilibrium is best summarized by the pressure-temperature diagram presented in Fig. 2.8, showing how the phase transition occurs under different thermodynamic conditions. The boiling line is made up of boiling points for subcritical pressures. As the temperature increases, an equilibrium vapor-liquid mixture may transit to super-heated vapor across this line. The critical mixing line registers the variation of the critical mixing temperature with pressure, and intersects the boiling line at the critical point of pure oxygen, the highest temperature at which the vapor and liquid phases of an O_2/H_2 binary system can coexist in equilibrium.

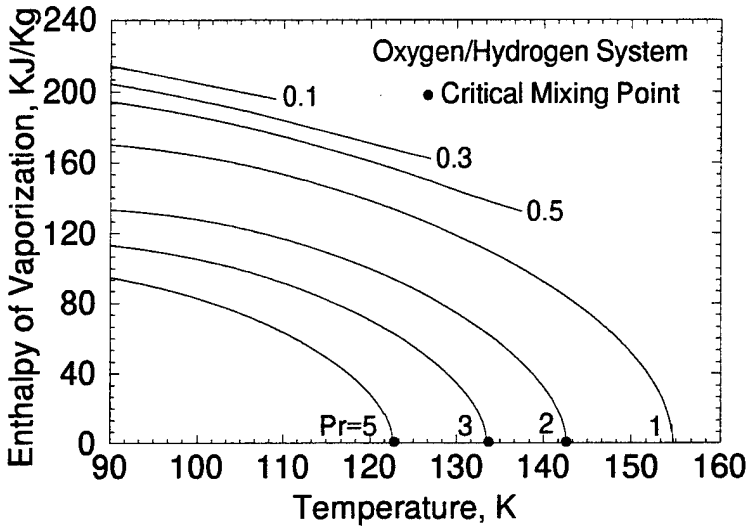

Figure 2.9. Effect of Pressure on Enthalpy of Vaporization of O_2 in an Equilibrium Mixture of O_2 and H_2.

Figure 2.9 shows the variations of the enthalpy of vaporization of oxygen in an equilibrium mixture of hydrogen and oxygen. In contrast to the conventional approach for low-pressure applications where the ambient gas solubility is ignored and the heat of vaporization depends on temperature only, the enthalpy of vaporization is a strong function of both temperature and pressure, decreasing with increasing pressure and dropping rapidly to zero at the critical mixing point.

2.5 Chemical Reactions

Finite-rate chemical reaction model is employed in the present study. When the droplet is introduced into a high-pressure environment, the gasification rate increases due to diminishing latent heat of vaporization. The transport processes in both the liquid and gas become compatible with each other. As a result, the mixing of fuels and oxidizers may occur in a time scale commensurate with the

chemical-reaction time. The use of a diffusion-controlled complete reaction (flame-sheet) model may lead to erroneous results for predicting the droplet burning mechanisms.

For combustion of gaseous hydrocarbon fuels with oxygen, a single-step global reaction mechanism suggested by Westbrook and Dryer[44] is adopted. This model is a simplification of reality, but provides reasonable predictions of chemical reaction rates over a wide range of equivalent ratio. The reaction step takes the form

$$C_nH_m + \left(n + \frac{m}{4}\right)O_2 \longrightarrow nCO_2 + \frac{m}{2}H_2O \tag{2.110}$$

The rates of production of species are

$$\dot{\omega}_{C_nH_m} = -M_{C_nH_m} A \exp\left(-\frac{E_a}{\mathcal{R}_u T}\right)[C]^a_{C_nH_m}[C]^b_{O_2} \tag{2.111}$$

$$\dot{\omega}_{O_2} = \left(n + \frac{m}{4}\right)\left(\frac{M_{O_2}}{M_{C_nH_m}}\right)\dot{\omega}_{C_nH_m} \tag{2.112}$$

$$\dot{\omega}_{CO_2} = -n\left(\frac{M_{CO_2}}{M_{C_nH_m}}\right)\dot{\omega}_{C_nH_m} \tag{2.113}$$

$$\dot{\omega}_{H_2O} = -\left(\frac{m}{2}\right)\left(\frac{M_{H_2O}}{M_{C_nH_m}}\right)\dot{\omega}_{C_nH_m} \tag{2.114}$$

where M and $[C]$ are the molecular weight and species concentration. The activation energy E_a and factors a and b, are dependent on the type of fuel species considered and their values are listed in Table 2.5.

TABLE 2.5

Single-Step Reaction Rate Parameters Proposed by Westbrook and Dryer in 1981; Units are cm-sec-mole-Kcal-Kelvin.

Fuels	*M*	*A*	E_a (Kcal/g-mole)	*a*	*b*
CH_4	16.043	$1.3E08$	48.4	−0.30	1.30
CH_4	16.043	$8.3E05$	30.0	−0.30	1.30
C_2H_6	30.070	$1.1E12$	30.0	0.10	1.65
C_3H_8	44.097	$8.6E11$	30.0	0.10	1.65
C_4H_{10}	58.124	$7.4E11$	30.0	0.15	1.60
C_5H_{12}	72.151	$6.4E11$	30.0	0.25	1.50
C_6H_{14}	86.178	$5.7E11$	30.0	0.25	1.50
C_7H_{16}	100.205	$5.1E11$	30.0	0.25	1.50
C_8H_{18}	114.232	$4.6E11$	30.0	0.25	1.50
C_8H_{18}	114.232	$7.2E12$	40.0	0.25	1.50
C_9H_{20}	128.259	$4.2E11$	30.0	0.25	1.50
$C_{10}H_{22}$	142.286	$3.8E11$	30.0	0.25	1.50
CH_3OH	32.043	$3.2E12$	30.0	0.25	1.50
C_2H_5OH	46.070	$1.5E12$	30.0	0.15	1.60
C_6H_6	78.114	$2.0E11$	30.0	−0.10	1.85
C_7H_8	92.141	$1.6E11$	30.0	−0.10	1.85
C_2H_4	28.054	$2.0E12$	30.0	0.10	1.65
C_3H_6	42.081	$4.2E11$	30.0	−0.10	1.85
C_2H_2	26.038	$6.5E12$	30.0	0.50	1.25

CHAPTER 3

NUMERICAL SCHEMES

The present analysis of droplet vaporization and combustion poses several difficulties to contemporary numerical algorithms. First, the model of interest is a subcritical liquid droplet being introduced into a supercritical gaseous environment. Due to the large temperature difference between the droplet and ambient gases, the density varies significantly from dilute gas to compressed liquid, and as such precludes the conventional approaches developed for incompressible flows. On the other hand, most existing numerical methods developed for compressible flow usually exhibit their best performance at moderate and high Mach numbers. When the Mach number becomes very small as in the present case, the sensible part of the fluid energy manifests itself in the form of pressure, with the energy equation decoupled from the rest of the governing equations. The associated difference among the eigenvalues adversely affects the convergence characteristics. Second, as velocity approaches zero, the pressure term in the momentum equation causes large round-off errors that prevent the solution from reaching sufficient accuracy. This error arises in the calculation of the pressure and convective momentum flux terms in the momentum equation when the computer is forced to truncate valuable digits. Since these two terms differ greatly in magnitude at low Mach number, significant errors are introduced that consequently contaminate the numerical solution. Chemical reactions exhibit another category of numerical difficulties because of the wide ranges of time and length scales involved in the

calculations. In regions where reaction rates are high, species concentrations may vary rapidly over a much shorter period of time than those of the fluid dynamic processes. This phenomenon hinders the numerical convergence efficiency, and requires a prohibitively large number of iterations to obtain converged solution.

The above difficulties are common to most studies of droplet vaporization and combustion, but become more pronounced at elevated pressure due to the high gasification rate of the droplet and rapid variations of fluid properties with temperature. To circumvent these problems, a dual time-stepping integration method with a low Mach-number treatment is chosen for the current study[45,46]. The scheme is constructed in two steps. First, since the roundoff error is caused by the singular pressure gradient term in the momentum equation (the pressure term is of order of $1/\mathcal{M}_a^2$, while the convective term is of order unity in the non-dimensional momentum equations)[46], the pressure is decomposed as the sum of a constant reference pressure and a gauge pressure.

$$p(x, y, t) = p_0 + p_g(x, y, t) \tag{3.1}$$

The second step incorporates pseudo-time iteration by adding a well-conditioned artificial time derivative term to the conservation laws. The equations are well posed by preconditioning the eigenvalues, effectively circumventing the singularity problem at low Mach numbers. An implicit iterative procedure is then used in pseudo time. This measure is equivalent to preconditioning the time derivative terms of the species concentration equations so that all the chemical and convective processes proceed at approximately the same numerical rate. As a result, a converged solution in pseudo time corresponds to a time-accurate solution in physical time.

3.1 One-Dimensional Treatment

In formulating the numerical integration procedure, Eq. (2.9) is modified by introducing pseudo-time terms, composed of a set of primitive variables (p_g, u_r, h, and Y_i), to the non-conservative form of the governing equations. In order to achieve better conservative characteristics, the conservative form of governing equations is restored by adding the modified continuity equation to the momentum, energy, and species equations. The resulting conservation equations for a system with $N-1$ species equations in 1-D spherical coordinate are written as

$$\Gamma \frac{\partial}{\partial \tau} \int_{\Delta V} \hat{Z} dV + \frac{\partial}{\partial t} \int_{\Delta V} Q dV + \int_A (E - E_v) dA - u_g \int_A Q dA = \int_{\Delta V} S dV \quad (3.2)$$

where

$$\hat{Z} = \begin{pmatrix} p_g \\ u_r \\ h \\ Y_1 \\ \vdots \\ Y_{N-1} \end{pmatrix} \quad and \; \Gamma = \begin{pmatrix} 1/\beta & 0 & 0 & 0 & \dots & 0 \\ u_r/\beta & \rho & 0 & 0 & \dots & 0 \\ h/\beta - 1 & \rho u_r & \rho & 0 & \dots & 0 \\ Y_1/\beta & 0 & 0 & \rho & \dots & 0 \\ \vdots & \vdots & \vdots & \vdots & \ddots & \vdots \\ Y_{N-1}/\beta & 0 & 0 & 0 & \dots & \rho \end{pmatrix},$$

where the scaling factor β is used to ensure that all the eigenvalues of the system have the same order of magnitude, a condition normally required for efficient numerical convergence. The vectors Q, E, E_v, E_g, and S have the same definition as those in Eq. (2.9), except the absolute pressure in the momentum equation is replaced by the gauge pressure p_g.

The terms at the $(p+1)^{th}$ time level need to be linearized for the construction of an implicit time marching scheme. The linearized representation of convective and diffusion fluxes and source term vectors are as follows.

$$\begin{aligned} Q^{p+1} &= Q^p + \mathbf{T}\Delta\hat{Z} \\ E^{p+1} &= E^p + \mathbf{A}\Delta\hat{Z} \\ E_v^{p+1} &= \mathbf{R}^{p+1}\frac{\partial \hat{Z}^{p+1}}{\partial r} \\ &\approx \mathbf{R}^p\frac{\partial(\hat{Z}+\Delta\hat{Z})^p}{\partial r} \\ S^{p+1} &= S^p + \mathbf{D}\Delta\hat{Z} \end{aligned} \tag{3.3}$$

where $\mathbf{T}$, $\mathbf{A}$, $\mathbf{R}$, and $\mathbf{D}$ are the Jacobian matrices defined as

$$\begin{aligned} \mathbf{T} &= \frac{\partial Q}{\partial \hat{Z}} \\ \mathbf{A} &= \frac{\partial E}{\partial \hat{Z}} \\ \mathbf{R} &= \frac{\partial E_v}{\partial(\frac{\partial \hat{Z}}{\partial r})} \\ \mathbf{D} &= \frac{\partial S}{\partial \hat{Z}} \end{aligned}$$

Complete expressions of these matrices can be found in Appendix C.

For second-order accuracy in physical time, Eq. (3.2) can be discretize in a fully implicit form as

$$\left[\frac{\boldsymbol{\Gamma}^p}{\Delta\tau}+\frac{3\mathbf{T}^p}{2\Delta t}-\mathbf{D}\right]\Delta\hat{Z}+\frac{1}{\Delta V}\int_{\Delta A}\left[(\mathbf{A}-u_g\mathbf{T})\Delta Z-\mathbf{R}\frac{\partial(\Delta\hat{Z})}{\partial r}\right]dA=-(RHS)^p \tag{3.4}$$

where

$$(RHS)^p = \frac{3Q^p - 4Q^n + Q^{n-1}}{2\Delta t} - S + \frac{1}{\Delta V}\int_{\Delta A}\Big[(E - u_g Q) - E_v\Big]dA + AD \quad (3.5)$$

AD is the artificial dissipation which is a blending of second-difference and fourth-difference dissipation terms. The second-difference terms are used to prevent oscillations at discontinuity in the flowfield, while the fourth-difference terms are important for numerical stability and convergence[47].

3.2 Two-Dimensional Treatment

To facilitate numerical manipulation, the conservation laws of physics, Eqs. (2.18)-(2.22), can be transform into a generalized coordinate system in the following vector form.

$$\frac{\partial \tilde{Q}}{\partial t} + \frac{\partial(\tilde{E} - \tilde{E}_v)}{\partial \xi} + \frac{\partial(\tilde{F} - \tilde{F}_v)}{\partial \eta} = \tilde{S} \quad (3.6)$$

where the quantities ξ and η are the spatial coordinates in generalized coordinates, and vectors $\tilde{Q}$, $\tilde{E}$, $\tilde{E}_v$, $\tilde{F}$, $\tilde{F}_v$ and $\tilde{S}$ are defined as

$$\tilde{Q} = \frac{r}{J}Q, \quad (3.7)$$

$$\tilde{E} = \frac{r}{J}(\xi_x E + \xi_y F), \quad (3.8)$$

$$\tilde{E}_v = \frac{r}{J}(\xi_x E_v + \xi_y F_v) \quad (3.9)$$

$$\tilde{F} = \frac{r}{J}(\eta_x E + \eta_y F), \quad (3.10)$$

$$\tilde{F}_v = \frac{r}{J}(\eta_x E_v + \eta_y F_v) \tag{3.11}$$

$$\tilde{S} = \frac{1}{J} S \tag{3.12}$$

with J the coordinate transformation Jacobian, and ξ_x, ξ_y, η_x, and η_y the metric terms. The conserved variable vector Q is defined as

$$Q = \begin{pmatrix} \rho \\ \rho u \\ \rho v \\ \rho e_t \\ \rho Y_i \end{pmatrix}$$

The convective-flux vectors, E and F, in the axial and radial directions take the forms

$$E = \begin{pmatrix} \rho u \\ \rho u^2 + p \\ \rho uv \\ (\rho e_t + p)u \\ \rho u Y_i \end{pmatrix} \qquad F = \begin{pmatrix} \rho v \\ \rho uv \\ \rho v^2 + p \\ (\rho e_t + p)v \\ \rho v Y_i \end{pmatrix}$$

The corresponding diffusion-flux vectors, E_v and F_v, are

$$E_v = \begin{pmatrix} 0 \\ \tau_{xx} \\ \tau_{xr} \\ u\tau_{xx} + v\tau_{xr} + (q_e)_x \\ (q_{m,i})_x \end{pmatrix} \qquad F_v = \begin{pmatrix} 0 \\ \tau_{rx} \\ \tau_{rr} \\ u\tau_{xr} + v\tau_{rr} + (q_e)_r \\ (q_{m,i})_r \end{pmatrix}$$

The source vector S includes parts associated with the axisymmetric geometry and remaining viscous terms and can be written as

$$S = \begin{pmatrix} 0 \\ -\frac{2}{3}(\xi_x \frac{\partial \mu v}{\partial \xi} + \eta_x \frac{\partial \mu v}{\partial \eta}) \\ p_g - \frac{4}{3}\frac{\mu v}{r} + \frac{2}{3}\mu(\xi_x \frac{\partial u}{\partial \xi} + \eta_x \frac{\partial u}{\partial \eta}) - \frac{2}{3}v(\xi_r \frac{\partial \mu}{\partial \xi} + \eta_r \frac{\partial \mu}{\partial \eta}) \\ -\frac{2}{3}(\xi_x \frac{\partial \mu u v}{\partial \xi} + \eta_x \frac{\partial \mu u v}{\partial \eta} + \xi_r \frac{\partial \mu v^2}{\partial \xi} + \eta_r \frac{\partial \mu v^2}{\partial \eta}) \\ 0 \end{pmatrix}$$

To obtain time-accurate solutions for time-evolving problems, a dual time-stepping integration method is chosen. Thus, the conservative equations in generalized curvilinear coordinates (ξ , η) are modified as

$$\boldsymbol{\Gamma}\frac{\partial \hat{Z}}{\partial \tau} + \frac{\partial \tilde{Q}}{\partial t} + \frac{\partial(\tilde{E} - \tilde{E}_v)}{\partial \xi} + \frac{\partial(\tilde{F} - \tilde{F}_v)}{\partial \eta} = \tilde{S} \tag{3.13}$$

where τ represents the pseudo time. The primitive variable vector $\hat{Z}$ and the preconditioning matrix $\boldsymbol{\Gamma}$ are expressed as

$$\hat{Z} = r \begin{pmatrix} p_g \\ u \\ v \\ h \\ Y_1 \\ \vdots \\ Y_{N-1} \end{pmatrix} \quad and \quad \boldsymbol{\Gamma} = \begin{pmatrix} 1/\beta & 0 & 0 & 0 & 0 & \dots & 0 \\ u/\beta & \rho & 0 & 0 & 0 & \dots & 0 \\ v/\beta & 0 & \rho & 0 & 0 & \dots & 0 \\ h/\beta - 1 & \rho u & \rho v & \rho & 0 & \dots & 0 \\ Y_1/\beta & 0 & 0 & 0 & \rho & \dots & 0 \\ \vdots & \vdots & \vdots & \vdots & \vdots & \ddots & \vdots \\ Y_{N-1}/\beta & 0 & 0 & 0 & 0 & \dots & \rho \end{pmatrix}$$

where the vectors $\tilde{Q}$, $\tilde{E}$, $\tilde{E}_v$, $\tilde{F}$, $\tilde{F}_v$ and $\tilde{S}$ remain the same definitions as those for Eq. (3.6). The quantities J, η_x, η_r, ξ_x, and ξ_r are derived directly from the coordinate transformation.

The equation for the $(p+1)^{th}$ iteration in pseudo time and the $(n+1)^{th}$ level in physical time is written as

$$\boldsymbol{\Gamma}\frac{\hat{Q}^{p+1} - \hat{Q}^{p}}{\Delta\tau} + \frac{a_1\tilde{Q}^{p+1} + a_2\tilde{Q}^{n} + a_3\tilde{Q}^{n-1}}{\Delta t} + \frac{\partial(\tilde{E} - \tilde{E}_v)^{p+1}}{\partial\xi} + \frac{\partial(\tilde{F} - \tilde{F}_v)^{p+1}}{\partial\eta} = \tilde{S}^{p+1} \quad (3.14)$$

Since the time step is set to be constant and the resolution accuracy is second-order, a_1, a_2, and a_3 are chosen as

$$a_1 = \frac{3}{2}, \quad a_2 = -2, \quad a_3 = \frac{1}{2} \quad (3.15)$$

The terms at the $(p+1)^{th}$ time level in Eq. (3.14) need to be linearized for the construction of an implicit time marching scheme. Using a first-order Tayler series expansion, the vectors $\tilde{Q}$, $\tilde{E}$, $\tilde{E}_v$, $\tilde{F}$, $\tilde{F}_v$, and $\tilde{S}$ may be linearized with respect to $\hat{Z}$ as follows

$$
\begin{aligned}
\tilde{Q}^{p+1} &= \tilde{Q}^{p} + \mathbf{T}^{p}\Delta\hat{Z} \\
\tilde{E}^{p+1} &= \tilde{E}^{p} + \mathbf{A}^{p}\Delta\hat{Z} \\
\tilde{E}_{v}^{p+1} &= \tilde{E}_{v}^{p} + \mathbf{R}_{\xi\xi}^{p}\Delta\left(\frac{\partial\hat{Z}}{\partial\xi}\right) \\
\tilde{F}^{p+1} &= \tilde{F}^{p} + \mathbf{B}^{p}\Delta\hat{Z} \\
\tilde{F}_{v}^{p+1} &= \tilde{F}_{v}^{p} + \mathbf{R}_{\eta\eta}^{p}\Delta\left(\frac{\partial\hat{Z}}{\partial\eta}\right) \\
\tilde{S}_{v}^{p+1} &= \tilde{S}_{v}^{p} + \mathbf{D}^{p}\Delta\hat{Z}
\end{aligned}
\tag{3.16}
$$

The eigenvalues (in ξ direction) in pseudo time can be obtained from the matrix $\boldsymbol{\Gamma}^{-1}\mathbf{A}$

$$
\lambda_e = U, U, \frac{1}{2}\left[U(1+\frac{\beta}{c^2}) \pm \sqrt{U^2(1-\frac{\beta}{c^2})^2 + 4\beta(\alpha_1^2+\alpha_2^2)}\ \right], U, U, \ldots \tag{3.17}
$$

where c is the speed of sound with $\alpha_1 = \xi_x$, $\alpha_2 = \xi_y$ and U is the contravariant velocity component defined as $U = \alpha_1 u + \alpha_2 v$. To obtain well-conditioned eigenvalues, the scaling factor β is taken to be

$$
\beta = u^2 + v^2 \tag{3.18}
$$

The discretized equation can be expressed in the following form

$$
\begin{aligned}
\left\{\boldsymbol{\Gamma} - \Delta\tau\mathbf{D} + a_1\frac{\Delta\tau}{\Delta t}\mathbf{T} + \Delta\tau\left(\frac{\partial\mathbf{A}}{\partial\xi} - \frac{\partial}{\partial\xi}\mathbf{R}_{\xi\xi}\frac{\partial}{\partial\xi}\right) \right. &+ \left. \Delta\tau\left(\frac{\partial\mathbf{B}}{\partial\eta} - \frac{\partial}{\partial\xi}\mathbf{R}_{\eta\eta}\frac{\partial}{\partial\xi}\right)\right\}\Delta Q \\
&= -\Delta\tau(RHS)^{p}
\end{aligned}
\tag{3.19}
$$

where

$$
(RHS)^{p} = \frac{a_1\tilde{Q}^{p} + a_2\tilde{Q}^{n} + a_3\tilde{Q}^{n-1}}{\Delta t} + \frac{\partial(\tilde{E}-\tilde{E}_v)^{p}}{\partial\xi} + \frac{\partial(\tilde{F}-\tilde{F}_v)^{p}}{\partial\eta}
$$

$$- \tilde{S}^p + AD \qquad (3.20)$$

where **A** and **B** are the convective flux Jacobians in ξ and η directions, respectively, **D** the source term, and $\mathbf{R}_{\xi\xi}$ and $\mathbf{R}_{\eta\eta}$ the viscous term Jacobians. Explicit expressions of these matrices can be found in Appendix C. The last term in Eq. (3.20) represents the fourth-order dissipation defined as

$$AD = \left(\frac{\epsilon_{\mathrm{AD}}}{\Delta\tau}\right)\boldsymbol{\Gamma}\left(\frac{\partial^4 \hat{Z}}{\partial\xi^4} + \frac{\partial^4 \hat{Z}}{\partial\eta^4}\right) \qquad (3.21)$$

where ϵ_{AD} is the artificial dissipation rate.

One significant advantage of the dual time-stepping method is that the convergence of the iterative process is determined by the eigenvalue characteristics in the pseudo-time domain, and not by the original eigenvalues which become stiff at low Mach numbers. This feature allows flexibility in the selection of time step sizes in both time frames. The physical time step is determined based on the characteristic evolution of the unsteady flow under consideration, while the pseudo-time step depends on the numerical stability of the algorithm and can be adjusted to obtain the optimum convergence.

3.2.1 Modified Strongly Implicit Solver

A new iterative method was proposed by Stone et al. [48]. The algorithm involving a 5-point configuration is briefly listed below for reference.

$$G^w_{i,j}\Delta\hat{Z}_{i-1,j} + G^e_{i,j}\Delta\hat{Z}_{i+1,j} + G^p_{i,j}\Delta\hat{Z}_{i,j} + G^s_{i,j}\Delta\hat{Z}_{i,j-1} + G^n_{i,j}\Delta\hat{Z}_{i,j+1} = q_{i,j} \quad (3.22)$$

where $G_{i,j}$ is an nxn block matrix and $q_{i,j}$ is a vector with length n. The superscripts w, e, s, n, and p denote respectively the cells on western, eastern, southern,

and northern sides with respect to the p cell. The above equation can be rewritten in a vector form as

$$\mathbf{G}\Delta\hat{Z} = q \tag{3.23}$$

where

$$\mathbf{G} = \begin{pmatrix}
G^p & G^e & & & & G^n & & & \\
\ddots & \ddots & \ddots & & & & \ddots & & \\
 & \ddots & \ddots & \ddots & & & & \ddots & \\
 & & \ddots & \ddots & \ddots & & & & \ddots \\
 & & & G^w & G^p & G^e & & & \\
G^s & & & & \ddots & \ddots & \ddots & & \\
 & \ddots & & & & \ddots & \ddots & \ddots & \\
 & & \ddots & & & & \ddots & \ddots & \ddots \\
 & & & G^s & & & & G^w & G^p
\end{pmatrix}$$

This matrix can be approximated into two triangle matrice($\mathbf{L}$ and $\mathbf{U}$), their structure are

$$\mathbf{L} = \begin{pmatrix}
\ddots & & & & & & & & \\
\ddots & \ddots & & & & & & & \\
 & \ddots & \ddots & & & & & & \\
 & & \ddots & \ddots & & & & & \\
 & & & \ddots & \ddots & & & & \\
a & & & & b & c & & & \\
 & \ddots & & & & \ddots & \ddots & & \\
 & & \ddots & & & & \ddots & \ddots & \\
 & & & \ddots & & & & \ddots & \ddots
\end{pmatrix}$$

$$\mathbf{U} = \begin{pmatrix} \ddots & \ddots & & & \ddots & & \\ & \ddots & \ddots & & & \ddots & \\ & & \ddots & \ddots & & & \ddots \\ & & & 1 \quad d & & & e \\ & & & & \ddots & \ddots & \\ & & & & & \ddots & \ddots \\ & & & & & & \ddots \end{pmatrix}$$

where

$$\begin{aligned} a_{i,j} &= G^s_{i,j} \\ b_{i,j} &= G^w_{i,j} \\ c_{i,j} &= G^p_{i,j} - a_{i,j}e_{i,j-1} - b_{i,j}d_{i-1,j} \\ d_{i,j} &= (c_{i,j})^{-1}G^e_{i,j} \\ e_{i,j} &= (c_{i,j})^{-1}G^n_{i,j} \end{aligned} \tag{3.24}$$

The solution of $\Delta\hat{Z}$ can be obtained by forward and backward substitutions as follows.

$$\mathbf{L}\Delta\hat{Z}^* = q \tag{3.25}$$

$$\mathbf{U}\Delta\hat{Z} = \Delta\hat{Z}^* \tag{3.26}$$

where $\hat{Z}^*$ is the provisional vector and is calculated from Eq. (3.25) first to serve as right hand side of Eq. (3.26).

CHAPTER 4

DROPLET COMBUSTION IN QUIESCENT ENVIRONMENTS

The combustion of an isolated n-pentane fuel droplet in air, as shown in Fig. 4.1, over a wide range of pressure has been studied systematically. The droplet is introduced instantaneously to a quiescent air environment with temperature of 1500 K. The initial droplet temperature and diameter are 300 K and 100 μm, respectively, and the ambient pressures are either in the subcritical or supercritical regime of the fuel species. The critical properties of the major constituent species in the gas and liquid phases are listed in Table 4.1. Figure 4.2 shows the time histories of the droplet surface temperature at various pressures. The impulsive rise of the surface temperature in the early stage of the droplet lifetime is caused by large temperature gradient near the droplet surface (i.e., a step function was used as the initial temperature distribution). Because the droplet temperature is initially lower than that of the ambient gases, heat is transferred from the hot air toward the droplet. Part of the heat is used for the phase transition from the liquid to the vapor phase, and the remainder goes to heating up the droplet interior. Once ignition is achieved in the gas phase, the energy feedback from the flame results in a rapid increase in the droplet surface temperature which can be observed by the change of slope in the time histories of surface temperature around the ignition time. At low pressures ($p \leq 20$ atm), the surface temperature varies slowly following onset of flame development. It then levels off at a temperature slightly lower than the droplet boiling temperature, a condition usually referred to as the pseudo

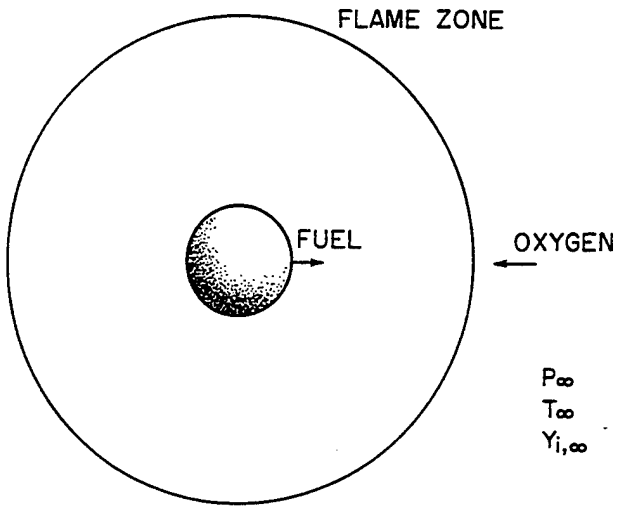

Figure 4.1. Schematic of a Burning Fuel Droplet.

wet-bulb state[49]. Under this condition, nearly all of the energy transferred from the ambient gas is used for the vaporization, with only a small fraction is used for droplet heatup. As the pressure increases to 33.3 atm, the transport processes between gas and liquid are commensurate with each other, the entire gasification process becomes transient with a continuous increase of liquid temperature, resulting in the disappearance of the pseudo wet-bulb state. At $p = 80$ atm, the droplet surface even reaches the critical mixing point (at $t = 3.61\ ms$) before the end of its lifetime. When this occurs, the fluid density and its gradient vary smoothly throughout the domain, the entire flowfield becomes a continuous medium with no distinct liquid/vapor interface as can be observed for the subcritical cases. Since there is no phase-equilibrium criterion posed on the droplet surface, the surface which attains the critical mixing temperature usually regresses at a speed different from that with the critical mixing composition due to the non-unity of the

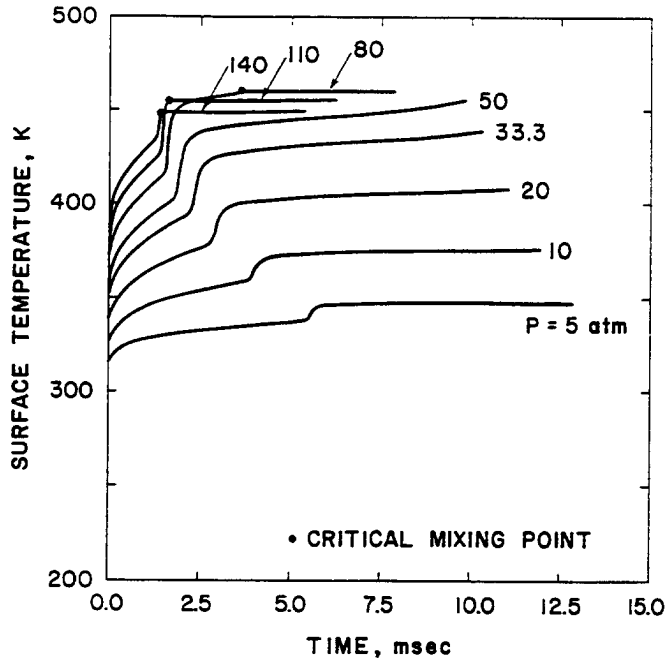

Figure 4.2. Time Variations of Droplet Surface Temperature at Various Pressures, n-Pentane/Air System.

Lewis number. For the convenience of discussion, the droplet gasification rate is defined herein in accordance with the motion of the surface which attains the critical mixing temperature. Within the present treatment, since only the dissolution of nitrogen in the liquid fuel is taken into account in the phase-equilibrium analysis, the critical mixing temperature depends solely on the pressures for such a binary system, as indicated by the horizontal straight lines in the plot for $p = 80$, 110, and 140 atm. The critical properties and milestone times associated with the fuel-droplet combustion are given in Table 4.2. As the ambient pressure increases, the high concentrations of oxygen in the gas phase and the fuel vapor issued from the droplet surface result in a high chemical reaction rate, consequently causing a progressive decrease in ignition time (defined as the time when the peak gas-phase temperature exceeds its initial value by 100 K, see Table 4.2). In addition, the

TABLE 4.1
Critical Properties of Major Constituent Species in the n-Pentane/Air System.

	n-Pentane	Nitrogen	Oxygen	Carbon Dioxide	Water
$T_c\ (K)$	469.6	126.2	154.5	304.2	647.3
$p_c\ (atm)$	33.3	33.5	49.8	72.8	217.6
$\mathrm{v}_c\ (cm^3/g-mole)$	304	89.5	73.4	94	56
Z_c	0.262	0.290	0.288	0.274	0.229

surface temperature jump during the flame-development stage appears an increase with increasing pressure. Since the critical mixing temperature decreases with pressure, the droplet reaches its critical condition more easily at higher pressures, almost immediately following establishment of the diffusion flame in the gas phase for $p \geq 110$ atm. The results displayed here are not very sensitive to the ignition transient for ambient pressure greater than 20 atm. If the preexponential constant in the Arrhenius law, Eq. (2.114) artificially increases by a factor of 10, the burnout times changes by less than 5 % for $p \geq 20$ atm. The lack of sensitivity in droplet lifetime calculations to the ignition process and chemical kinetics at high pressure may be attributed to the fact that the ignition transient period is taken out only a very small fraction of the total burnout time.

Figure 4.3 shows the temporal variations of the latent heat of vaporization at various pressures. Since the latent heat of vaporization depends on both temperature and pressure, it decreases with increasing temperature as well as pressure, and reduces acceleratively to zero as the critical mixing point is approached[49]. The sudden decrease in each of the latent-heat profiles after ignition arises from the rapid increase in the droplet surface temperature during the flame development stage. At $p = 80$ atm, another rapid decrease in the latent heat is observed

TABLE 4.2

Milestone Times and Critical Properties for Combustion of n-Pentane Fuel Droplet in Air at Various Pressures; $D_0 = 100\ \mu m$, $T_0 = 300\ K$, $T_\infty = 1000\ K$.

Pressure (atm)	Pseudo Wet-Bulb Temp. (k)	Critical Mixing Temp. (k)	Peak Flame Temp. (k)	Ignition Time[a] (ms)	Critical Mixing Time[b] (ms)	Gasification Lifetime[c] (ms)	Burnout Time[d] (ms)	Combustion Lifetime[e] (ms)	Droplet Burning Lifetime[f] (ms)	Single-phase Combustion Lifetime[g] (ms)	Critical Burning Lifetime[h] (ms)
5	347.4	--	2847.9	4.38	--	12.88	13.25	8.88	8.50	0.37	--
10	376.1	--	2885.5	3.12	--	11.91	12.42	9.30	8.79	0.51	--
20	409.0	--	2943.8	2.27	--	11.08	12.19	9.92	8.81	1.11	--
33.3	439.3	--	2958.7	1.82	--	10.40	12.26	10.44	8.58	1.86	--
50	455.6	466.3	2962.2	1.52	--	9.89	12.61	11.09	8.37	2.72	--
80	--	460.3	2948.6	1.28	3.61	7.94	11.90	10.62	6.66	3.96	8.29
110	--	455.0	2846.0	1.16	1.59	6.26	11.38	10.23	5.10	5.13	9.80
140	--	449.1	2732.9	1.10	1.39	5.39	11.58	10.47	4.29	6.18	10.18

a Time at which the peak gas-phase temperature exceeds its initial value by 100 K.
b Time at which the droplet surface reaches its critical condition.
c Time between $t = 0$ and the end of liquid droplet lifetime.
d Time between $t = 0$ and the end of gas-phase reaction.
e (Burnout time) - (ignition time).
f (Gasification time) - (ignition time).
g (Burnout time) - (gasification time).
h (Burnout time) - (critical mixing time).

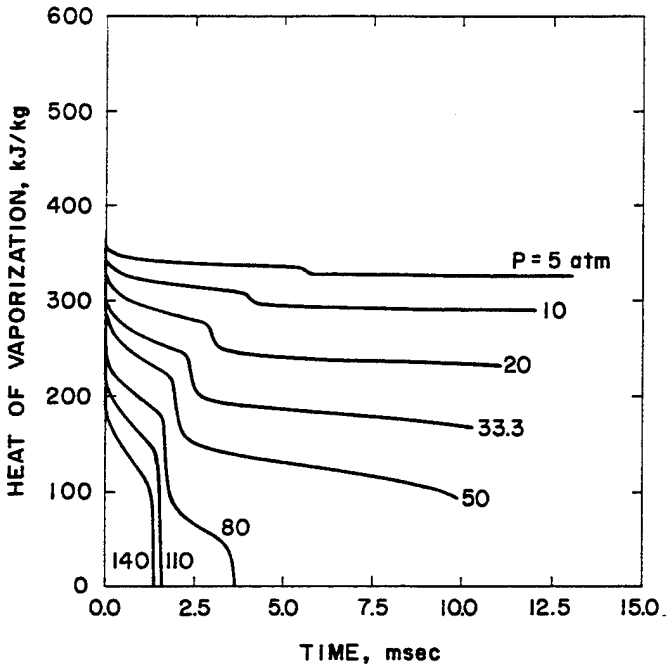

Figure 4.3. Time Variations of Latent Heat of Vaporization at Various Pressures, n-Pentane/Air System.

when the droplet surface approaches its critical mixing state. The situation becomes more conspicuous at higher pressures (e.g., $p = 110$, 140 atm), because the ignition takes place slightly prior to occurrence of the critical mixing point at the droplet surface (see Table 4.2 for numerical values). The overlapping effect causes the latent heat to drop almost instantaneously to zero after onset of the flame.

Figure 4.4 depicts the time variations of the gaseous n-pentane mole fraction at the droplet surface. In the initial stage during which the droplet surface temperature is relatively low, the n-pentane mole fraction decreases with increasing pressure. Figure 4.4(a) shows that as the droplet heats up, the rapid increase in the surface temperature at high pressures (e.g., $p = 50$ atm) allows the fuel-vapor mole fraction to grow at a faster rate and consequently exceeds that at lower pressures (e.g., $p = 5$ atm). When the droplet surface approaches the critical mixing state

for $p \geq 80$ atm, the n-pentane concentration increases exceedingly fast and finally stabilizes at a level set by the critical mixing condition, as shown in Fig. 4.4(b).

The time histories of liquid n-pentane fuel and dissolved nitrogen at the droplet surface are shown in Fig. 4.5. In the subcritical regime, with the ambient pressure less than the critical pressure of pure n-pentane, the amount of nitrogen dissolved in the liquid phase is very limited. It decreases with increasing temperature and finally vanishes at the boiling temperature of the fuel. However, the situation in a supercritical environment exhibits the opposite trend. The ambient gas solubility in the droplet is quite significant, and increases with temperature. For instance, the liquid phase contains more than 35 % nitrogen at the surface for $p = 110$ atm when the critical mixing condition is reached. The ensuing change in the thermophysical properties of the droplet may cause an intrinsic modification of the fuel gasification behavior.

Figure 4.6 presents the histories of the square of droplet diameter at various pressures. The droplet surface regression rate increases persistently with pressure, mainly due to the reduced latent heat of vaporization at high pressures. Although a decrease of mass diffusivity takes place at high pressures and gives rise to an adverse influence on the gasification process, this effect is usually overridden by the reduced latent heat of vaporization. Consequently, a net increase of the surface regression rate is observed. At high pressures, the relatively fast increase in temperature leads to a rapid decrease in liquid density during the initial heatup period. The resulting volume expansion may offset the regression arising from the vaporization process, and cause the droplet to exceed its initial droplet diameter which varies slowly during the initial heatup period, with very little gas-phase reaction involved in the gasification mechanism. It then regresses at a much faster rate subsequent

(a)

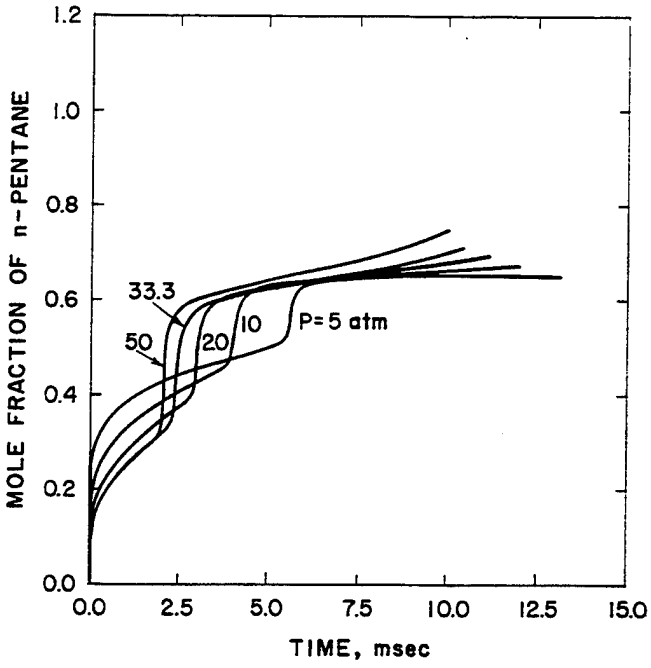

(b)

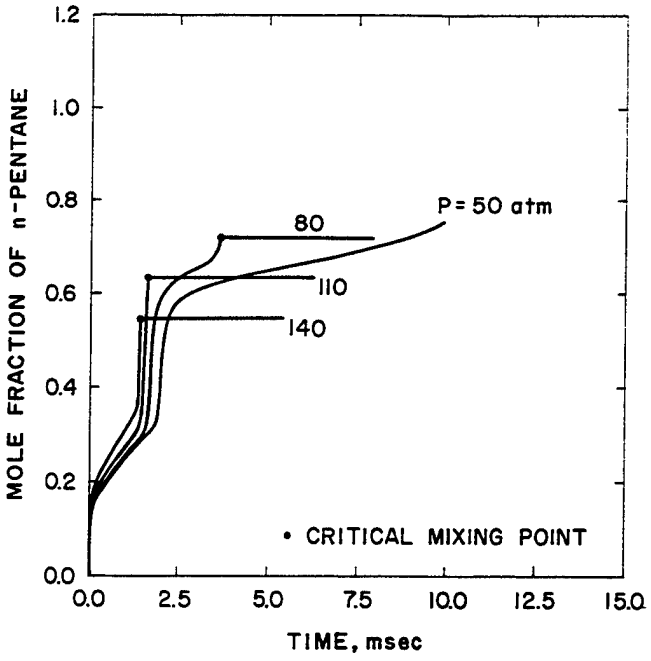

Figure 4.4. Time Variations of n-Pentane Mole Fraction on Droplet Surface at Various Pressures, n-Pentane/Air System: (a) $p \leq 50$ atm. (b) $p \geq 50$ atm.

(a)

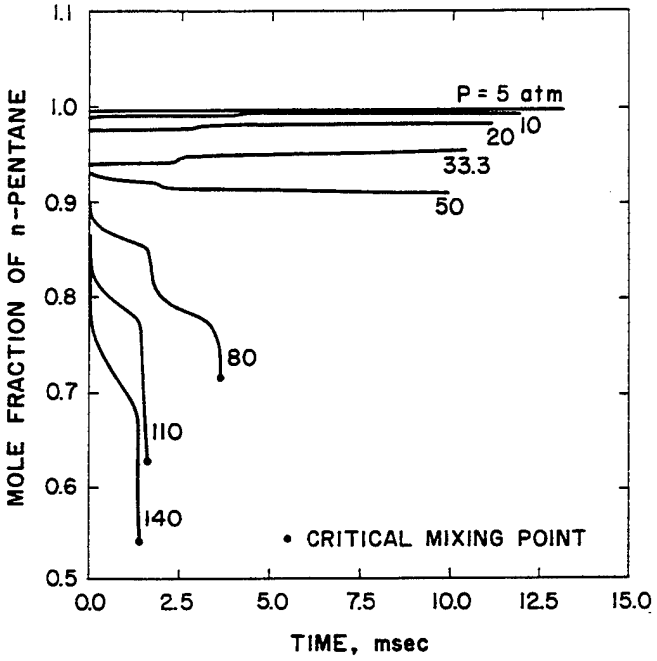

(b)

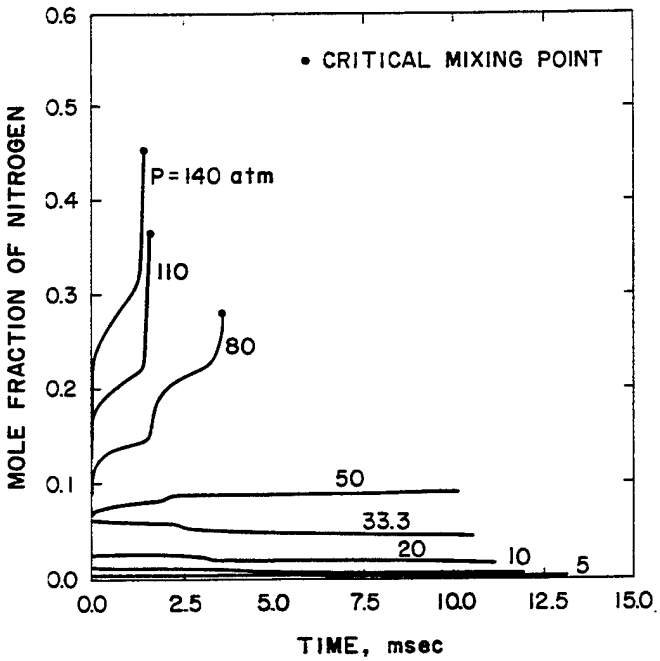

Figure 4.5. Time Variations of Liquid Mole Fraction on Droplet Surface at Various Pressures, n-Pentane/Air System: (a) n-Pentane. (b) Nitrogen.

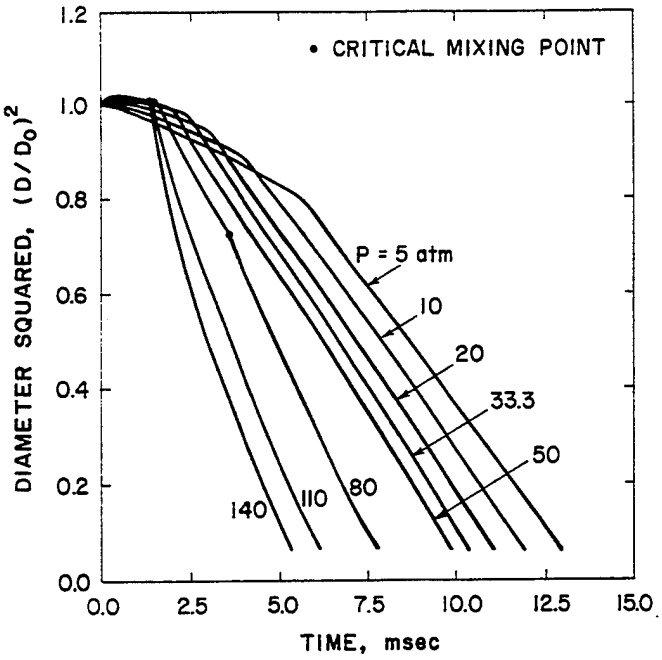

Figure 4.6. Time Variations of the Square of Droplet Diameter at Various Pressures, n-Pentane/Air System.

to onset of the flame in the gas phase, mainly because of the enhanced heat transfer to the liquid phase and the increased mass transfer arising from the higher fuel-vapor concentration at the surface. At low pressures ($p < 20$ atm), when the droplet reaches its pseudo wet-bulb state, the surface area varies almost linearly with time, and the classical d^2-law provides a faithful description of the regression behavior. However, the situation at high pressures becomes quite different. The continuous variations of the droplet interior and surface properties prohibit the use of the d^2-law in predicting the surface regression rate. Furthermore, as the droplet surface reaches its critical mixing point, the latent heat of vaporization drops rapidly to zero and the regression rate accelerates, as indicated by the kinks in the profiles for $p \geq 80$ atm. The rapid increase of the regression rate caused by the change of gasification mechanism after reaching the critical mixing point is a predominant phenomenon in high-pressure vaporization processes and must be

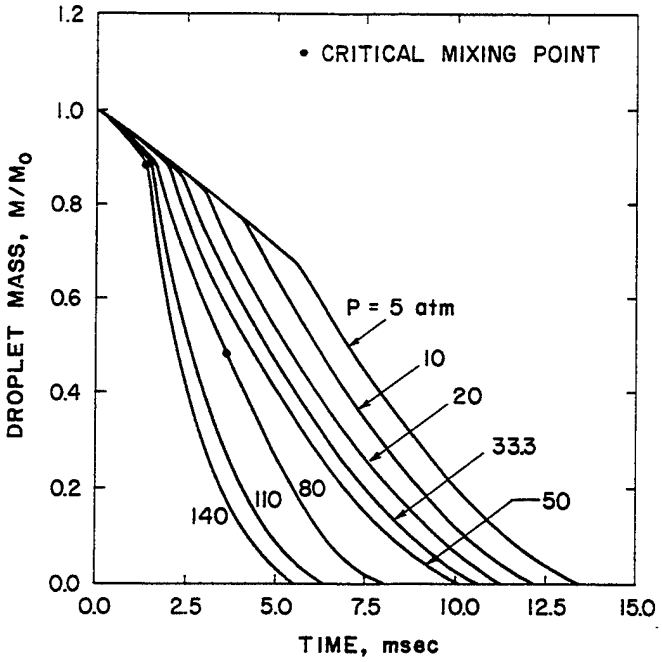

Figure 4.7. Time Variations of Fuel Droplet Mass at Various Pressures, n-Pentane/ Air System.

considered in a supercritical spray analysis. When the ambient pressure increases from 110 to 140 atm, the reduced mass diffusion results in a slowdown in the increase of regression rate with pressure.

The time variations of the liquid fuel mass are displayed in Fig. 4.7. Although Fig. 4.6 shows the time history of the surface regression rate, little information about the fuel mass gasification rate is given unless the variable-property effect is properly taken into account. This point can be easily elaborated by considering the global mass balance of the liquid fuel.

$$\frac{dm_F}{dt}\Big|_{droplet} = \frac{d}{dt}\int_0^R 4\pi r^2 \rho_\ell Y_F dr$$

$$= 4\pi R^2 \rho_\ell Y_F \dot{R}\Big|_{r=R_-} + \int_0^R 4\pi r^2 \frac{d}{dt}(\rho_\ell Y_{fuel}) dr \qquad (4.1)$$

where m_F is the total mass of the liquid fuel. The gasification rate contains contributions from both surface regression and fuel-density variation, as indicated by the first and second terms on the right-hand side of the above equation, respectively.

Figures 4.8(a) and (b) show the spatial distributions of temperature and density in the droplet interior, respectively. The droplet surface temperature increases rapidly in the initial stage, then remains fixed after it reaches the critical mixing state. As a result, all of the thermal energy transferred from the ambient gas is used to heat up the droplet, which, in turn, causes the critical surface to propagate toward the interior of the liquid phase. The temperature also indicates a continuous reduction of liquid density, as shown in Fig. 4.8(b). In particular, a steep variation of density occurs near the droplet critical surface, since the liquid density decreases exceedingly fast with temperature in the vicinity of the critical mixing point. Two points must be noted during this process. First, the time-varying reduction of liquid density causes the droplet to swell; the ensuing volume dilatation is significant and must be accounted for in determining the droplet regression behavior. Second, the non-uniformity of density distribution results in a significant outward convection that may effectively retard energy transfer to the droplet interior.

The time histories of flame development can be examined by plotting the distributions of gas-phase temperature and species concentrations at various times. Figures 4.9(a) and (b) show a typical set of temperature profiles for $p = 80$ atm. The corresponding distributions of n-pentane species concentration are given in Figs. 4.10(a) and (b). The droplet ignition is achieved around $t = 1.28$ ms. The

(a)

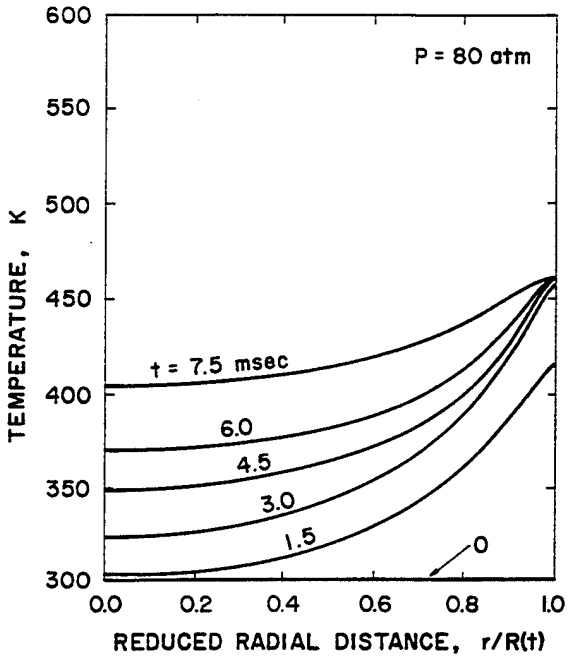

(b)

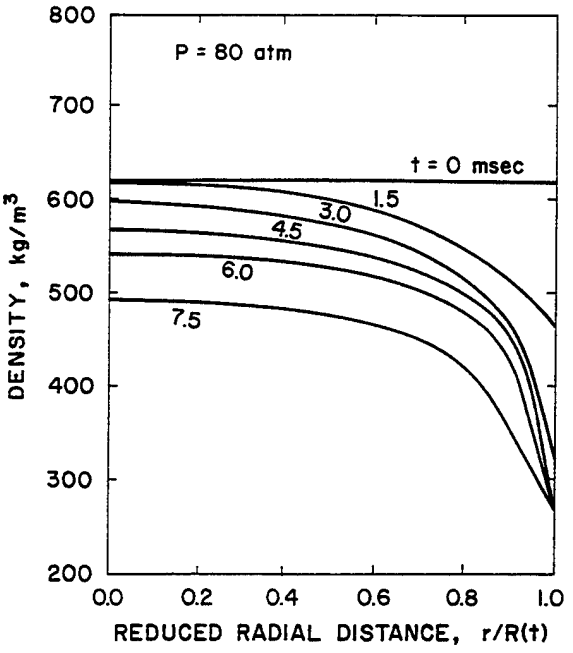

Figure 4.8. Distributions of Liquid-Phase Properties at Various Times, n-Pentane/ Air System at $p = 80$ atm: (a) Temperature. (b) Density.

(a)

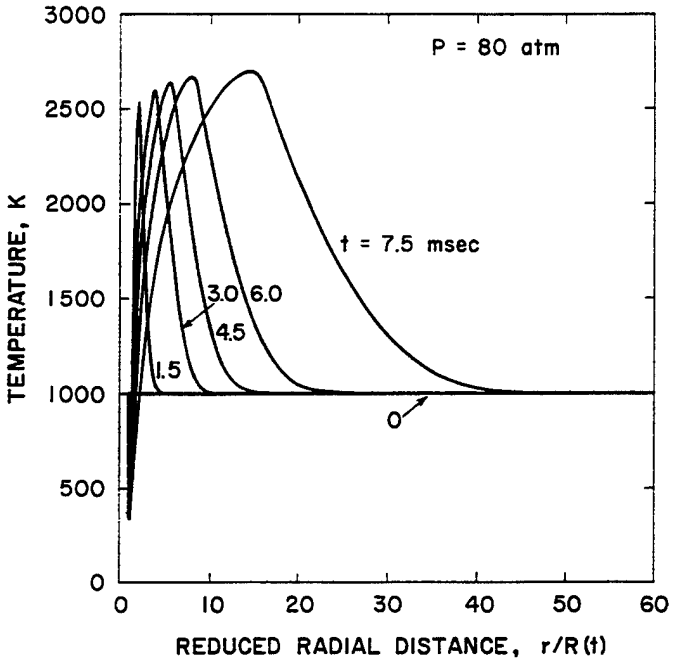

(b)

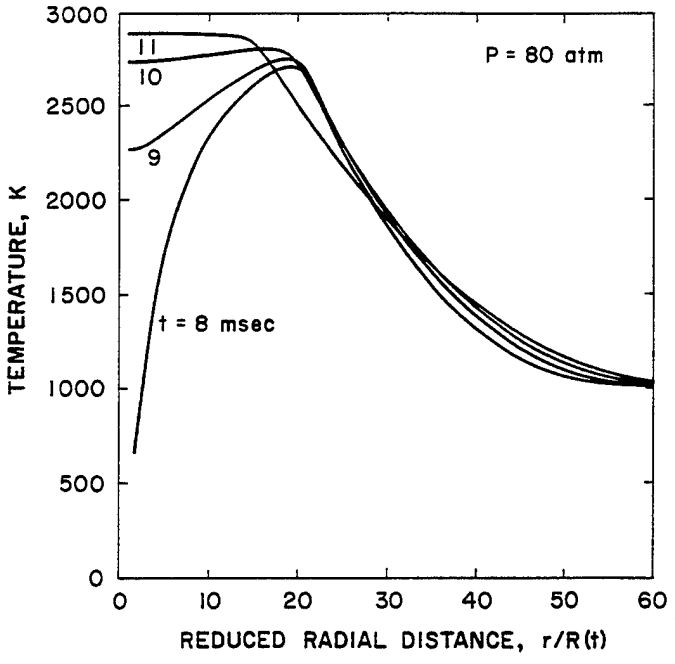

Figure 4.9. Distributions of Gas-Phase Temperature at Various Times, n-Pentane/ Air System at $p = 80$ atm: (a) prior to End of Droplet Gasification Lifetime. (b) after End of Droplet Gasification Lifetime.

(a)

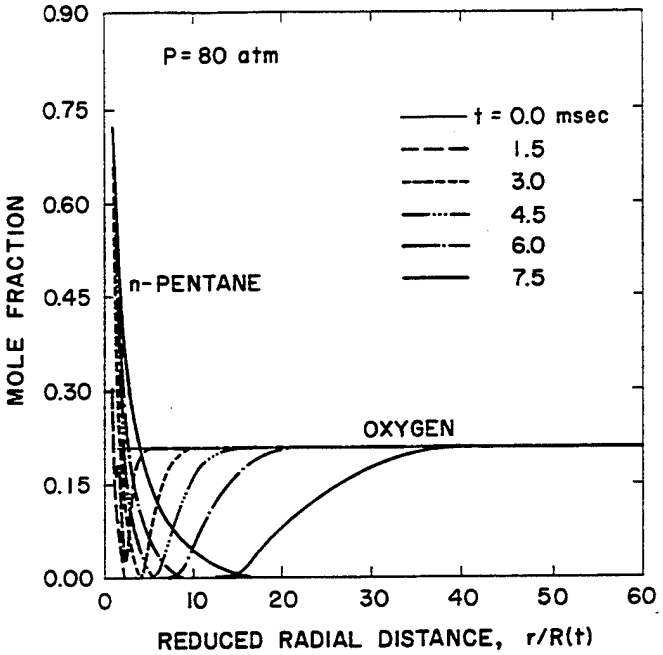

(b)

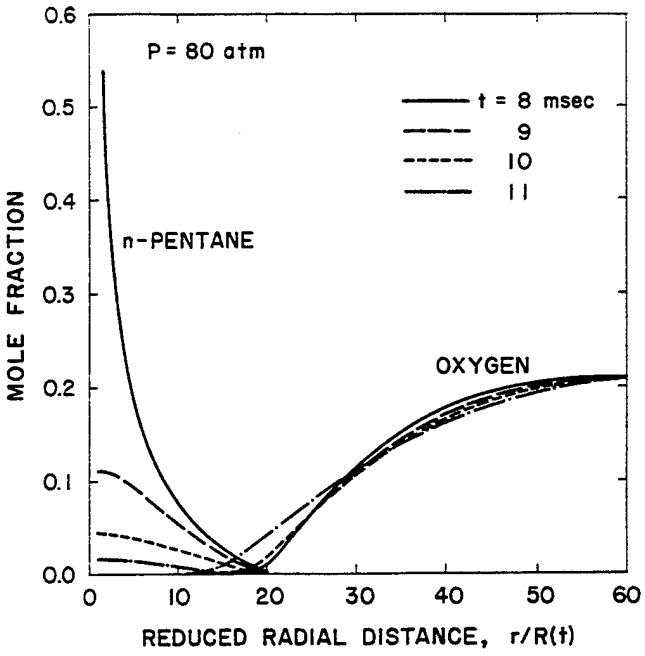

Figure 4.10. Distributions of Gas-Phase Species Concentrations at Various Times, n-Pentane/Air System at $p = 80$ atm: (a) prior to End of Droplet Gasification Lifetime. (b) after End of Droplet Gasification Lifetime.

resulting flame then spreads outward progressively during the droplet gasification lifetime ($t \leq 7.94$ ms). After completion of the fuel gasification process, the residual fuel vapor in the gas phase continues to react with air and causes the flame to shrink. The gas-phase reaction ends at $t = 11.90$ ms, at which point the fuel vapor is completely consumed. The overall flame development is further illustrated by the photographs in Fig. 4.11. The top figure shows the time history of the droplet surface temperature. The instantaneous temperature contours, including both the droplet interior and ambient gases, are presented at six different times. The color scale at the left indicates temperature, increasing from the blue ($T = 300\ K$) toward the red ($T = 2900\ K$). The dark blue region at the center corresponds to the liquid droplet. The motion of the flame front is clearly observed, as shown by the red zone.

The flame development process is further studied by examining the loci of the peak gas-phase temperatures at various ambient pressures. Figures 4.12(a) and (b) show the flame movement (as depicted by the location of the peak temperature) in terms of the reduced distance. Owing to the relatively higher concentrations of fuel vapor and oxygen and slower diffusion of fuel vapor away from the surface at higher pressures, the gas-phase ignition occurs at a radial position which continues to move closer to the droplet surface with increasing pressure. Immediately after ignition, the flame front moves inward due to the shift in the location of the stoichiometric composition. It then spreads outward because of the increase in the gasification rate, until the liquid droplet disappears. Finally, the termination of the fuel supply from the liquid droplet causes the flame to shrink and eventually disappear at the burnout point. During the flame history, the peak gas-phase

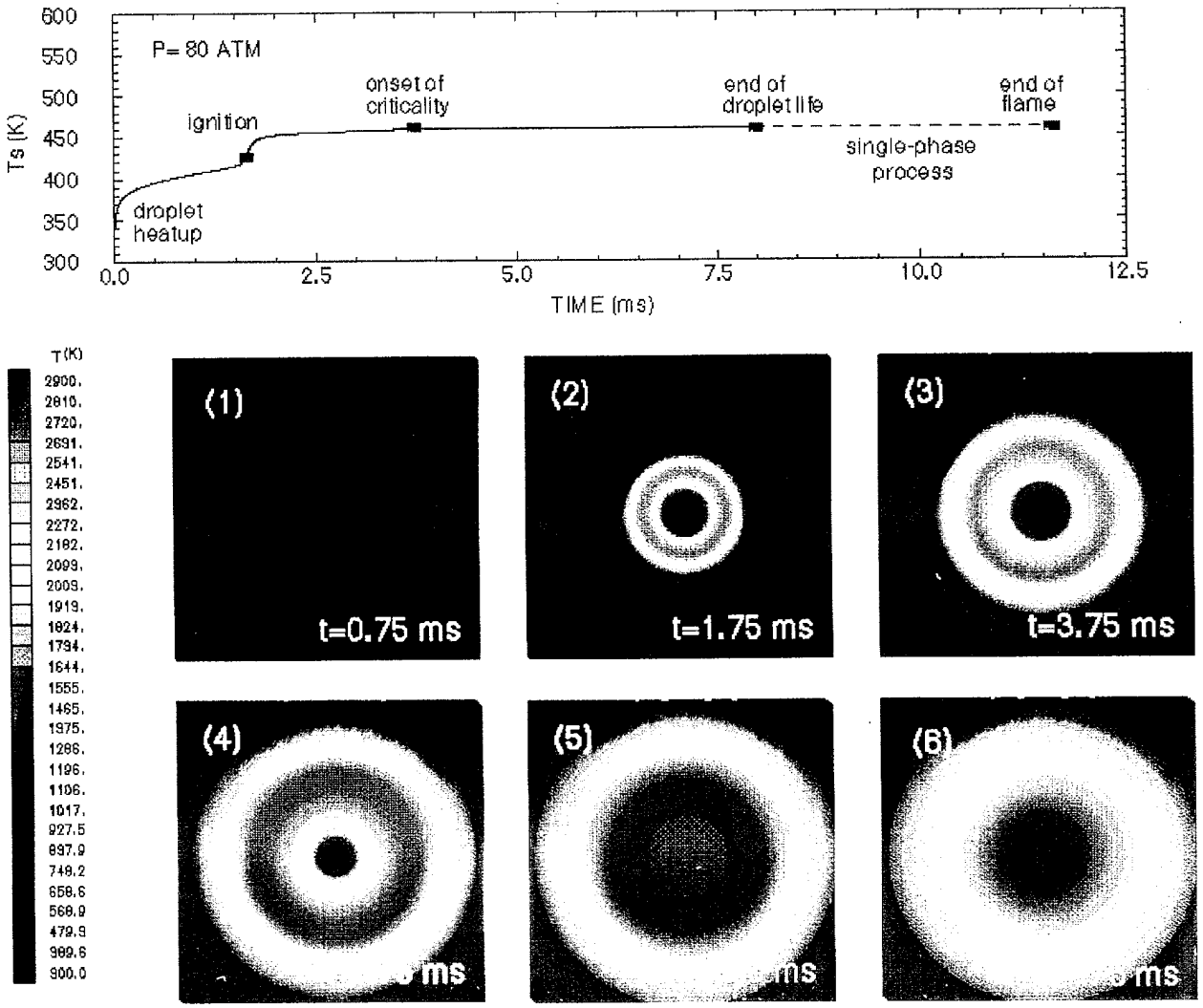

Figure 4.11. Instantaneous Temperature Contours in the Field at Various Times, n-Pentane/Air System at $p = 80$ atm.

(a)

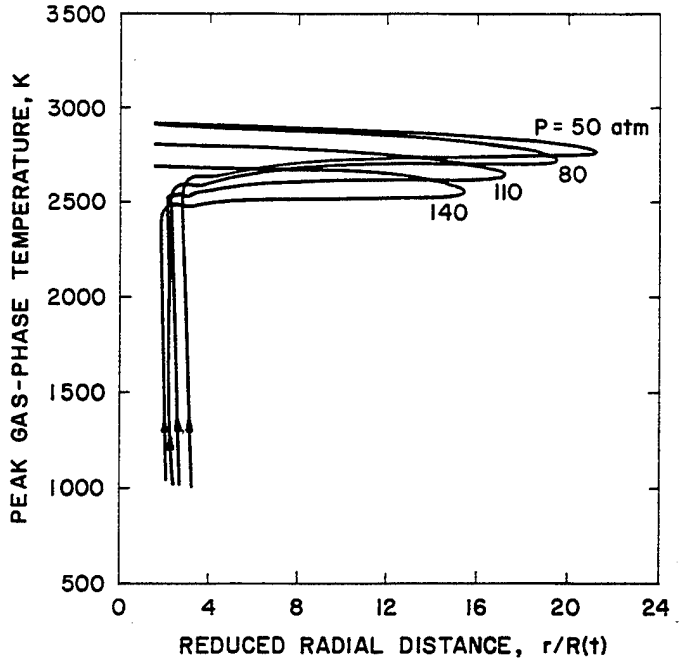

(b)

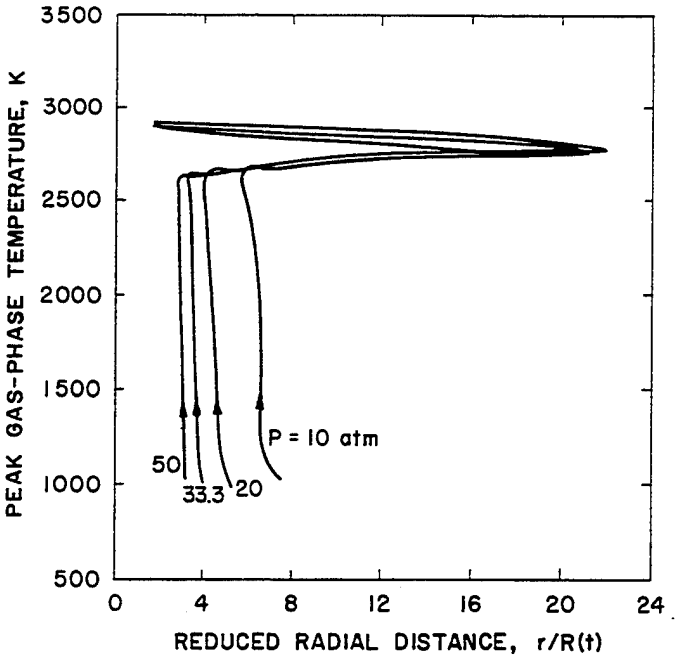

Figure 4.12. Loci of Peak Temperature in the Gas Phase at Various Pressures, n-Pentane/Air System.

temperature increases continuously, except for the slight set back following the onset of the flame. The peak temperature increases with pressure in the subcritical region($p \leq 50$ atm), due to the increased chemical reaction rates at higher pressures. On the other hand, for $p \geq 50$ atm, the peak flame temperature decreases as pressure increases. This is mainly caused by the decrease in fuel-vapor mass diffusivity at high pressures, which subsequently results in an increase in the Lewis number (note that pressure exerts a much stronger adverse influence on mass diffusion than on thermal diffusion). As a consequence of the reduced rate of mass diffusion of the gaseous fuel to the flame zone, the rate of thermal energy produced by chemical reactions also decreases, rendering a lower flame temperature as the rate of heat transferred away from the flame varies only slightly with pressure.

Figure 4.13(a) presents the effect of pressure on various milestone times associated with droplet gasification and burning process. Here gasification lifetime is the time required for complete gasification, droplet burning lifetime is the gasification lifetime minus ignition time, single-phase combustion lifetime is the time duration from complete gasification to burnout of all fuel vapor, and combustion lifetime is the sum of single-phase combustion lifetime and droplet burning lifetime. The gasification lifetime decreases continuously with pressure, whereas the single-phase combustion lifetime increases progressively with pressure due to its adverse effect on mass diffusion. More importantly, the pressure dependence of combustion lifetime exhibits irregular behavior. This phenomenon may be attributed to the overlapping effect of reduced enthalpy of vaporization and mass diffusion with increasing pressure.

Since the time scales for diffusion processes are inversely proportional to the droplet diameter squared, it is important to examine the effect of droplet

size on the burning characteristics. In this regard, calculations were conducted for large droplets having an initial diameter of 1000 μm, which is comparable to the sizes considered in most experimental studies of supercritical droplet combustion[11,50]. Furthermore, the ignition transient occupies only a very small fraction of the entire droplet lifetime for large droplets. The uncertainties associated with the ignition procedure in determining the characteristics of droplet gasification can be minimized. Consequently, a more meaningful comparison with experimental data can be made. Figure 4.13(b) shows the milestone times for $D_0 = 1000\ \mu m$. The combustion behavior of a large droplet reveals several characteristics distinct from those of a small droplet. First, ignition for large droplets occurs in the very early stage of the entire droplet lifetime. The influence of gasification prior to ignition on the overall burning mechanisms appears to be quite limited. Second, the combustion lifetime decreases with increasing pressure, reaching a minimum near the critical pressure of the liquid fuel. As the pressure further increases, the combustion time increases due to reduced mass diffusivity at high pressures. The gasification lifetime decreases continuously with pressure, whereas the single-phase combustion lifetime increases progressively with pressure. This phenomenon is in qualitative agreement with the experimental observations of Faeth *et al.*[11] and Sato *et al.*[50], and suggests a change of the burning characteristics across the critical pressure. At low pressures, the gasification of liquid fuel primarily controls the combustion process, while in a supercritical environment, the transient gas-phase diffusion plays a more important role.

While the present work provides new insights to and enhances current understanding of supercritical combustion of fuel droplets, a quantitative comparison

(a)

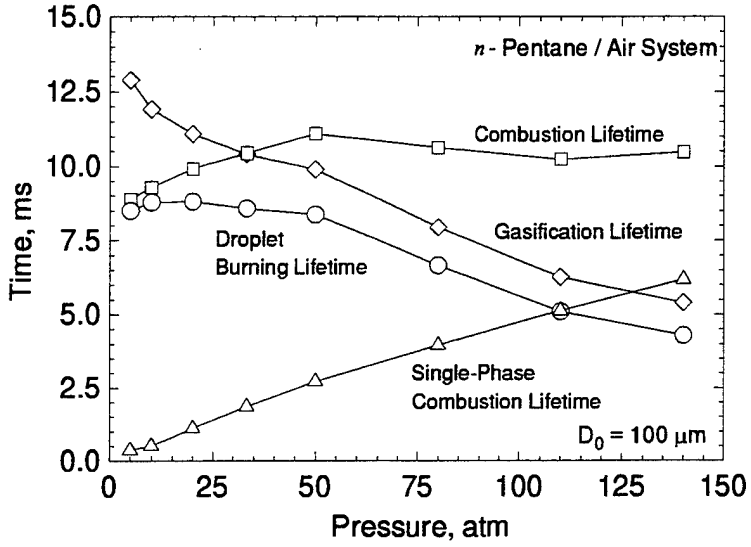

(b)

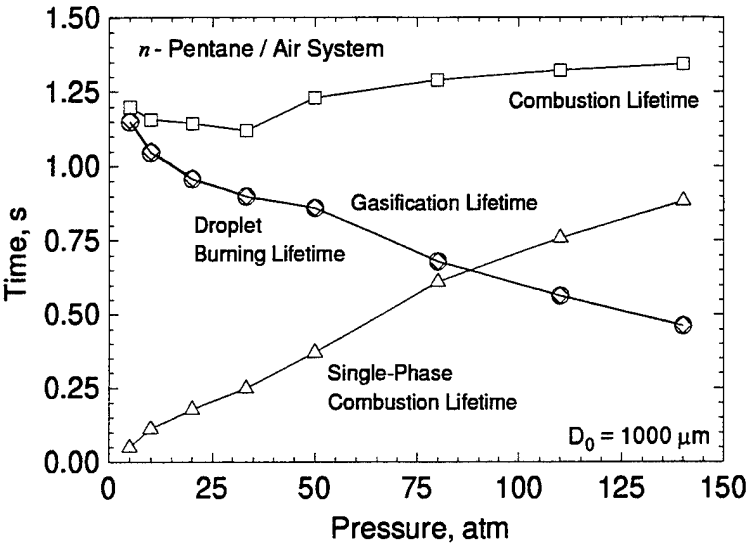

Figure 4.13. Effect of Pressure on Milestone Times Associated with Droplet Gasification and Burning Processes, n-Pentane/Air System: (a) $D_0 = 100\ \mu m$. (b) $D_0 = 1000\ \mu m$.

of calculated results with experimental data is rather difficult to make, mainly because of the neglect of radiation heat transfer in the analysis. The lack of reliable radiant transport properties at high pressures also poses a problem. Thermal radiation from the flame to the droplet can be substantial for large droplets at high pressures. Thus, without a full account of radiation heat transfer in the analysis, any attempt of quantitative comparison will be futile.

CHAPTER 5

PRESSURE-COUPLED VAPORIZATION RESPONSES

Combustion instability has haunted development of many high performance combustors for almost forty years. This problem severely impairs engine operation and often leads to catastrophic consequence[2]. For the past three decades, a considerable amount of effort has been devoted to seek a deeper understanding of this undesirable phenomenon. It is generally accepted that unsteady motions will grow if heat and mass are added in phase with unsteady waves. Conversely, it will damp if the mass and energy additions are out of phase with pressure oscillation. For most liquid-fueled systems, propellants are delivered into a combustion chamber as a spray of droplets. Since droplet vaporization represents a rate controlling process in the combustors, the dynamic behavior of spray combustion is indeed a statistic consequence of the vaporization characteristic of an individual droplet. A knowledge of the vaporization response of an isolated droplet to ambient flow oscillations becomes essential in treating combustion instability[51].

Investigation of dynamic responses of droplet vaporization and combustion to ambient flow fluctuations started in the 60s. Strahle[52] examined droplet-burning responses in a forced convective field in which a small-amplitude sound wave was introduced into the free stream. Since the exact solution can only be found near the forward stagnation point, his primary interests were focused on the local vaporization responses under the action of forced oscillations. He examined the boundary layer surrounding the droplet, and showed that the amplitude

of vaporization response increases with increasing frequency. However, his model erroneously predicts that the vaporization response to pressure oscillation is unbounded, approaching infinity as the square root of frequency goes to infinity. Heidmann and Wieber[53] studied the vaporization processes of an n-heptane droplet in combustors with superimposed traveling transverse oscillations. The response functions were evaluated over fairly wide range of flow conditions, and the data was correlated with a dimensionless parameter which is the frequency normalized by one half of the droplet lifetime. In their study, the peak response occurs when the droplet lifetime approximately equal to the oscillation period. Negative gains (phase lag is more than 90^o) may happen when the vaporization time is greater than about three times the oscillation period. Allison and Faeth[54] studied the response function of a burning liquid monopropellant surface to imposed pressure oscillation, and found that the combustion response tends to peak in two frequency ranges; one corresponding to interaction with liquid-phase transient effects, which could be verified both theoretically and experimentally; the other corresponding to gas-phase transient effects, which could only be examined theoretically. Recently, Tong and Sirignano[55–57] implemented transient heating and mass diffusion models for the liquid phase and proposed that the unsteady droplet vaporization is a potential mechanism for driving combustion instabilities. Although the preceding studies have provided significant information about the underlying mechanisms involved in droplet vaporization response, a number of fundamental problems remain unresolved for high-pressure conditions.

In the following, a series of numerical simulations of droplet vaporization in a forced-oscillatory environment are performed. Because the model is based on

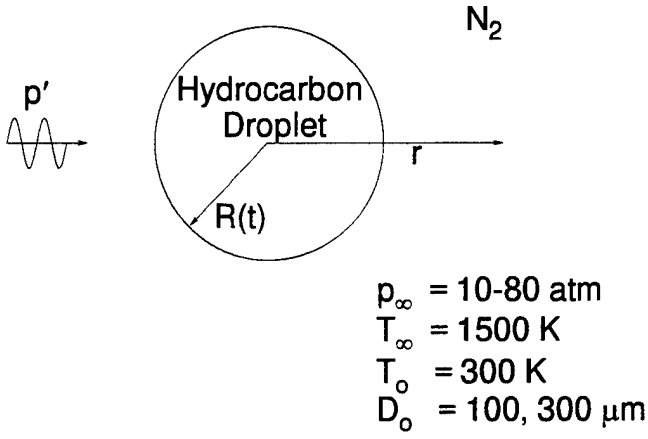

Figure 5.1. Schematic of An Isolated Droplet Vaporizing in Forced Oscillatory Environment.

first principles, a systematic investigation into couplings between pressure oscillation and transient mechanisms involved in droplet vaporization becomes feasible. Figure 5.1 shows the situation examined, a vaporizing droplet in a quiescent environment superimposed with a periodic pressure oscillation. This approach allows researchers to focus on the various mechanisms that influence the dynamic response of droplet vaporization to ambient pressure oscillations..

5.1 Discussion of Results

Vaporization responses of an isolated droplet to ambient pressure oscillations at high pressures have been conducted systematically. The analysis treats an n-pentane droplet in nitrogen gas. The initial droplet temperature is 300 K and the ambient nitrogen temperature is 1500 K. The mean pressure is either in the subcritical (10 and 20 atm) or supercritical (50 and 80 atm) regime of the fuel. In

the early stage of the droplet lifetime, a large temperature gradient exists across the liquid/vapor interface, rendering a strong heat flux conducted into the droplet interior. Part of the energy is used to gasify the liquid, while the remainder goes to heat up the droplet interior. As a consequence, droplet surface temperature increases and may lead to two different scenarios (i.e., subcritical and supercritical vaporization). First, if the ambient pressure is much less than the critical value of the fuel, the surface temperature increases and approaches the pseudo wet-bulb state[49]. The droplet surface provides a well-defined boundary which separates the liquid from the ambient gases. The vaporization rate can be easily quantified by evaluating the mass flux through the surface. Second, if the ambient temperature and pressure are both in the supercritical regime of the fuel, the characteristic times of the transport processes in both liquid and gas phases approach the same order of magnitude as a result of increasing surface temperature. At some point during the droplet lifetime, the distinction between these two phases disappears, rendering a continuous medium in the entire domain. Under this condition, the transport processes in the liquid phase become as important as those in the gas phase, the vaporization response is expected to exhibit phenomena different from the low pressure cases. As mentioned in Chapter 4, the droplet regression is best characterized by the motion of the surface which attains the critical mixing temperature. The vaporization rate can be obtained by tracking the time variation of the droplet residual mass which is the total mass confined by the critical-temperature surface. It is worth noting that the critical mixing properties vary with pressure fluctuation. To avoid unnecessary confusion, the surface for supercritical gasification is selected based on the critical value at the mean pressure.

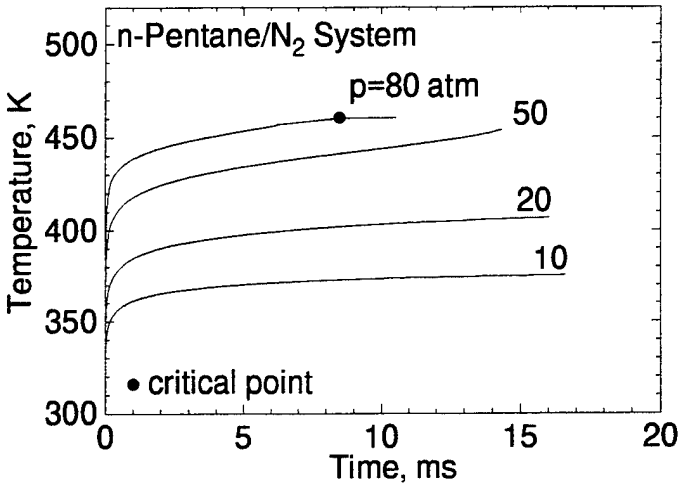

Figure 5.2. Temporal Evolution of Droplet Surface Temperature at Various Mean Pressures, n-Pentane/Nitrogen System; $D_0 = 100\ \mu m$, $T_\infty = 1500\ K$, $T_0 = 300\ K$.

Figure 5.2 shows the temporal evolution of droplet surface temperature at various mean pressures. The rapid heatup immediately after $t = 0$ results from the large temperature gradient near the surface (i.e., a step function was used as the initial temperature distribution). At low to moderate pressures ($p \leq 20$ atm), the droplet surface temperature increases rapidly during the heat up period, then levels off slight lower than the boiling temperature of n-pentane. As the pressure increases to 50 atm, the surface temperature increases continuously, and no pseudo wet-bulb state can be found during the droplet lifetime. For $p = 80\ atm$, the droplet surface even reaches its critical mixing state at $t = 8.3\ ms$. When this occurs, the droplet surface essentially becomes a critical surface where the liquid and gas phases coexist at the critical mixing condition. Figure 5.3 displays the time histories of droplet diameter squared at various pressures. The droplet surface regression rate increases persistently with pressure.

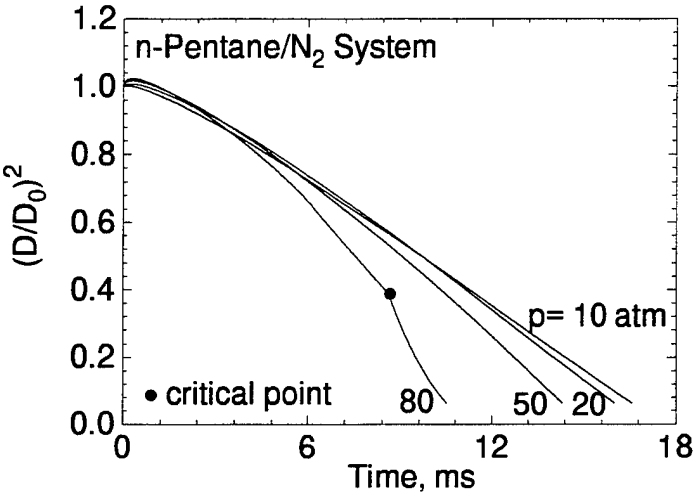

Figure 5.3. Time Histories of the Droplet Diameter Square at Various Pressures, n-Pentane/Nitrogen System; $D_0 = 100\ \mu m$, $T_\infty = 1500\ K$, $T_0 = 300\ K$.

To quantify the dynamic behavior of droplet vaporization, a pressure-coupled response function is defined as follows.

$$R_p = \frac{(\tilde{\mathrm{w}} - \bar{\mathrm{w}})/\bar{\mathrm{w}}}{|(\tilde{p} - \bar{p})/\bar{p}|} \tag{5.1}$$

where $\tilde{\mathrm{w}}$ is the instantaneous vaporization rate in an oscillating condition, and $\bar{\mathrm{w}}$ is that in a quiescent environment. Figure 5.4 presents the time variations of droplet vaporization rate and pressure oscillations for $\bar{p} = 50$ atm, marked respectively by the solid and dashed lines. The vaporization rate does not respond instantaneously to the pressure variation, showing a time lag between these two periodic oscillations. The amplitude of the induced vaporization fluctuation varies throughout the droplet lifetime.

To clarify the physical mechanisms involved in the transient response of droplet vaporization to ambient pressure oscillation, it is useful to examine the

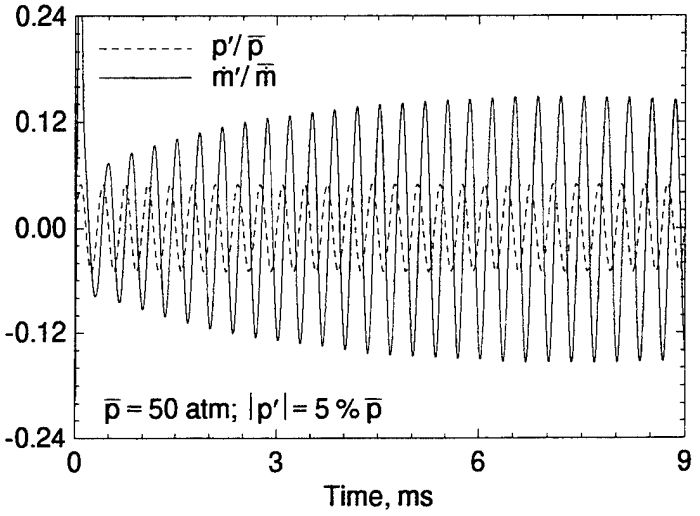

Figure 5.4. Time Variations of Pressure and Droplet Vaporization Rate Fluctuations.

variations of the various time scales throughout the droplet lifetime. Five characteristic times are generally of interest: droplet residual time τ_1, droplet lifetime τ_2, liquid thermal inertia time τ_3, liquid thermal diffusion time τ_4, and gas-phase thermal diffusion time τ_5, as listed in Table 5.1. The droplet lifetime τ_2 should not be confused with the droplet residual time τ_1 which is a measure of the remaining lifetime of a droplet at a given instant of time. Figure 5.5 shows the time variations of these characteristic times for $p_\infty = 10\ atm$. The droplet residual time τ_1 decreases persistently with time. The other characteristic times (τ_2, τ_3, τ_4, and τ_5) first increase in the early stage and then drop to zero at the end of the droplet lifetime. During the heatup period, the predominant factor is the increase of surface temperature induced by the energy transferred from the ambient

TABLE 5.1
Characteristic Times Involved in Droplet Vaporization.

τ_1	Droplet residual time	$\tau_v - t$
τ_2	Droplet lifetime	$\frac{\rho_\ell C_{p,s} r_s^2}{\lambda_s}$
τ_3	Liquid thermal inertia	$\frac{\rho_\ell C_{p,\ell} r_s^2}{\lambda_s}$
τ_4	Liquid thermal diffusion	$\frac{\rho_\ell C_{p,\ell} r_s^2}{\lambda_\ell}$
τ_5	Gas phase diffusion	$\frac{\rho_s C_{p,s} r_s^2}{\lambda_s}$

gases. The increasing temperature modifies thermophysical properties (i.e., density, specific heat, thermal conductivity) on the droplet surface, showing increases of characteristic times. When the surface condition approaches the thermodynamic wet-bulb stage, the decreases in characteristic times are mainly contributed by the decreasing droplet radius.

Figure 5.6 represents the effect of frequency on the vaporization responses. The initial droplet temperature and diameter are 300 K and 100 μm, respectively, and the ambient mean pressure is 50 atm. Three different frequencies(i.e., 500, 2000, and 6000 Hz) are considered. Since the physical mechanisms associated with the vaporization process are intrinsically transient in time, the pressure oscillation can easily couple with these processes and exert significant influences on the vaporization rate. Results indicate that the magnitude of vaporization response increases with frequency. In the high frequency regime, the time period for pressure oscillation is much smaller than the liquid thermal inertia time in the droplet interior. The variation of the surface temperature is too slow to keep in pace with the ambient pressure variation. Since the phase-equilibrium condition is posed at

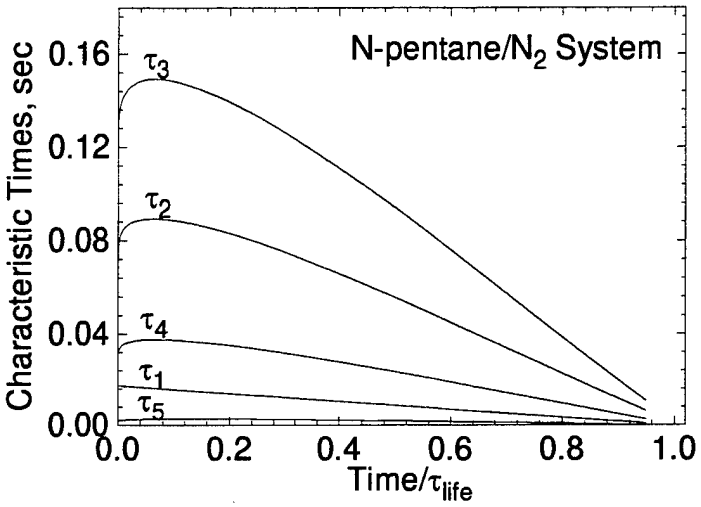

Figure 5.5. Time Variations of Characteristic Times of Transient Mechanisms Involved in Droplet Vaporization, n-Pentane/Nitrogen System.

the droplet surface, the variation in surface composition due to pressure fluctuation becomes a dominant factor, showing an amplitude enhancement. At low to moderate frequency, the heat transfer from the ambient is used either to gasify the liquid fuel or to heat up the droplet interior, the droplet surface temperature fluctuates as a result of unsteady heat transfer into the droplet. However, the thermal diffusion and relaxation processes in the droplet interior possesses transient features characterized respectively by their characteristic times. A time delay for the surface temperature to response to the pressure fluctuation is presented. As a result, the surface properties (including vapor pressure, species concentration, and latent heat of vaporization) which depend strongly on the surface temperature vary with pressure fluctuation. This variation changes the driving force for

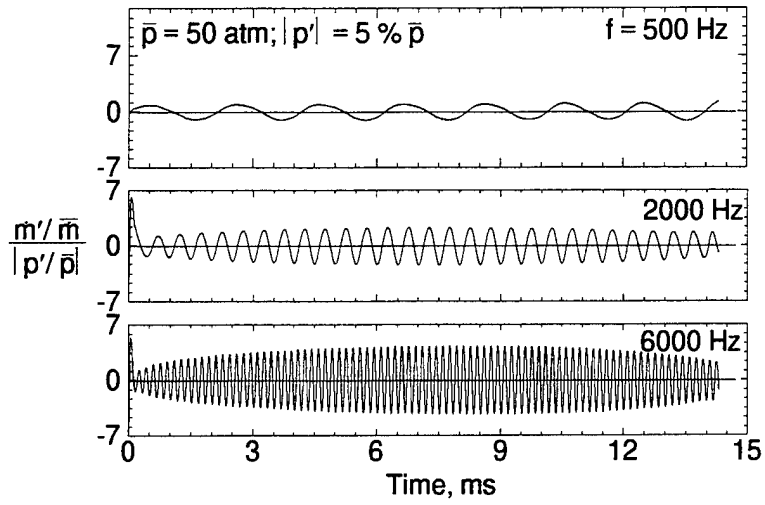

Figure 5.6. Effects of Frequency of Pressure Fluctuation on Time Histories of Vaporization Rate Fluctuation, n-Pentane/Nitrogen System.

gasification process, and as such influences the dynamic behavior of droplet vaporization responses. The time histories show that the magnitude of the response function increases first, mainly because of the initial heat-up period in the early stage of vaporization. The magnitude of vaporization response reaches a maximum and then decreases. It is attributed to the decreases of the characteristic time resulting from decreasing of droplet radius, and as such reduces the magnitude of vaporization responses.

Figure 5.7 depicts the effects of mean pressure on droplet vaporization responses. The ambient mean pressure exerts significant influence on the magnitude of droplet vaporization response. At a given frequency of pressure disturbance, the amplitude of response function increases with increasing pressure. Although all of the pressure-dependent mechanisms (e.g., liquid/vapor phase equilibrium,

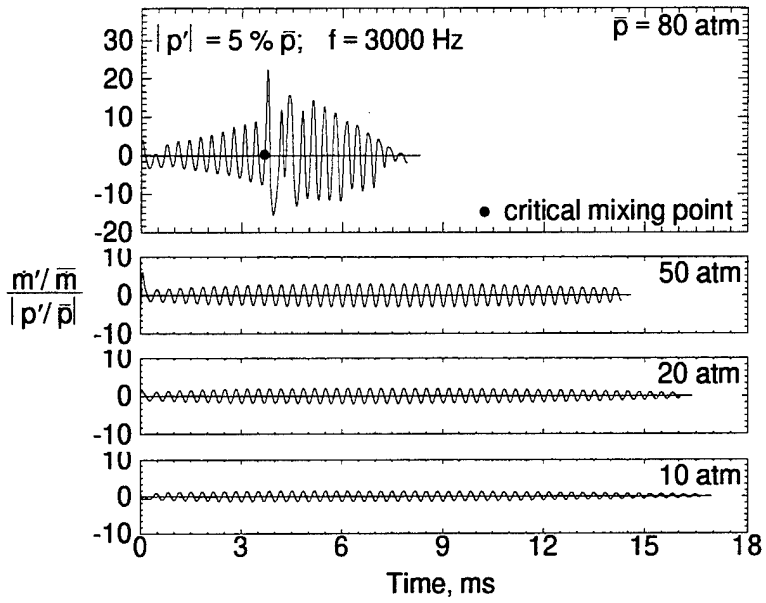

Figure 5.7. Effect of Mean Pressure on Vaporization Rate Fluctuation, n-Pentane/ Nitrogen System; $f = 3000$ Hz.

heat transfer, mass and thermal diffusions) involved in the vaporization process are contributed to this phenomenon, one major contributing factor is the effect of pressure on the latent heat of vaporization. It is because the energy required for phase transition decreases with increasing pressure. As a result, a large amplification gain is observed at high pressure. When the droplet surface reaches the critical mixing state, the latent heat of vaporization drops to zero. All of the heat transfer into the droplet is used to increase the liquid temperature and to transform the liquid phase smoothly into the vapor phase. As a consequence, the vaporization response changes significantly once the critical mixing conditions is reached.

Figure 5.8 shows the time history of the vaporization response function for $\overline{p} = 80$ atm. The vaporization rate fluctuates, with an increasing amplitude

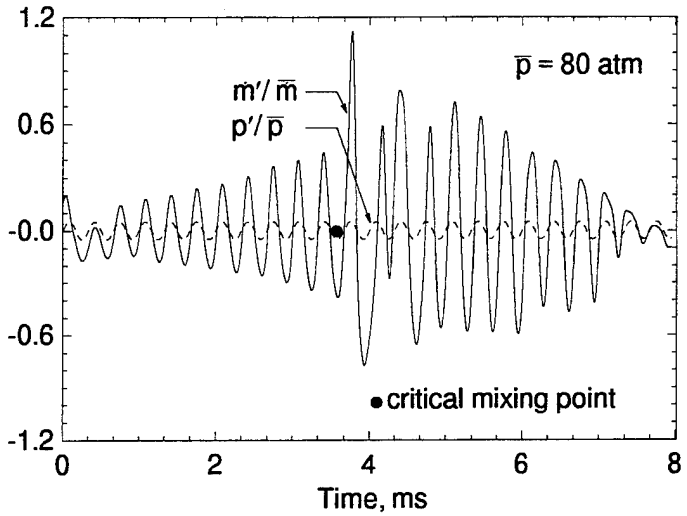

Figure 5.8. Time Variation of Vaporization Rate Fluctuation, n-Pentane/Nitrogen System; $p = 80$ atm, $f = 3000$ Hz.

in the early stage of the droplet lifetime. Interestingly, when the droplet surface reaches the critical point, this fluctuation increases abruptly due to rapid variations of thermophysical properties of the droplet. To explain this phenomenon, the temperature dependence of latent heat of vaporization at three different pressure ($\overline{p} = 72, 80, 88$ atm) is shown in Fig. 5.9. If the ambient pressure executes an isothermal oscillation with a 10 % decreases in amplitude (from point A to point B), the latent heat of vaporization increases by 50 KJ/Kg. The ensuring influence on the vaporization rate is obviously profound. On the other hand, if the ambient pressure increases by 10 % in amplitude (from point A to point C), the droplet surface remains critical with a vanished latent heat of vaporization. However, the continuous changes in the critical mixing properties with pressure modify the heat

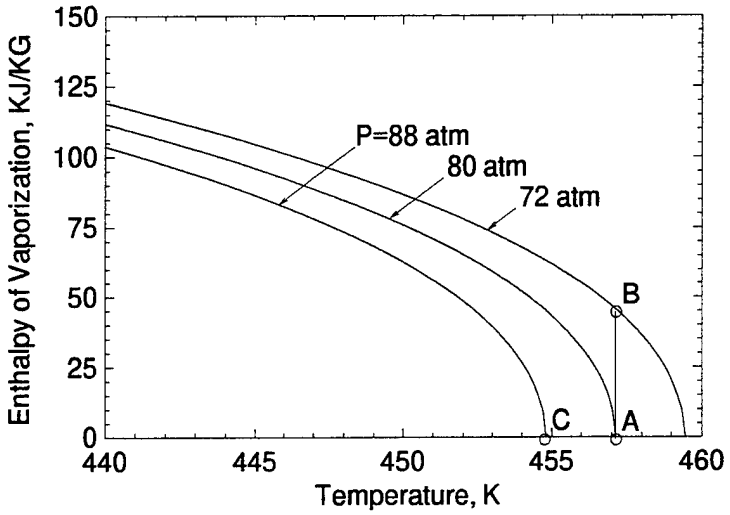

Figure 5.9. Temperature Dependence of Latent Heat of Vaporization at Three Different Pressures, n-Pentane/Nitrogen System.

transfer and mass diffusion processes near the droplet surface, and exert strong influences on the vaporization behavior.

Figure 5.10 shows the magnitudes of instantaneous droplet vaporization response $|R_p|$ as a function of normalized liquid thermal inertia time at various ambient pressures(i.e., 10, 20, and 50 atm). Curves a - b plotted in solid lines are the instantaneous magnitudes of the response function over a broad range of frequency ($f = 250, 500, 1000, 2000, \cdots, 9000$ Hz, respectively) with the initial introductory droplet diameter of $100\mu m$. Curves c - d drawn in dashed line are for droplets with an initial diameter of $300\mu m$ and the frequency range from $10, 50, 100, 250, 500, 1000, 2000, \cdots,$ to 7000 Hz, respectively. For all the cases considered here, the amplitude of the pressure oscillation remains at 5 % the mean value. Results show that the droplet heat up process which occurs in the early

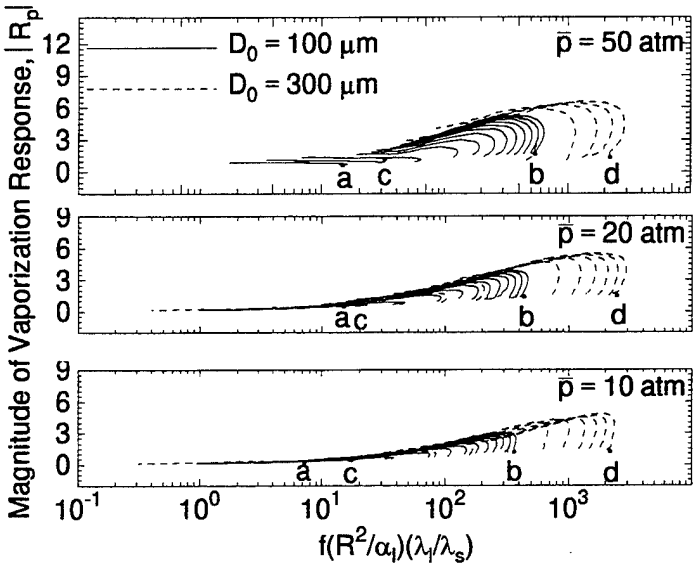

Figure 5.10. Magnitude of Droplet Vaporization Response at Various Mean Pressures, n-Pentane/Nitrogen System.

stage of vaporization has a strong influence on the magnitude of the droplet vaporization response. When the droplet surface approaches the quasi-steady state, all the lines seems to merge together for both large ($D_0 = 300\ \mu m$) and small ($D_0 = 100\ \mu m$) droplets.

Figure 5.11 presents the phases of the instantaneous droplet vaporization responses Θ_p. The notations is the same as those in Fig. 5.10. During the initial heat-up period, droplet liquid thermal inertia and transient diffusion strongly influence the vaporization rate, showing an increases of phase angle as surface temperature increases. The phase lag increases from 0^o toward 180^o as the frequency increases, due to the large deviation of the characteristic times between pressure oscillation and transient vaporization in the high frequency range. One

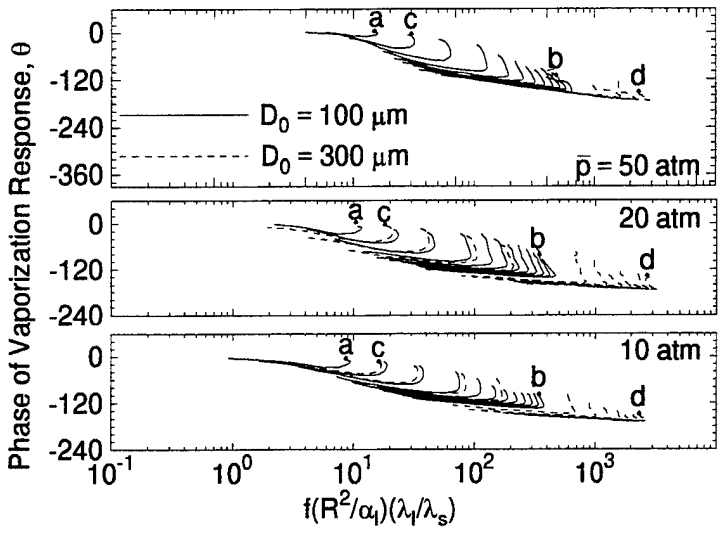

Figure 5.11. Phase of Droplet Vaporization Response at Various Mean Pressures, n-Pentane/Nitrogen System.

interesting result is that the data obtained for the large ($D_0 = 300\ \mu m$) and small ($D_0 = 100\ \mu m$) droplets essentially follow the same trend closely.

Figures 5.12(a) and (b) show the effects of pressure on the magnitude and phase angle of droplet vaporization response. The data points are sampled sequentially throughout the droplet lifetime ($t/\tau_v = 0.1$, 0.3, 0.5, 0.7, and 0.9). The filled symbols depict the data for droplets with an initial diameter of 100 μm, while the hollow symbols depict the cases for droplets with an initial diameter of 300 μm. The effect of initial heatup on magnitude and phase angle are compensated using the following corrections

$$|R_p|^* = |R_p|\left[1 + 20\left(\frac{T_{ref} - T_s}{T_{ref} - T_0}\right)^{2.2}\right]$$

(a)

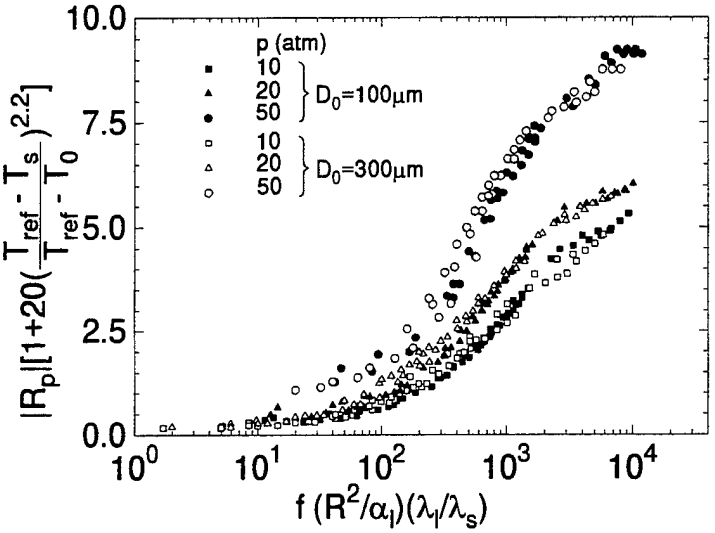

(b)

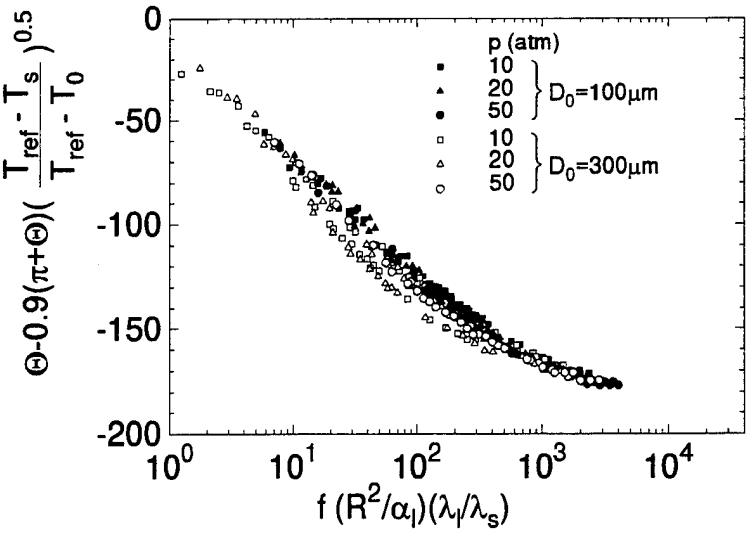

Figure 5.12. Correlations of Droplet Vaporization Responses, n-Pentane/Nitrogen System: (a) Magnitude. (b) Phase Angle.

$$\Theta_p^* = \Theta_p - 0.9(\Theta_p + \pi)\left(\frac{T_{ref} - T_s}{T_{ref} - T_0}\right)^{0.65} \tag{5.2}$$

where T_0 is the droplet averaged temperature and T_{ref} is defined as

$$T_{ref} = \begin{cases} pseudo\ wet{-}bulb\ temperature & \text{if } p \leq p_c \\ critical\ mixing\ temperature & \text{otherwise} \end{cases}$$

where the pseudo wet-bulb and critical mixing temperatures can be found in Table. 4.2. Results for the initial droplet diameters of 100 and 300 μm, shown respectively by the filled and hollow symbols, scatter along the same curve at a given pressure, regardless of the droplet size. The amplitude of the response function increases with increasing pressure owing to the susceptibility of enthalpy of vaporization to ambient flow oscillations at high pressures. On the other hand, the effect of mean pressure on the phase angle appears quite limited. The phase decreases from zero in the low-frequency limit to -180^o at high frequency, a phenomenon which can be easily explained by comparing various time scales associated with fluid transport and ambient disturbance.

In order to decide whether the droplet vaporization process is a driving or damping mechanism in a force oscillatory environment, the real and imaginary parts of vaporization response function are evaluated.

$$\begin{aligned} Re[R_p]^* &= |R_p|^* cos(\Theta_p^*) \\ Im[R_p]^* &= |R_p|^* sin(\Theta_p^*) \end{aligned} \tag{5.3}$$

The results are shown in Figs. 5.13(a) and (b). Based on the dynamic theory, a positive real part represents the driving of the instability. On the other hand, the

(a)

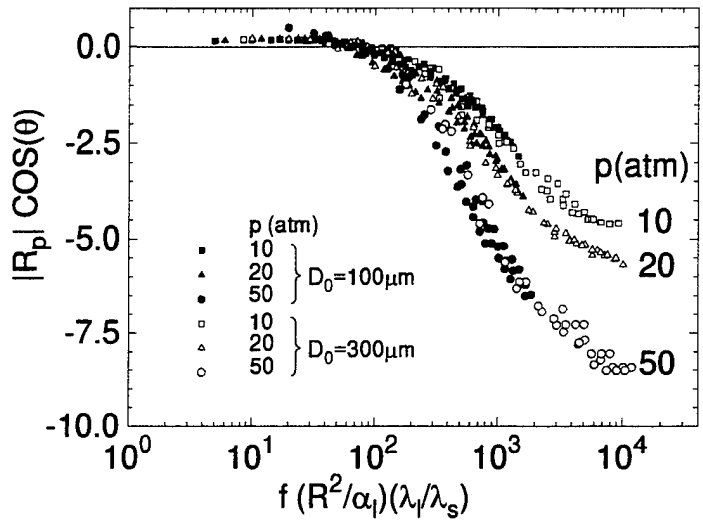

(b)

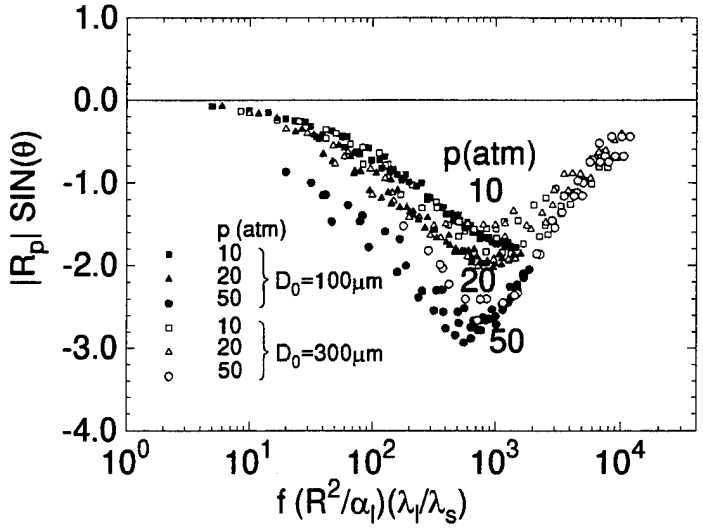

Figure 5.13. Correlations of Droplet Vaporization Responses Function, n-Pentane/ Nitrogen System: (a) Real Part. (b) Imaginary Part.

negative value depicts a damping mechanism. The peaks occur when the normalized liquid thermal inertia time reaches a value around 20. The frequency response will not show these phenomena unless the period of the forcing oscillation becomes commensurate with some characteristic times of the vaporization mechanism. This implies that the strongest coupling occurs between pressure fluctuation and vaporization process. The high-frequency cut-off appears when the value reaches 200, where the vaporization rate response switches from positive to negative, changing the driving mechanism of combustion instability to damping effect.

5.2 Approximate Analyses

In parallel to the numerical calculation, a linear approximate analysis based on simplified assumptions is developed. The purpose is to assist the understanding of the effects of various dynamic mechanisms on droplet vaporization responses. In addition, the non-dimensional parameters identified in the analysis are related to propellant properties that may be used to characterize and examine the dynamic behavior of the vaporization process for any other propellants. The analysis can also be used to validate numerical calculations, especially for low-pressure conditions. We consider a droplet with a mass of $\bar{m}$ and a mean lifetime of $\bar{\tau}_v$ in a forced-oscillatory environment. Due to the periodic variation of the ambient pressure, the properties of the flowfield (e.g., velocity, pressure, vaporization rate, surface temperature, surface vapor pressure, etc.) also feature the oscillatory characteristics. Assuming the deviations of these properties from their mean values are small enough and can be approximated linearly, they are decomposed into a time averaged term plus a small fluctuating value. For any property P, the definition of a small perturbation takes the form

$$P = (1 + P')\frac{1}{\Delta t}\int_{t}^{t+\Delta t} P dt = \bar{P} + \bar{P}P' \tag{5.4}$$

with P' the fluctuation percentage. In order to avoid the influence of disturbance into the mean value, $\bar{P}$, the time period Δt is chosen to be relatively large compared with the period of fluctuation. The equations required in the analysis are summarized in Table 5.2, with the detailed derivation given in Appendix C. It is worth noting that the transient thermal-diffusion process in the droplet interior is modelled using two different approaches: the lumped capacity (infinite liquid thermal conductivity, $\lambda_\ell \longrightarrow \infty$) and the finite thermal diffusion (finite liquid thermal conductivity) models.

lumped capacity model:

The essence of the lumped capacity method is based on the assumption that the temperature of the droplet interior is spatially uniform at any instant during the transient process, implying that the liquid thermal conductivity within the droplet are infinite. The transient temperature response is determined by formulating an overall energy balance for the droplet.

$$\bar{m}C_{p,\ell}\frac{\partial T_s}{\partial t} = Q_{s\rightarrow\ell} \tag{5.5}$$

where $C_{p,\ell}$ and $Q_{s\rightarrow\ell}$ are the liquid specific heat and conduction heat flux conducted into the droplet interior, respectively. With the use of perturbation technique, the linearized equation Eq. (5.5) is written as

$$\bar{m}C_{p,\ell}\bar{T}_s\frac{dT_s'}{dt} = \bar{Q}_{s\rightarrow\ell}Q'_{s\rightarrow\ell} \tag{5.6}$$

The droplet vaporization response function can be obtained as

TABLE 5.2
Simplified Analysis of Droplet Vaporization Response.

Equations	Governing Equations	Linear Analysis
Mass Balance	$\mathrm{w} = -\dfrac{dm}{dt}$	$m' = \dfrac{\mathrm{w}'}{1 - \bar{\tau}_v s}$
Vaporization Rate	$\mathrm{w} = 4\pi r_s \rho_s \alpha_s \ln(1 + \mathcal{B}_T)$	$\mathrm{w}' = \dfrac{1}{3}m' + \beta p'_{F,s} - \beta p'_{\infty}$
Vapor Pressure	$\ln p_{F,s} = a_1 - \dfrac{a_2}{T_s - a_3}$	$p'_{F,s} = bT'_s$
Droplet Surface Temperature	(1) $\dfrac{dT_s}{dt} = \dfrac{1}{\bar{m}C_{p,\ell}}(Q_{g\to s} - Q_{s\to g})$	$\dfrac{C_{p,\ell}\bar{T}_s\bar{\tau}_v}{\Delta h_v}\dfrac{dT'_s}{dt} = \bar{Q}_{s\to\ell}Q'_{s\to\ell}$
	(2) $\dfrac{1}{\alpha}\dfrac{\partial T}{\partial t} = \dfrac{1}{r^2}\dfrac{\partial}{\partial r}(r^2\dfrac{\partial T}{\partial r})$	$Ts' = \dfrac{1}{4\pi\bar{r}_s\bar{\lambda}_\ell\bar{T}_s F(\bar{w}^*)}\bar{Q}_{s\to\ell}Q'_{s\to\ell}$
Energy Balance	$Q_{s\to\ell} = Q_{g\to s} - Q_{s\to g}$	$\bar{Q}_{s\to\ell}Q'_{s\to\ell} = \Delta h_v \mathrm{w}(Q'_{g\to s} - Q'_{s\to g})$
Heat Carried by Gasified Gases	$Q_{s\to g} = \Delta h_v \mathrm{w}$	$Q'_{s\to g} = \mathrm{w}' + d_1 T'_s + d_2 T'_{\infty}$
Heat Transfer from Ambient	$Q_{g\to s} = 4\pi r_s^2 h(T_\infty - T_s)$	$Q'_{g\to s} = \dfrac{2}{3}m' - \dfrac{T_s}{T_\infty - T_s}T'_s$

where $\tau_v = \dfrac{\rho_\ell r_s^2}{2\rho_s\alpha_s\ln(1+\mathcal{B})}$; $\beta = \dfrac{p_s/(p_\infty - p_s)}{\ln(p_\infty/(p_\infty - p_{F,s})}$; $F(\bar{\omega}^*) = (i\omega^*)^{\frac{1}{2}}coth(i\omega^*)^{\frac{1}{2}} - 1$; $b = \dfrac{a_2 T_s}{(T_s - a_3)^2}$;
$d_1 = \left(\dfrac{\partial\Delta h_v}{\partial T}\right)_{p_\infty}\dfrac{T_s}{\Delta h_v}$; $d_2 = \left(\dfrac{\partial\Delta h_v}{\partial p_\infty}\right)_{T_s}\dfrac{p_\infty}{\Delta h_v}$; ω = the Pitzer's acentric factor.

$$R_p = \frac{\mathrm{w}'}{p'_\infty} = \frac{-3\beta(1 - i\tau_v w)\Big[(bd_1 + \Psi_R) + i\Psi_I\Big]}{\Big[2\Psi_R + 3\tau_v w\Psi_I + b\beta\Big] + i\Big[2\Psi_I - 3\Psi_R\tau_v w - 3b\beta\tau_v w\Big]} \tag{5.7}$$

where

$$\Psi_R = \left(\frac{T_s}{T_\infty - T_s} + d_2\right) \tag{5.8}$$

$$\Psi_I = \frac{C_{p,\ell}T_s\tau_v w}{\Delta h_v} \tag{5.9}$$

$$d_1 = \left(\frac{\partial \Delta h_v}{\partial p_\infty}\right)_{T_s}\frac{p_\infty}{\Delta h_v} \tag{5.10}$$

$$d_2 = \left(\frac{\partial \Delta h_v}{\partial T_s}\right)_{p_\infty}\frac{T_s}{\Delta h_v} \tag{5.11}$$

This transfer function represents the dynamic relationship between the vaporization rate and ambient pressure oscillations. When a sinusoidal pressure fluctuation, $p'_\infty(t) = |p'|sin(\omega t)$, is superimposed to the ambient condition, the corresponding vaporization rate variation can be written as $\mathrm{w}'(t) = |\mathrm{w}'|sin(wt + \Theta_p)$, where $|\mathrm{w}'|$ and Θ_p are the amplitude and phase lag, respectively, and take the form

$$|R_p| = \left\{9\beta^2\frac{\Big[1 + (\tau_v w)^2\Big]\Big[(bd_1 + \Psi_R)^2 + \Psi_I^2\Big]}{\Big[2\Psi_R + 3\tau_v w\Psi_I + b\beta\Big]^2 + \Big[2\Psi_I - 3\Psi_R\tau_v w - 3b\beta\tau_v w\Big]^2}\right\}^{0.5} \tag{5.12}$$

$$\Theta_p = tan^{-1}(-\tau_v w) + tan^{-1}\left(\frac{-\Psi_I}{-bd_1 - \Psi_R}\right) - tan^{-1}\left(\frac{2\Psi_R + 3\tau_v w\Psi_I + b\beta}{2\Psi_I - 3\Psi_R\tau_v w - 3b\beta\tau_v w}\right) \tag{5.13}$$

thermal diffusion model:

The transient one-dimensional heat conduction equation in a spherical coordinate system is solved to obtain the droplet surface temperature response to a periodic energy flux.

$$\frac{1}{\alpha}\frac{\partial T}{\partial t} = \frac{1}{r^2}\frac{\partial}{\partial r}\left(r^2\frac{\partial T}{\partial r}\right) \tag{5.14}$$

The energy-flux variation at the droplet surface takes the form

$$\bar{Q}_{s\to\ell}Q'_{s\to\ell} = 4\pi r_s \lambda_\ell T_s F(w^*)T'_s \tag{5.15}$$

where

$$F(w^*) = (iw^*)^{1/2}coth(iw^*)^{1/2} - 1 \tag{5.16}$$

$$w^* = R^2 w/\alpha \tag{5.17}$$

The droplet vaporization response function takes the form

$$R_p = \frac{\mathrm{w}'}{p'_\infty} = \frac{-3\beta(1-i\tau_v w)\Big[(b\Delta h_v \mathrm{w} d_1 + \Psi_R) + i\Psi_I\Big]}{\Big[2\Psi_R + 3\tau_v w\Psi_I + b\beta\Delta h_v \mathrm{w}\Big] + i\Big[2\Psi_I - 3\tau_v w\Psi_R - 3\tau_v w b\beta\Delta h_v \mathrm{w}\Big]} \tag{5.18}$$

where

$$\Psi_R = 4\pi R\lambda_\ell T_s Re[F(w^*)] + \Delta h_v\left(\frac{T_s}{T_\infty - T_s}\right) + d_2\Delta h_v \mathrm{w} \tag{5.19}$$

$$\Psi_I = 4\pi R\lambda_\ell T_s Im[F(w^*)] \tag{5.20}$$

The magnitude and phase angle of the response function R_p are

$$|R_p| = \left\{ \frac{9\beta^2\Big[1+(\tau_v w)^2\Big]\Big[(b\Delta h_v \mathrm{w} d_1 + \Psi_R)^2 + \Psi_I^2\Big]}{\Big[2\Psi_R + 3\tau_v w\Psi_I + b\beta\Delta h_v \mathrm{w}\Big]^2 + \Big[2\Psi_I - 3\tau_v w\Psi_R - 3\tau_v w b\beta\Delta h_v \mathrm{w}\Big]^2} \right\}^{0.5} \tag{5.21}$$

$$\Theta_p = tan^{-1}(-\tau_v w) \quad + \quad tan^{-1}\left(\frac{\Psi_I}{b\Delta h_v w d_1 + \Psi_R}\right)$$

$$- \quad tan^{-1}\left(\frac{2\Psi_I - 3\tau_v w\Psi_R - 3\tau_v w b\beta\Delta h_v \mathrm{w}}{2\Psi_R + 3\tau_v w\Psi_I + b\beta\Delta h_v \mathrm{w}}\right) \tag{5.22}$$

To evaluate Eqs. (5.5)-(5.22), a knowledge of the surface properties (T_s, Δh_v, p_s, and λ_ℓ) is required. These unknowns can be solved using

$$\mathcal{B} = \frac{C_{p,s}(T_\infty - T_s)}{\Delta h_v} = \frac{Y_{F,\infty} - Y_{F,s}}{Y_{F,s} - 1} \tag{5.23}$$

in conjunction with

$$Y_F = \frac{\rho_F}{\rho_s} = \frac{n_F M_F}{n_s M_{F,s}} = \frac{p_F M_F}{p_s M_{F,s}} \tag{5.24}$$

where the partial pressure of fuel can be related to the surface temperature through the Clausius-Clapeyon equation.

$$\frac{d\ln p_F}{dT} = \frac{\Delta h_v}{\mathcal{R} T_s^2} \tag{5.25}$$

Three unknowns($Y_{F,s}$, T_s, and p_F) are involved in Eqs. (5.23)-(5.25), and the final solutions are obtained through an iterative procedure[58].

Since the equations governing the droplet vaporization are linearized using the small perturbation method, a block diagram derived from the simplified analysis is shown in Fig. 5.14. This plot illustrates the connections among the

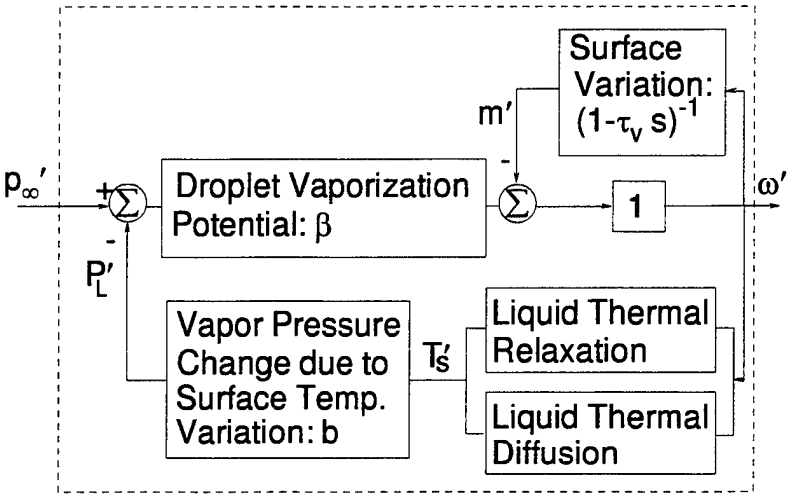

Figure 5.14. Block Diagram of Approximate Analysis.

characteristic processes involved in droplet vaporization. Although an open-loop vaporization response function to ambient pressure fluctuation is under consideration, the analysis shows that a closed-loop mechanism controls the dynamic behavior. When a forced pressure oscillation is introduced to the ambiance of a vaporizing droplet, the amount of heat conducted to the droplet interior is influenced by two factors. First, the heat transfer rate varies with the ambient pressure, showing an enhancement in the energy transfer from the gas phase once the pressure raises above its mean value. Second, the equilibrium species concentrations at the surface is sensitive to both pressure and temperature. This can be further illustrated by the thermodynamic phase equilibrium analysis, showing that the presence of a second species at the droplet surface may alter the latent heat of vaporization, and as such induces a variation in vaporization rate[46].

In Fig. 5.12, the effect of pressure on the magnitude of droplet vaporization response can be correlated using

$$|R_p|^* = \left(\frac{p}{p_{ref}}\right)^{0.4} |R_p|_{p=10\text{atm}} \tag{5.26}$$

where p_{ref} is 10 atm. Figures 5.15(a) and (b) show the comparison of droplet vaporization response between correlations from numerical calculations (Eq. (5.26)) and approximate analytical data(Eqs. (5.7) and (5.20)) at $p = 1$ atm. The dashed lines depict the lumped capacity model, and dotted line the finite diffusion model. The results obtained from simplified analyses deviate substantially from the numerical data, mainly due to the spatial non-uniformity of thermal properties in the droplet interior. To compensate this effect, a correction parameter ε is introduced into the lumped capacity model.

$$\varepsilon \bar{m} C_{p,\ell} \frac{\partial T_s}{\partial t} = Q_{s\to\ell} \tag{5.27}$$

The linearized perturbation equation is written as

$$\varepsilon \bar{m} C_{p,\ell} \bar{T}_s \frac{dT_s'}{dt} = \bar{Q}_{s\to\ell} Q'_{s\to\ell} \tag{5.28}$$

The droplet vaporization response function can be obtained as

$$R_p = \frac{\mathrm{w}'}{p'_\infty} = \frac{-3\beta(1 - i\tau_v w)\Big[(bd_1 + \Psi_R) + i\Psi_I\Big]}{\Big[2\Psi_R + 3\tau_v w \Psi_I + b\beta\Big] + i\Big[2\Psi_I - 3\Psi_R \tau_v w - 3b\beta\tau_v w\Big]} \tag{5.29}$$

where

$$\Psi_R = \left(\frac{T_s}{T_\infty - T_s} + d_2\right) \tag{5.30}$$

$$\Psi_I = \frac{\varepsilon C_{p,\ell} T_s \tau_v w}{\Delta h_v} \tag{5.31}$$

The amplitude and phase lag, respectively, and take the form

(a)

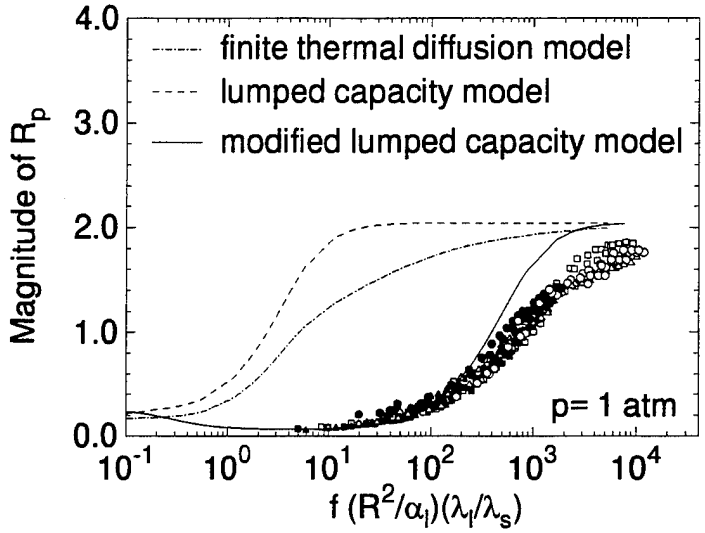

(b)

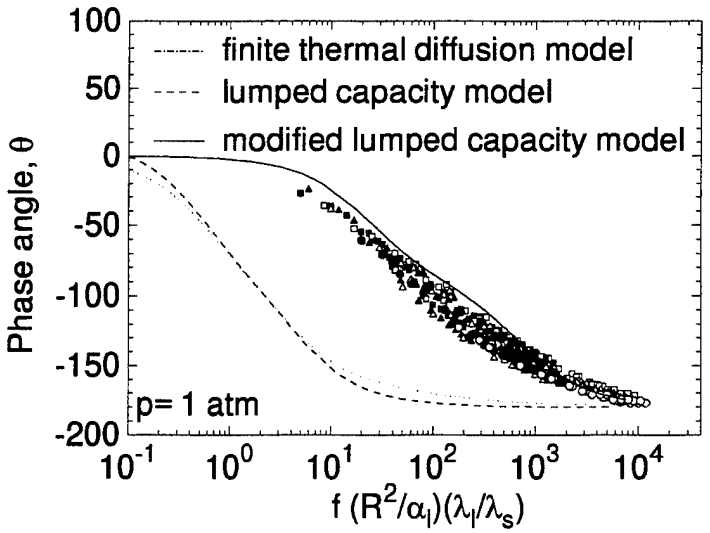

Figure 5.15. Comparison of Droplet Vaporization Response Function with Approximate Analyses, n-Pentane/Nitrogen System: (a) Magnitude. (b) Phase Angle.

$$|R_p| = \left\{ 9\beta^2 \frac{\left[1+(\tau_v w)^2\right]\left[(bd_1+\Psi_R)^2+\Psi_I^2\right]}{\left[2\Psi_R+3\tau_v w\Psi_I+b\beta\right]^2+\left[2\Psi_I-3\Psi_R\tau_v w-3b\beta\tau_v w\right]^2} \right\}^{0.5} \tag{5.32}$$

$$\Theta_p = tan^{-1}(-\tau_v w) \;+\; tan^{-1}\left(\frac{-\Psi_I}{-bd_1-\Psi_R}\right)$$

$$-\; tan^{-1}\left(\frac{2\Psi_R+3\tau_v w\Psi_I+b\beta}{2\Psi_I-3\Psi_R\tau_v w-3b\beta\tau_v w}\right) \tag{5.33}$$

For the n-pentane/N_2 system, ε is chosen to be 0.01. Results based on Eqs. (5.32) and (5.33) are plotted in solid lines, and match the numerical calculations quite well.

CHAPTER 6

DROPLET VAPORIZATION IN FORCED-CONVECTIVE ENVIRONMENTS

The gasification characteristics of liquid oxygen(LOX) droplet in a supercritical hydrogen flow is studied in this chapter. The initial droplet temperature and diameter are 100 K and 100 μm, respectively, and the ambient hydrogen temperature is 1000 K. In order to examine effects of the convective velocity and ambient pressure on the transient behavior of the droplet, including interphase mass, momentum, and energy transport, a parametric study is conducted. The flow conditions cover a wide range of pressure(p=$100-400$ atm) and velocity($U_\infty = 0.1-15\ m/s$). The black dots in Fig. 6.1 marks the scenarios under consideration, with the corresponding Reynolds number shown in the y-axis.

Immediately after the droplet confronts the supercritical hydrogen flow, part of the heat transferred from the gas phase goes into the phase transition from liquid to vapor, while the remainder heats up of the droplet interior. In contrast to the subcritical droplet vaporization, no thermodynamic web-bulb state exists at the surface, and the entire gasification process becomes transient with a continuous increase of the surface temperature. In addition, because the critical mixing temperature of the oxygen/hydrogen system is slightly higher than the droplet initial temperature and decreases with increasing pressure (e.g., T_c = 116 K at p=400 atm), the thermodynamic criticality is reached at the droplet surface almost instantaneous upon its introduction to the flow. Once this occurs, the latent

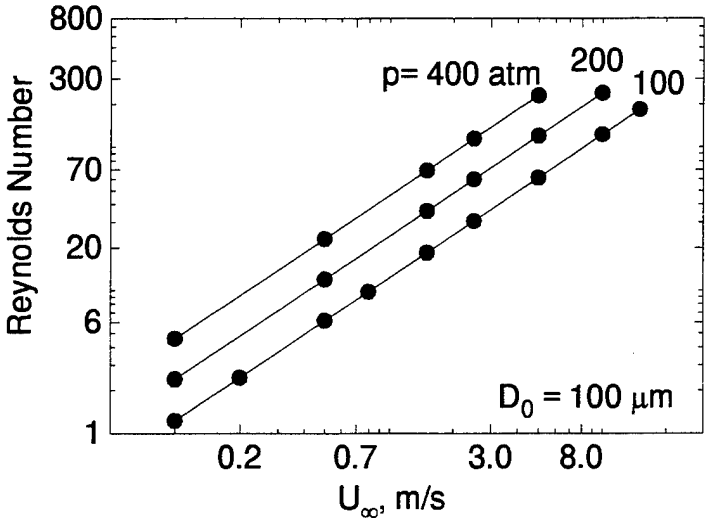

Figure 6.1. Droplet Reynolds Number as a Function of Freestream Velocity and Ambient Pressure; $D_0 = 100\mu m$, $T_\infty = 1000K$, $T_0 = 100K$.

heat of vaporization and surface tension of the droplet vanish, rendering essentially a continuous medium with no abrupt phase change as exists for a subcritical droplet. Although the interior region of the droplet remains at a liquid state with a subcritical temperature distribution, the fluid properties and their gradients vary continuously between the liquid core and the ambient gas. Since there is no distinct boundary existing between the liquid and vapor phases, for convenience of analysis, the surface of the droplet is deliberately defined as the surface at which the temperature attains the value of the critical mixing temperature.

Several snapshots of the flowfields under various conditions are presented in Figs. 6.2-6.4. Figure 6.2 shows six frames of isothermal and isoconcentration of oxygen at a convective velocity of 2.5 m/s and an ambient pressure of 100 atm. The free-stream Reynolds number, Re, is 30.56 based on the initial droplet

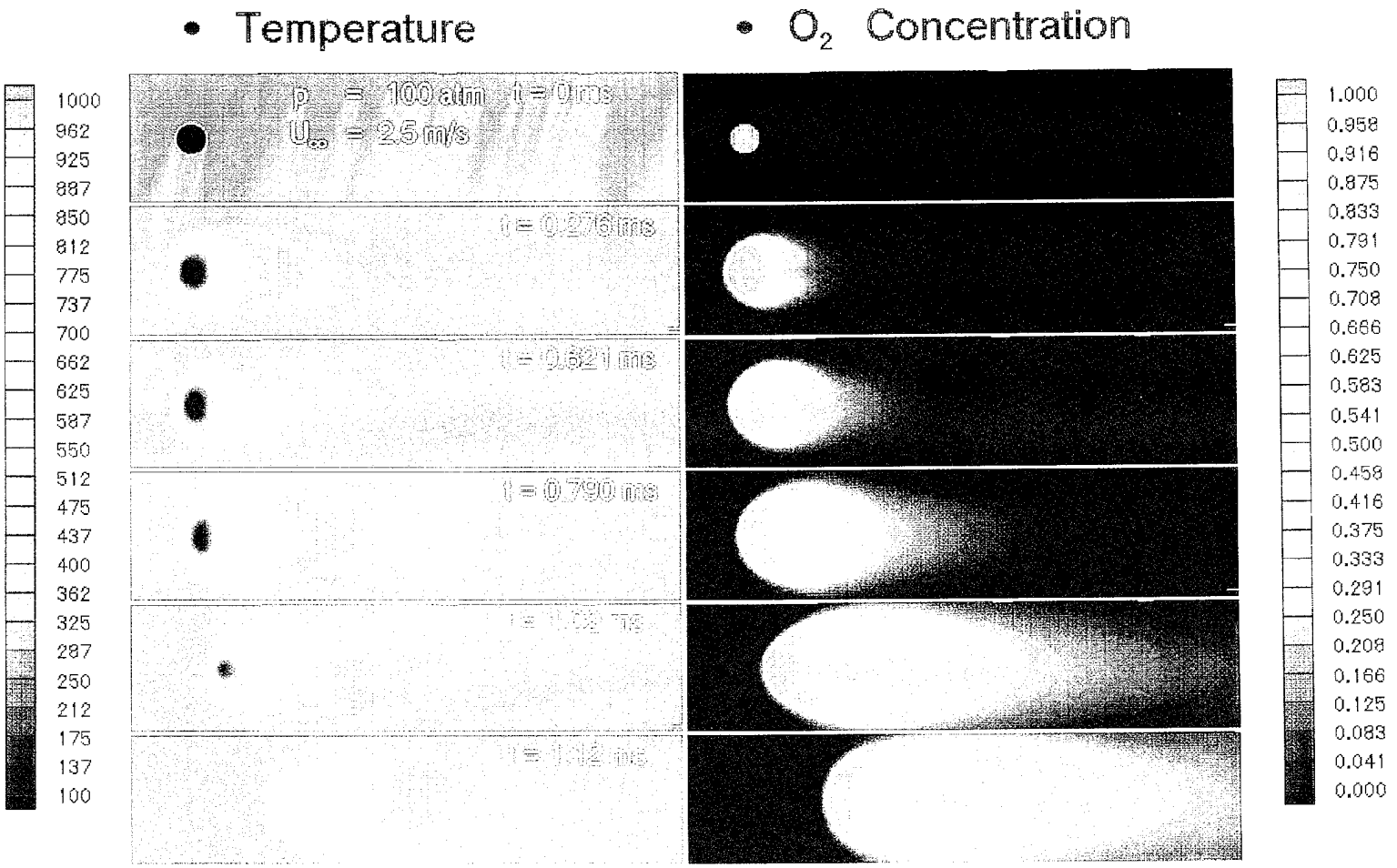

Figure 6.2. LOX Droplet Vaporization in Supercritical Hydrogen Flow; $p = 100$ atm, $U_\infty = 2.5\ m/s$.

diameter. The evolution of the temperature field exhibits features distinct from that of the concentration field due to the disparate time scales between mass and thermal diffusion processes (Lewis number $\neq 1$). The gasified oxygen is convected downstream from its edge. Meanwhile, the liquid core with large momentum inertia, moves slower compared with the gasified oxygen. The oxygen concentration contours reveal crescent shapes with the edge bent downstream. At t=1.08 ms, the subcritical liquid core disappears, leaving behind a puff of dense oxygen fluid which is convected further downstream with increasing velocity until it reaches the momentum equilibrium with the ambient hydrogen flow.

Figure 6.3 depicts a scenario identical to that of Fig. 6.2, but with an increased convective velocity of 15 m/s. The droplet evolution is substantially different, exhibiting several distinct modes such as deformation, viscous stripping, and secondary breakup. When the droplet is introduced into the strong convective flow (Re=183.36), fast vorticity generation resulting from the velocity difference between the liquid core and ambient flow promotes the formation of an attached eddy behind the droplet. This recirculating eddy induces a slightly higher pressure region in the attached wake, and exerts dynamic loading over the rear of the droplet. Meanwhile, the free stream also exert forces to the front surface. As a result, the droplet deforms and extends in the direction normal to the approaching flow. The flattened edge then turns to the streamwise direction, stretches downstream, and forms a skirt. The length of the skirt increases with time, and is controlled by the balance of viscous shear force between the dense oxygen and the ambient flow. At t=92 μs, an annulus of gaseous oxygen is detached from the growing skirt due to the local flow motion and volume dilatation resulting from penetration of the thermal wave into the skirt. The stripped oxygen from the edge

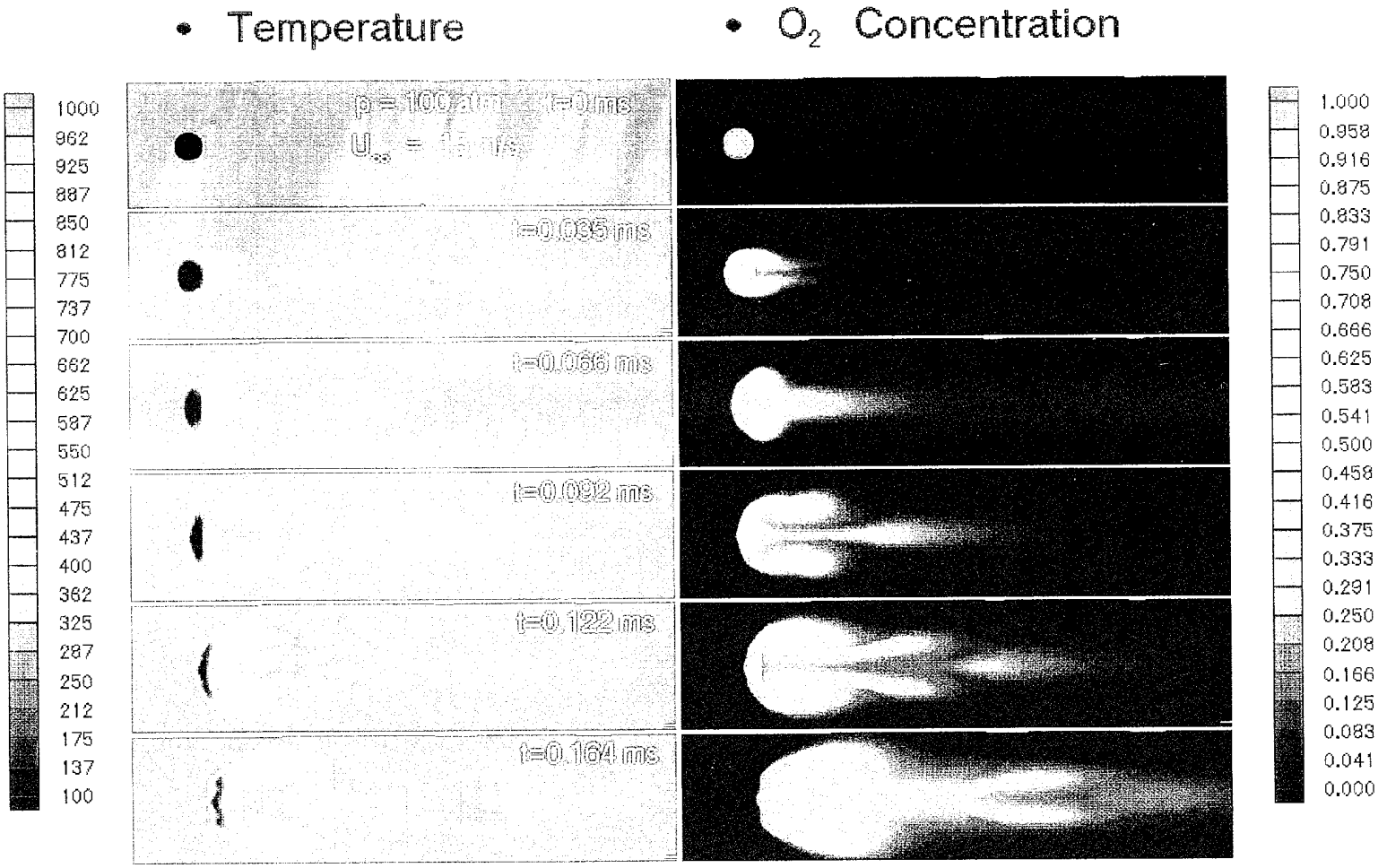

Figure 6.3. LOX Droplet Vaporization in Supercritical Hydrogen Flow; $p = 100$ atm, $U_\infty = 15\ m/s$.

of the droplet is entrained by the recirculating flow, forming an oxygen tongue. The dense oxygen influenced by the eddy recirculation may bend toward the rear of the droplet. This process carries the momentum from the eddy to the rear of the droplet and deforms it into a spherical cape. The associated cusp-like rim may catalyze the vorticity generation and further enhance the strength of the recirculating eddy. Since the viscosity of the droplet interior is greatly reduced by the energy transfer from the hot stream, the liquid oxygen eventually breaks up and forms a secondary ring around its core. Another significant phenomenon is the distribution of oxygen concentration. The gasified oxygen stripped from the edge of the droplet leaves the recirculating region and is swept downstream, forming a cylindrical tail.

Figure 6.4 presents a sequence of droplet evolution under the same flow conditions as in Fig. 6.2, but at an ambient pressure of 400 atm. The effect of pressure on droplet dynamics can be determined by a direct comparison between these two figures. Two distinct phenomena are observed. First, droplet deformation is enhanced by the increase in ambient pressure. Here, the corresponding Reynolds number is 3.75 times that of the 100 atm case. The hydrogen stream carries higher dynamic momentum and consequently exerts stronger force on the droplet, and as such promotes its deformation. Second, the lifetime of the droplet decreases with increasing ambient pressure mainly because that the higher Reynolds number at higher pressure increases the convective heat transfer rate and as a result accelerates evaporization.

Figures 6.5 and 6.6 show the evolution of droplet critical surfaces. The solid lines represent the instantaneous isotherms of the critical mixing temperature, while the dashed lines mark the surfaces of critical mixing composition. For a

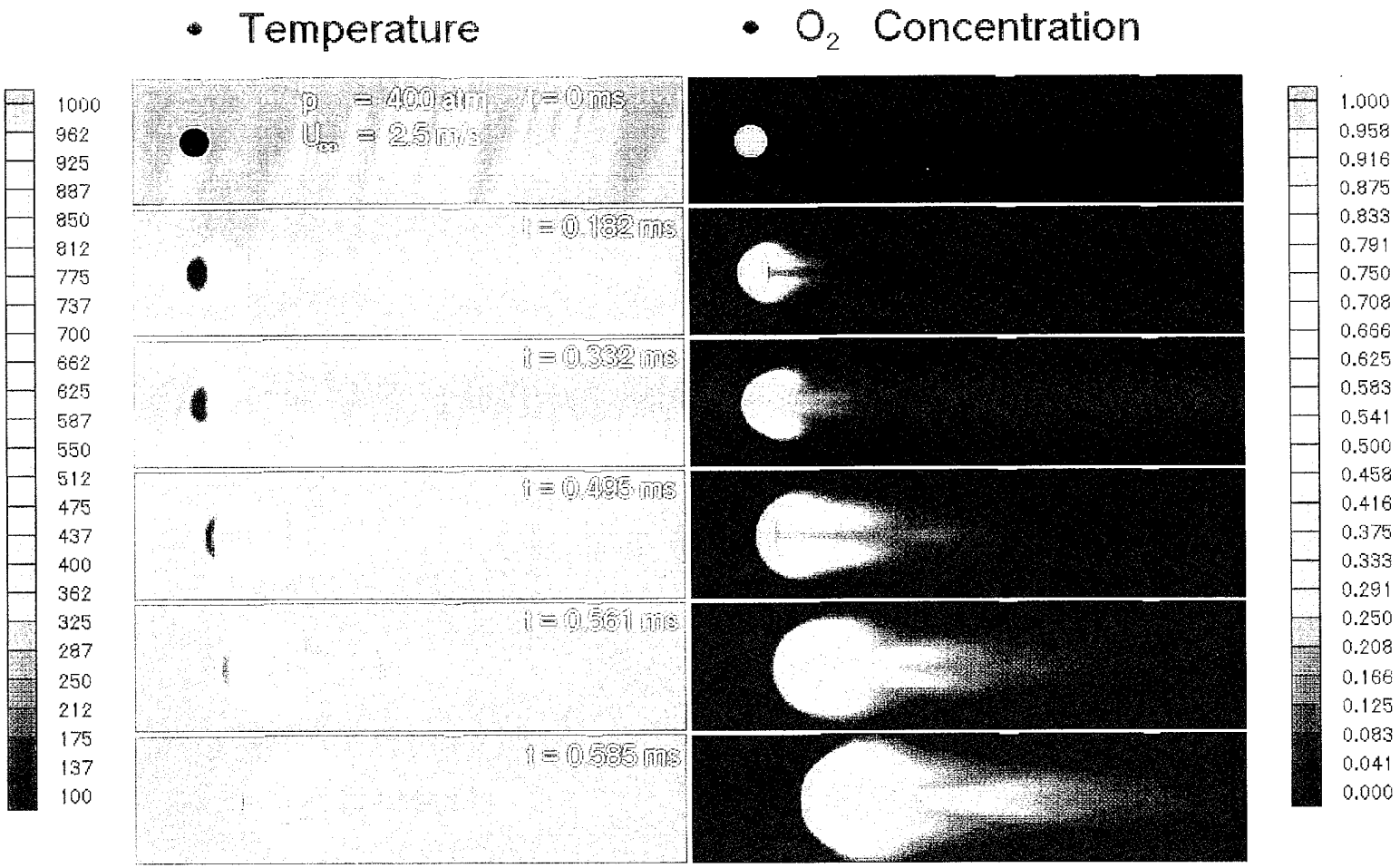

Figure 6.4. LOX Droplet Vaporization in Supercritical Hydrogen Flow; $p = 400$ atm, $U_\infty = 2.5\ m/s$.

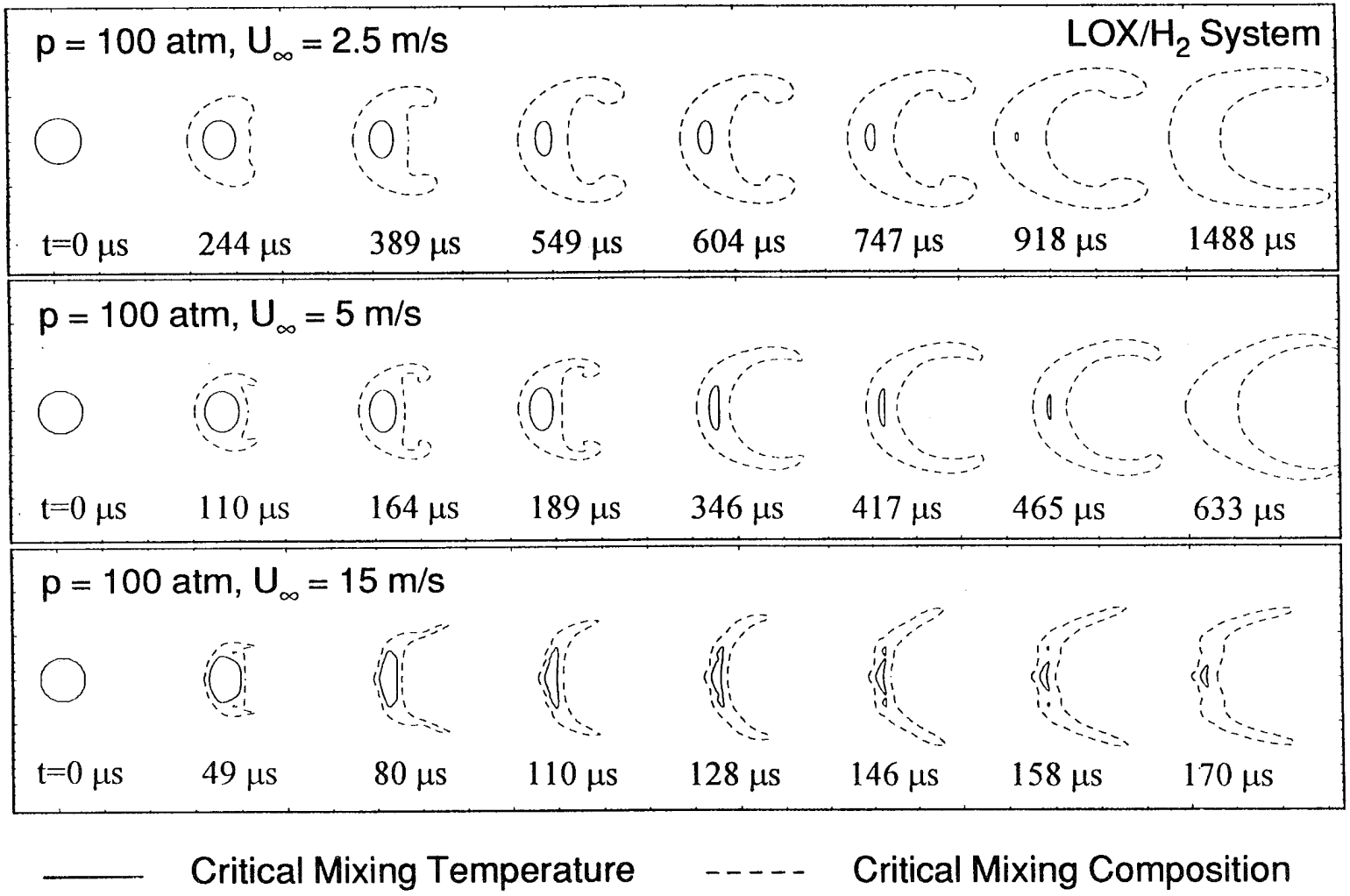

Figure 6.5. Effects of Ambient Velocity on Evolution of Droplet Critical Surfaces, LOX/H_2 System at $p = 100$ atm.

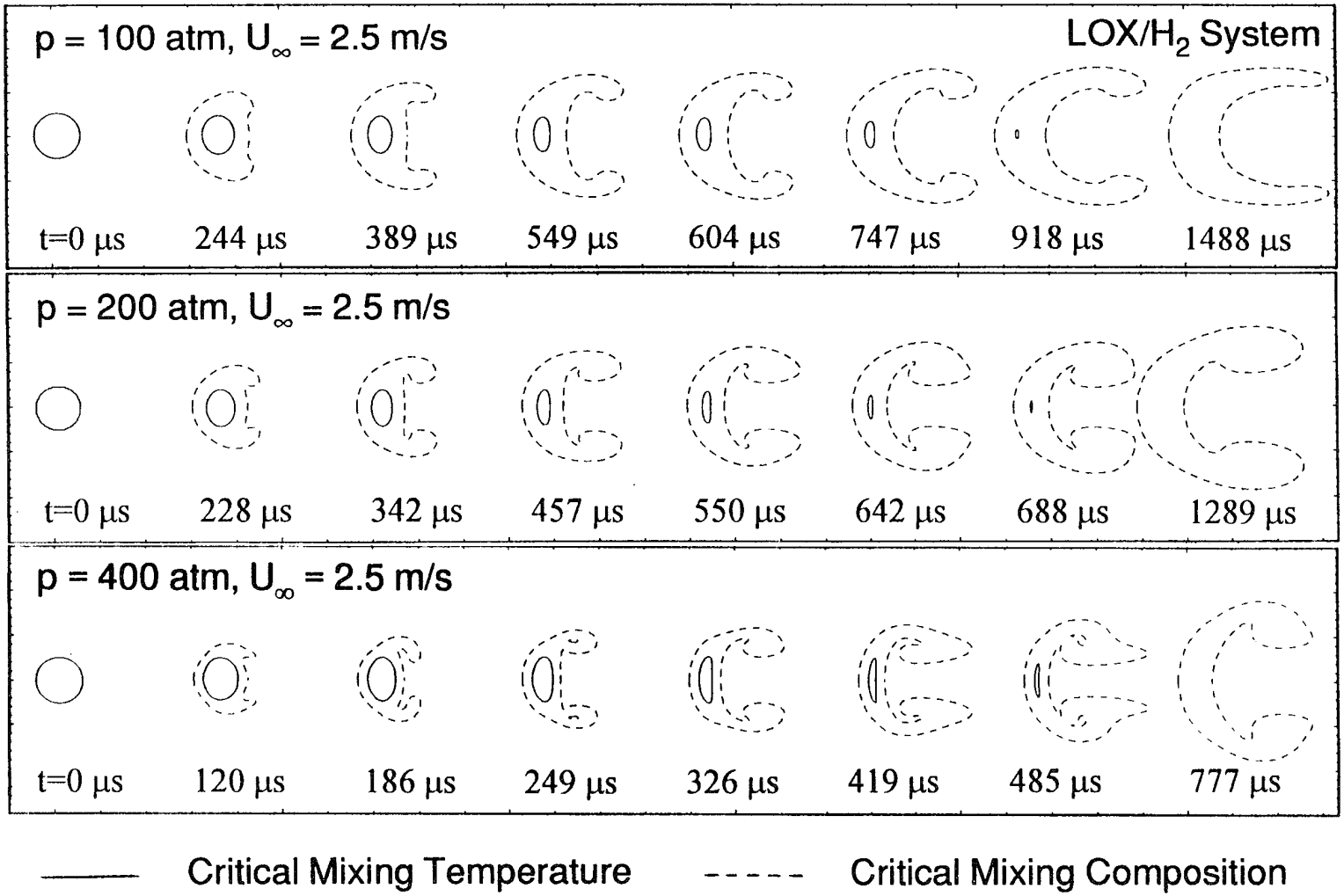

Figure 6.6. Effect of Ambient Pressure on Evolution of Droplet Critical Surfaces, LOX/H_2 System at $U_\infty = 2.5\ m/s$.

binary system of oxygen and hydrogen, the critical mixing temperature and composition can be obtained through a phase equilibrium analysis and are given in the Table 6.1. Because of the non-unity Lewis number (the ambient Lewis number is

TABLE 6.1
Critical Mixing Properties of O_2/H_2 System.

pressure (atm)	critical mixing temperature (k)	critical mixing composition
100	142.79	0.735
200	127.21	0.561
400	116.0	0.496

about 2.0 at 100 atm, and increases toward the droplet surface), the critical mixing isotherm propagates at a speed different from the surface of critical mixing composition. The critical isotherm disappears before the ambient hydrogen penetrates into the droplet center. Figure 6.5 depicts the effects of convective velocity on the evolution of droplet critical surface. The dynamic deformation of the droplet is substantially enhanced by increasing the momentum carried by the ambient flow. Figure 6.6 illustrates the effects of pressure on the evolution of the critical surfaces. Entrainment of gasified oxygen into the attached recirculation eddy seems to be augmented with increasing pressure. At high pressures, the motion of the skirt even reveals a periodic pattern. The gaseous oxygen entrapped by the recirculating flow tends to move with the strong eddy and may run forward into the rear of the droplet. This process drives the skirt to expand in the cross stream direction. Yet, the convective flow suppresses the expansion and forces the skirt to bend and

stretch downstream. As a result, more oxygen is trapped into the vortex eddy and therefore, starts another locomotion again.

Figures 6.7(a)-(d) show the streamline patterns at different flow conditions. Four distinct modes are observed, namely spherical, deformation, stripping, and breakup modes. Unlike low-pressure cases, no discernible flow recirculation takes place in the droplet interior, regardless of the Reynolds number. This may be attributed to the diminished surface tension at the droplet surface at supercritical conditions. In addition, the blowing effect induced by droplet vaporization increases the boundary layer thickness and obstructs the formation of a shear vortex in the droplet interior. The rapid change of the droplet shape precludes a stable shear stress field in the liquid core which in turn contributes to the absence of liquid recirculation.

For all the cases considered here, the convective stream is from the left to right, and a stagnation point where the velocity induced by gasification is cancelled by the approaching flow can be located on the left side of the droplet. Stagnation streamlines originated from the stagnation point divide the flowfield into two regions: internal and external flows. The spherical mode shown in Fig. 6.7(a) is typically observed when the droplet is introduced into an environment with a very low Reynolds number (Re=2.5). Although flow separation is encouraged by vaporization blowing, no recirculation eddy is found in the wake behind the droplet. This is because the vorticity generated from the shear flow is too weak to form any confined eddy. Further increase of the convective Reynolds number may cause the formation of recirculation eddy, as shown in Fig. 6.7(b). This plot is taken from the LOX droplet vaporization in a convective hydrogen flow with an initial Reynolds number of 18.34 (p=100 atm, U_∞ = 1.5 m/s). At t=0.61 ms, the droplet deforms

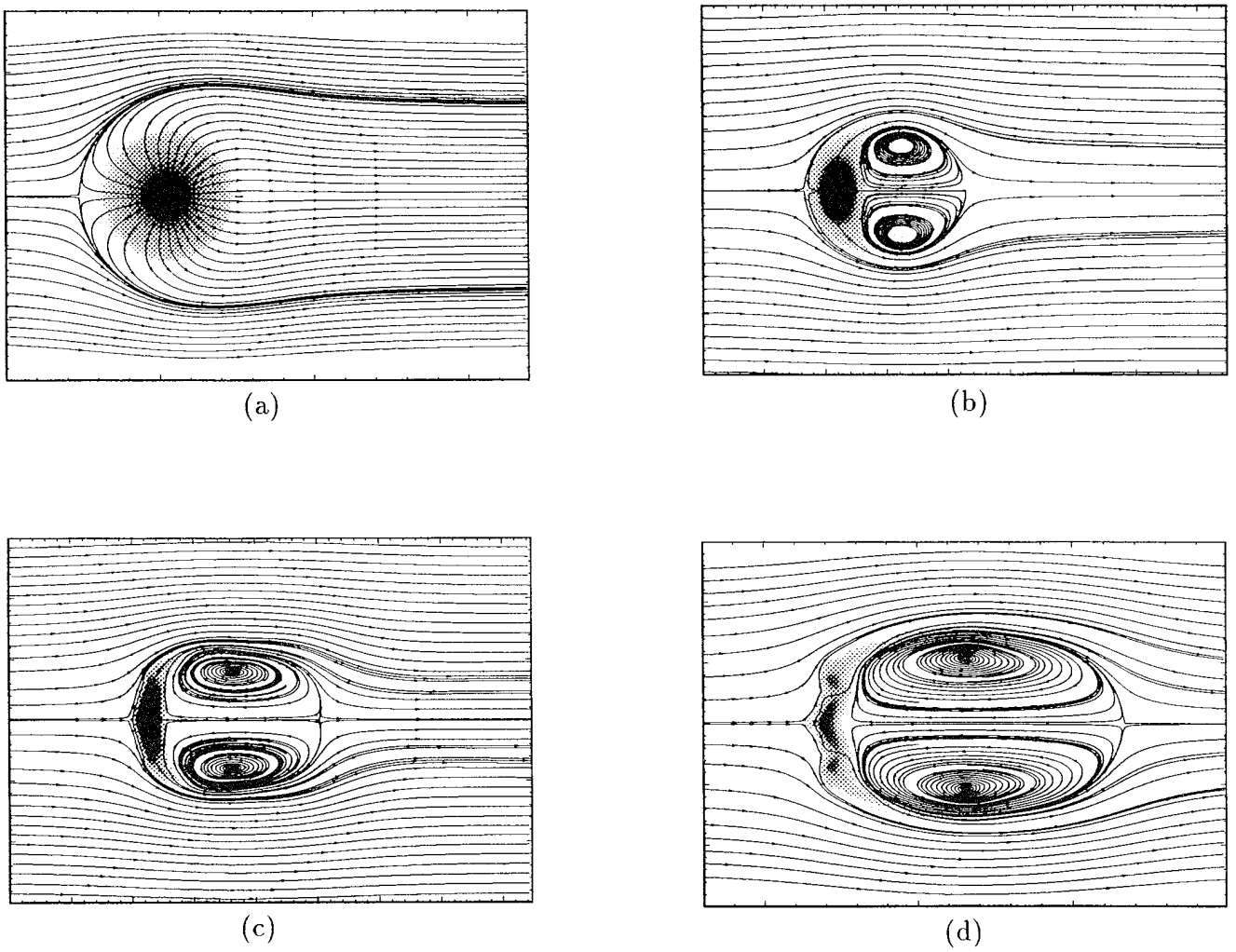

Figure 6.7. LOX Droplet Vaporization in Supercritical Hydrogen Flow at $p = 100$ atm: (a) Spherical Mode; $U_\infty = 0.2\ m/s$, t=0.61 ms. (b) Deformation Mode; $U_\infty = 1.5\ m/s$, t=0.61 ms. (c) Stripping Mode; $U_\infty = 5\ m/s$, t=0.17 ms. (d) Breakup Mode; $U_\infty = 15\ m/s$, t=0.17 ms.

into an olive shape with a spherical-like recirculation ring attached behind it. It is worth noting that the droplet deformation and surface blowing effect tend to elevate the threshold Reynolds number above which the recirculation eddy forms. This result is in close agreement with numerical solutions by other researchers (Dennis *et al.* 1971; LeClair 1970; LeClair *et al.* 1970; Masliyah 1970; Woo 1971). Figure 6.7(c) depicts the flow structure with viscous stripping, showing an oblate droplet with a deformed vortex ring. Lane (1951) has shown experimentally that, and Hinze (1955) has confirmed theoretically when a droplet is suddenly exposed to a high-velocity gas stream, the droplet aspect ratio increases with time. The flattened edge of the droplet enhances the strength of the recirculating eddies and as such increases the viscous shear stress dramatically. As a consequence, a thin sheet of dense oxygen may be stripped from the edge of the droplet and swept toward the outer boundary of the recirculation eddy. The secondary breakup mode is clearly illustrated in Fig. 6.7(d). At $Re = 183.36$, hydrogen penetrates through the liquid phase, breaking the droplet into two parts: the core disk and the surrounding ring. The flow structure also indicates that the volume of the attached vortex ring increases significantly.

Figure 6.8(a) presents the effects of free-stream velocity on the instantaneous variation of droplet mass at p=100 atm. The droplet residual mass is defined herein as the mass confined by the isothermal surface at the critical mixing temperature. In a slow convective stream ($U_\infty = 0.2$ m/s), heat conduction plays an important role during the vaporization process. The rapid droplet gasification in the early stage of its lifetime results from the large temperature gradient near the liquid/vapor interface. After the initial heatup period, the blowing from the droplet surface hinders the thermal wave propagation and results in a slower

(a)

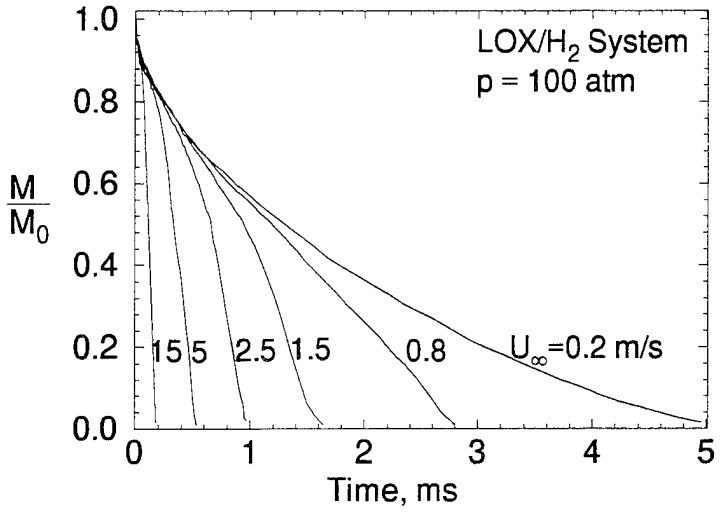

(b)

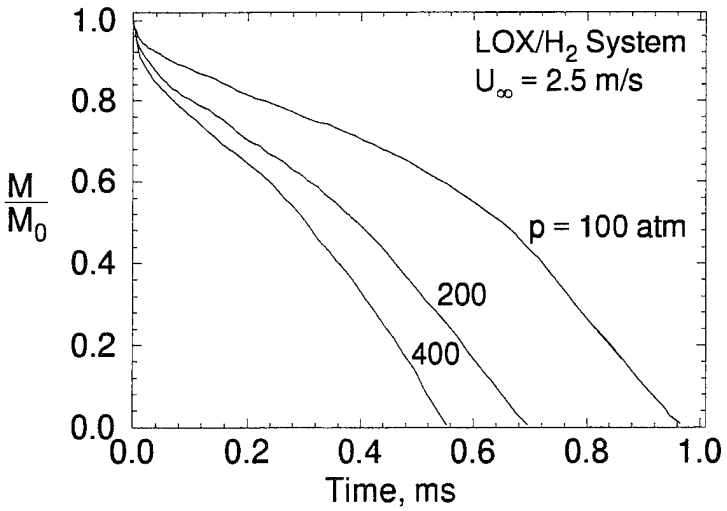

Figure 6.8. Time Variations of Droplet Residual Mass at Various Convective Velocities, LOX/H_2 System: (a) Effect of Convective Velocity at $p = 100$ atm. (b) Effect of Ambient Pressure at $U_\infty = 5.0\ m/s$.

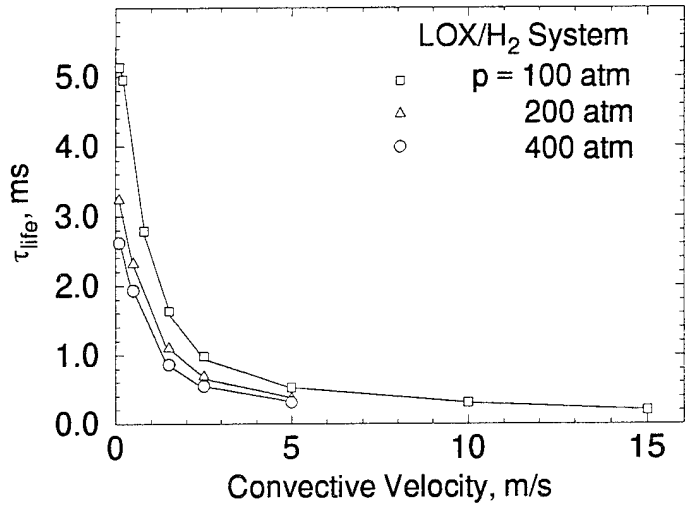

Figure 6.9. Dependences of Droplet Lifetime on Freestream Velocity and Ambient Pressure, LOX/H_2 System.

gasification rate. In a high Reynolds-number flow, increased free-stream velocity enhances the convective heat transfer, and as an outcome, the droplet vaporizes faster. Additionally, droplet deformation resulting from stronger dynamic loading from the approaching flow also encourages the vaporization processes. The effects of pressure on the droplet vaporization behavior are illustrated in Fig. 6.8(b). As the pressure increases, the convective heat transfer which depends strongly on the Reynolds number increases since the Reynolds number also increases with pressure. In addition, the critical mixing temperature used to define the droplet surface decreases with increasing pressure. As a result, the droplet gasification rate increases with the pressure.

Figure 6.9 presents the droplet lifetime as a function of ambient pressure and velocity. When a droplet is vaporizing in a quiescent environment (Re=0),

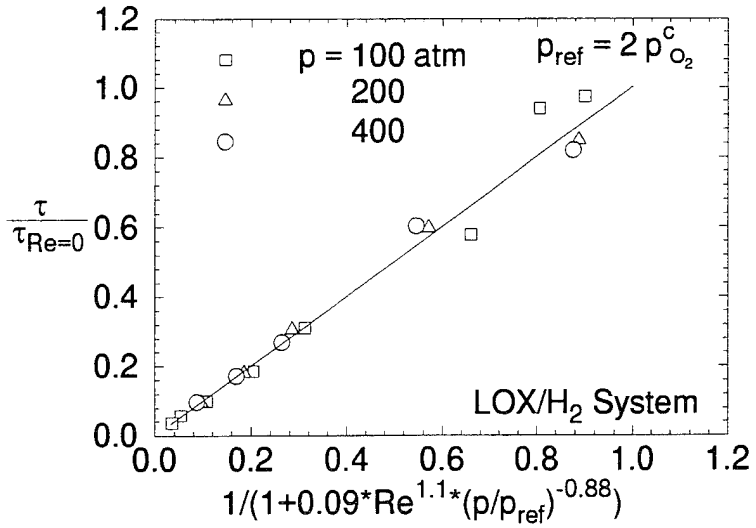

Figure 6.10. Correlation of Droplet Lifetime as a Function of Free-Stream Reynolds Number and Pressure.

the primary mode of energy transfer is heat conduction. The gasification rate is enhanced by convection, when a relative motion is present between the droplet and surrounding gases. A correlation is developed for the convective correction to the droplet lifetime as a function of ambient pressure and droplet Reynolds number. The correlation is given as

$$\frac{\tau_f}{\tau_{f,Re=0}} = \frac{1}{1 + 0.165634 Re^{1.1} (p_{r,O_2})^{-0.88}} \tag{6.1}$$

where Re is the Reynolds number based on the initial droplet diameter and p_{r,O_2} the reduced pressure in reference to the critical pressure of oxygen. The comparison of the correlation with the numerical data is shown in Fig. 6.10. Equation (6.1) bears a resemblance to the popular Ranz and Marshall correlation [59] for droplet heat transfer correction due to convective effect, which takes the form

$$\frac{\tau_f}{\tau_{f,Re=0}} \propto \frac{h_{Re=0}}{h} = \frac{1}{1+0.3Re^{1/2}Pr^{1/3}} \tag{6.2}$$

However, the Ranz and Marshall correlation is only applicable to low pressure flows, and shows a weaker Reynolds-number dependency.

Figures 6.11(a) and (b) show the location of droplet center of gravity at different free-stream velocities and pressures. Because there is no distinct vapor/liquid interface for a supercritical droplet, droplet motion is best characterized by the movement of the droplet center of gravity which can be located by dividing the first moment of the droplet mass by its total mass confined by the critical surface. Results show that droplet travel distance depends on both the drag force and the total lifetime over which the force acts on the droplet. For instance, at p=100 atm, even though the convective Reynolds number at $U_\infty = 5$ m/s is larger than that at $U_\infty = 1.5$ m/s, the droplet move further for the low velocity case, simply due to its longer lifetime.

The acceleration of the droplet center of gravity can be determined by taking the time derivative of droplet velocity, which is obtained by dividing the total momentum of liquid droplet by its mass. The results show that the droplet accelerates faster with increasing Reynolds number. At a given ambient velocity, momentum transfer between the ambient flow and droplet is also encouraged by increasing the ambient pressure. By applying a least-square curve fitting to these data, the droplet acceleration is expressed by a first order polynomial of time,

(a)

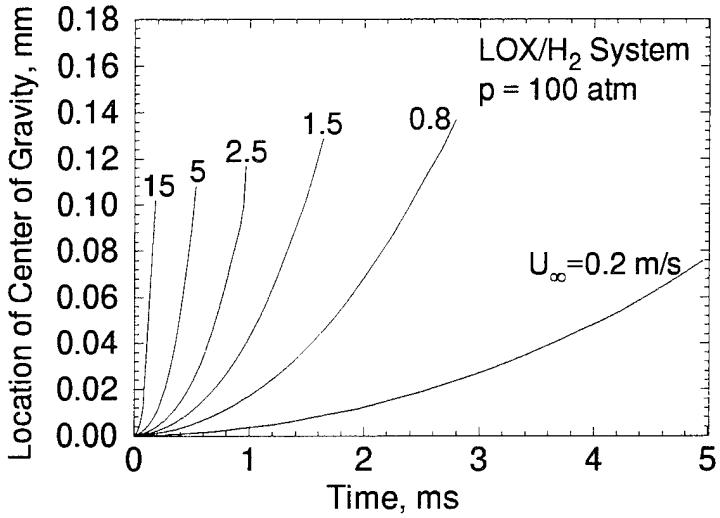

(b)

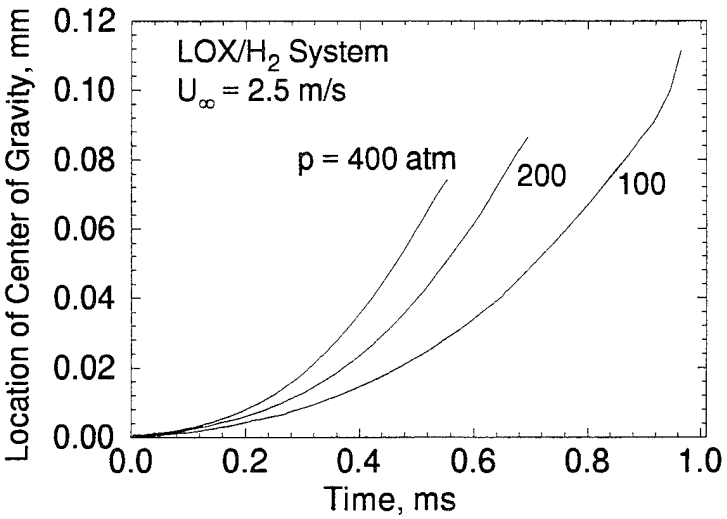

Figure 6.11. Time Variations of Location of Droplet Center of Gravity, LOX/H_2 System: (a) Effects of Convective Velocity at $p = 100$ atm. (b) Effects of Ambient Pressure at $U_\infty = 2.5\ m/s$.

$$a = \alpha_a + \beta_a t \tag{6.3}$$

where α_a and β_a are constants given in Figs. 6.12(a) and (b), being functions of initial Reynolds number.

The motion of a droplet is essentially a result of forces acting on its surface, including form drag, aerodynamic normal force, and viscous shear force. Since the droplet motion is tracked by its center of gravity, the drag force is best evaluated by the net momentum transfer to the droplet. Figure 6.13 presents the time histories of the total drag force, aerodynamic loading, and drag coefficient at $p = 100$ atm and $U_\infty = 5.0$. The drag coefficient is defined as the ratio of the drag force to the aerodynamic normal force.

$$\begin{aligned} C_D &= \frac{\text{net momentum transfer to the droplet}}{\text{aerodynamic loading}} \\ &= \frac{\frac{\partial}{\partial t}\left[\int_{drop} u dm\right] - U_{drop}\frac{\partial}{\partial t}\left[\int_{drop} dm\right]}{\frac{1}{2}\rho_\infty (U_\infty - U_{drop})^2 \pi R_c^2} \end{aligned} \tag{6.4}$$

where $(U_\infty - U_{drop})$ is the relative convective velocity and R_c is the radius of the mass-equivalent sphere with a uniform density distribution of its initial value. The drag force acting on the droplet first increases with time due to the large form drag arising from the high aspect ratio. It then drops to zero at the end of droplet lifetime.

Chen and Yuen[60] found that the drag coefficients of evaporating droplets are small compared to those of a non-vaporizing solid sphere at the same Reynolds numbers. Several researchers [61,62] numerically analyzed evaporating droplet motion by solving the Navier-Stokes equations and proposed the following correlation

(a)

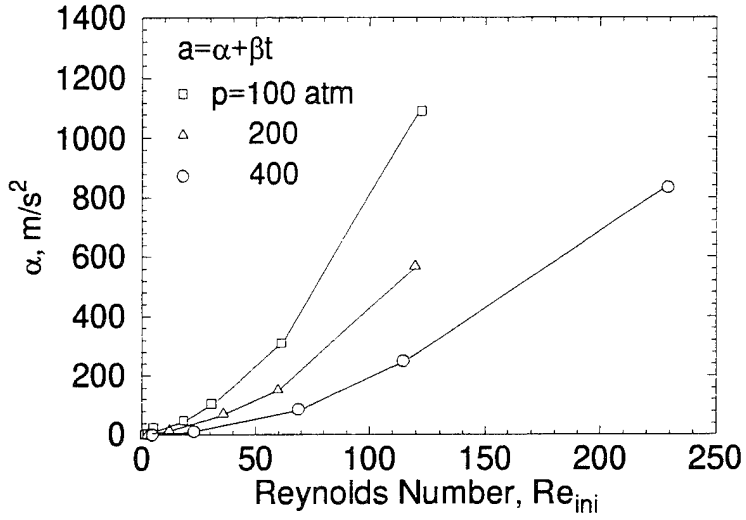

(b)

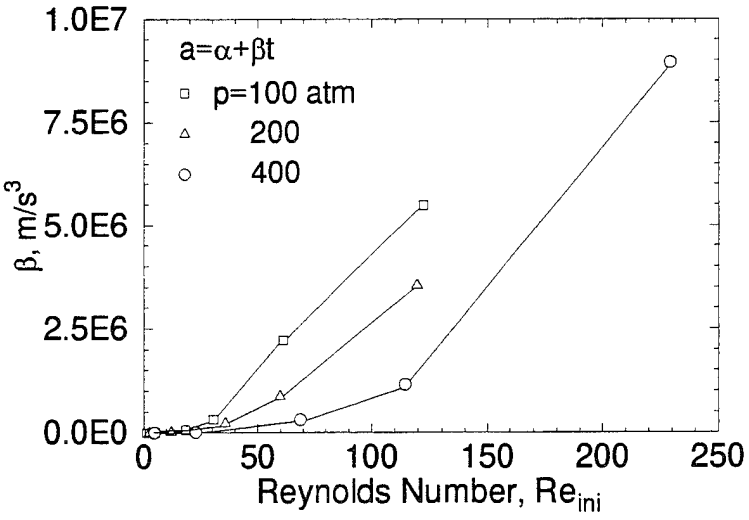

Figure 6.12. Dependences of Acceleration Coefficients on Free-stream Reynolds Number and Ambient Pressure, LOX/H_2 System: (a) Droplet Acceleration at $t = 0$ *sec.* (b) Droplet Acceleration Rate.

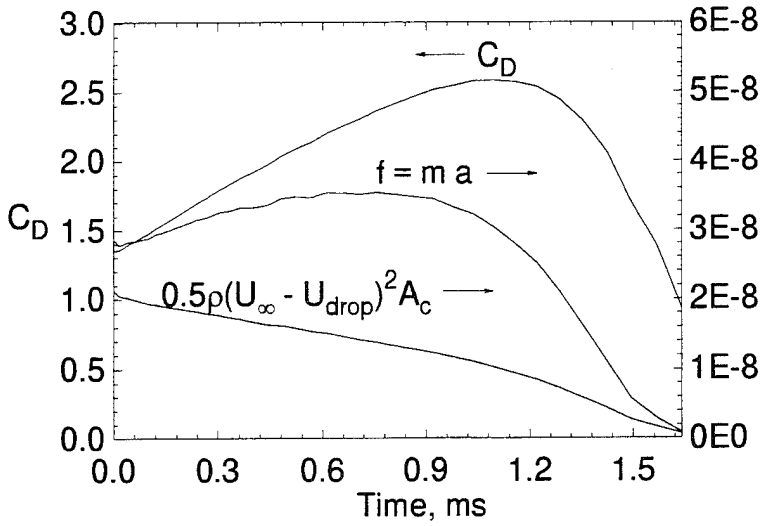

Figure 6.13. Time Variations of Droplet Total Drag Force, Aerodynamic Loading, and Drag Coefficient, LOX/H_2 System; p=100 atm, $U_\infty = 5\ m/s$.

$$C_D = \frac{C_D^0}{(1+B)^b} \tag{6.5}$$

where C_D^0 denotes the drag coefficient for non-vaporizing hard sphere, and b a constant which has a value of 0.2 for Renksitzbulut's model[61] and 0.32 for Chiang's model[62]. A transfer number B is adopted to account for the effect of blowing on momentum transfer to the droplet. For droplet vaporization at low to moderate pressures ($p_r \leq 0.5$), Spalding transfer number is widely used to characterize the vaporization rate.

$$B = \frac{C_p(T_\infty - T_s)}{\Delta h_v} \tag{6.6}$$

with C_p, T_∞, and T_s the constant-pressure specific heat, ambient temperature, and droplet surface temperature, respectively. The variable Δh_v represents the latent

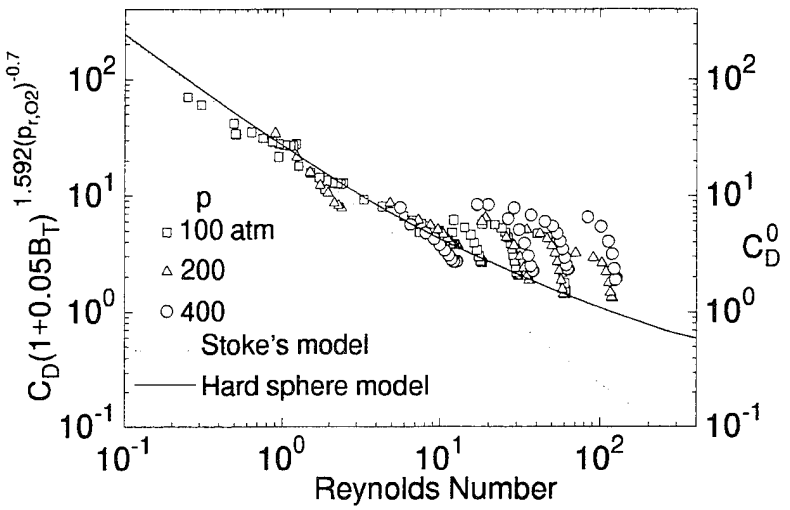

Figure 6.14. Effects of Ambient Reynolds Number, Pressure, and Vaporization Number on Droplet Drag Coefficient.

heat of vaporization which becomes zero at critical point, rendering an infinite value for the transfer number.

Data points used to obtain the correlation are sampled sequentially throughout the droplet lifetime for all the scenarios under consideration. To quantify the droplet vaporization rate, a transfer number B_T, which is suited for supercritical droplet vaporization, is proposed as

$$B_T = \left(\frac{T_\infty - T_s}{T_s - T_\ell}\right) \tag{6.7}$$

where the quantities T_s and T_ℓ denote the critical mixing temperature and the averaged temperature of droplet, respectively.

The drag coefficient can be correlated as a function of Reynolds number, ambient pressure, and vaporization transfer number, as shown in Fig. 6.14.

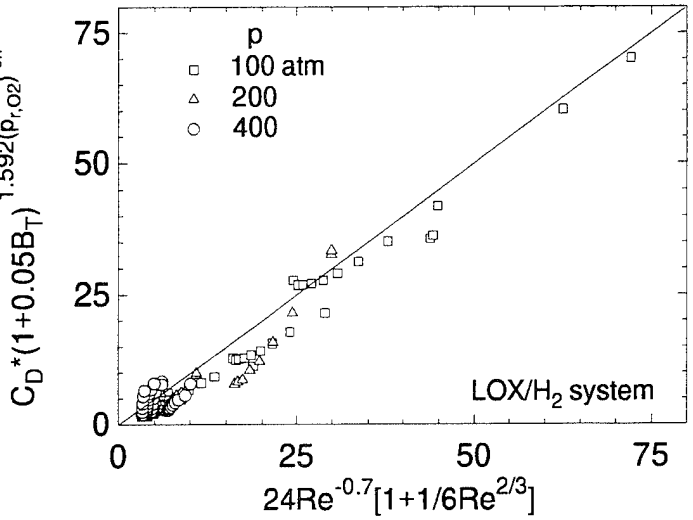

Figure 6.15. Correlation for Droplet Drag Coefficient.

$$C_D = \frac{C_D^0}{(1 + aB_T)^b} \tag{6.8}$$

with a and b selected to be 0.05 and 1.592 $(p_{r,O_2})^{-0.7}$. C_D^0 is the reference drag coefficient, for a hard sphere[63] and takes the form

$$C_D^0 = \frac{24}{Re}\left[1 + \frac{1}{6}Re^{\frac{2}{3}}\right] \tag{6.9}$$

The data points cluster along the drag curve in the low Reynolds-number region. However, deviation from the reference drag curve defined in Eq. (6.9) occurs at high Reynolds numbers (Re > 10). This is mainly attributed to the increase in form drag which results from increasing droplet aspect ratio due to strong convective stream. Although the shape aspect ratio serves as a good parameter to correlate the data, it is not practical to use in spray combustion analyses. A correction factor

$Re^{0.3}$ is incorporated into Eq.(6.9) to compensate this geometric factor. The final correlation shown in Fig. 6.15 is given as

$$C_D = \frac{C_D^0 Re^{0.3}}{(1 + aB_T)^{1.592\ (p_{r,O_2})^{-0.7}}} \tag{6.10}$$

with

$$C_D^0 = \frac{24}{Re}\left[1 + \frac{1}{6}Re^{\frac{2}{3}}\right] \tag{6.11}$$

CHAPTER 7

CONCLUING REMARKS

A systematic investigation has been conducted to study supercritical droplet gasification and combustion in both quiescent and forced-convective environments. The formulation is based on the time-dependent conservation equations of mass, momentum, energy, and species concentration in axisymmetric coordinates for both the droplet interior and ambient gases. Full account is taken of thermodynamic non-ideality and transport anomaly during the transition of droplet surface from the subcritical to supercritical state. In addition, a unified property evaluation scheme based on the Benedict-Webb-Rubin (BWR) equation of state and the extended corresponding-state principle is established to predict fluid thermophysical properties over the entire thermodynamic regime. The governing equations and associated boundary conditions are solved numerically using an implicit finite-volume scheme with a dual time-stepping integration technique.

A series of calculations have been carried out to study the behavior of both hydrocarbon and cryogenic liquid droplets over a wide range of thermodynamic state, including both sub- and super-critical conditions. The vaporization and combustion of an isolated liquid droplet in a quiescent environment are first investigated in Chapter 4. This configuration allows attention to be focused on the effects of ambient thermodynamic states on the interphase transport between droplet and the surroundings. Results show that the ambient gas pressure exerts significant control of droplet gasification and burning processes through its

influence on fluid transport, gas-liquid interfacial thermodynamics, and chemical reactions. The droplet gasification rate increases progressively with pressure. However, the data for the overall burnout time exhibits a considerable change of combustion mechanism at the critical pressure, mainly as a result of reduced mass diffusivity and latent heat of vaporization with increased pressure. The influence of droplet size on burnout characteristics is also noted.

The dynamic responses of droplet vaporization to the ambient flow oscillations are presented in Chapter 5. The analysis extends the work of droplet vaporization in quiescent environments and imposes a periodic pressure oscillation to ambient flow. The purpose is to assess the effect of flow oscillations on vaporization processes as a function of frequency and amplitude of the fluctuation, as well as the type of oscillation. Representative environmental conditions are simulated. Effects of ambient pressure and droplet heatup on the magnitude and phase angle of the vaporization response are quantified by means of numerical calculations. The amplitude of response function increases with increasing pressure owing to the susceptibility of enthalpy of vaporization to ambient flow oscillations at high pressures. On the other hand, the effect of mean pressure on the phase angle appears quite limited. The phase decreases from zero in the low-frequency limit to -180^o at high frequency, a phenomenon which can be easily explained by comparing various time scales associated with fluid transport and ambient disturbance. When the droplet surface approaches the thermodynamic critical mixing state, an abnormal amplification of vaporization rate caused by rapid variations of thermophysical properties is clearly observed.

Vaporization of cryogenic fluid droplets in supercritical streams is also investigated systematically. A series of calculations have been carried out to study

the gasification of an isolated oxygen (LOX) droplet in a hydrogen stream over a broad range of pressure (100-400 atm) and Reynolds number (20-300). Results indicate that forced convection exerts profound influence on droplet dynamics and gasification characteristics. The droplet lifetime decreases with increasing ambient Reynolds number, mainly due to increased momentum transfer in the boundary layer which intensifies the convective heat transfer into the droplet and consequently expedites the gasification process. Furthermore, as a result of stronger dynamic loading on the droplet, high Reynolds-number flows ($Re \geq 200$) tend to facilitate droplet breakup and shattering as a result of stronger dynamic loading on the droplet. In all the cases considered here, no discernible flow recirculation takes place in the droplet interior, regardless of the Reynolds number. This may be attributed to the diminished surface tension at supercritical conditions. The blowing effect induced by droplet vaporization increases the boundary layer thickness and obstructs the formation of a shear vortex in the droplet interior. The short local residence time of the droplet surface layer arising from the large droplet gasification rate at high pressure also contributes to this phenomenon.

Effects of ambient conditions (temperature, pressure, and convective velocity) on droplet gasification lifetime and drag coefficient are investigated parametrically. Data obtained are correlated as functions of ambient pressure, Reynolds number, and vaporization transfer number.

$$\frac{\tau_f}{\tau_{f,Re=0}} = \frac{1}{1 + 0.165634 Re^{1.1} (p_{r,O_2})^{-0.88}} \tag{7.1}$$

where Re and p_{r,O_2} refer to the Reynolds number based on the initial droplet diameter and the reduced pressure by the critical pressure of oxygen.

$$C_D = \frac{C_D^0 Re^{0.3}}{(1+aB_T)^{1.592\ (p_{r,O_2})^{-0.7}}} \tag{7.2}$$

with

$$C_D^0 = \frac{24}{Re}\left[1 + \frac{1}{6}Re^{\frac{2}{3}}\right] \tag{7.3}$$

Although the current research has provided significant information to understanding the underlying mechanisms involved in supercritical droplet vaporization and combustion, a systematic verification of these models is still lacking. Future work in supercritical droplet modelling should emphasize model validation against experimental data.

REFERENCES

[1] Huzel, D. K., and Huang, D. H., "Design of Liquid-Propellant Rocket Engines," NASA SP-125, 1971.

[2] Harrje, D. T., and Reardon, F. A., "Liquid Propellant Rocket Combustion Instability," NASA SP-194, 1972.

[3] Faeth, G. M., "Current Status of Droplet and Liquid Combustion," *Progress in Energy and Combustion Science*, Vol. 3, 1977, pp. 191–224.

[4] Spalding, D. B., "Theory of Particle Combustion at High Pressures," *ARS Journal*, Vol. 29, 1959, pp. 828–835.

[5] Rosner, D. E., "On Liquid Droplet Combustion at High Pressures," *AIAA Journal*, Vol. 5, 1967, pp. 163–166.

[6] Brzustowski, T. A., "Chemical and Physical Limits on Vapor-Phase Diffusion Flame of Droplets," *Canadian Journal of Chemical Engineering*, Vol. 43, 1965, pp. 30–36.

[7] Chervinsky, A., "Supercritical Burning of Liquid Droplets in a Stagnant Environment," *AIAA Journal*, Vol. 7, 1969, pp. 1815–1817.

[8] Polymeropoulos, C. E., and Peskin, R. L., "Combustion of Fuel Vapor in a Hot Stagnant Oxidizing Environment," *Combustion Science and Technology*, Vol. 5, 1972, pp. 165–174.

[9] Lee, H. S., Fernandez-Pello, A. C., and Oppenheim, A. K., "Stagnation Point Evaporation of a Liquid Fuel at Near and Supercritical Conditions," ASME Paper 86-WA/HT-15, 1986.

[10] Wieber, P. R., "Calculated Temperature Histories of Vaporizing Droplets to the Critical Point," *AIAA Journal*, Vol. 1, No. 12, 1963, pp. 2764–2770.

[11] Faeth, G. M., Dominicis, D. P., Tulpinsky, J. F., and Olson, D. R., "Supercritical Bipropellant Droplet Combustion," Proceedings of Twelfth Symposium

(International) on Combustion, The Combustion Institute, Pittsburgh, PA, 1969, pp. 9–18.

[12] Manrique, J. A., and Borman, G. L., "Calculations of Steady State Droplet Vaporization at High Ambient Pressures," *International Journal of Heat and Mass Transfer*, Vol. 12, 1969, pp. 1081–1094.

[13] Savery, W., and Borman, G. L., "Experiments on Droplet Vaporization at Supercritical Pressures," AIAA Paper No. 70-6, 1970.

[14] Lazar, R. S., and Faeth, G. M., "Bipropellant Droplet Combustion in the Vicinity of the Critical Point," Proceedings of Thirteenth Symposium (International) on Combustion, The Combustion Institute, Pittsburgh, PA, 1971, pp. 801–811.

[15] Canada, G. S., and Faeth, G. M., "Combustion of Liquid Fuels in a Flowing Combustion Gas Environment at High Pressures," Proceedings of Fifteenth Symposium (International) on Combustion, The Combustion Institute, Pittsburg, PA, 1975, pp. 418–428.

[16] Matlosz, R. L., Leipziger, S., and Tosda, T. P., "Investigation of Liquid Drop Evaporation in a High Temperature and High Pressure Environment," *International Journal of Heat and Mass Transfer*, Vol. 15, 1972, pp. 831–852.

[17] Rosner, D. E., and Chang, W. S., "Transient Evaporation and Combustion of a Fuel Droplet Near its Critical Temperature," *Combustion Science and Technology*, Vol. 7, 1973, pp. 145–158.

[18] Kadata, T., and Hiroyasu, H., "A Model for Multicomponent Droplet Vaporization at High Ambient Pressures," SAE Paper No. 85-0264, 1976.

[19] Curtis, E. W., and Farrel, P. V., "Droplet Vaporization in Supercritical Microgravity Environment," IAF Paper 87-384, 36th Congress of the International Astronautical Federation, 1987.

[20] Jin, J. D., and Borman, G. L., "A Model for Multicomponent Droplet Vaporization at High Ambient Pressures," SAE Paper No. 850264, 1985.

[21] Hsieh, K. C., Shuen, J. S., and Yang, V., "Droplet Vaporization in High-Pressure Environments, I: Near-Critical Conditions," *Combustion Science and Technology*, Vol. 76, 1991, pp. 111–132.

[22] Ely, J. F., and Hanley, H. J. M., "Predictions of Transport Properties. 1. Viscosity of Fluids and Mixtures," *Industrial and Engineering Chemistry Fundamentals*, Vol. 20, No. 4, 1981, pp. 323–332.

[23] Ely, J. F., and Hanley, H. J. M., "Predictions of Transport Properties. 2. Thermal Conductivity of Pure Fluids and Mixtures," *Industrial and Engineering Chemistry Fundamentals*, Vol. 22, No. 1, 1983, pp. 90–97.

[24] Valderrama, J. O., and Reyes, L. R., "Vapor-Liquid Equilibria of Hydrogen-Containing Mixtures," *Fluid Phase Equilibria*, Vol. 13, 1983, pp. 195–202.

[25] Leach, J. W., Chappelear, P. S., and Leland, T. W., "Use of Molecular Shape Factors in Vapor-Liquid Equilibrium Calculations with the Corresponding States Principle," *AIChE Journal*, Vol. 14, No. 4, 1968, pp. 568–576.

[26] Prausnitz, J. M., Lichtenthaler, R. N., and de Azevedo, E. G., *Molecular Thermodynamics of Fluid-Phase Equilibria* , Prentice-Hall, Englewood Cliffs, NJ, 1986.

[27] Graboski, M. S., and Daubert, T. E., "A Modified Soave Equation of State for Phase Equilibrium Calculation. 1. Hydrocarbon Systems," *Industrial and Engineering Chemistry Process Design and Development*, Vol. 17, No. 4, 1978, pp. 443–448.

[28] Cooper, H. W., and Goldfrank, J. C., "B-W-R Constants and New Correlations," *Hydrocarbon Processing and Petroleum Refiners*, Vol. 46, No. 12, 1967, pp. 141–146.

[29] Orye, R. V., "Prediction and Correlation of Phase Equilibria and Thermal Properties with the BWR Equation of State," *Industrial and Engineering Chemistry process design and development*, Vol. 8, 1969, pp. 579–588.

[30] Perry, R. H., Gree, D. W., and Maloney, J. O., *Perry's Chemical Engineers' Handbook* , McGrall-Hill, New York, 1984.

[31] Van Wylen, G. J., and Sonntag, R. E., *Fundamentals of Classical Thermodynamics*, 3rd edition , Wiley, 1986.

[32] Jacobsen, R. T., and Stewart, R. B. J., "Thermodynamic Properties of Nitrogen Including Liquid and Vapor Phases from 63K to 2000K with Pressure to 10,000 Bar," *Journal of Physical and Chemical Reference Data*, Vol. 2, No. 4, 1973, pp. 757–922.

[33] Ely, J. F., "An Enskog Correction for Size and Mass Difference Effects in Mixture Viscosity Prediction," *Journal of Research of the National Bureau of Standards*, Vol. 86, No. 6, 1981, pp. 597–604.

[34] Hanley, H. J. M., McCarty, R. D., and Cohen, E. G. D., "Analysis of the Transport Coefficients for Simple Dense Fluids: Application of the Modified Enskog Theory," *Physica*, Vol. 60, 1972, pp. 322–356.

[35] Reid, R. C., Prausnitz, J. M., and Poling, B. E., *The Properties of Gases and Liquids* , McGraw-Hill, Inc., 1988.

[36] Senger, J. V., *Critical Phenomena, Proceedings of Int. School of Physics* , Academic Press, New York, 1971.

[37] Senger, J. V., *Physical Chemistry*, Vol. 76, 1972, 234.

[38] Swinney, H. L., and Henry, D. L., "Dynamics of Fluids near the Critical Point: Decay Rate of Order-Parameter Fluctuations," *Physical Review*, Vol. A8, 1973, pp. 2586–2617.

[39] Roder, H. M., "The Thermal Conductivity of Oxygen," *Journal of Research, National Bureau of Standards*, Vol. 87, No. 4, 1982, pp. 279–310.

[40] Hirschfelder, J. O., Curtiss, C. F., and Bird, R. B., *Molecular Theory of Gas and Liquids* , John Wiley and Sons, New York, 1964.

[41] Takahashi, S., "Preparation of a Generalized Chart for the Diffusion Coefficients of Gases at High Pressures," *Journal of Chemical Engineering (Japan)*, Vol. 7, 1974, pp. 417–420.

[42] Wilke, C. R., and Lee, C. Y., "Estimation of Diffusion Coefficients for Gases and Vapors," *Industrial Engineering Chemistry*, Vol. 47, 1955, pp. 1253–1257.

[43] Perkins, L. R., and J., G. C., *Chemical Engineering Science*, Vol. 24, 1969, 1035.

[44] Hayduk, W., and Minhas, B. S., "Correlations for Prediction of Molecular Diffusivities in Liquid," *Canadian Journal of Chemical Engineering*, Vol. 60, 1982, pp. 295–299.

[45] Westbrook, C. K., and Dryer, F. L., "Simplified Reaction Mechanisms for the Oxidation of Hydrocarbon Fuels in Flames," *Combustion Science and Technology*, Vol. 27, 1981, pp. 31–43.

[46] Merkle, C. L., and Choi, Y. H., "Computation of Low-Speed Flow with Heat Addition," *AIAA Journal*, Vol. 25, No. 6, 1987, pp. 831–838.

[47] Shuen, J. S., Yang, V., and Hsiao, G. C., "Combustion of Liquid-Fuel Droplets in Supercritical Conditions," *Combustion and Flame*, Vol. 89, 1992, pp. 299–319.

[48] Jameson, A., Schmidt, W., and Turkel, E., "Numerical Solutions of the Euler Equation by Finite Volume Mechods Using Runge-Kutta Time-Stepping Schemes," AIAA Paper 81-1259, June 1981.

[49] Stone, H. L., "Iterative Solution of Implicit Approximations of Multidimensional Partial Differential Equations," *SIAM Journal on Numerical Analysis*, Vol. 5, No. 3, pp. 530–558.

[50] Sato, J., Tsue, M., Niwa, M., and Kono, M., "Effects of Natural Convection of High-Pressure Droplet Combustion," *Combustion and Flame*, Vol. 82, No. 2, 1990, pp. 142–150.

[51] Priem, R. J., and Guentert, D. C., "Combustion Instability Limits Determined by a Nonlinear Theory and a One-Dimensional Model," NASA TN-1409, 1962.

[52] Strahle, W. C., "Periodic Solutions to a Convective Droplet Burning Problem: The Stagnation Point," Proceedings of Tenth Symposium (International) on Combustion, The Combustion Institute, Pittsburgh, PA, 1965, pp. 1315–1325.

[53] Heidmann, M. F., and Wieber, P. R., "An Analysis of the Frequency Response Characteristics of Propellant Vaporization," NASA TN D-3749, 1966.

[54] Allison, C. B., and Faeth, G. M., "Open-Loop Response of a Burning Liquid Monopropellant," *AIAA Journal*, Vol. 13, October 1975, pp. 1287–1294.

[55] Tong, A. Y., and Sirignano, W. A., "Multicomponent Droplet Vaporization in a High Temperature Gas," *Combustion and Flame*, Vol. 66, 1986, pp. 221–235.

[56] Tong, A. Y., and Sirignano, W. A., "Multicomponent Transient Droplet Vaporization: Integral Equation Formulation and Approximate Solution," *Numerical Heat Transfer*, Vol. 10, 1986, pp. 253–278.

[57] Tong, A. Y., and Sirignano, W. A., "Vaporization Response of Fuel Droplet in Oscillatory Field," ASME National Heat Transfer Conference, Paper No. 87-HT-58, 1987.

[58] Williams, F. A., *Combustion Theory* , The Benjamin/Cummings Publishing Company, Inc., 1984.

[59] Ranz, W. E., and Marshall, W. R., "Evaporization from drops I and II," *Chemical Engineering Progress*, Vol. 48, 1952, pp. 141–173.

[60] Chen, L. W., and Yuen, M. C., "On Drag of Evaporating Liquid Droplets," *Combustion Science and Technology*, Vol. 14, 1976, pp. 147–154.

[61] Renksizbulut, M., Haywood, R.J., "Transient Droplet Evaporation with Variable Properties and Internal Circulation at Intermediate Reynolds Numbers," *International Journal of Multiphase Flow*, Vol. 14, No. 2, 1988, pp. 189–202.

[62] Chiang, C. H., Raju, M. S., and Sirignano, W. A., "Numerical Analysis of Convecting, Vaporizing Fuel Droplets with Variable Properties," *International Journal of Heat and Mass Transfer*, Vol. 35, 1992, pp. 1307–1324.

[63] Putnam, A., "Integratable Form of Droplet Drag Coefficient," *ARS Journal*, Vol. 31, 1961, pp. 1467–1468.

APPENDIX A

THERMODYNAMIC PROPERTIES

Prediction of thermodynamic properties plays a very important role in analyzing high-pressure droplet behavior. From a microscopic viewpoint, intermolecular mean free path tends to decrease with increasing pressure, and the molecular size effect as well as intermolecular force are enhanced and cause the gas and liquid behavior deviates away from the ideal fluid. Property evaluation in the near critical regime also brings up another challenge. When approaching the thermodynamic critical point, fluid exhibits anomalous behavior and are extremely sensitive to pressure and temperature. For a multicomponent system, change of properties due to mixing is even more complicated which ideal gas theory is not sufficient to predict thermodynamic non-idealities at high pressure.

In order to establish a unified evaluation scheme for real-gas properties, a pseudo-pure substance model of real fluid mixture is adopted. This approach treats a mixture as a pseudo-pure substance having its own set of properties. The difference between these properties and those at a reference state at the same temperature are represented by thermodynamic departure functions which are functions of p-V-T properties of the fluid. A basic prerequisite of this treatment is the concept and use of appropriate reference state. Generally, a thermodynamic state which reveals ideal gas behavior is preferred. For an ideal gas, the internal energy is a function of temperature only. This means that an ideal gas at a given temperature has certain definite thermodynamic properties (i.e., specific internal

energy, specific enthalpy, fugacity, etc.), regardless of the pressure. Under these conditions, the departure function becomes a high-density correction and can be evaluated accurately with the help of a precise equation of state. For an ideal mixture, change of properties on mixing is also negligibly small. Only using a simple mixing rule is required to accurately predict the mixture properties.

specific enthalpy

Since the SRK and BWR equations of state are both pressure explicit in nature, i.e., pressure is expressible as a function of temperature and density, the evaluation of thermodynamic properties starts with the definition of the Helmholtz function, a

$$\begin{aligned} a &= e - Ts \\ da &= de - Tds - sdT \end{aligned} \tag{A.1}$$

Since $e = h - p/\rho$, Eq. (A.1) yields

$$dh = da + Tds + sdT + d\left(\frac{p}{\rho}\right) \tag{A.2}$$

This can be further illustrated by integrating along an isotherm from a reference state (where the ideal gas behavior can be assumed) to the state of interest. With the ideal gas equation of state ($p = \rho\mathcal{R}T$), Eq. (A.2) becomes

$$h = h^0 + \Big[(a - a^0) + T(s - s^0) + \mathcal{R}T(Z - 1)\Big] \tag{A.3}$$

where Z is the compressibility and the superscript 0 represents the values at the ideal state. The second term of Eq. (A.3) is the density correction for the Helmholtz free energy. Since

$$dh = Tds + \frac{dp}{\rho} \tag{A.4}$$

Equation (A.2) can be written as

$$da = \left(\frac{p}{\rho^2}\right)d\rho - sdT \tag{A.5}$$

Along an isotherm, Eq. (A.5) is integrated from an ideal state with a density of ρ^0 to a thermodynamic state of interest with a density of ρ to form

$$a = a^0 + \int_{\rho^0}^{\rho}\left(\frac{p}{\rho^2}\right)d\rho \tag{A.6}$$

where ρ^0 is chosen with which the gas reveals the ideal gas behavior at 1 atm. Following Maxwell's equation, the entropy can be expressed as the first derivative of the Helmholtz free energy with respect to temperature at a constant density

$$s = -\left(\frac{\partial a}{\partial T}\right)_{\rho} \tag{A.7}$$

Substituting (A.6) into (A.7) to obtain the departure function of entropy as

$$\begin{aligned} s &= -\left(\frac{\partial a^0}{\partial T}\right)_{\rho} - \int_{\rho^0}^{\rho}\frac{1}{\rho^2}\left(\frac{\partial p}{\partial T}\right)_{\rho}d\rho \\ &= s^0 - \int_{\rho^0}^{\rho}\frac{1}{\rho^2}\left(\frac{\partial p}{\partial T}\right)_{\rho}d\rho \end{aligned} \tag{A.8}$$

Enthalpy of a mixture can be obtained by substituting Eqs. (A.6) and (A.8) into (A.3) to get

$$h = h^0 + \int_{\rho^0}^{\rho}\frac{1}{\rho^2}\left[p - T\left(\frac{\partial p}{\partial T}\right)_{\rho}\right]d\rho + \mathcal{R}T(Z-1) \tag{A.9}$$

where h^0 is the ideal-gas enthalpy which is a function of temperature only. If the constant-pressure specific heats of all components are given, the specific enthalpy of an ideal mixture can be expressed as

$$h^0 = \sum_{i=1}^{N} Y_i \Big[h^0_{ref,i} + \int_{T_{ref}}^{T} C^0_{p,i} dT \Big] \tag{A.10}$$

where $h^0_{ref,i}$ and Y_i are the enthalpy of formation at a reference temperature of T_{ref} and the mass fraction of i component, respectively.

specific internal energy

Based on the definition of specific enthalpy,

$$h = e + \frac{p}{\rho} \tag{A.11}$$

or

$$dh = de + d\Big(\frac{p}{\rho}\Big) \tag{A.12}$$

the specific internal energy can be obtained by integrating along an isotherm from a reference state where the ideal gas behavior can be assumed to the state of interest.

$$e = e^0 + (h - h^0) - \mathcal{R}T(Z - 1) \tag{A.13}$$

Substituting Eqs. (A.9) and (A.15) into (A.13) to obtain

$$e = e^0 + \int_{\rho^0}^{\rho} \frac{1}{\rho^2} \Big[p - T\Big(\frac{\partial p}{\partial T}\Big)_{\rho} \Big] d\rho \tag{A.14}$$

The first term on the right hand side is the specific internal energy of an ideal gas which is a function of temperature only, and can be expressed as

$$\begin{aligned} e^0 &= \sum_{i=1}^{N} Y_i \Big[e^0_{ref,i} + \int_{T_{ref}}^{T} C^0_{v,i} dT \Big] \\ &= \sum_{i=1}^{N} Y_i \Big[e^0_{ref,i} + \int_{T_{ref}}^{T} (C^0_{p,i} - \mathcal{R}_u) dT \Big] \end{aligned} \tag{A.15}$$

specific heat

Two parallel expressions can be found for the change of entropy. First, if entropy is treated as a function of temperature and pressure

$$s = s(T, p)$$

Therefore,

$$ds = \left(\frac{\partial s}{\partial T}\right)_p dT + \left(\frac{\partial s}{\partial p}\right)_T dp \tag{A.16}$$

From Maxwell's equations,

$$C_p = \left(\frac{\partial h}{\partial T}\right)_p = T\left(\frac{\partial s}{\partial T}\right)_p \tag{A.17}$$

$$\frac{1}{\rho^2}\left(\frac{\partial \rho}{\partial T}\right)_p = \left(\frac{\partial s}{\partial p}\right)_T \tag{A.18}$$

Substituting Eqs. (A.17) and (A.18) into (A.16) to get

$$ds = C_p \frac{dT}{T} + \frac{1}{\rho^2}\left(\frac{\partial \rho}{\partial T}\right)_p dp \tag{A.19}$$

Secondly, entropy can also be expressed as a function of temperature and density as

$$s = s(T, \rho)$$

Therefore,

$$ds = \left(\frac{\partial s}{\partial T}\right)_\rho dT + \left(\frac{\partial s}{\partial \rho}\right)_T d\rho \tag{A.20}$$

Similarly, from Maxwell's equations,

$$C_v = \left(\frac{\partial e}{\partial T}\right)_\rho = T\left(\frac{\partial s}{\partial T}\right)_\rho$$

$$\left(\frac{\partial p}{\partial T}\right)_\rho = -\rho^2\left(\frac{\partial s}{\partial \rho}\right)_T$$

Equation (A.20) can be expressed as

$$ds = C_v \frac{dT}{T} - \frac{1}{\rho^2}\left(\frac{\partial p}{\partial T}\right)_\rho d\rho \tag{A.21}$$

Combine Eq. (A.19) and (A.21) to obtain

$$\begin{aligned} C_p \frac{dT}{T} \quad + \quad & \frac{1}{\rho^2}\left(\frac{\partial \rho}{\partial T}\right)_p dp = C_v \frac{dT}{T} - \frac{1}{\rho^2}\left(\frac{\partial p}{\partial T}\right)_\rho d\rho \\ dT \quad = \quad & -\left(\frac{T}{\rho^2}\right)\frac{\left(\frac{\partial p}{\partial T}\right)_\rho}{C_p - C_v} d\rho - \left(\frac{T}{\rho^2}\right)\frac{\left(\frac{\partial \rho}{\partial T}\right)_p}{C_p - C_v} dp \end{aligned} \tag{A.22}$$

Temperature can be expressed as a function of pressure and specific volume

$$T = f(p, \rho)$$

Therefore,

$$dT = \left(\frac{\partial T}{\partial \rho}\right)_p d\rho + \left(\frac{\partial T}{\partial p}\right)_\rho dp \tag{A.23}$$

Compare (A.22) with (A.23) to obtain

$$\begin{aligned} \left(\frac{\partial T}{\partial \rho}\right)_p \quad &= \quad -\left(\frac{T}{\rho^2}\right)\frac{\left(\frac{\partial p}{\partial T}\right)_\rho}{C_p - C_v} \\ \left(\frac{\partial T}{\partial p}\right)_\rho \quad &= \quad -\left(\frac{T}{\rho^2}\right)\frac{\left(\frac{\partial \rho}{\partial T}\right)_p}{C_p - C_v} \end{aligned}$$

When these equations are solved for $C_p - C_v$, they yield the same result as

$$C_p - C_v = -\left(\frac{T}{\rho^2}\right)\left(\frac{\partial p}{\partial T}\right)_\rho \Big/ \left(\frac{\partial T}{\partial \rho}\right)_p \tag{A.24}$$

But

$$\left(\frac{\partial T}{\partial \rho}\right)_p = -\left(\frac{\partial T}{\partial p}\right)_\rho \left(\frac{\partial p}{\partial \rho}\right)_T \tag{A.25}$$

Therefore,

$$C_p = C_v - \left(\frac{T}{\rho^2}\right)\left(\frac{\partial p}{\partial T}\right)_\rho^2 \Big/ \left(\frac{\partial p}{\partial \rho}\right)_T \tag{A.26}$$

For a pressure-explicit equation of state, the specific heat at constant volume can be derived using

$$\begin{aligned} C_v &= \left(\frac{\partial e}{\partial T}\right)_\rho \\ &= \left(\frac{\partial e^0}{\partial T}\right)_\rho + \left\{\frac{\partial}{\partial T}\int_{\rho^0}^{\rho}\frac{1}{\rho^2}\left[p - T\left(\frac{\partial p}{\partial T}\right)_\rho\right]d\rho\right\}_\rho \\ &= C_p^0 - \mathcal{R} - \int_{\rho^0}^{\rho}\frac{T}{\rho^2}\left(\frac{\partial^2 p}{\partial T^2}\right)_\rho d\rho \end{aligned} \tag{A.27}$$

Therefore, the constant pressure specific heat can be obtained by substituting Eq. A.27) into (A.26)

$$C_p = C_p^0 - \mathcal{R} - \int_{\rho^0}^{\rho}\frac{T}{\rho^2}\left(\frac{\partial^2 p}{\partial T^2}\right)_\rho d\rho - \left(\frac{T}{\rho^2}\right)\frac{\left(\frac{\partial p}{\partial T}\right)_\rho^2}{\left(\frac{\partial p}{\partial \rho}\right)_T} \tag{A.28}$$

fugacity

Fugacity is particularly important when considering mixtures at equilibrium. Fugacity f is defined herein as[30]

$$\mathcal{R}T d(\ln \boldsymbol{f})_T = dg_T \tag{A.29}$$

with the requirement that

$$\lim_{p\to 0}\left(\frac{\boldsymbol{f}}{p}\right) = 1$$

In a mixture, the fugacity of component i can be expressed in a similar form.

$$\mathcal{R}T d(\ln \boldsymbol{f}_i)_T = (dg_i)_T \qquad i = 1...N \tag{A.30}$$

along with

$$\lim_{p\to 0}\left(\frac{\boldsymbol{f}_i}{X_i p}\right) = 1 \qquad i = 1...N \tag{A.31}$$

The fugacity approaches the partial pressure of component i in an ideal gas mixture as pressure approaches zero. Integrate Eq. (A.30) at constant temperature from the reference state to state of interest to obtain

$$\int_{f_i{}^0 \to X_i p}^{f_i} \mathcal{R}T\, d(\ln \boldsymbol{f}_i)_T = \int_{g_i^0}^{g_i} (dg_i)_T \tag{A.32}$$

therefore

$$\begin{aligned}
\ln\left(\frac{\boldsymbol{f}_i}{X_i p}\right) &= \frac{1}{\mathcal{R}T}(g_i - g_i^0) \\
&= \frac{1}{\mathcal{R}T}(\boldsymbol{\mu}_i - \boldsymbol{\mu}_i^0) \\
&= \frac{1}{\mathcal{R}T}\left[\left(\frac{\partial a}{\partial n_i}\right)_{T,p,n_{j\neq i},\ldots} - \left(\frac{\partial a^0}{\partial n_i}\right)_{T,p,n_{j\neq i},\ldots}\right]
\end{aligned}$$

where $\boldsymbol{\mu}_i$ is called the chemical potential. Therefore, the fugacity can be evaluated via

$$\ln\left(\frac{\boldsymbol{f}_i}{X_i p}\right) = \frac{1}{\mathcal{R}T}\frac{\partial}{\partial n_i}\left[\int_{\rho^0}^{\rho} \frac{p}{\rho^2} d\rho\right]_{T,\rho,n_{j\neq i},\ldots} \tag{A.33}$$

APPENDIX B

ENTHALPY OF VAPORIZATION

$$\begin{aligned}\frac{\partial}{\partial T}\left[\ln\left(\frac{f_i}{pX_i}\right)\right] &= \frac{b_i}{b}\frac{\partial Z}{\partial T} - \frac{1}{Z-B}\left(\frac{\partial Z}{\partial T} - \frac{\partial B}{\partial T}\right) \\ &- Q_2Q_3\frac{B\frac{\partial A}{\partial T} - A\frac{\partial B}{\partial T}}{B^2} - Q_1Q_3\frac{\partial Q_2}{\partial T} \\ &- Q_1Q_2\frac{Z}{Z+B}\frac{\left(\frac{\partial Z}{\partial T} + \frac{\partial B}{\partial T}\right)Z - (Z+B)\frac{\partial Z}{\partial T}}{Z^2} \end{aligned} \tag{B.1}$$

where

$$\begin{aligned} Q_1 &= \frac{A}{B} \\ Q_2 &= \left[\frac{2\sum_{j=1}^{N} X_j\alpha_{ij}a_{ij}}{\alpha a} - \frac{b_i}{b}\right] \\ Q_3 &= \ln\left(1+\frac{B}{Z}\right) \end{aligned} \tag{B.2}$$

and

$$\begin{aligned} \frac{\partial Z}{\partial T} &= \frac{\frac{\partial A}{\partial T}(-Z+B) + \frac{\partial B}{\partial T}(Z+2BZ+A)}{3Z^2 - 2Z + A - B - B^2} \\ \frac{\partial A}{\partial T} &= \frac{-2\alpha a p + pT\frac{\partial(\alpha a)}{\partial T}}{\mathcal{R}_u^2 T^3} \\ \frac{\partial B}{\partial T} &= \frac{-bp}{\mathcal{R}_u T^2} \\ \frac{\partial(\alpha a)}{\partial T} &= \sum_{i=1}^{N}\sum_{j=1}^{N} x_i x_j (1-k_{ij})\sqrt{a_i a_j}\frac{\alpha_i\frac{\partial \alpha_j}{\partial T} + \alpha_j\frac{\partial \alpha_i}{\partial T}}{2\sqrt{\alpha_i\alpha_j}} \\ \frac{\partial \alpha_i}{\partial T} &= 2\left[1 + S_i(1-\sqrt{T_r})\right]\left[\frac{-S_i}{2T_c\sqrt{T_r}}\right] \end{aligned}$$

$$
\begin{aligned}
\frac{\partial Q_2}{\partial T} &= \frac{\partial}{\partial T}\left[\frac{2\sum_{j=1}^{N} x_j\alpha_{ij}a_{ij}}{\alpha a} - \frac{b_i}{b}\right] \\
&= \frac{\partial}{\partial T}\left[\frac{2\sum_{j=1}^{N} x_j(1-k_{ij})\sqrt{\alpha_i a_i \alpha_j a_j}}{\alpha a}\right] \\
&= \frac{\left[2\sum_{j=1}^{N} x_j(1-k_{ij})\sqrt{a_i a_j}\right]}{\alpha a}\frac{\alpha_i\frac{\partial \alpha_j}{\partial T} + \alpha_j\frac{\partial \alpha_i}{\partial T}}{2\sqrt{\alpha_i\alpha_j}} \\
&- \frac{2\sum_{j=1}^{N} x_j\alpha_{ij}a_{ij}}{(\alpha a)^2}\frac{\partial(\alpha a)}{\partial T}
\end{aligned}
\tag{B.3}
$$

where

$$
\begin{aligned}
a_i &= 0.42747\frac{\mathcal{R}_u^2 T_{c_i}^2}{p_{c_i}} \\
b_i &= 0.08664\frac{\mathcal{R}_u T_{c_i}}{p_{c_i}} \\
\alpha_i &= [1 + S_i(1-\sqrt{T_{r_i}})]^2 \\
S_i &= 0.48508 + 1.55171\omega_i - 0.15613\omega_i^2 \\
\alpha a &= \sum_{i=1}^{N}\sum_{j=1}^{N} x_i x_j \alpha_{ij} a_{ij} \\
&= \sum_{i=1}^{N}\sum_{j=1}^{N} x_i x_j (1-k_{ij})\sqrt{\alpha_i a_i \alpha_j a_j} \\
b &= \sum_{i=1}^{N} x_i b_i \\
A &= \frac{\alpha a p}{\mathcal{R}_u^2 T^2} \\
B &= \frac{bp}{\mathcal{R}_u T}
\end{aligned}
\tag{B.4}
$$

APPENDIX C

JACOBIAN MATRICES

C.1 One-Dimensional Analysis

$$\mathbf{T} = \begin{pmatrix} \frac{1}{Z\mathcal{R}T} & 0 & -\frac{\rho}{C_pT} & \rho\Omega_1 & \cdots & \rho\Omega_{N-1} \\ \frac{u_r}{Z\mathcal{R}T} & \rho & -\frac{\rho u_R}{C_pT} & \rho u_r\Omega_1 & \cdots & \rho u_r\Omega_{N-1} \\ \frac{H}{Z\mathcal{R}T} - 1 & \rho u_r & \rho(1-\frac{H}{C_pT}) & \rho H\Omega_1 & \cdots & \rho H\Omega_{N-1} \\ \frac{Y_1}{Z\mathcal{R}T} & 0 & -\frac{\rho Y_1}{C_pT} & \rho\Theta_1 & \cdots & \rho Y_1\Omega_{N-1} \\ \vdots & \vdots & \vdots & \vdots & \ddots & \vdots \\ \frac{Y_{N_1}}{Z\mathcal{R}T} & 0 & -\frac{\rho Y_{N-1}}{C_pT} & \rho Y_{N-1}\Omega_1 & \cdots & \rho\Theta_{N-1} \end{pmatrix}$$

$$\mathbf{A} = \begin{pmatrix} \frac{u_r}{Z\mathcal{R}T} & \rho & -\frac{\rho u_r}{C_pT} & \rho u_r\Omega_1 & \ldots & \rho u_r\Omega_{N-1} \\ 1+\frac{u_r^2}{Z\mathcal{R}T} & 2\rho u_r & -\frac{\rho u_r^2}{C_pT} & \rho u_r^2\Omega_1 & \ldots & \rho u_r^2\Omega_{N-1} \\ \frac{u_rH}{Z\mathcal{R}T} & \rho(H+u_r^2) & \rho u_r(1-\frac{H}{C_pT}) & \rho u_RH\Omega_1 & \ldots & \rho u_rH\Omega_{N-1} \\ \frac{u_rY_1}{Z\mathcal{R}T} & \rho Y_1 & -\frac{\rho u_rY_1}{C_pT} & \rho u_r\Theta_1 & \ldots & \rho u_rY_1\Omega_{N-1} \\ \vdots & \vdots & \vdots & \vdots & \ddots & \vdots \\ \frac{u_rY_{N-1}}{Z\mathcal{R}T} & \rho Y_{N-1}\alpha_1 & -\frac{\rho u_rY_{N-1}}{C_pT} & \rho u_rY_{N-1}\Omega_1 & \ldots & \rho u_r\Theta_{N-1} \end{pmatrix},$$

where

$$\Omega_i = -M\left(\frac{1}{M_i} - \frac{1}{M_N}\right) + \frac{(h_i - h_N)}{C_pT}, \text{ and } \Theta_i = 1 + Y_i\Omega_i \qquad \text{(C.1)}$$

and M is the molecular weight of the mixture.

$$\mathbf{R} = \begin{pmatrix} 0 & 0 & 0 & 0 & \dots & 0 \\ 0 & \mu & 0 & 0 & \dots & 0 \\ 0 & -\frac{u_r\lambda}{C_p} & \frac{\lambda}{C_p} & R_1 & \dots & R_{N-1} \\ 0 & 0 & 0 & \rho\mathcal{D}_{1m} & \dots & 0 \\ \vdots & \vdots & \vdots & \vdots & \ddots & \vdots \\ 0 & 0 & 0 & 0 & \dots & \rho\mathcal{D}_{(N-1)m} \end{pmatrix}$$

where

$$R_i = -\frac{\lambda}{C_p}(h_i - h_N) + \rho\mathcal{D}_{im}(h_i - h_N) \tag{C.2}$$

C.2 Two-Dimensional Analysis

The number of species components involved in the system is assumed to be N. The Jacobian matrices are given below

$$\mathbf{T} = \begin{pmatrix} \frac{1}{Z\mathcal{R}T} & 0 & 0 & -\frac{\rho}{C_pT} & \rho\Omega_1 & \cdots & \rho\Omega_{N-1} \\ \frac{u}{Z\mathcal{R}T} & \rho & 0 & -\frac{\rho u}{C_pT} & \rho u\Omega_1 & \cdots & \rho u\Omega_{N-1} \\ \frac{v}{Z\mathcal{R}T} & 0 & \rho & -\frac{\rho v}{C_pT} & \rho v\Omega_1 & \cdots & \rho v\Omega_{N-1} \\ \frac{H}{Z\mathcal{R}T} - 1 & \rho u & \rho v & \rho(1 - \frac{H}{C_pT}) & \rho H\Omega_1 & \cdots & \rho H\Omega_{N-1} \\ \frac{Y_1}{Z\mathcal{R}T} & 0 & 0 & -\frac{\rho Y_1}{C_pT} & \rho\Theta_1 & \cdots & \rho Y_1\Omega_{N-1} \\ \vdots & \vdots & \vdots & \vdots & \vdots & \ddots & \vdots \\ \frac{Y_{N_1}}{Z\mathcal{R}T} & 0 & 0 & -\frac{\rho Y_{N-1}}{C_pT} & \rho Y_{N-1}\Omega_1 & \cdots & \rho\Theta_{N-1} \end{pmatrix}$$

where M is the molecular weight of the mixture and

$$\Omega_i = -M(\frac{1}{M_i} - \frac{1}{M_N}) + \frac{(h_i - h_N)}{C_p T}, \quad \text{and} \quad \Theta_i = 1 + Y_i \Omega_i$$

The convective term Jacobians A in the ξ direction is written as

$$\mathbf{A} = \begin{pmatrix} \frac{U}{Z\mathcal{R}T} & \rho\alpha_1 & \rho\alpha_2 & -\frac{\rho U}{C_p T} & \rho U\Omega_1 & \dots & \rho U\Omega_{N-1} \\ \alpha_1 + \frac{uU}{Z\mathcal{R}T} & \rho(U + u\alpha_1) & \rho u\alpha_2 & -\frac{\rho uU}{C_p T} & \rho uU\Omega_1 & \dots & \rho uU\Omega_{N-1} \\ \alpha_2 + \frac{vU}{Z\mathcal{R}T} & \rho v\alpha_1 & \rho(U + v\alpha_2) & -\frac{\rho vU}{C_p T} & \rho vU\Omega_1 & \dots & \rho vU\Omega_{N-1} \\ \frac{UH}{Z\mathcal{R}T} & \rho(H\alpha_1 + uU) & \rho(H\alpha_2 + vU) & \rho U(1 - \frac{H}{C_p T}) & \rho UH\Omega_1 & \dots & \rho UH\Omega_{N-1} \\ \frac{UY_1}{Z\mathcal{R}T} & \rho Y_1\alpha_1 & \rho Y_1\alpha_2 & -\frac{\rho UY_1}{C_p T} & \rho U\Theta_1 & \dots & \rho UY_1\Omega_{N-1} \\ \vdots & \vdots & \vdots & \vdots & \vdots & \ddots & \vdots \\ \frac{UY_{N-1}}{Z\mathcal{R}T} & \rho Y_{N-1}\alpha_1 & \rho Y_{N-1}\alpha_2 & -\frac{\rho UY_{N-1}}{C_p T} & \rho UY_{N-1}\Omega_1 & \dots & \rho U\Theta_{N-1} \end{pmatrix},$$

$$\mathbf{R}_{\eta\eta} = \begin{pmatrix} 0 & 0 & 0 & 0 & 0 & \dots & 0 \\ 0 & R_{22} & R_{23} & 0 & 0 & \dots & 0 \\ 0 & R_{32} & R_{33} & 0 & 0 & \dots & 0 \\ 0 & R_{42} & R_{43} & R_{44} & R_{45} & \dots & R_{46} \\ 0 & 0 & 0 & 0 & R_{55} & \dots & 0 \\ \vdots & \vdots & \vdots & \vdots & \vdots & \ddots & \vdots \\ 0 & 0 & 0 & 0 & 0 & \dots & R_{66} \end{pmatrix},$$

where

$$R_{22} = \left(\frac{4}{3}\alpha_1^2 + \alpha_2^2\right)\mu \tag{C.3}$$

$$R_{23} = \frac{1}{3}\alpha_1\alpha_2\mu \tag{C.4}$$

$$R_{32} = \frac{1}{3}\alpha_1\alpha_2\mu \tag{C.5}$$

$$R_{33} = \left(\alpha_1^2 + \frac{4}{3}\alpha_2^2\right)\mu \tag{C.6}$$

$$R_{42} = \left(\frac{4}{3}\alpha_1^2 + \alpha_2^2\right)\mu u + \frac{1}{3}\alpha_1\alpha_2\mu v - \left(\alpha_1^2 + \alpha_2^2\right)v\frac{\lambda}{C_p} \tag{C.7}$$

$$R_{43} = \frac{1}{3}\alpha_1\alpha_2\mu u + \left(\alpha_1^2 + \frac{4}{3}\alpha_2^2\right)\mu v - \left(\alpha_1^2 + \alpha_2^2\right)v\frac{\lambda}{C_p} \tag{C.8}$$

$$R_{44} = \left(\alpha_1^2 + \alpha_2^2\right)\frac{\lambda}{C_p} \tag{C.9}$$

$$R_{45} = \rho\left(h_1\mathcal{D}_1 - h_N\mathcal{D}_N\right) - \frac{\lambda}{C_p}\left(h_1 - h_N\right)\left(\alpha_1^2 + \alpha_2^2\right) \tag{C.10}$$

$$R_{46} = \rho\left(h_{N-1}\mathcal{D}_{N-1} - h_N\mathcal{D}_N\right) - \frac{\lambda}{C_p}\left(h_{N-1} - h_N\right)\left(\alpha_1^2 + \alpha_2^2\right) \tag{C.11}$$

$$R_{55} = \rho\mathcal{D}_1\left(\alpha_1^2 + \alpha_2^2\right) \tag{C.12}$$

$$R_{66} = \rho\mathcal{D}_{N-1}\left(\alpha_1^2 + \alpha_2^2\right) \tag{C.13}$$

where $U = \alpha_1 u + \alpha_2 v, \quad \alpha_1 = \xi_x, \alpha_2 = \xi_y$. The Jacobian matrices $\mathbf{B}$ and $\mathbf{R}_{\eta\eta}$ in the η direction is obtained by substitute α_1 with η_x and α_2 with η_y in matrices $\mathbf{A}$ and $\mathbf{R}_{\xi\xi}$, respectively.

APPENDIX D

SIMPLIFIED ANALYSIS OF DROPLET VAPORIZATION RESPONSE

The characteristics of unsteady droplet vaporization are examined here by means of a simplified analysis. A droplet with a mass $\bar{m}$ and a mean lifetime $\bar{\tau}_v$ is vaporizing in a forced oscillatory environment. The variations in vaporization rate depend on the difference between the vapor pressure at the droplet surface and the ambient pressure. However, the vapor pressure is mainly determined by the droplet surface temperature. Heat transferred into the droplet is induced by the temperature difference between the ambient gases and liquid droplet. There are several assumptions involved in the current analysis. First, the flow is treated in a one-dimensional spherical coordinate system. Second, the liquid temperature is considered to be uniform over the entire droplet but varies with time. The mass diffusivity is assumed to be inversely proportional to ambient pressure. Furthermore, a quasi-steady theory is needed to obtain the droplet lifetime.

Vaporization Rate:

The droplet vaporization rate can be determined by the time variation of total droplet mass

$$\mathrm{w} = -\frac{dm}{dt}, \tag{D.1}$$

where m and w are the instantaneous mass and vaporization rate, respectively. Using the perturbation concept, Eq. (D.1) can be developed into

$$-\frac{d}{dt}(m'\bar{m}+\bar{m}) = \mathrm{w}'\bar{\mathrm{w}}+\bar{\mathrm{w}} \tag{D.2}$$

After time averaging the above equation, the mean vaporization rate is

$$\bar{\mathrm{w}} = -\frac{d\bar{m}}{dt} \tag{D.3}$$

Substitute Eq. (D.3) into (D.2) to obtain

$$\frac{\bar{m}}{\bar{\mathrm{w}}}\frac{dm'}{dt} - m' = -\mathrm{w}'. \tag{D.4}$$

or

$$(1-\tau_v s)m' = \mathrm{w}' \tag{D.5}$$

where s is the Laplace operator and τ_v is the droplet lifetime and can be approximated by dividing the instantaneous mass with the vaporization rate

$$\bar{\tau_v} = \frac{\bar{m}}{\bar{\mathrm{w}}} \tag{D.6}$$

Assuming that the period of oscillation is much larger than the local gas residual time. Using the quasi-steady state theory, the droplet lifetime can be evaluated by the classical d^2-law.

$$\bar{\tau_v} = \frac{\bar{m}}{\bar{\mathrm{w}}} = \frac{r_s^2\bar{\rho}_\ell}{2\bar{\mathcal{D}}_s\bar{\rho}_s\ln(1+\bar{\mathcal{B}})}, \tag{D.7}$$

The quantities r, ρ_ℓ, ρ_s, and $\mathcal{D}_s$ are instantaneous droplet radius, liquid density, surface density and mass diffusivity, respectively. The variable, $\mathcal{B}$, is called the Spalding transfer number and is defined as

$$\mathcal{B} = \frac{C_{p,s}(T_\infty - T_s)}{\Delta h_v} = \frac{Y_{F,\infty} - Y_{F,s}}{Y_{F,s} - 1} \tag{D.8}$$

Since the surrounding gas is pure nitrogen, $Y_{F\infty}$ can be set to zero. Other quantities Y_{Fs}, T_∞, T_s, C_p, and Δh_v are the n-pentane concentration at the droplet surface, ambient temperature, surface temperature, specific heat on droplet surface, and latent heat of vaporization, respectively.

The vaporization rate predicted by the quasi-steady state theory can be expressed as

$$\mathrm{w} \;=\; 4\pi r_s^2 \rho_s v_s = 4\pi r_s \rho_s \mathcal{D}_s \ln \phi. \tag{D.9}$$

At low to moderate pressures, the diffusion coefficients vary inversely with density. Assuming $\mathcal{D}_s \propto \frac{1}{\rho_s}$ and $r \propto m^{1/3}$, Eq. (D.9) can be further developed into

$$\mathrm{w} = C_1 m^{1/3} \ln(1 + \mathcal{B}), \tag{D.10}$$

where C_1 is a constant. Again, as before, apply the small perturbation technique to this equation, a linearized equation is obtained.

$$\mathrm{w}' = \frac{1}{3} m' + \beta(p_s' - p_\infty') \tag{D.11}$$

where p_s and p_∞ are the surface vapor pressure and ambient pressure, respectively. The scaling factor β is written as

$$\beta = \frac{\dfrac{\bar{p}_s}{(\bar{p}_\infty - \bar{p}_s)}}{\ln[\dfrac{\bar{p}_\infty}{(\bar{p}_\infty - \bar{p}_s)}]}. \tag{D.12}$$

Vapor Pressure:

The vapor pressure on the droplet surface can be evaluated by Antoine's equation.

$$\ln p_s = a_1 - \frac{a_2}{T_s - a_3} \tag{D.13}$$

where a_1, a_2 and a_3 are constants depending on the mixture of concern[34]. The linearized perturbation equation is found to be

$$p'_s \approx bT'_s, \tag{D.14}$$

where b is defined as

$$b = \frac{a_2 \bar{T}_s}{(\bar{T}_s - a_3)^2} \tag{D.15}$$

Energy Balance on Droplet Surface:

The conservation law of energy must be satisfied at the droplet surface.

$$Q_{s\to\ell} = Q_{g\to s} - Q_{s\to g} \tag{D.16}$$

Using the perturbation technique together with the quasi-steady assumption, the linearized equation is written as

$$\bar{Q}_{s\to\ell} Q'_{s\to\ell} = \Delta h_v \mathrm{w}(Q'_{g\to s} - Q'_{s\to g}) \tag{D.17}$$

Heat Transfer from Ambient Gases:

The heat conducted into the droplet is treated as

$$Q_{g\to s} = 4\pi r_s^2 h(T_\infty - T_s) \tag{D.18}$$

Therefore,

$$Q'_{g\to s} = \frac{2}{3}m' - \frac{T_s}{T_\infty - T_s}T'_s \tag{D.19}$$

Heat Carried with Vaporized Fuel:

Energy convected away from the droplet can be obtained by evaluating the enthalpy increase in the vaporized fuel.

$$Q_{s\to g} = \Delta h_v \mathrm{w}. \tag{D.20}$$

The perturbed equation can be approximated by

$$\begin{aligned} Q'_{s\to g} &= \Delta h'_v + \mathrm{w}' \\ &= d_1 p'_\infty + d_2 T'_s + \mathrm{w}' \end{aligned} \tag{D.21}$$

where d_1 and d_2 are scaling constants and take the form

$$d_1 = \left(\frac{\partial \Delta h_v}{\partial T}\right)_{p\infty} \frac{T_s}{\Delta h_v} \tag{D.22}$$

$$d_2 = \left(\frac{\partial \Delta h_v}{\partial p_\infty}\right)_{T_s} \frac{p_\infty}{\Delta h_v} \tag{D.23}$$

Energy Transferred into Droplet:

Lumped Capacity Model:

Under the assumption that the droplet is treated as a lump of substance with an infinite thermal conductivity ($\lambda_\ell \longrightarrow \infty$). The transient temperature variation is determined by formulating an overall energy balance for the droplet.

$$\bar{m} C_{p,\ell} \frac{\partial T_s}{\partial t} = Q_{s\to\ell} \tag{D.24}$$

where $C_{p,\ell}$ and $q_{s\to\ell}$ are the liquid specific heat and heat flux conducted into the droplet interior, respectively. The linearized perturbation equation is written as

$$\bar{m}C_{p,\ell}\bar{T}_s\frac{dT_s'}{dt} = \bar{Q}_{s\to\ell}Q'_{s\to\ell} \tag{D.25}$$

Combine Eqs. (D.5), (D.11), (D.14), (D.17), (D.19), (D.21), and (D.25), and substitute dt/t with the Laplace parameter, $s = iw$, the droplet vaporization response function can be obtained as

$$R_p = \frac{\mathrm{w}'}{p'_\infty} = \frac{-3\beta(1-i\tau_v w)\Big[(bd_1+\Psi_R)+i\Psi_I\Big]}{\Big[2\Psi_R+3\tau_v w\Psi_I+b\beta\Big]+i\Big[2\Psi_I-3\Psi_R\tau_v w-3b\beta\tau_v w\Big]} \tag{D.26}$$

where

$$\Psi_R = \left(\frac{T_s}{T_\infty - T_s}+d_2\right) \tag{D.27}$$

$$\Psi_I = \frac{C_{p,\ell}T_s\tau_v w}{\Delta h_v} \tag{D.28}$$

$$d_1 = \left(\frac{\partial\Delta h_v}{\partial p_\infty}\right)_{T_s}\frac{p_\infty}{\Delta h_v} \tag{D.29}$$

$$d_2 = \left(\frac{\partial\Delta h_v}{\partial T_s}\right)_{p\infty}\frac{T_s}{\Delta h_v} \tag{D.30}$$

This transfer function represents the dynamic relationship between vaporization rate and ambient pressure oscillations. When a sinusoidal pressure fluctuation, $p'_\infty(t) = |p'|sin(\omega t)$, is superimposed to the ambient condition, the corresponding vaporization rate variation can be written as $\mathrm{w}'(t) = |\mathrm{w}'|sin(wt+\Theta_p)$, where $|\mathrm{w}'|$ and Θ_p are the amplitude and phase lag, respectively, and take the form

$$|R_p| = \left\{9\beta^2\frac{\Big[1+(\tau_v w)^2\Big]\Big[(bd_1+\Psi_R)^2+\Psi_I^2\Big]}{\Big[2\Psi_R+3\tau_v w\Psi_I+b\beta\Big]^2+\Big[2\Psi_I-3\Psi_R\tau_v w-3b\beta\tau_v w\Big]^2}\right\}^{0.5} \tag{D.31}$$

$$\Theta_p = tan^{-1}(-\tau_v w) \quad + \quad tan^{-1}\left(\frac{-\Psi_I}{-bd_1-\Psi_R}\right)$$

$$- \quad tan^{-1}\left(\frac{2\Psi_R + 3\tau_v w\Psi_I + b\beta}{2\Psi_I - 3\Psi_R\tau_v w - 3b\beta\tau_v w}\right) \qquad \text{(D.32)}$$

Finite Diffusion Model:

The transient diffusion response of energy transferred from the ambiance can be approximated by solving the transient one-dimensional heat conduction equation in a spherical coordinate with a forced-oscillatory surface temperature.

$$\frac{1}{\alpha}\frac{\partial T}{\partial t} = \frac{1}{r^2}\frac{\partial}{\partial r}\left(r^2\frac{\partial T}{\partial r}\right), \qquad \text{(D.33)}$$

Assuming the droplet temperature is uniformly distributed in space but varies with time. The initial temperature is selected to be equal to the surface temperature

$$t = 0 \quad , \quad T = \bar{T}_s$$

A prescribed temperature oscillation is first specified at the droplet surface to simulate the dynamic behavior of energy transfer into the liquid phase,

$$r = R \quad , \quad T = \bar{T}_s + |\bar{T}_s T_s'|e^{i\omega t}$$

$$r = 0 \quad , \quad T = \bar{T}_s,$$

where ω is the angular frequency. To solve this equation, four dimensionless parameters are introduced herein,

$$\eta = \frac{r}{R}, \quad \tau = \frac{\alpha t}{r^2}, \quad \Theta = \frac{T - \bar{T}_s}{|\bar{T}_s T_s'|}, \quad w^* = \frac{r^2 w}{\alpha}, \qquad \text{(D.34)}$$

where R is the initial droplet radius and α is the thermal diffusivity in the liquid phase. Thus, Eq. (D.33) becomes

$$\frac{\partial\Theta}{\partial\tau} = \frac{1}{\eta^2}\frac{\partial}{\partial\eta}\left[\eta^2\frac{\partial\Theta}{\partial\eta}\right] \qquad \text{(D.35)}$$

subject to the initial and boundary conditions

$$\tau = 0 \quad , \quad \Theta = 0$$

$$\eta = 1 \quad , \quad \Theta = e^{i\omega^*\tau}$$

$$\eta = 0 \quad , \quad \Theta = 0. \tag{D.36}$$

Therefore, Eq. (D.35) can be solved to obtain

$$\Theta = \frac{1}{\eta}\frac{sinh\left[\sqrt{\omega^*/2}(1+i)\eta\right]}{sinh\left[\sqrt{\omega^*/2}(1+i)\right]}e^{iw^*\tau}. \tag{D.37}$$

This equation provides the temperature profile and can be used to calculate the energy flux variation at the droplet surface.

$$\begin{aligned}
\bar{Q}_{s\to\ell}Q'_{s\to\ell} &= \left[\lambda A\frac{\partial T}{\partial r}\right]_{r=r_s} = 4\pi r_s^2\lambda_\ell\frac{\partial T}{\partial r}\bigg|_{r=r_s} \\
&= 4\pi r_s\lambda_\ell\bar{T}_s|T'_s|\left.\frac{\partial\Theta}{\partial\eta}\right|_{\eta=1} \\
&= 4\pi r_s\lambda_\ell\bar{T}_sF(\bar{w}^*)T'_s
\end{aligned} \tag{D.38}$$

where λ_ℓ is the liquid thermal conductivity, and

$$F(\bar{w}^*) = (i\bar{w}^*)^{\frac{1}{2}}coth(i\bar{w}^*)^{\frac{1}{2}} - 1$$

Combine Eqs. (D.5), (D.11), (D.14), (D.17), (D.19), (D.21), and (D.38), and substitute dt/t with the Laplace parameter, $s = iw$, the droplet vaporization response function can be obtained as

$$R_p = \frac{\mathrm{w}'}{p'_\infty} = \frac{-3\beta(1-i\tau_v w)\Big[(b\Delta h_v \mathrm{w}d_1 + \Psi_R) + i\Psi_I\Big]}{\Big[2\Psi_R + 3\tau_v w\Psi_I + b\beta\Delta h_v\mathrm{w}\Big] + i\Big[2\Psi_I - 3\tau_v w\Psi_R - 3\tau_v wb\beta\Delta h_v\mathrm{w}\Big]} \tag{D.39}$$

where

$$\Psi_R = 4\pi R\lambda_\ell T_s Re[F(w^*)] + \Delta h_v\left(\frac{T_s}{T_\infty - T_s}\right) + d_2\Delta h_v \mathrm{w} \quad \text{(D.40)}$$

$$\Psi_I = 4\pi R\lambda_\ell T_s Im[F(w^*)] \quad \text{(D.41)}$$

The magnitude and phase angle of the response function R_p are

$$|R_p| = \left\{ \frac{9\beta^2\Big[1+(\tau_v w)^2\Big]\Big[(b\Delta h_v \mathrm{w} d_1 + \Psi_R)^2 + \Psi_I^2\Big]}{\Big[2\Psi_R + 3\tau_v w\Psi_I + b\beta\Delta h_v \mathrm{w}\Big]^2 + \Big[2\Psi_I - 3\tau_v w\Psi_R - 3\tau_v wb\beta\Delta h_v \mathrm{w}\Big]^2} \right\}^{0.5} \quad \text{(D.42)}$$

$$\Theta_p = tan^{-1}(-\tau_v w) + tan^{-1}\left(\frac{\Psi_I}{b\Delta h_v w d_1 + \Psi_R}\right) - tan^{-1}\left(\frac{2\Psi_I - 3\tau_v w\Psi_R - 3\tau_v wb\beta\Delta h_v \mathrm{w}}{2\Psi_R + 3\tau_v w\Psi_I + b\beta\Delta h_v \mathrm{w}}\right) \quad \text{(D.43)}$$